

# **The Temple Scroll and the Structural Properties of Collagen**

vorgelegt von Diplom-Physiker

**Roman Schütz**

geb. in Omsk

Von der Fakultät II - Mathematik und Naturwissenschaften  
der Technischen Universität Berlin  
zur Erlangung des akademischen Grades  
Doktor der Naturwissenschaften  
Dr. rer. nat.

**genehmigte Dissertation**

Promotionsausschuss:

Vorsitzende:	Prof. Dr. Birgit Kanngießer
Gutachter:	Prof. Dr. Christian Thomsen
Gutachter:	Prof. Dr. Peter Fratzl

Tag der wissenschaftlichen Aussprache: 16. September 2015

Berlin 2015



## Zusammenfassung

Die „Schriftrollen vom Toten Meer“ stoßen seit ihrer Entdeckung Mitte des letzten Jahrhunderts bei den Religionshistorikern und in der breiten Öffentlichkeit auf großes Interesse. Sie stammen aus der Zeit der Zweiten Tempelperiode - der Wiege des Christentums und dem Vorabend der Zerstörung des Tempels von Jerusalem durch die Römer. Diese Ereignisse haben den weiteren Verlauf der Menschheitsgeschichte entscheidend mitgeprägt.

Dem Text der Rollen hat die Forschung sehr viel Aufmerksamkeit gewidmet, denn er enthält einen gewaltigen Schatz an archäologisch und historisch relevanten Informationen. Wichtige Informationen aus der Zeit der Herstellung, Benutzung und Lagerung verbergen sich aber auch in den bisher weniger erforschten Materialcharakteristiken des Pergaments, auf das die meisten der Texte geschrieben wurden. Traditionell wurde das Pergament aus Tierhäuten hergestellt.

Wie schon der Titel suggeriert, behandelt die vorliegende Arbeit im Wesentlichen zwei Forschungsprojekte. Zum einen wurde das Material einer dieser antiken Schriftrollen, der Tempelrolle, erforscht und dabei der Zustand der Kollagenfasern darin charakterisiert. Das Kollagen ist das meistvorkommende Protein bei Säugetieren wie dem Menschen, es ist ein wichtiger Bestandteil von Knochen, Sehnen sowie der Haut und damit auch vom Pergament. Zum anderen wurde das Kollagen als biologisches Material hinsichtlich seiner natürlichen Funktionalität untersucht.

Von besonderem Interesse waren dabei Veränderungen der strukturellen und mechanischen Eigenschaften des Kollagens in Abhängigkeit von der Feuchtigkeit. Es ist bekannt, dass sich Kollagenfasern bei Dehydrierung verkürzen und dabei erhebliche Zugkräfte entwickeln. Unsere Messergebnisse haben gezeigt, dass dies bereits bei so geringer Dehydrierung der Fall ist, wie sie in biologischer Umgebung über die dort herrschenden osmotischen Drücke auftritt. Es ist daher davon auszugehen, dass diese Effekte auch im lebenden Organismus von Bedeutung sind. Für das physikalische Verständnis der Verkürzungsmechanismen spielt es eine große Rolle, auf welcher hierarchischen Organisationsebene der Kollagenfasern die strukturellen Veränderungen auftreten. Untersucht wurde dieser Aspekt im Rahmen der vorliegenden Arbeit durch Experimente mit synchrotron-basierter Röntgenstreuung und Polarisations-Raman-Spektroskopie (PRS), die bei kontrollierter Feuchtigkeit und in Kombination mit gleichzeitigen Dehnexperimenten durchgeführt wurden.

Mit Hilfe von Raman-Spektroskopie und Absorptionsspektroskopie in Ferninfrarotem Bereich (Far-IR) wurde darüber hinaus der Einfluss von Dehnung und Luftfeuchtigkeit auf das Kollagen-Schwingungsspektrum bestimmt. Letzteres lässt Rückschlüsse auf die molekulare Umgebung bestimmter chemischer Gruppen in den Kollagenfasern zu. Dabei hat sich gezeigt, dass der Wassergehalt die chemischen Eigenschaften der Fasern weitaus stärker beeinflusst als eine erzwungene mechanische Dehnung. Zusammen mit der beobachteten Reversibilität der Dehydrierung lässt dieser Sachverhalt darauf schließen, dass Wasser eine entscheidende Rolle für die Stabilität der Faserstruktur spielt und als integraler Bestandteil der Kollagenmoleküle verstanden werden muss.

Im Zuge der Untersuchungen an Kollagen haben sich die beschriebenen Spektroskopietechniken unter Berücksichtigung der Polarisierung auch als vielversprechend für die Degradationsanalyse kollagenhaltiger Pergamente erwiesen. Intaktes Kollagen bildet in seiner molekularen Packungsorganisation einen sehr hohen Orientierungsgrad, sodass die Amid I Bande im Raman Spektrum eine starke Anisotropie aufweist. Eine Reduktion dieser Anisotropie bei historischem Pergament lässt auf zerfallsbedingte strukturelle Veränderungen schließen, die im Extremfall auf vollständige Gelatinisierung des Kollagens, also der Auflösung der inneren Faserstruktur, hindeuten.

Bei der Untersuchung der Tempelrolle ist es uns gelungen, den Degradationsgrad der Kollagenfasern mikroskopisch ortsaufgelöst zu quantifizieren. Dabei stellte sich heraus, dass die Rolle im Wesentlichen aus zwei Schichten besteht, einer üblichen Hautschicht und einer darauf aufgetragenen anorganischen Schicht. Unter der anorganischen Schicht ließen sich weitgehend intakte Kollagenfasern nachweisen. Aufgrund von früheren Röntgenuntersuchungen, denen die beschriebene Ortsauflösung fehlte, war man bisher davon ausgegangen, dass die Tempelrolle stark gelatiniert sei. Der in Bezug auf den Degradationsgrad des Kollagens heterogene Aufbau der Rollen, den unsere Experimente offenbart haben, deutet nun auf eine besondere Herstellungsmethode hin: Demnach wurde möglicherweise die zur Pergamentherstellung verwendete Haut zunächst entlang der Fläche gespalten. Im Anschluss wurde der kollagenhaltige Hautanteil der Fleischseite in einer wässrigen Lösung von Kalzium- und Natriumsulfaten gekocht und somit gelatinisiert. Die resultierende Paste wurde dann auf die Fleischseite der verbliebenen dünnen und vermutlich völlig transparenten Haut wieder aufgetragen. Das degradierte Kollagen derselben Haut in gelatinisierter Form wirkte dabei als Stabilisator und Bindemittel der anorganischen Schicht auf der Fleischseite der Haut. Anschließend wurde der Text nicht wie üblich auf der äußeren Haarseite des Pergaments, sondern auf der inneren anorganischen Schicht der weißlich durchschimmernden Schriftrolle geschrieben.



Wie eingangs erwähnt, gehört die Tempelrolle zu den Schriftenrollen vom Toten Meer, auch bekannt als „Qumran Rollen“. Der Inhalt des Manuskripts überliefert eine zuvor unbekannte, detaillierte Anleitung zum Tempelbau. Zusammen mit Beschreibungen ritueller Vorschriften und Feste bildet dieses Manuskript ein Zeitzeugnis, das bis zur seiner Entdeckung unbekannte Facetten der damaligen Jüdischen Kultur offenbart. Die Rolle überrascht aber nicht nur inhaltlich, auch das Material weist eine völlig unbekannte und für den Fundort untypische Herstellungsmethode für Schriftrollen auf. Mit einem interdisziplinären archeometrischen Ansatz und unter Anwendung von zerstörungsfreien Messmethoden zur Materialanalyse ist es uns in der vorliegenden Arbeit gelungen, die Herstellung der Tempelrolle zu rekonstruieren. Viele der neu gewonnen Erkenntnisse über das Material der Tempelrolle, wie z.B. das Auftreten von Nitraten ausschließlich im Kollagen, werfen allerdings noch Fragen auf und motivieren weitergehende Untersuchungen.



## Abstract

Since their discovery in the late 1940s, the Dead Sea Scrolls have not stopped attracting the attention of scholars and the broad public alike, because they were created towards the end of the Second Temple period and the “time of Christ”. Most of the research on the Dead Sea Scrolls has been dedicated to the information contained in the scrolls’ text, even though the physical aspects of the writing materials also contain important information with archaeological and historical value. The research presented in this work can be subdivided in two tracks that are also described in the title: the study of an ancient manuscript written on parchment, which is a writing material derived from animal skin, and the structural properties of collagen interacting with water. Collagen is the most abundant protein in mammals, as it is found in bone, tendons, and skin - and as a consequence, also in parchments. The properties of collagen are the link between the two main subjects of this research project.

The structural and material properties of the collagen -water system play a significant role in both the context of an extracellular matrix biomaterial with specific properties in the physiological conditions in the body, and the skin which is treated during the parchment production process. Furthermore, understanding the influence of changes in the environmental temperature and humidity during the use and the storage of fragile ancient documents is crucial for developing parchment conservation strategies. In this work, a large effort was dedicated towards improved understanding of the range of structural features throughout the hierarchical levels of collagen - from the nanoscale helical, up through the fibrillar and the macroscopic scales. In physiological conditions, this knowledge improves our understanding of the intimate interactions between the proteinaceous material and the surrounding tissue. The analyzes were performed on collagen from rat tail tendons (RTT) using polarized Raman Spectroscopy (PRS) and *in situ* synchrotron X-Ray scattering with humidity-controlled mechanical testing. Dehydration experiments showed that the drying collagen molecule shrinks differently throughout the hierarchical levels, and that this generates surprisingly high stresses. The drying stresses generated are so large that even slight changes in osmotic pressure in fully hydrated condition lead to significant force generation. This result suggests a possible role of extracellular collagen matrix in fundamental, biologically relevant processes such as signaling, tissue prestress and tissue biomechanics.

Complementary to the PRS and X-rays scattering studies, the vibrational absorbance of collagen in the far infra-red region (Far-IR, 80-500cm<sup>-1</sup>) has been explored and elaborated for damage assessment of parchments. Because the far-IR measurements must be performed in

vacuum, a sealed humidity-controlled chamber was built to investigate the stress and humidity influences onto collagen-based materials. In this context, thin lamellar bovine bone slices were stepwise demineralized, and the spectral features of mineral and collagen in the far-IR region were also resolved for the first time.

Furthering the use of this acquired, basic knowledge on collagen, a multidisciplinary approach was designed to study an ancient manuscript belonging to the collection of Dead Sea Scrolls, namely the Temple Scroll. The main goals in this study were non-invasive assessment of the preservation state of the precious Scroll material, and the reconstruction of the manuscript manufacturing technique. For these purposes, a confocal PRS approach was applied towards the study of fresh and fully deteriorated collagenous reference materials: tendon collagen and gelatin. Native collagen molecules stagger into a hierarchically organized scaffold that can be affected by deterioration and aging processes. The main effect of this deterioration process is that the well-organized collagen structure transforms into random-coiled structures that are equivalent to gelatine. Once measureable limits of defined parameters were defined with structurally well-organized and disordered reference samples, the preservation state of the collagen fibers within the scroll was characterized.

In the ancient fragment, two different regions of interest were observed. The bulk, collagen-based, organic substrate was covered with an inorganic layer consisting mainly of calcium and sodium sulfate compounds. PRS characterization of the TS layered system revealed the presence of well-preserved collagen fibers within the deeper, collagenous bulk layer. The relatively good collagen preservation is in agreement with the macroscopic appearance of the scroll material, but it contradicts the X-Ray diffraction studies from the literature that showed a strong gelatinization and racemization of the TS collagen. This contradictory result could be explained by the use of gelatin as a binding material within the inorganic layer, which could not be distinguished from the bulk material by the previous X-Ray studies.

Taking into consideration all the findings, a model of an unknown ancient manufacturing procedure was proposed. The skin was probably split, and the flesh-side was gelatinized in order to bind material within an inorganic layer that is meant to cover the gaunt and transparent bulk layer. The text was then written on top of this inorganic layer that was laid on the flesh-side, instead on the hair-side of the skin, which may also explain the extraordinary beauty of the ancient Temple scroll.

# Index of content

ZUSAMMENFASSUNG.....	3
ABSTRACT .....	7
INDEX OF CONTENT.....	9
<b>1 INTRODUCTION.....</b>	<b>11</b>
1.1 THE TEMPLE SCROLL.....	14
<i>Textual content of the Temple Scroll .....</i>	<i>16</i>
<i>Physical Appearance of the Temple Scroll.....</i>	<i>19</i>
1.2 COLLAGEN .....	20
1.3 COLLAGEN IN PARCHMENT.....	25
1.4 POLARIZED RAMAN SPECTROSCOPY ON UNIAXIAL SYMMETRY .....	30
<b>2 INFLUENCE OF HYDRATION ON MOLECULAR STRUCTURE AND MECHANICAL BEHAVIOUR OF COLLAGEN.</b>	<b>37</b>
2.1 MATERIALS AND METHODS .....	40
<i>Rat tail tendon (collagen) – RTT.....</i>	<i>40</i>
<i>The relationship of relative humidity to osmotic pressure .....</i>	<i>40</i>
<i>Uni-Axial tensile testing in a controlled environment.....</i>	<i>41</i>
<i>Polarized Raman spectroscopy – PRS.....</i>	<i>42</i>
<i>X-Ray diffraction – XRD .....</i>	<i>43</i>
2.2 RESULTS AND DISCUSSION .....	43
2.2.1 PRS applied to observe molecular deformation in RTT while stretching in hydrated condition.....	44
2.2.2 Dehydration of RTT induces high tensile forces and conformational changes on intermolecular levels	48
2.3 STRUCTURAL MODEL FOR THE INTERACTION OF WATER AND COLLAGEN.....	61
<b>3 DETERIORATION ANALYSIS OF COLLAGEN STUDIED BY FAR INFRA-RED SPECTROSCOPY .....</b>	<b>67</b>
3.1 EXPERIMENTAL SET UP AND MATERIALS MEASURED .....	71
3.1.1 Focal spot.....	73
3.1.2 Controlled environment sample chamber.....	75
3.1.1 Materials .....	77
3.2 RESULTS .....	78
3.2.1 Mineral and collagen contribution in the bone spectrum.....	78
3.2.2 Linear dichroism on mineral and collagen in bone.....	80
3.2.3 Moisture and stress influence on spectral characteristics of collagen.....	82
3.2.4 Spectral comparison between demineralized bone collagen, gelatin and modern parchment.....	83
3.3 DISCUSSION.....	86

<b>4</b>	<b>IN-SITU DAMAGE ASSESSMENT OF COLLAGEN WITHIN THE TEMPLE SCROLL ON MICROSCOPIC SCALE.</b>	<b>91</b>
4.1	MATERIALS AND METHODS .....	93
4.2	RESULTS .....	94
4.3	DISCUSSION.....	100
<b>5</b>	<b>THE TEMPLE SCROLL ANALYSIS .....</b>	<b>103</b>
5.1	MATERIALS AND METHODS .....	103
5.2	RESULTS .....	106
5.3	DISCUSSION.....	120
<b>6</b>	<b>RECONSTRUCTION OF AN UNKNOWN ANCIENT MANUFACTURE PRACTICE.....</b>	<b>129</b>
	<i>Split and unstretched parchment in the Temple Scroll .....</i>	<i>129</i>
	<i>Treatment with DS water .....</i>	<i>130</i>
	<i>Presence of nitrates.....</i>	<i>133</i>
	<i>Text written on the inorganic layer on the skin's flesh side.....</i>	<i>135</i>
	<i>Preparation of the inorganic layer .....</i>	<i>136</i>
<b>7</b>	<b>CONCLUSION.....</b>	<b>141</b>
	<b>LIST OF ABBREVIATIONS .....</b>	<b>144</b>
	<b>REFERENCES .....</b>	<b>145</b>
	<b>LIST OF AUTHORS' PUBLICATIONS RELATED TO THIS WORK .....</b>	<b>A-I</b>
	<b>SUPPLEMENTAL MATERIALS .....</b>	<b>A-II</b>
	<b>EIDESSTATTLICHE ERKLÄRUNG.....</b>	<b>A-V</b>
	<b>DANKSAGUNG.....</b>	<b>A-VII</b>

# 1 Introduction

TS-11Q19, Col.47:4-17 [13]

“... The city <sup>4</sup>that I shall sanctify by establishing My name and temp[le] there must be holy and <sup>5</sup>pure from anything that is in any way unclean, by which one might be defiled. ... No skin of a clean animal that has been slaughtered <sup>8</sup>in other cities is to enter My city. ... If <sup>16</sup>you have sacrificed the animal in My temple, the skin is pure for use in My temple; but if you have slaughtered the animal in another city, it is pure <sup>17</sup>only for use in other cities. ...”

The efforts made by religious people in ancient Israel associated with manuscript manufacturing, to use only carefully selected materials and proper techniques for the production of such a unique medium being worthy to carry the words of God himself, must have been enormous. The Temple Scroll (TS-11Q19), made of treated animal skin (parchment), was discovered in the middle of the last century, almost two millennia after its deposition at the destruction time of the Second Temple (Jerusalem). It was deposited and remained hidden for centuries in a cave close to the archaeological site called Qumran at the north-west shore of the Dead Sea. With many other biblical and parabiblical manuscripts, it belongs to the Qumran or Dead Sea Scrolls (DSS) collection but it is distinct from other manuscripts through its appearance and the unique content.

This manuscript earned its name because fifty percent of its content is dedicated to detailed instructions of the architectonic construction of the Temple, a place of God's Shekhinah (dwelling of the Divine Presence of God). In such or a similar way it was considered by the people who probably produced and later used the scroll. The TS is not only important because of its content revealing unknown aspects of the multifaceted spectrum of the Jewish religion in those days, but also because of its physical material, which might provide information about ancient knowledge and technology in scroll production. More details about the background, content and the origin of the TS are provided in the next chapter section 1.0.

Biological materials studied within an archaeological context, such as the TS and other ancient manuscripts made of animal skin/ parchment, carry many types of information, namely:

1) Manufacture: How it was produced? Which materials were used? Where was the manufacturing site? Where and how did the possible technological knowledge exchange between different cultures take place?

2) Usage: How and where was the scroll used?

3) Storage: What can we learn about the place, the environmental and maybe even climate issues during the storage duration? Can we learn about those conditions that will ultimately help us in defining the optimal preservation conditions to optimize the storage of these magnificent documents for generations to come?

Answers to these questions can contribute to the basic understanding of our past, which formed our cultures in various ways. They, however, cannot be revealed by the classical archaeology and related social sciences alone. The natural sciences are called upon to contribute with the latest technical developments and scientific achievements. In the last decades, it has been pioneered by the group of Professor Steve Weiner and also others to turn archaeological sites into “outdoor laboratories”. These outdoor laboratories interactively increase the quality and precision of reconstructions during digging. The joint work of different scientific fields in the multidisciplinary approach offers a huge potential in the context of modern research.

Furthermore, the efforts that advance research of one subject area can in turn be useful in another very important scientific field, and vice versa. For example, developments and discoveries in the medical fields were quickly transferred into the archaeological world. Advanced  $\mu$ -CT devices normally used to diagnose diseases were used in fantastic studies of Egyptian mummies. However, sometimes advances in archaeometrically motivated research on biological materials can in turn bring forward the fundamental understanding of medical science [14-16]. This work is a contribution to such a multidisciplinary research that reveals new understanding of a biological material, namely collagen, where the main findings show potential applications in both biological and biomedical fields, as well as in the production of the man-made materials, such as parchment.

As the title of this work reveals; “The Temple Scroll and the structural properties of collagen”, this research follows equally two main tracks of interest. It is the Temple Scroll analysis with the goal of its material characterization leading to a reconstruction of an unknown ancient manufacture practice on the one hand and the deepening of fundamental knowledge of the structural properties and functionalities of collagen under influence of dehydration on the other hand. Collagen, the most abundant protein in mammals, is a versatile structural molecule and is used as a building block in many highly organized tissues, such as bone, skin, and



cornea. The functionality and performance of these tissues is controlled by their hierarchical organization ranging from the molecular up to macroscopic length scales.

The molecular structure and the integrity of organization within the collagen fibrils comprise the bridge between the two tracks of interest of this research. Modern and ancient leather and parchment production involves an extensive procedure of hydration and dehydration cycles with different chemical agents that can influence the properties and structure of collagen, its main constituent material. On the other hand, time induces collagen deterioration, a process that affects the molecular structure of collagen, leading to a process called gelatinization, where the intermolecular structure loosens its organization and becomes more disordered. It is of great importance, and the responsibility of our generation to characterize the state of degradation within the parchment properly, and to try to slow down the processes that lead to further destruction of these precious artefacts. The challenge hereby is: whatever analyses need to be performed on materials with cultural heritage, they should not damage or anyhow harm the materials.

In this work, we therefore explored a noninvasive method based on a confocal polarized Raman spectroscopy (PRS), which allows *in-situ* monitoring of the orientation and disordering of collagen on molecular and fibrillar levels. The methodology was first characterized on fresh collagen fibers from rat tail tendon (chapter 2), a material that is a good reference material, because of its high order of molecular anisotropy. In this thesis, the influence of humidity and stress on the structural and mechanical properties of rat tail tendon was studied extensively by a multi technical approach. The findings were then applied on the collagen characterization within the Temple Scroll (chapter 4). In chapter 3 we alternatively explored the use of Far Infrared (Far-IR) spectroscopy to analyze collagen deterioration. Along the work done on the characterization of collagen in the Far-IR region, the spectral and anisotropic properties of the mineral within the lamellar bovine bone were investigated and reported as well. In chapter 5 we applied all of our understanding of collagen analysis and a further set of non-destructive techniques to characterize the material composition of the Temple Scroll.

These research findings combined with an interdisciplinary approach of carefully studying the scroll's content and other related textual sources, allowed us to develop a model for the possible ancient manufacturing technique of the fascinating ancient manuscript; the Temple Scroll, from now on abbreviated as TS (Chapter 6).

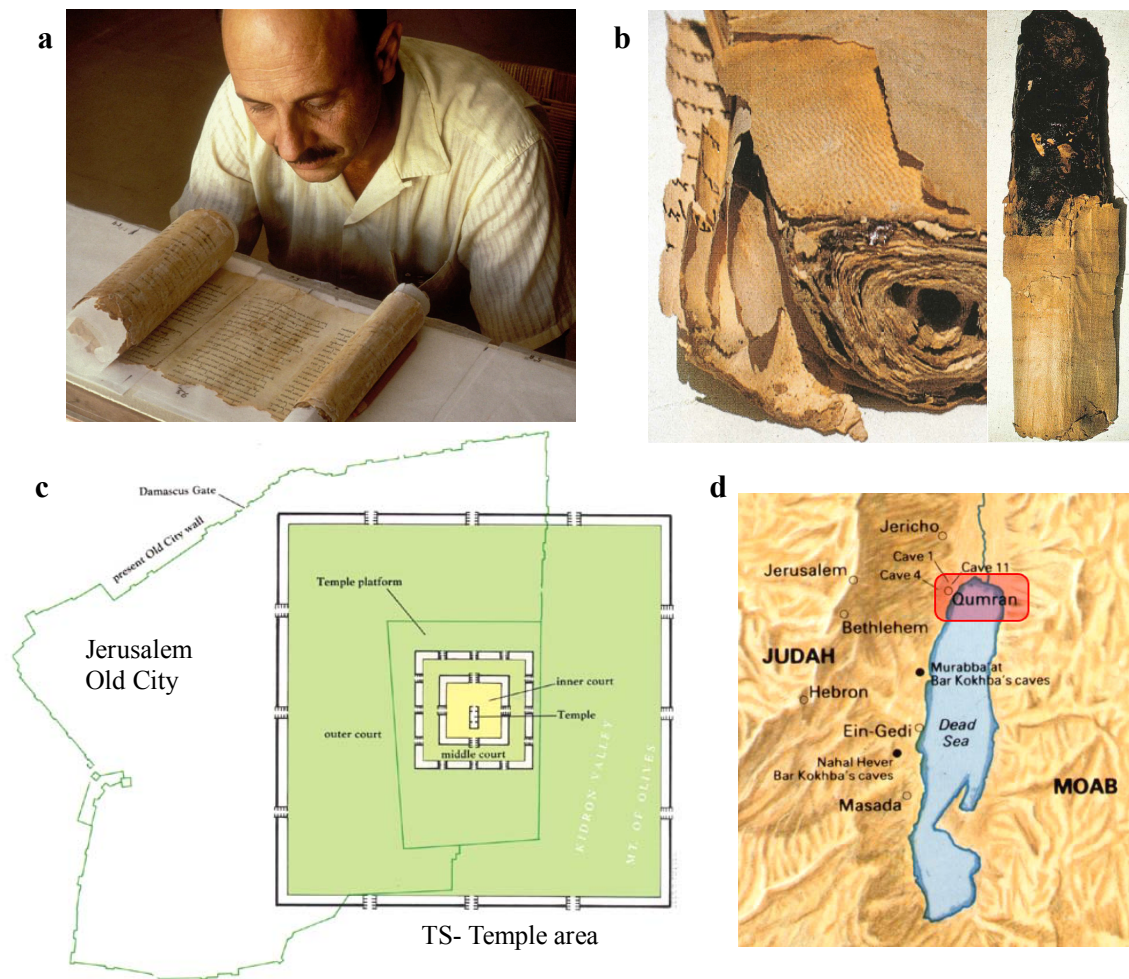
## **1.1 The Temple Scroll**

*Almost 2000 years have passed until the priceless treasure, a contemporary witness of the Second Temple period known as the Qumran Scrolls (QS) or the Dead Sea Scrolls (DSS), saw daylight again and attracted the attention of historians, scholars and the general public. In the middle of the last century, between 1947 and 1956, in times of turbulent developments of the modern history of Israel, an accidental discovery of ancient Jewish texts offered an insight into a decisive historical period of the region. These scripts witnessed historical turbulences and upheavals that shaped the society to come. The youngest scrolls were written at the eve of the destruction of the Second Temple and the longest exile of Israel that followed. They are physical witnesses from the time when expectation of Messiah became prominent in the landscape of various religious sects within Judaism, from the time Christianity was born.*

The fascination about the discovery of the DSS can also be expressed through multiple other perspectives. The DSS were found in different places along the western shore of the Dead Sea; the largest collection were discovered in caves close to the ruins of an ancient settlement today called Khirbet Qumran (Arabic: “Ancient ruins”), Figure 1d. There is still an ongoing debate among scholars about the mystery of the origin of the Qumran scrolls. Qumran is located in the north western part of the Dead Sea, not far away from the area where the itinerant preacher “John the Baptist” lived and baptized in the Jordan River (according to the gospels in Matthew 3, Mark 1, Luke 3, John 1 and to Josephus Flavius in Antiq. 18.5.2, a Jewish historian from the first century AD). It is the location with the shortest connection to Jerusalem from the Jordan River and the Dead Sea, an important and geographically strategic location for Israel’s biblical history. According to the Bible (book of Joshua) the Israelites crossed the Jordan River and entered the Promised Land at that location after wandering in the desert for 40 years.

The Qumran Scrolls collection comprises some 18000 fragments that amount to ca. 700 – 900 manuscripts made of parchment, leather or in some rare cases, papyrus. A small number of scrolls were allegedly found in clay vessels. The larger part of the collection was composed of fragments lying unprotected on the floors of the caves. Accordingly, their state of preserva-

tion often varied from poor to very bad, whereas the scrolls stored over the centuries in clay jars found us in a relatively good condition.



**Figure 1:** a) Yigael Yadin with the Temple Scroll (TS) (Photo: Zev Radovan); b) TS-photography from Yadin's Book – The Temple Scroll [1]: the upper part of the scroll was very damaged, on the more preserved section, the pattern of removed hairs can be recognized on the opposite side of the text. The writing on the flesh side is uncommon for the DSS. c) Depiction of the Temple area as described in TS compared with the Old City of Jerusalem (by Leen Ritmeyer) [3]. Three separated courts surround the Temple, but only the two inner courts fit into the area of the Temple Rock and the area of the second Temple (Herodian); d) Location of Qumran and cave 11, where the TS was found near the Dead Sea [10].

The Qumran collection contains multiple copies of every book of the Hebrew Bible except the Book of Esther. But it was the presence of apocryphal works known from the Christian literature and unknown sectarian writings that triggered the major change in our understanding of the society at the turn of the era about Judaism and early Christianity.

The Temple Scroll (TS) is one of the books considered to be a sacred para-biblical scripture. It is a very special scroll with regard to its content and material properties. The TS was found by Bedouins in 1956 in cave 11 near Qumran; the cave is visible from the outside, but

was probably hardly used by people because it was inhabited by bats for at least hundreds of years, and has a distinctly foul smell. Allegedly, the scroll, wrapped in a cloth, was found in a clay jar. After its discovery it took another 11 years until it found its way to scholars. Following the battle for Jerusalem in the 6-days-war in 1967, a special unit of the Israeli Intelligence Corps initialized by Yigael Yadin found and confiscated the scroll at the house of an antiquity dealer (Kando) in Bethlehem, who used to buy the scrolls from the Bedouins and to resell them. Kando kept the scroll covered in plastic foil and stored in a shoebox in the basement of his shop, waiting for the right moment to sell it for a high price. Kando was later reimbursed with US \$105,000 by the Israeli government. The scroll was purchased for the Shrine of the Book, a Museum build especially for the Dead Sea Scrolls, where it still resides today.

Yigael Yadin (born Yigael Sukenik), the Chief of Staff of the IDF (1949-52), politician and outstanding archaeologist was the first person to work on the TS (Figure 1a). It is curious that the history of the DSS is closely connected with the family Sukenik. Yadin's father, Eliezer Sukenik, archeologist and professor of the Hebrew University, was the first person who recognized the old age and the authenticity of the scrolls, two days before the UN voted for the partition plan and creation of Jewish and Arab states in Palestine (November 1947). Despite the erupting war, Eliezer Sukenik traveled under risk to his own life to Bethlehem to acquire the first scrolls. Yadin followed in the footsteps of his father, as he was captivated by the DSS, particularly by the most special among them, which he named the "Temple Scroll", the study of which may have become his life's destiny. In June 1984, Yigael Yadin died of a heart attack only three months after finishing the writings on his last work, the popular book: "The Temple Scroll: The Hidden Law of the Dead Sea Sect" [1].

### **Textual content of the Temple Scroll**

Yadin named the scroll "Temple Scroll" because 50 % of its content is used for the detailed and precise description of how the temple must be build, and how the offering rituals must be performed. Although it describes a real Temple on earth, rather than a celestial of Ezekiel, the biblical prophet, the description in the TS differs in many significant architectonic aspects from the first and second temples. The most striking difference is the additional large third court, the size of which goes far beyond the Temple Mount and covers half of today's Old City Jerusalem to its west, and the Mount of Olives to its east, Figure 1c. The topography of

the area would not allow for the realization of such an architectural plan, as the Temple Mount and the Mount of Olives are separated by a very deep valley, which conducts regularly a significant amount of water. Moreover, the TS was dated to the Second Temple period, when it was in use. The TS plans were probably conceptualized at the time when the Second Temple was not yet destroyed, and stood with its two courts on the Temple Mount. Were the TS to describe a future temple, for instance as a prophecy, it would parallel with the messianic prophecies found throughout the Bible - that the hills around Jerusalem will be flattened by a strong earthquake (Isaiah 40:1-5; Ezekiel 38:18-22; Zechariah 14:2-10; Revelation 16:17-21). This interpretation however, cannot be fully confirmed by the text of the TS, as it claims to be an original instruction given to Moses for the Temple to be built by the Israelites when they enter the Land of Canaan – the Promised Land.

Beside the description of the Temple, the TS also contains laws that are written in the same style as the Pentateuch, but the laws differ in conceptual characteristics. The parts of the law commandment in the Pentateuch are a compilation of sometimes inconsistently joint passages with repetitions, while the TS is a thoroughly elaborated work containing phrases that refer to other passages in the text, such as:

“Any man ... who touches the bone of a dead person, or ...., or a grave – let him purify himself by the procedure of the ordinance already described [earlier in the text]. ...” (11Q19 Column 50:5-9)[13].

It also differs by consistently not mentioning Moses as a mediator in the third person, for example, “Moses did ...” or in the first person, whereas the narrator, Moses would have written phrases such as “the Lord said” or “to the Lord” as it can be found variably in the Pentateuch. Instead, the TS text is written directly, with God as the first person singular: “I said” or “to me” addresses a second person singular, who obviously is supposed to be Moses, as it says in one place in the scroll: “...to the sons of Aaron your brother...”; Aaron was the brother of Moses. Some commandments, especially those which have been debated during the time of the Second Temple period, are slightly rephrased for clarification purposes as Yadin interprets it [1]. Others are new or different to established traditions, though not contradicting the other commandments of the Torah, especially those, in which Yadin sees the obvious precursors for some laws in later Christianity. For example, one finds the prohibition for the king to be married to more than one woman at the same time, or to divorce. This differed from the common practice among Israel’s and Judah’s Kings. Although the TS is not a part of the biblical canon

today, it is very important for the cultural and historical studies of both Judaism and Christianity.

Our interest in the TS lies in the information that can be extracted from the physical scroll material. Probably, more information will be accessible and implementable in the future, for generations to come. For now, it is our responsibility to prepare the methods for “reading the information from the material”, and to preserve the treasure that was entrusted to us for the generations to come after us.

Before beginning to describe the physical properties of the TS, it might be useful to consult a passage concerning ritual purity of animal skins, since it might contain information relevant to our studies.

TS-11Q19, Col.47:4-18 [13]

“The city <sup>4</sup>that I shall sanctify by establishing My name and temp[le] there must be holy and <sup>5</sup>pure from anything that is in any way unclean, by which one might be defiled. Everything inside it must be <sup>6</sup>pure, and everything that enters it must be pure: wine, oil, edibles, <sup>7</sup>and any foodstuff upon which liquid is poured – all must be pure.

No skin of a clean animal that has been slaughtered <sup>8</sup>in other cities is to enter My city. Certain in other cities they may use <sup>9</sup>them for their work, whatever the need may be, but such skins are not to be brought into My city. <sup>10</sup>The reason: their degree of purity corresponds with that of the animals flesh. Therefore you are not to defile the city <sup>11</sup>that I sanctify, where I have established My name and temple. No, they must use skins of animals sacrificed <sup>12</sup>in the temple of My temple city, where they bring their wine, oil, and <sup>13</sup>edibles. They must not defile My temple with the skins of improper <sup>14</sup>offerings that they have slaughtered elsewhere in the land. Nor are you to consecrate a skin from <sup>15</sup>another city for use in My city; for the skins are only as pure as the flesh from which they come. If <sup>16</sup>you have sacrificed the animal in My temple, the skin is pure for use in My temple; but if you have slaughtered the animal in another city, it is pure <sup>17</sup>only for use in other cities. In sum, all pure foods sent to the temple must be brought in skins originating in the temple. You must not defile <sup>18</sup>either My temple or My city with improper skins, for I dwell in its midst.”

This passage and many others reflect how delicate and important the proper and pure preparation of the Temple Scroll must have been. It is highly probable that the manufacturers took the greatest care to use only proper materials with careful preparation methods in the making of the TS.

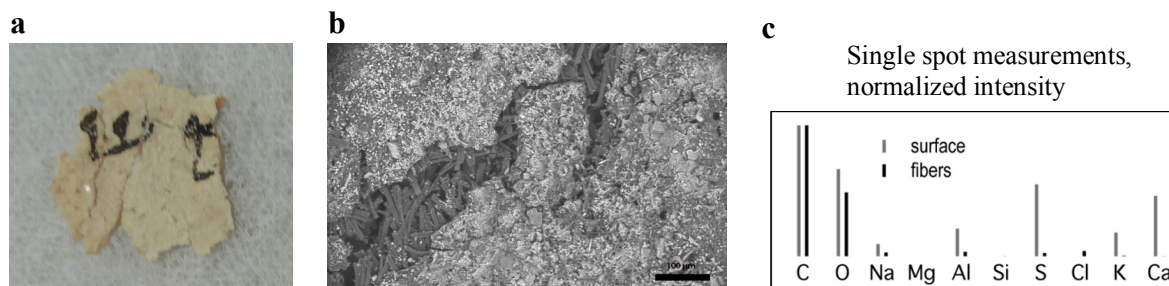
### **Physical Appearance of the Temple Scroll**

When the TS was received by scholars, it was very damaged by moisture, especially at the upper edge, where a part with the written text was completely destroyed (Figure 1b). The scroll was rolled very tightly, with the first sheet located on the outside of the roll. The first sheet was therefore most exposed to the ambient environment and consequently was more damaged than the other TS sheets. In order to unroll it, the scroll was treated in accordance to the Plenderleith method [17].

The Plenderleith method consists in softening the scroll by exposing it to an atmosphere with 100% relative humidity and subsequently dry freezing in order to arrest the gelatinization process. The unrolling process revealed the longest scroll amongst the DSS, with its total length of 8.15 m (compared with The Great Isaiah Scroll: 7.3 m, the best preserved of the biblical scrolls found at Qumran). The inner part of the TS with its ivory color gives a beautiful appearance of a well preserved ancient scripture (Figure 1a). The thickness of the TS is about 100  $\mu\text{m}$ , which makes the scroll the thinnest amongst all scrolls that have ever been found in Qumran. The regular thickness of the other scrolls lies in the range of 200-300  $\mu\text{m}$ , i.e. at least double the thickness of the TS.

These dimensions suggest that the TS text was written on a split parchment. The question of the applied splitting technique will be discussed in chapter 6. Furthermore, as can be recognized from the photographs of the backside of the sheets (Figure 1b) the text is not written on the hair side of the skin as it is common for the other scrolls found in Qumran. Unfortunately, till now we had no direct access to the scrolls backside for closer investigation. The larger part of the scroll is fixed in the display and storage cases and can be observed from its written side only. Its unique appearance, i.e. color, thickness and writing on the flesh side as well as the spectroscopic features of the material, that will be addressed in chapter 5.2, show that the TS was subjected to a unique manufacturing treatment. It is noteworthy that the text was not written directly on the surface of the flesh side of the skin, but on an additional layer

that is rich in inorganic materials as can be seen in Figure 2, which is 5-30  $\mu\text{m}$  thick, and covers the full area of the skin.



**Figure 2:** a) TS fragment from inner sheet with some letters written on a bright layer with cracks. b) SEM pattern of a crack on the TS fragment from inner sheet. Collagen fibers beneath the layer are visible inside the cracks. c) Elemental presence (by EDX) in a single spot measurements on the upper layer and on the collagen fibers beneath the layer. It shows a high presence of inorganic substances containing; Na, Al, S, K and Ca in the upper layer.

Yadin reported that after the unrolling process, the scroll's state of deterioration varied from sheet to sheet, and attributed the range in deterioration to different treatments in antiquity [18]. At some places on the outer sheets, whole text sections, including the inorganic layer on which the text was written, were detached and transferred onto the backside of the adjacent sheet [1]. In other cases, only the ink was transferred to the adjacent sheet. Finally, palaeographic studies revealed that the first outer sheet was produced approximately fifty to one hundred years after the sheets located in the inner part of the scroll [1]. The outer sheet was probably most damaged through antiquity since it frequently served as the outer covering sheet of the scroll, was therefore exposed to the environment, and therefore needed to be replaced.

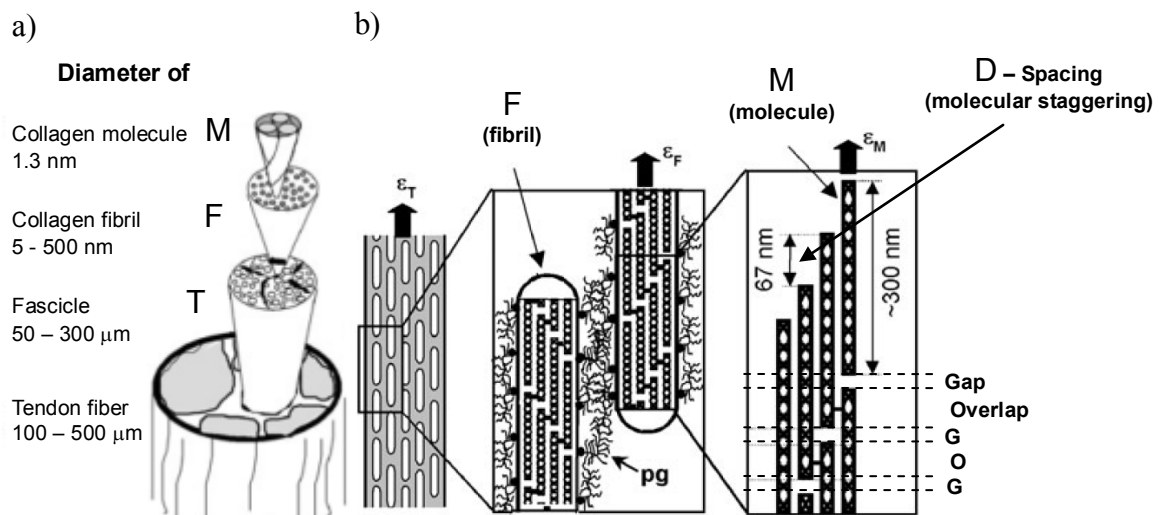
## 1.2 Collagen

Collagen is the most abundant protein in the mammalian body. It can be sub classified in up to 29 types [19], which are indicated by Roman numbers, and were given by order of their discovery. The common feature of all collagen types is their triple-helical molecular basic structure. However, the differences in the chemical composition lead their helical and nonhelical regions to associate into various types of supramolecular (three-dimensional) structures. The main focus of this work is the fibrillar type I collagen, which is the most abundant type of collagen found in a variety of tissues such as skin, tendons, and bones [20]. For that reason we will refer mainly to collagen type I. Depending on its morphology on the higher hierarchical



level collagen shows different physical properties. For instance, collagen fibrils in bone are embedded with mineral plates; with this composition, bone shows higher stiffness but lower toughness due to low extensibility [21]. The high tensile strength of collagen plays the significant role in skin and tendon functionality.

In skin (dermis), thin collagen fibers are intertwined in a tissue offering both strength and elasticity. Collagen fibers appear also in tendons that are very suitable for presenting the different hierarchical levels of collagen organization. In physiological condition they are composed of 65%-75% water by weight [22-24]. The solid phase consists primarily of collagen type I (60%-80%), with the remainder that is composed of proteoglycans (PG's) and glycosaminoglycans (GAG's), other types of collagen (types III, IV, V, VI), elastin, fibrillin and other proteins [25-27]. In tendons the collagen molecules are organized in regular and parallel assemblies throughout all the hierarchical levels, up to the macroscopic scale.



**Figure 3: Collagen staggering scheme of a tendon in native humidity condition through all hierarchical levels. a) Rough thickness dimensions of molecule: M, fibril: F, fascicle and tendon: T. b) The fascicle fibrils of several hundred nm are embedded in a PG matrix that can uptake shear stress among others. An applied macroscopic strain on the fiber level differs to the strains that simultaneously appear at the fascicular  $\epsilon_T$ , the fibrillar  $\epsilon_F$ , and the molecular  $\epsilon_M$  levels. Molecular staggering D inside the fibril results in an alteration of overlap and gap regions by a period of  $D=67\text{nm}$  (physiological condition). Adopted from [9].**

In Figure 3, the hierarchical levels of a rat tail tendon (RTT) in its native state are schematically presented. At the macroscopic level, the tendon fibers have a diameter of 100-500  $\mu\text{m}$ , which is a bundle of some thinner fascicles that further divide into closely packed collagen fibrils that are 5-500 nm in diameter [28]. Fibrils are block-units of thoroughly, regularly staggered tropocollagen molecules (triple helixes) of about 1.5 nm in diameter and ca. 300 nm

in length. Along the axial direction of the fibers, these helical molecules are connected by a small section of non-helical and less dense molecular structure (so-called C-terminal and N-terminal telopeptides) [29]. Laterally, helical molecules are stabilized by electrostatic and hydrophobic interactions as well as covalent cross-links [20, 30-35].

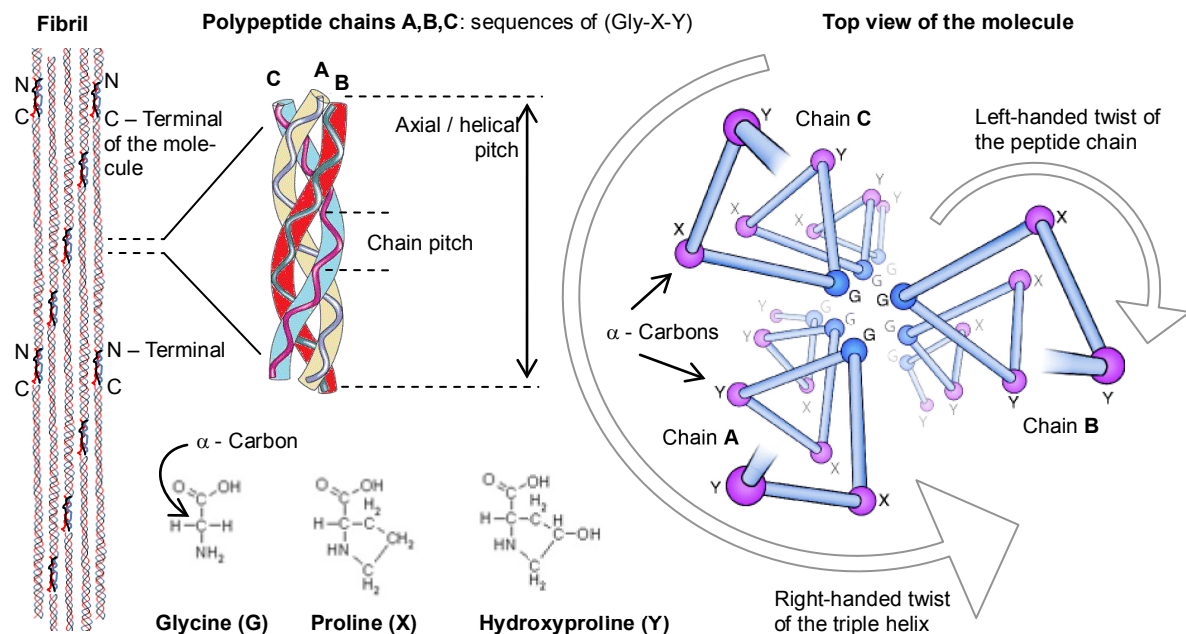
The molecular arrays are displaced in the axial direction by  $D \sim 67$  nm with respect to the adjacent molecules [36, 37]. In that way, every fifth lateral molecule appears at the same height along the fibrillar axis. This so-called “quarter staggered” structure leads to a periodic gap and overlap regions in the inter-fibrillar structure where the gap region has 20% less packing density and hence lower electronic density than the overlap region [38].

In the context of this work, which deals with the question how humidity influences the structure and properties of collagen, it is worth mentioning that when collagen dries, it shrinks in both axial and lateral directions through all the hierarchical levels. The axial molecular staggering  $D$  (typically  $\sim 67$  nm in wet condition) reduces to about 64 nm. The lateral spacing of the molecular packing shrinks to 1.1 nm (typically  $\sim 1.5$  nm when wet) when water is removed [39, 40]. The influence of water on collagen will be addressed in more detail in chapter 2.

Not only water affects the properties of collagen; collagen fibrils are embedded in a hydrophilic proteoglycan-rich (PG) matrix [41]. PGs are believed to play an important role in tendon and ligament mechanics although they compose only 0.5%-3% of the whole tendon [26]. The PG matrix allows for shearing and gliding of collagen fibrils when stress is applied [9]. Different types and sizes of PGs are found in tendons [42], which serve different functions. For example, small PGs such as decorin are responsible for transmitting tensile stresses and maintaining tendon shape, while modulation of compressive stresses are implemented by the larger PGs/ aggrecans. Their common structural feature is a central link protein that holds one or more (up to 10-1000's) glycan chains (anionic glycosaminoglycans or AGAGs). This core protein is bound at specific sites predominately in the gap region of the collagen fibrils [43]. The PG-collagen interaction is a strong, partly ionic bond, whereas the AGAG-AGAG chain interactions combine hydrophobic and hydrogen bonding for tissue stability [44].

The hydrated PG-matrix gel has a mesh-like structure that coats and interconnects the collagen fibrils; it plays a significant role for the strain distribution within the hierarchical levels because the PGs act as a medium to transfer shear stresses between the fibrils. The amorphous PG matrix is considerably less stiff than the collagenous fibrils. Thus, the collagen fibrillar strain is always smaller than the macroscopic tendon strain by a factor of 2 to 5 [45]. Moreo-

ver, as it has been found by several diffraction studies, an applied macroscopic strain on the fiber level differs from the strains that simultaneously occur at the fascicular  $\epsilon_T$ , the fibrillar  $\epsilon_F$ , and the molecular  $\epsilon_M$  levels (Figure 3) [45–47]. Time-resolved measurements of tendon strain on the inter-fibrillar and molecular levels revealed that two mechanisms contribute to the elongation of fibrils, namely the elongation of the triple helical collagen molecule, and their sliding relative to each other inside the fibril [46]. It was observed that these two processes do not take place simultaneously. At the initiation of tissue strain, the increase of the D period from  $D=67.0$  nm to about 67.6 nm is correlated with the stretching of the triple helices. The further increase of the D period is due to a continuous increase of the D stagger, which is directly related to the sliding of helical collagen molecules relative to each other [48].



**Figure 4: Intermolecular structure of collagen.** A fibril is structured with regular staggering of collagen molecules. A collagen molecule is a right handed triple helix of three polypeptide  $\alpha$ -chains A, B and C. Each of the chains is build up by a repeating G–X–Y peptide sequence that is twisting into a left-handed rope. G represents the smallest amino acid: glycine. In collagen type I, two of the chains are  $\alpha 1(I)$  and one is  $\alpha 2(I)$  chain, whereas typically proline and hydroxyproline can be found the X and Y positions, respectively. Furthermore, because of the common Gly–Pro–Hyp sequence in type I collagen, the “helical ratio” responds to the „7/2“ staggering model. The chain counts 7 twisting pitches for the same molecular section of 2 axial pitches at the triple helix level. Adopted from [5].

A helical collagen molecule is composed of three distinct polypeptide  $\alpha$ -chains (A, B and C in Figure 4), which are twisted together in a right-hand triple helix (top view in Figure 4) [5, 49]. In type I collagen, two of the chains ( $\alpha 1(I)$ ) are identical and one ( $\alpha 2(I)$ ) has a different

amino acid sequence. At the (C- and N-) ends of the helix there are short non-helical regions, the so-called C-terminal and N-terminal telopeptides. As it has been mentioned before, in these disordered regions, the collagen shows lower packing density.

In collagen type I, each polypeptide  $\alpha$ -chain is composed of about 1000 amino acid residues that have a characteristic repetitive G-X-Y sequences organized into a left-handed helix (see top view in Figure 4), whereas G (every third amino acid compound) is the small and compact glycine that fits well into the narrow coiled molecule. Glycine always appears in the center of the triple helix, and links by hydrogen bonds to the counterpart glycine of the other two polypeptide chains [5].

Remarkable for fibrillar collagen, known for its high molecular packing density, are the commonly occurring carboxyl rings of the side chains at the X and Y residues. This structural feature is characteristic for the glycine – proline (X) – hydroxyproline (Y) formation, which is characteristic of type I collagen. The side chain rings of proline and hydroxyproline stabilize the narrow and dense helical formation of the molecule [49, 50]. Proline often appears at the X position, and has the function of an edge in the narrow packed helices because of its stiff ring structure. Hydroxyproline can be often found on the Y position of the chain sequence; it stabilizes the triple helix through the hydrogen bonds between adjacent polypeptide chains.

Another remarkable characteristic of the Gly-Pro-Hyp sequence that is important in the context of this study (chapter 2), is that the polypeptide  $\alpha$ -chains make seven left-handed integer twists while the axial / helical pitch of the whole triple helix twist two times to meet together at the next identical winding point. Therefore, the Gly-Pro-Hyp sequence follows the so called „7/2“ staggering model (Figure 4) [51-53]. In other, less fibrillar collagen types, a „10/3“ integer staggering can be adopted instead of „7/2“ [51]. In general, for amino acid sequences with many side chains composed of aliphatic rings, as it is typical for type I collagen with its Gly-Pro-Hyp structure, the „7/2“ staggering model for this structure is valid, and hence we will be using it in our studies of rat tail tendons.

The structure and stability of collagen is also affected by the water present throughout the entire hierarchical structure [54]. “Structural water” bound tightly the structure inside the triple helix, either through a double or a triple hydrogen bond. “Bound water” act as receptors for CH-O hydrogen bonds building bridges between neighboring polypeptide chains [55]. “Free water” molecules are fixed by one hydrogen bond embedding the triple helix or in the telopeptide regions at the end of the polypeptide chains. “Transition water” also called the unperturbed bulk water interacts with the PGs between the fibrils [56, 57]. The first two types

(structural- and bound water) contribute to the molecular weight approximately with 0.5g/g [58-60]. The contribution of bulk water comprised by the free and the transition water distributed in the collagen tissue can vary depending on the osmotic pressure or the RH.

### 1.3 Collagen in parchment

Parchment is a predominantly collagen based material produced from animal skin. It typically has a flat and stiff surface for writing purposes, which is a result of its manufacturing procedure.

**Architecture of skin:** Skin is a multilayered cell system, which can be roughly grouped in three major layers: the most outer thin epidermis, the following thicker collagen-rich dermis, and the underlying subcutaneous tissue (hypodermis) containing fat-producing cells [7].

The epidermis, which can be further subdivided in cell-layers, is rich in protein keratin highly concentrated in the most outer part. The most outer fully keratinized fused flat cells are to seal and to protect the skin from the environmental impact such as microorganisms or chemicals that may damage the body.

The dermis, separated by a basement membrane, follows the epidermis layer. It is mostly composed by a fibrilous collagen network with thinner fibers close to the epidermis and thicker fibers in a more dense fiber network further inside the body. Collagen presented in skin is composed by the main contribution of type I accompanied by type III with a proportion that is very much dependent on the age. In the fetus collagen type III can reach the equal contribution as type I, later it reduces drastically to 25 – 10% [61]. Differently to type I (see previous section 1.1, Figure 4) the molecule of type III collagen is composed by three equal  $\alpha 1(\text{III})$  polypeptide chains winded to a triple helix instead by two  $\alpha 1(\text{I})$  and one  $\alpha 2(\text{I})$ . Type III collagen molecules are longer than type I molecules and they are usually present in tissues with elastic requirements at the macroscopic level [62]. The organization of the collagen network provides the skin with the required mechanical properties. Depending on the place on the body fibers can be predominantly oriented in the direction of higher exertion or be fully randomly distributed in plane with the skin surface. Fibroblasts within the dermis cells repair damaged collagen fibers in vivo conditions providing the dermis with new collagen and elastin.

The subcutaneous tissue, also called the hypodermis is unevenly distributed beneath the dermis providing the body with fat reserves under the skin. The loose connective tissue of the

hypodermis contains lobules of fat and larger blood vessels and nerves than those found in the dermis.

**Principle processes of ancient and modern parchment making procedures:** After flaying the animal the hide is usually stored in salt for conservation before next treatments. This is known as curing of the skin. The basic treatment steps to follow can be roughly comprised to 1) removing almost all non-collagenous material by breaking down the skins configuration, 2) restoring and stabilizing the remaining collagen matrix and 3) flattening the skin by drying under tension and preparing it mechanically for the final condition for use.

Typically, farm animals such as cattle, goat, sheep or pig are used for parchment production. In Jewish religious context, including the ancient manuscripts found near the Dead Sea, only pure animals in terms of ritual regulations were used. Breeder, shepherds or other skin providers are usually different professionals than parchment makers and hence in the most of the cases, to avoid the putrefaction, the skins stayed cured for a while before being supplied to the parchment maker and his first actions. Curing the skin can be realized in different ways, such as drying the skin in air, dry-salting the skin with sodium chloride or wet salting also known as brining. Already at this stage the moisture content of the skin would ideally be reduced to approximately 40%. During the next treatment steps further wetting and subsequent drying cycles will follow. Therefore, the effect of collagen drying on molecular level belongs to one of the scopes of this work and will be intensively addressed in chapters 2 and 3.

Before the next step of parchment preparation can be done the hide needs to be washed extensively to remove dirt, possible dung, blood and a part of non-collagenous proteins etc. but also the salt from the curing process. It is likely as well that during the parchment preparation process the proteoglycans, which protein core is bound to fibrilous collagen through hydrogen bonds, are partly removed [43, 63, 64]. (for PGs see Figure 3 in chapter section 1.1). However, next stage is to remove almost everything but collagen from the hide including hairs, fat and flesh. Therefore, in order to remove the non-collagenous materials the dermal fiber network needs to be loosened and expanded, which can be achieved with different ways after the hide has been soaked and gets swollen.

The ancient approach of skin treatment to achieve the expanding of fiber network might differ from the usual alkaline practice applied today, which is known since the Middle Ages. The historical methodologies from the times of the Dead Sea Scrolls were more likely conducted with enzymatic approaches using water, flour or other vegetable materials or even excrements [65]. Those approaches, however, were less efficient in fat removal and are more

time-consuming compared to liming and hence they can cause stronger deterioration of collagen. Nevertheless, modern developments and improvements for environmental issues have shown advantages in enzymatic de-hairing treatments of skins using a bacterial alkaline protease [66]. Enzymes are natural catalysts that act by converting starting molecules (substrates) into different molecules (products). Like all catalysts, enzymes increase the rate of a reaction by lowering its activation energy. However their difference to the most other catalyst is that they are highly selective for their substrates and speed up only a few particular reactions from among many possibilities. So for example carbohydrases are used in the fibre opening process. They degrade specifically the PGs whereby the fibre get opened so that water can enter to cause the swelling.

Liming is still the commonly applied process today also in Jewish religious context as well as in conventional parchment and leather production. At this stage the skin is soaked in calcium hydroxide  $[\text{Ca}(\text{OH})_2]$  solution where the dermal fiber network is loosened and expanded for removing the non-collagenous materials like PGs, hairs, epidermis, subcutaneous fat muscular layer, mucopolysaccharides, lipids, etc.. The same result can be achieved with other alkaline agents as well. The swelling of the skin during the liming process results in the splitting of the fibre bundle sheath, which burst open because they cannot hold the thicker fibres anymore while diameter is increasing.

Due to the high pH (typically 10-12) in the alkaline lime solution the most amino acid residues are placed above their pI (isoelectric point), which is typically 4,7 for collagen in lime. pI is the pH at which the positive and the negative charges are equally numbered or the colloidal particle remains stationary in an electrical field. Therefore, at a pH above their pI, the C-terminus of the proteins carries a net negative charge favoring the strong hydrolysis particularly in some of the amido groups attached to the aspartic and glutamic acid residues in the material of the soaked and swollen skin.

For more efficient hair removing, in the lime solution can be added sodium-  $[\text{Na}_2\text{S}]$  or other sulfides, which hydrolyze the proteins of the hair bulb and attack the keratinized hair shaft by cleaving the disulfide bridges found in keratin protein [67]. The hairs and the flesh can then be removed mechanically very easy by means of scrubbing tools. The remaining cleaved collagen matrix of the dermis needs subsequently to be washed again by water alternating with further acidic baths, such as weak solutions of various ammonium salts, in order to remove the waste from the liming process and to adjust the pH value to about 8-9 for collagen stabilization. Nevertheless, residues from the liming process in form of calcium carbonate

[CaCO<sub>3</sub>] can always be found in the final product. It is formed from the lime's calcium hydroxide [Ca(OH)<sub>2</sub>] in parchment reacting with the carbon dioxide [CO<sub>2</sub>] from the air.

Optionally tanning processes can be applied to the skin for the parchment production as it is obligatory done in leather production today. This step is typically conducted before the pH is brought down, i.e. when the cleaned collagen fiber network is still swollen and opened up so that the tanning agents can easily enter the fibrils and approach the collagen molecules. The tanning agents give the final product more chemical stability by covalently cross-linking with the collagen.

In the finishing step of the preparation the wet parchment is fixed on a frame under tension for drying. At that step it can be mechanically treated accordingly to the final use i.e. mechanically thinning, bleaching, scrapping or polishing etc. Subsequently, after the drying under tension the parchment becomes opaque and non-transparent.

**Deterioration of collagen in parchment:** Non-reversible deterioration of collagen occurs from the moment the parchment is produced [7]. The chemical treatment during the parchment production intervenes to a certain degree into the molecular conformation. The deterioration from that moment on is an ongoing process that can only be restricted in its accelerating progress. The speed of the deterioration progress is influenced by many factors such as the conservative and stabilizing treatment aspects of the parchment making process like tanning, where the induced cross-linking of collagen can play a significant role. Environmental factors or the way how the parchment (e.g. scroll) is used, stored or conserved after its production influence the speed of molecular deterioration as well.

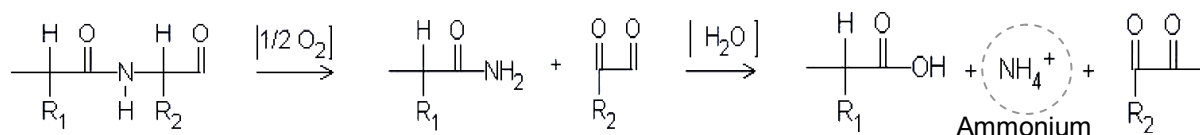
At the moment of its genesis the molecular and fibrillar structure of the collagen fiber is poorly cross linked (for collagen molecular structure see chapter section 1.1). With the time more randomly distributed cross-links between molecules occur and increase the insolubility and rigidity of the fiber. Whereas, during the fibril formation, at the moment when the helical structure is freshly generated the neighboring molecules can cross-link only at a few particular sites due to its staggering arrangement. Thereby, the telopeptide (non-spiral) regions play an essential role. The freshly generated type I collagen molecule has two particular sites in the helical domain (at the Hydroxylysine residues 87 and 930), which cross-link covalently with the counterpart Lysine residues in the non-helical telopeptide region of the neighboring molecule. Once the perfect structure of the triple helix is disturbed new potential cross-link sides can occur. Beside the stabilization brought by the cross-links, the triple helix is hold together



by hydrogen bonds within the helix. New cross-links occurring at the disruptions of the polypeptide chains can on one hand strengthen and stabilize the fibrillar collagen but on the other hand absorbed water molecules can enter the helix at these arrested disruption sites and help to progress the unfolding by hydrolysis. In extreme situations this process can cause cleavage of the molecular collagen structure unfolding further triple helices until the fragmented polypeptide chains loosens their conformation through all the hierarchical levels and transform into a random coiled configuration of ruptured polypeptide chain sequences. The later stage of deterioration, also called gelatinization, can be accelerated by high temperature and moisture. Gelatin can often be found at the very outer layers of parchment, where the collagen fiber network is exposed directly to the environmental agents such as pollutants, bacteria, UV light or humidity [68-70].

The main triggering processes for cleavage or disruption of the peptide chains are oxidation and hydrolysis.

Oxidation of collagen can occur when free radicals appear inside the molecular system. They can be formed by UV light splitting up the hydrogen from a chemical compound such as water, but also others [71]. Free radicals are capable to break the N-C covalent bonds that compounds the sequenced amino acid residues, with the consequence of cleavage of the main chain of the collagen molecule (Figure 5).



**Figure 5: An example for an oxidative cleavage of the main chain of collagen is shown in schematic representation. The ejected ammonium can compound further and progress the denaturation of collagen. Schematic adopted from [7].**

Beside its occurrence between the amino group of an amino acid residue and its associated C $\alpha$ -atom, oxidation of collagen affects also the side chains of individual amino acid residuals. The later subsequently reduces the number of the basic amino acids such as arginine, hydroxyllysine or lysine and increases the number of acidic amino acids such as glutamic acid and aspartic acid. Therefore measuring the ratio between the basic and the acidic amino acids can indicate the degree of deterioration caused by the oxidative processes [72].

Hydrolysis, that often accompanies the process of oxidation, can be also initiated by means of acids from atmospheric pollutants, such as NO<sub>x</sub> and SO<sub>2</sub>, which mix with water to form

nitric and sulphuric acids, respectively. Those are capable to cause cleavage in the main chain of collagen so that water can enter the helical formation. Water allows the space for the collagen helix to unwind and the hydrogen bonding to be redistributed [73]. When unfolding and fracturing of the molecular structure progress collagen increases its affinity to water and turns to gelatin and the collagen/gelatin tissue concomitantly loosens its mechanical strength [74].

It's conceivable that under certain circumstances (Figure 5) traces of some by-products can appear, which give insights about the denaturation processes. Consequently, further interaction with molecules from the environment forming new products (such as ammonium nitrate  $[\text{NH}_4\text{NO}_3]$  for example) witnesses about the circumstances of the parchment's history either related to its treatment during the manufacture or to the environmental circumstances to which it was exposed during the post manufacturing time period.

The later statement is based on the author's personal considerations animated by an interesting observation done on the Temple Scroll's collagenous material that we are forestalling mentioning now. Ammonium nitrate  $[\text{NH}_4\text{NO}_3]$  has been identified all over the collagen in the fragments of the ancient manuscript. This has been revealed by means of Raman spectroscopy and will be discussed in chapter 5. The investigation of the related chemical deterioration processes and their possible conclusions on the scroll's history, however, is not in the scope of this work, though this discovery could encourage further research.

### 1.4 Polarized Raman Spectroscopy on Uniaxial Symmetry

The analytical technic known as the Raman Spectroscopy (less popular are also the names: Smekal-Raman or Mandelstam-Landsberg) received its name from one of its discoverers; the Indian physicist Sir Chandrasekhara Venkata Raman, in the beginning of last century (1923-28) [75, 76]. Since then the technique has been established for various branches of material characterization and the literature on Raman spectroscopy nowadays is quite prodigious [77].

Its principle is based on a weak inelastic scattering effect of incident light after interacting with matter, whereas some photons of the incident light scatter with a different wavelengths, which energy changes correspond to the characteristic vibrational (i.e. stretching, rotation, bending etc.) energies of the molecular compounds (or lattice phonons in crystals). The energy can either be transferred to or gained from the molecular vibration.

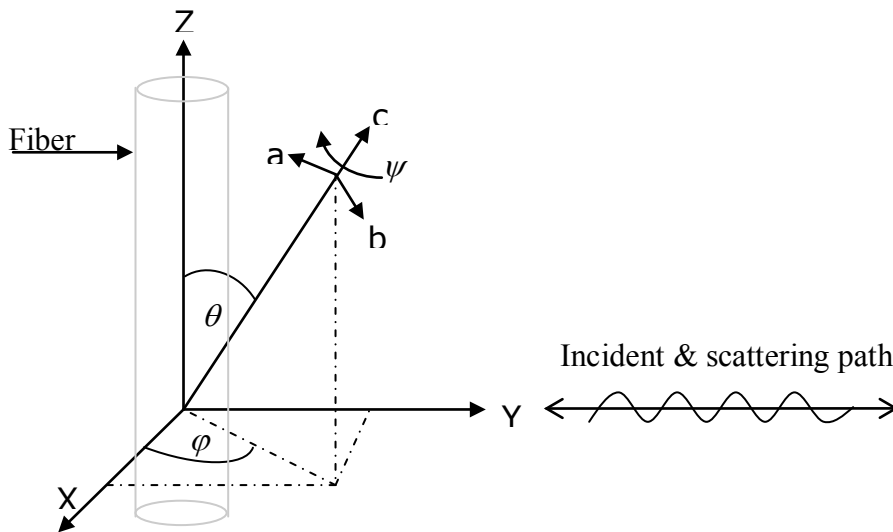
Monochromatic light is used for excitation typically in the visible range but also in the UV and NIR regions. If the energy of the incident light corresponds to the electronic transition

energy of the material, fluorescence of huge intensity compared to that of Raman can appear and make the weak Raman signal undetectable. In such cases excitation with monochromatic light of bigger wavelength such as NIR is preferable. After its establishment the technique has been improved on the detection side but also variously developed on the enhancement of the weak Raman Effect on the interaction side, which meanwhile makes the Raman Spectroscopy to an analytical technique [78].

The analytical technique of polarized Raman spectroscopy (PRS) has been developed and applied more often in the last decade. The description of the PRS technique has been presented in detail by Bower et al. [79, 80], Turrell et al. [81-85], Ikeda et al. [86], and others like Rousseau et al. [87, 88] and Sourisseau et. al. [89, 90], as well. Based on the theoretical description of these authors a compact guide through the basic concepts of a vibrational system of uniaxial symmetry will be presented in this chapter section. Scattered Raman spectral intensity of an anisotropic specimen ( $I_s$ ) is dependent on the polarization direction of the incident laser ( $I_e$ ) and on the polarizability of the particular vibration centers. The latter is described by the polarizability tensor of that particular bond.

$$I_s \sim I_e [e_e \alpha e_s]^2 \quad (1)$$

Where  $\alpha$  is the polarizability tensor in laboratory coordinates,  $e$  = directions of the excitation ( $e_e$ ) and scattered ( $e_s$ ) light. We consider the coordinate system as described in Figure 6, where the linearly polarized laser light can be oriented in the  $z$ - $x$  plane (laboratorial coordinates) by a “polarizer” ( $\lambda/2$ -plate) before it interacts with the sample, and  $y$  is the direction of both the incoming and scattered laser path in a confocal arrangement.



**Figure 6: Definition of the molecular (abc) and the laboratorial (XYZ) coordinates used in the text and Euler Angles used for the transformation.**

By means of a polarization filter- “analyzer” that is placed in the path of the scattered light, the intensity can be also analyzed with respect to the orientation of scattered polarization. The sample, which is in this case a cylindrical fiber, is oriented with its long axis along the z-direction.

Here is an example of the notation: if the incident light is polarized along the long axis of the fiber, and we analyze only the scattered intensity with polarization perpendicular to the long axis of the fiber, the measured intensity would be described by the square of the  $\alpha_{ZX}$  component of the polarizability tensor in laboratorial coordinates (equation (2)).

$$\Rightarrow I_{(ZX)} \sim [e_e \alpha e_s]^2 = \left[ (0 \ 0 \ 1) \begin{pmatrix} \alpha_{XX} & \alpha_{XY} & \alpha_{XZ} \\ \alpha_{YX} & \alpha_{YY} & \alpha_{YZ} \\ \alpha_{ZX} & \alpha_{ZY} & \alpha_{ZZ} \end{pmatrix} \begin{pmatrix} 1 \\ 0 \\ 0 \end{pmatrix} \right]^2 = (\alpha_{ZX})^2 \quad (2)$$

The scattered spectral frequency (1665 1/cm) that is the focus of this study arises from the C=O stretching in an amine compound, known as amide I. The C=O is oriented along the c axis in the molecular coordinates as indicated in Figure 6. The polarizability response of this bond in molecular coordinates is described by a diagonal polarizability tensor of the form in equation (3) [87]:

$$[\alpha_{abc}] = \alpha_3 \begin{pmatrix} a & 0 & 0 \\ 0 & a & 0 \\ 0 & 0 & 1 \end{pmatrix}, \text{ with } a = \alpha_1 / \alpha_3 = \alpha_2 / \alpha_3 \quad (3)$$

Due to the stretching symmetry of the amide I bond, the polarizability properties of the tensor do not differ in the a or b directions, which means that it is independent of the angle  $\psi$ . However, the polarizability tensor  $[\alpha_{XYZ}]$  in the laboratory coordinates of the fiber, which corresponds to the hierarchically higher molecular and fibrillar assembling symmetry on the macroscopic level, can be calculated from the transformation of the molecular polarizability tensor  $[\alpha_{abc}]$  by means of the Euler transformation (equation (4)) [79, 86].

$$[\alpha_{XYZ}] = [T^t \alpha_{abc} T]: \text{Transformation of coordinates with Euler angles } (\psi, \varphi, \theta) \quad (4)$$

Since the measured Raman scattering intensity ( $I_{\text{Raman}(i,j)}$ ) is a response of a multitude of vibrational centers, it is expressed by an average  $\langle (\alpha_{i,j})^2 \rangle$ , which is the integration over the orientation distribution  $N(\psi, \varphi, \theta)$  of the vibrational centers inside the fiber.

$$I_{\text{Raman}(i,j)} \sim \langle (\alpha_{i,j})^2 \rangle = \frac{1}{4\pi^2} \int_0^{2\pi} d\psi \int_0^{2\pi} d\varphi \int_{-1}^1 d(\cos\theta) ([T^t \alpha_{\text{abc}} T]_{i,j})^2 N(\psi, \varphi, \theta) \quad (5)$$

In the cylindrical uniaxial fiber symmetry the variation of the distribution function depends only on  $\theta$ , *i.e.*  $N(\psi, \varphi, \theta) = N(\theta)$ . The distribution with respect to the angles  $\varphi$  and  $\psi$  is constant, and the integrals can be reduced to equation (6).

$$\Rightarrow \langle (\alpha_{i,j})^2 \rangle = \int_{-1}^1 d(\cos\theta) (\alpha_{i,j})^2 N(\theta) \quad (6)$$

An appropriate approach for the representation of the distribution function is given by a series of even Legendre Polynomials.

$$\begin{aligned} N(\cos\theta) &= \sum_l^{\text{even}} \left(1 + \frac{1}{2}\right) \langle P_l \rangle P_l(\cos\theta) \\ &= \frac{1}{2} \left[ 1 + P_2 \frac{5}{2} (3 \cos^2 \theta - 1) + P_4 \frac{9}{8} (35 \cos^4 \theta - 30 \cos^2 \theta + 3) + \dots \right] \end{aligned} \quad (7)$$

Where,  $P_l(\cos\theta)$  are Legendre polynomials and  $P_2, P_4$  are the first two even Legendre coefficients, which can be determined by Raman scattering data. These coefficients are the average values over the orientation distribution of the Legendre polynomials, and are given as:

$$\langle P_l \rangle = \int_0^\pi \sin\theta P_l(\cos\theta) N(\theta) d\theta \quad (8)$$

The coefficients can be determined experimentally. The relationship between the scattered Raman intensities and the Legendre coefficients are given by following equations (9)-(12) [87], by solving the integral in equation (6).

$$\langle \alpha_{xz}^2 \rangle = \alpha_3^2 \left\{ \left[ \frac{a^2 - 2a + 1}{15} \right] + P_2 \left[ \frac{a^2 - 2a + 1}{21} \right] - 4P_4 \left[ \frac{a^2 - 2a + 1}{35} \right] \right\} = \langle \alpha_{zx}^2 \rangle = \langle \alpha_{zy}^2 \rangle \quad (9)$$

$$\langle \alpha_{xy}^2 \rangle = \alpha_3^2 \left\{ \left[ \frac{a^2 - 2a + 1}{15} \right] - 2P_2 \left[ \frac{a^2 - 2a + 1}{21} \right] + P_4 \left[ \frac{a^2 - 2a + 1}{35} \right] \right\} \quad (10)$$

$$\langle \alpha_{xx}^2 \rangle = \alpha_3^2 \left\{ \left[ \frac{8a^2 + 4a + 3}{15} \right] + 2P_2 \left[ \frac{4a^2 - a - 3}{21} \right] + 3P_4 \left[ \frac{a^2 - 2a + 1}{35} \right] \right\} \quad (11)$$

$$\langle \alpha_{zz}^2 \rangle = \alpha_3^2 \left\{ \left[ \frac{8a^2 + 4a + 3}{15} \right] - 4P_2 \left[ \frac{4a^2 - a - 3}{21} \right] + 8P_4 \left[ \frac{a^2 - 2a + 1}{35} \right] \right\} \quad (12)$$

Where  $a$  and  $\alpha_3$  are the principle components of the polarizability tensor on the molecular frame as defined in equation (3).

If a high magnification lens (100x) with a wide numerical aperture  $NA$  of 0.95 is used to collect the Raman scattering spectra, corrections for resulting scattered intensities must be applied [81, 91]. A wide  $NA$  causes a wide cone of a solid angle  $\Omega = 2\theta_c$  over which the scattered light is collected. The cone angle  $\theta_c$  depends on the reflective index  $n$  of the sample material as follows:

$$n \sin \theta_c = NA \quad (13)$$

Because of the 180° backscattering geometry the radiation propagating along the outer parts of the wide cone have additional polarization components. The corrections for the four significant measured intensities are represented by the following equations (14)-(17) [90]:

$$I_{(zx)} \sim (\langle \alpha_{zx}^2 \rangle A + \langle \alpha_{zy}^2 \rangle B)(2C_0 + C_2) + (\langle \alpha_{yx}^2 \rangle A + \langle \alpha_{yy}^2 \rangle B)(4C_1) + (\langle \alpha_{xx}^2 \rangle A + \langle \alpha_{xy}^2 \rangle B)(C_2) \quad (14)$$

$$I_{(zz)} \sim (\langle \alpha_{zz}^2 \rangle A + \langle \alpha_{zy}^2 \rangle B)(2C_0 + C_2) + (\langle \alpha_{yz}^2 \rangle A + \langle \alpha_{yy}^2 \rangle B)(4C_1) + (\langle \alpha_{xz}^2 \rangle A + \langle \alpha_{xy}^2 \rangle B)(C_2) \quad (15)$$

$$I_{(xz)} \sim (\langle \alpha_{xz}^2 \rangle A + \langle \alpha_{xy}^2 \rangle B)(2C_0 + C_2) + (\langle \alpha_{yz}^2 \rangle A + \langle \alpha_{yy}^2 \rangle B)(4C_1) + (\langle \alpha_{zz}^2 \rangle A + \langle \alpha_{zy}^2 \rangle B)(C_2) \quad (16)$$

$$I_{(xx)} \sim (\langle \alpha_{xx}^2 \rangle A + \langle \alpha_{xy}^2 \rangle B)(2C_0 + C_2) + (\langle \alpha_{yx}^2 \rangle A + \langle \alpha_{yy}^2 \rangle B)(4C_1) + (\langle \alpha_{zx}^2 \rangle A + \langle \alpha_{zy}^2 \rangle B)(C_2) \quad (17)$$

$$\text{Where } A = \pi^2 \int_0^{\theta_c} (\cos^2 \vartheta + 1) \sin \vartheta d\vartheta = \pi^2 \left( \frac{4}{3} - \cos \theta_c - \frac{1}{3} \cos^3 \theta_c \right) \quad (18)$$

$$\text{and } B = 2\pi^2 \int_0^{\theta_c} \sin^3 \vartheta d\vartheta = 2\pi^2 \left( \frac{2}{3} - \cos \theta_c + \frac{1}{3} \cos^3 \theta_c \right) \quad (19)$$

Since  $C_1$  and  $C_2$  are several orders of magnitude lower than  $C_0$ , they can be neglected. If intensity ratios are considered,  $C_0$  also vanishes from the previous equations [88].

Two independent intensity ratios can be calculated by measuring four linearly polarized spectra:

$$R_1 = \frac{I_{(ZX)}}{I_{(ZZ)}} = \frac{\langle \alpha_{ZX}^2 \rangle A + \langle \alpha_{ZY}^2 \rangle B}{\langle \alpha_{ZZ}^2 \rangle A + \langle \alpha_{ZY}^2 \rangle B}; \quad R_2 = \frac{I_{(XZ)}}{I_{(XX)}} = \frac{\langle \alpha_{XZ}^2 \rangle A + \langle \alpha_{XY}^2 \rangle B}{\langle \alpha_{XX}^2 \rangle A + \langle \alpha_{XY}^2 \rangle B} \quad (20),(21)$$

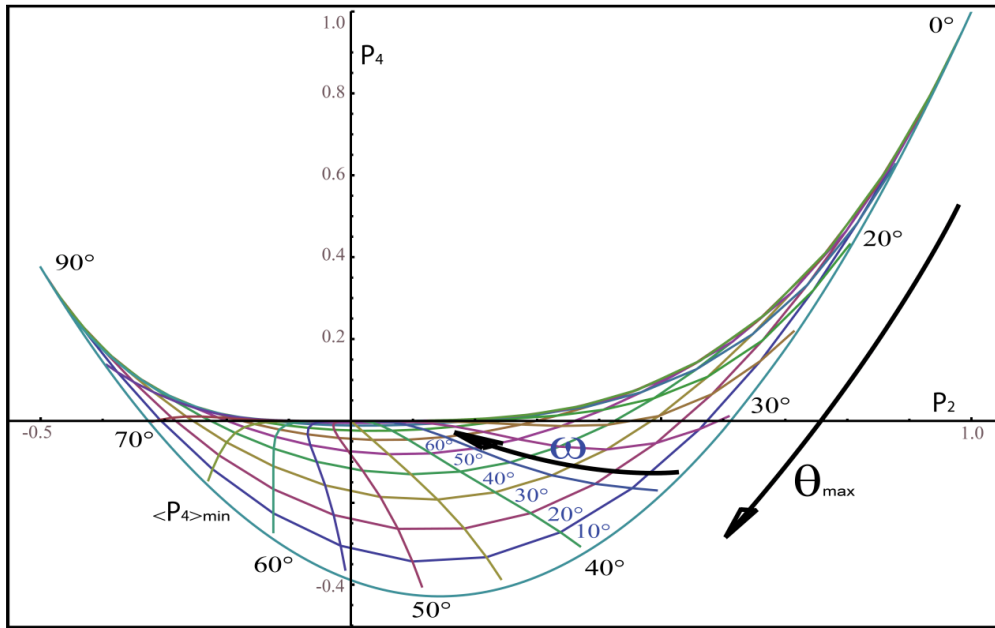
The approach of calculating intensity ratios has several advantages. Beside the elimination of all issues related to the polarization dependent instrument throughputs and other constant components such as laser incident intensities, it also reduces the problem to solving only three unknowns:  $P_2$ ,  $P_4$  and  $a$ . However, to solve this system of equations, a further experimental ratio is needed. It can be provided by the measurement of an isotropic sample, where it is known that due to a constant distribution function  $R_{iso} = R_1 = R_2$  and  $P_2 = P_4 = 0$ . In our case, disordered collagen (gelatin) can be used as an isotropic sample of a collagen-based material. With this data, “ $a$ ” can be calculated. At this stage, with the knowledge of “ $a$ ”, only two unknowns remain:  $R_1$  and  $R_2$ . The  $P_2$  and  $P_4$  of an anisotropic sample can be determined by measurements of the two ratios  $R_1$  and  $R_2$ .

Solving for  $P_2$  and  $P_4$  leads to a Legendre series expansion truncated at the second even term ( $P_4$ ), providing a first approximation of the orientation distribution function. However, this approximation can differ significantly from the real distribution function, and in some case might take negative values. According to Pottel et al.[92], a more realistic distribution function can be obtained from any set of  $P_l$  values maximizing the information entropy of the distribution, subjected to the constraint that  $N(\theta)$  is always positive and that its integral over the range  $[0, \pi]$  is equal to 1 (i.e., requiring that  $N(\theta)$  is a probability distribution).

The function satisfying these constraints is called the most probable distribution function ( $f(\theta)_{mp}$ ) that is given by equation (22):

$$f(\theta)_{mp} = \frac{e^{\lambda_2 P_2(\cos \theta) + \lambda_4 P_4(\cos \theta)}}{\int_0^\pi e^{\lambda_2 P_2(\cos \theta) + \lambda_4 P_4(\cos \theta)} \sin \theta d\theta} \quad (22)$$

when the series is limited to the first two polynomials. The Lagrange multipliers  $\lambda_2$  and  $\lambda_4$  can be calculated numerically, considering that the average values of each Legendre polynomial weighted with  $f(\theta)_{mp}$  must be equal to the corresponding order parameter obtained by the PR measurements.



**Figure 7: Gaussian Iso- $\theta_{max}$  and Iso- $\omega$  curves in P2-P4 space.**

Here in our study, we focused on the orientation of the C=O bonds in collagen molecules. We considered the Raman tensor of the C=O vibration as cylindrically symmetric, and we estimated that the distribution function  $N(\theta)$  follows a Gaussian shape with a particular central angle  $\theta$  and a width  $\omega$  (FWHM). Therefore, the first two even Legendre coefficients  $P_2$  and  $P_4$  can also be calculated for the corresponding Gaussians using equation (8). Doing so, each of the  $P_2$  and  $P_4$  pairs determined through PRS measurements can be linked to a  $\theta_{max}$  and  $\omega$  pair, which describes a particular distribution function  $N(\theta)$  of a Gaussian shape (Figure 7).



## 2 Influence of Hydration on Molecular Structure and Mechanical Behaviour of Collagen

This chapter focuses on the structural and mechanical behavior of collagen induced by moisture changes on different scale levels, from molecule to fibrils. In its native physiological environment collagen can experience changes of moisture induced by osmotic pressure and react to it with volume changes taking influence onto the whole biological system. Hereby, one has to take into account that structural and mechanical changes on different scale levels affect differently its biological environment. Therefore, the study of the extent of this influence, i.e. the strength and the volume changes on different scales is of great importance for the understanding of the physiological interplay in the tissue.

This topic is also of great importance for studying the materials of ancient manuscripts, and also affects the methodological developments for collagen preservation that are addressed by our studies on the TS in chapter 3. The effect of hydration on collagen is important for the study of parchment, as it is the final product of animal skin, which is a collagen based material. Animal skin that undergoes different treatment stages involving water and dehydration while under strain before it gains and maintains its intended shape, and the physical properties of parchment. Our main attention, therefore, lies on water and its affect on the conformational and physical features of collagen throughout its hierarchical levels. In this chapter we explore the use of PRS for studying the conformation of collagen in RTT. These results are accompanied with dehydration experiments using *in-situ* synchrotron x-rays scattering and video – microtensometry. The interesting results open new perceptions in parchment and other collagen-related fields such as medicine, and fundamental studies on collagen functionalities in living tissues.

Hierarchical structuring from molecular to tissue levels (chapter 1.1) allows collagen to fulfill a variety of mechanical functions. Collagen is a major constituent of tendons and ligaments, as well as the periodically organized organic matrix of bone, and the mostly randomly oriented fibrillar network in skin. In all of these biological materials, the collagen orientation plays a fundamental role in the overall mechanical properties of the tissue [40, 93, 94]. The collagen orientation may be altered by various diseases such as skin cancer [95], keratoconus of the cornea [96], or osteogenesis imperfecta [97]. In parchment, collagen deterioration occurs through oxidation, hydrolysis and gelatinization processes (chapter 1.1), which affect the molecular and interfibrillar properties. These small-scale molecular and interfibrillar proper-

ties affect the properties of collagen at higher hierarchical levels of organization, up to the fiber network on the macroscopic scale. The macroscopic material properties result therefore from the superposition of the specific molecular features and the behaviors of the fiber network organization. In order to understand the material behavior of a macroscopic collagen based matrix assembly properly, the physical and chemical features of collagen need to be distinguished by the level of its hierarchy and macroscopic organization. Therefore in this chapter we start to focus on the interfibrillar features by means of uniaxial experiments on fascicles before describing the next step of the bi-dimensional analysis of the fibrillar network behavior. The later (bi-axial) is not part of this study, but it is planned for the future.

The mechanical properties of different types of collagen-containing tissues have been already extensively investigated on various hierarchical, structural levels [30, 98-100]. However, the important question remains: how do these levels of structure contribute to the macroscopic mechanical behavior? In this context, polarized Raman spectroscopic techniques (PRS) (chapter 1.4) can provide several length scales of information, contributing to an understanding of the role of molecular-level features to tissue behavior.

Polarized-light microscopy was one of the physical techniques to be used to study the morphology of collagen-rich tissues [101]. Recently, second harmonic generation (SHG) microscopy, a technique that exploits nonlinear optical properties of molecules for imaging [102], became one of the main techniques used to analyze morphology and therefore orientation of collagen in tissues [103]. PRS has an advantage with respect to most of the other advanced optical methods to evaluate collagen orientation that lies in its reliable chemical fingerprint that is acquired in real time. Such information allows for the study of molecular- and atomic-level properties that are fundamental in material behavior. Recently, potential uses of the PRS approach in measuring collagen orientation within tissue have been reported [12, 104-106].

Rat tail tendon (RTT) is composed entirely of type I collagen fibrils with small amounts of proteoglycans [107] (Figure 3). Tendons transmit force between muscles and bone, and are highly ordered tissues. The collagen organization from the molecular to the tissue length scales shows a high degree of fibril alignment [30]. Using Raman spectroscopy, the orientation of one molecular unit within each collagenous macromolecule can be derived from Raman band anisotropy measurements, assuming that Raman band tensors of the relevant molecular unit are already known [108-110]. From the parameters provided by the Raman tensor, the molecular structure arrangement or orientation with respect to the biological sample can be determined [87, 111-115] (chapter 1.4). For example, scattering of the amide I band ( $C=O$ )

is more intense in the direction which is perpendicular to the collagen fibril orientation [116] compared to the direction parallel to the fibril because the collagen carbonyl groups are mainly oriented perpendicular to the collagen chains.

Water is an important component of collagen in tendons, as it constitutes more than 60 wt % of the tissue [24] and therefore it may play a significant role in the already mentioned force transmission. However, the significance of the role of water in collagenous material properties generally does not attract wide interest, except in the case of collagen dehydration processes, such as in the fabrication of leather or parchment [117, 118]. It is well-known that the mechanical properties of collagen change drastically upon dehydration. It was not clear whether there is a direct role of water for the function of collagen in the native (hydrated) state [119-122], therefore we combined many experimental approaches to unravel the role of water in type I collagen structure and mechanical behavior.

A detailed description of collagen was presented in chapter 1.1. Here is a short summary of the elements that are most relevant for this chapter. Collagen is built in a hierarchical fashion, with triple-helical collagen molecules assembled in a staggered fashion into fibrils, which are embedded in a proteoglycan-rich matrix, and further assembled into fascicles and fibers [45, 123-125]. The axial molecular staggering (D) within fibrils is typically 67 nm in water-saturated type I collagen, and reduces to about 64 nm in dry collagen [120]. Laterally, the molecules are packed with the lateral spacing in the order of 1.5 nm, which reduces to 1.1 nm when the sample is dried [39, 40]. When loaded in tension along the fiber orientation, collagen fibrils deform in a complex scale-dependent fashion, where fibrils stretch more than the helical collagen molecules, and the whole tendon deforms more than fibrils [47, 100, 126, 127]. This has been explained through a side-by-side gliding of molecules and fibrils, enabled by the multi-scale structure of the tendon, based on *In-Situ* experimentation with synchrotron radiation [126] and on multi-scale computational modeling [128].

The part “Results and Discussion” is sub divided in two sections as follows:

- 1) analyzing the fully hydrated (physiological hydration state of collagen) RTT by means of PRS while stretching and comparing the results with the reported XRD investigations at different strain stages. (Chapter section 2.2.0)
- 2) monitoring of mechanical and structural properties during stepwise dehydration of clamped RT fascicles by means of video – microtensometry, XRD and PRS. For un-

derstanding the conformational processes during the dehydration, we compared two experimental strategies: the Iso-Strain and Zero-Stress experiments. In Iso-Strain experiments the fascicle was kept at a fixed pre-stretched length and the rising forces caused due to the dehydration were measured. In Zero-Stress experiments, extension/contraction motors were permanently kept in the interactive driving mode in order to maintain the force within the fascicle at almost zero, while the fascicular strain was measured with changes in dehydration. (Chapter section 2.2.1)

## **2.1 Materials and methods**

### **Rat tail tendon (collagen) – RTT**

Tendons were extracted from the tail of 4 to 12 month-old rats. The sex of the animals was not known or recorded. Before the tendons were extracted, the tail was kept frozen at  $-18^{\circ}\text{C}$ . For the extraction, a section of 30 mm length was cut from the tail, and thawed in distilled water to room temperature. The fibers (bundle of three to four fascicles) and the fascicles were extracted by the use of tweezers. The tendon was pulled intact from one side of the tail section. With this technique, the tendons slid very smoothly from the tail section without any significant resistant force, so they kept the crimp. Fascicles were obtained from an extracted tendon fiber in the same way, after the cortical membrane was removed. Before the experiment, the extracted fibers were stored at  $4^{\circ}\text{C}$  in PBS solution. For all dehydration experiments the fascicles, of approximately  $200\text{ }\mu\text{m}$  in diameter, were washed in distilled water and exposed to the ambient environmental air humidity for a few minutes while it was clamped into the tensile machine.

The animal welfare as well as method of sacrifice was approved by the local authority Landesamt für Gesundheit und Soziales. (Berlin, Germany).

### **The relationship of relative humidity to osmotic pressure**

Relative humidity (RH) is related to the osmotic pressure and the chemical potential of water. The native environment of the tendon is the humid living body with possible changes of osmotic pressures due to factors such as pH or salinity changes. In this work, we therefore refer to the osmotic pressure of water as a measure of its chemical potential with respect to the

pure liquid water. The chemical potential of water is defined as  $\mu = \mu^0 + RT \ln(a)$  where  $a$  is the water activity,  $\mu^0$  is the standard chemical potential of the reference state (the liquid in this case) so that  $\mu - \mu^0 = RT \ln(a)$  is the partial molar energy difference with respect to the liquid. For an ideal gas, the activity is defined as the ratio between the actual water vapor pressure and the saturated vapor pressure at the same temperature. We consider the relative humidity below 0.95 as a measure of the water activity. The osmotic pressure relates to the chemical potential by the equation  $\Pi = \mu/V_m$ , where  $V_m$  is the molar volume of the liquid water.

## Uni-Axial tensile testing in a controlled environment

### Measurement chamber

Samples were tested in a sealed chamber with a volume of about 140 cm<sup>3</sup> (Figure 8a). During the experiment, the chamber was kept at a constant temperature of 25° by means of a circulating cooling bath thermostat (Huber). The humidity inside the chamber was controlled by means of “Wetsys (Setaram)” humidity generator, which was operated with a flow of 200 ml/min. Temperature and humidity were monitored via a SHT75 digital humidity and temperature sensor (SENSIRION) that was placed in the vicinity of the sample. Samples were clamped at both ends to two aluminum holders. The strain was controlled by one of the holders which was connected to a PI (Physik-Instrumente) M-126.DG1 linear motor stage, while the axial tensile forces were measured using a Honeywell R-31E load cell (50 N max. load), attached to the other holder.

### Measuring procedure

In stress–strain experiments, the fascicle was pulled with the speed of 2 µm per second in the wet state. The dehydration tests were performed optionally in a “Zero-Stress” mode, or in “Iso-Strain” mode. In a typical dehydration test, as the RH in the chamber was changed stepwise, the length change (Zero-Stress mode) or the arising force (Iso-Strain mode) were measured. For all measurements, a wet fascicle sample was clamped initially at a length of about 10-15mm, and equilibrated for at least 30 minutes in wet conditions, while the motors were engaged to maintain a constant force of approximately 50 mN on the fascicle. This force is less than 2-3% of the typical highest forces measured after a fascicle was completely dried, while maintained at fixed length). For an Iso-Strain test, after the equilibrium wet length ( $L_0$ ) was reached, the motors were stopped and the force was measured during stepwise changes of

relative humidity. For the Zero-Stress experiments, the motors continued to drive interactively, modifying the strain to maintain a constant 50 mN force while the RH was changed. At humidity higher than 20 % RH, for each step, a 2h time was allowed for equilibration, although the environmental equilibrium of the chamber was reached already after 30 minutes. At lower RH values, the time for sample equilibrium was increased to 3-5 h.

In both Zero-Stress and Iso-Strain experiments, the changes in the fiber diameter were determined by means of videoextensometry. For the calculation of strain with the equation  $\epsilon_L = (L - L_0)/L_0$ , the length  $L_0$  and thickness in wet condition were measured, whereas for the stress the fiber diameter in dry state was used. The precise areas of the polygonally shaped fiber cross sections were measured by means of  $\mu$ -CT (Figure 12a). For the force per molecule calculation, stress was multiplied by the area of a dry molecule  $1.0479\text{nm}^2$ , which results from the assumption of a hexagonal equidistant arrangement of molecules in a distance of 1.1nm (1.55nm for wet condition).

## **Polarized Raman spectroscopy – PRS**

For the theoretical background of polarized Raman spectroscopy, please see Chapter 1.4. For Raman  $\mu$ -spectroscopy, a continuous laser beam was focused down to a micrometer sized spot on the sample through a confocal Raman microscope (CRM200, WITec, Ulm, Germany) equipped with a piezo-scanner (P-500, Physik Instrumente, Karlsruhe, Germany). The diode-pumped 785 nm near-infrared (NIR) laser excitation (Toptica Photonics AG, Graefelfing, Germany) was used in combination with a water immersed 60 $\times$  (Nikon, NA = 1.0) microscope objective. For in situ mechanical tests, a 20 $\times$  (Nikon, NA = 0.4) objective was used. The linearly polarized laser light was rotated using a half-wave plate and scattered light was filtered introducing a further polarizer (analyzer) before the confocal microscope pinhole. The depolarization caused by the experimental setup is negligible [91]. The spectra were acquired using a CCD (PI-MAX, Princeton Instruments Inc., Trenton, NJ) behind a grating (300 g mm<sup>-1</sup>) spectrograph (Acton, Princeton Instruments Inc., Trenton, NJ) with a spectral resolution of  $\sim 6\text{ cm}^{-1}$ . Thirty accumulations with integration time of 1 s were used for single spot analyses.

## X-Ray diffraction – XRD

Small angle x-ray scattering (SAXS) measurements with synchrotron radiation were performed at the  $\mu$ spot beamline, BESSY II, at the Helmholtz Zentrum Berlin (Berlin, Germany). X-ray patterns were recorded with a 2D CCD detector (MarMosaic 225, Rayonix Inc., Evanston, U.S.A.) with a pixel size of 73  $\mu$ m and an array of 3072 x 3072 pixels. For the acquisition of the 2D pattern, the energy of the X-ray beam (100  $\mu$ m in diameter) was 15 keV, and a sample-to-detector distance of 652 mm were calibrated using a silver behenate (AgBeh) standard. In order to obtain the small momentum transfer required to reach the first three meridional peaks, a smaller beam size of 30  $\mu$ m was used, with an energy of 8 keV and a sample-to-detector distance of 852 mm that were calibrated with the same standard. All patterns were corrected for empty beam background and variations in incident beam intensity.

## 2.2 Results and Discussion

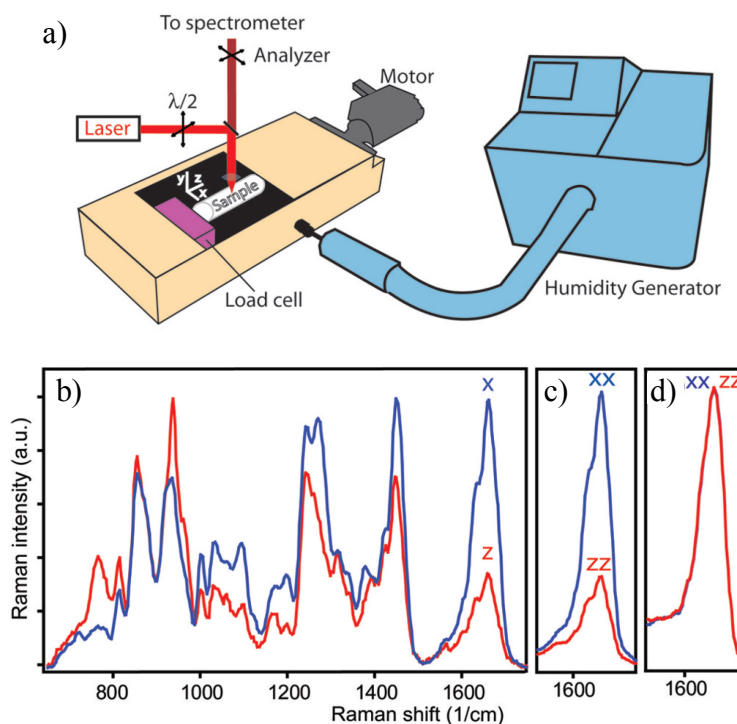
This chapter section is divided in two parts. The first part (1.1.1) presents the spectroscopic changes related to the recrimping and stretching of the RTT in wet condition. The main scope was to use Polarized Raman Spectroscopy (PRS) to monitor conformational changes of collagen-based tissue. The second part (1.1.1) analyzes the physical, structural and conformational properties of collagen in RTT caused by its dehydration, where a multi-technical approach including mechanical testing, XRD and PRS was used.

Collagen in RTT shows a high degree of alignment from the molecular length scale up to the macroscopic length scale [30]. Of specific interest to this work are macroscopic crimp structures that exist at the molecular scale [129, 130]. The crimp corresponds to regions of the collagen fibrils where molecular kinking occurs. This is due to a realignment of the fibril orientation that maximizes inter-fibrillar interactions and releases intra-fibrillar strains from the helical arrangement [131]. At the level of the tissue, a sharp change in the orientation of collagen fibrils can be observed even by optical microscopy. In a uniaxial tensile experiment, a macroscopic crimp is the first structural motif involved in dissipation of applied stress, giving rise to the “toe” region of the stress–strain curve [132]. At strains beyond  $\sim 3\%$ , the stiffness of rat tail tendon increases considerably (heel region) with deformation that involves realignment of molecular kinks in the gap region that become straightened with increasing strain

levels [127, 133, 134]. When tendon is stretched beyond the heel region of the stress/strain curve, gliding of molecules within the fibril takes place before failure of the tendon occurs [100, 134].

### 2.2.1 PRS applied to observe molecular deformation in RTT while stretching in hydrated condition

To examine changes in the RTT under uniaxial loading, simultaneous uniaxial tensile stretching and PRS of RTT fascicles were performed in a humidity-controlled environmental chamber [2]. A schematic sketch of the experimental setup is presented in Figure 8a. The tensile test chamber was placed under the Raman confocal microscope, where the sample was stretched to the desired strain level.

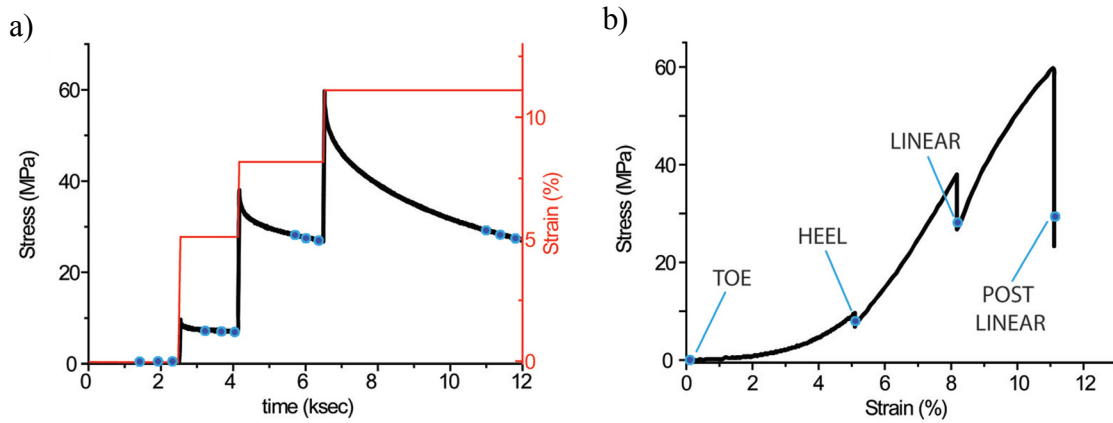


**Figure 8: a) A schematic drawing of the experimental setup used for the PRS measurements. b) Raman spectra taken on stretched RTT oriented parallel (red) and perpendicular (blue) to the polarization of incident laser beam (no analyzer was used). c) The same experiment as in b) with the analyzer inserted in the beam path. Signals from cross-polarized experiments are not shown. d) The same experiment as in c) on thermally denatured RTT. No amide I anisotropy can be observed. [2]**



In Figure 8b, spectra taken on stretched RTT (5% tissue strain, 95% RH) were collected with two different laser polarization orientations: parallel (z, red line) and perpendicular (x, blue line) to the fascicle long axis. The band at  $1665\text{ cm}^{-1}$  arises from the amide I collagen vibration (mainly C=O stretching of the protein backbone), whereas the other major bands at  $\sim 1450$  and  $\sim 1250\text{ cm}^{-1}$  are assigned to C–H bending and amide III vibrations, respectively. Prominent differences in intensities of most Raman bands (especially amide I) in the two different laser-to-fiber configurations were found. A second, similar experiment, that included an analyzer in the optical path to filter the scattered light (see Figure 8a), produced the results shown in Figure 8c. The anisotropy of Raman bands has its origin in the preferential orientation of vibrating molecular bonds with respect to the fiber axis and incident light polarization. The higher intensity of the amide I band in the direction perpendicular to the fiber axis (x) is in agreement with results reported in the literature [12, 116].

To verify this anisotropic observation, an experiment was undertaken to simulate the degradation of collagen. This was accomplished by denaturing collagen by thermal disruption of the collagen structure in the RTT sample. The sample was thermally denatured by exposing it to an elevated temperature of  $80\text{ }^{\circ}\text{C}$  for 2 h. The PR results are shown in Figure 8d. No amide I anisotropy can be observed, confirming a random orientation of C=O groups in the gelatin sample that is disorganized on a molecular scale.



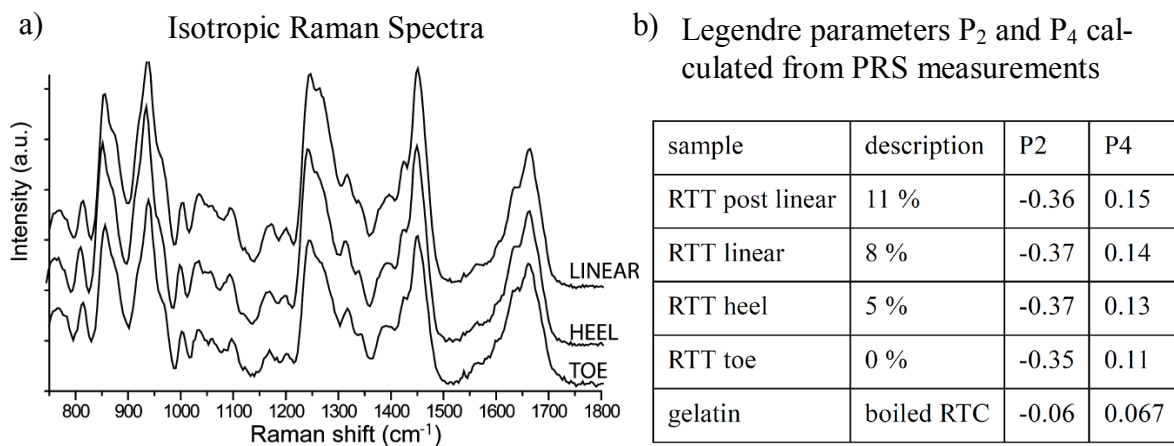
**Figure 9:** *In-situ* tensile experiment. a) Stress and strain curves versus time registered during the tensile experiment and b) corresponding engineering stress–strain curve. Time/strain positions where Raman spectra were collected are indicated with blue dots. The drop down of the stress at the measurement positions is caused by the relaxation as presented in a). [2]

An opposite effect – increasing the molecular order in collagen - can be accomplished by straightening the crimp in RTT by applying a tensile load in the direction along the main axis

of the collagen fiber in tendon [129]. The alignment of collagen fibers is easily monitored by optical microscopy [96]. In Figure 9, representative stress and strain vs time (a) and corresponding stress–strain curves (b) obtained from tensile experiment are shown. Raman spectra (indicated by blue dots in Figure 9a,b) were collected after the time required for stress relaxation (as demonstrated in Figure 9a).

The stress–strain curve in Figure 9b is in agreement with data reported in the literature [135]. The data demonstrate the four characteristic regions, namely: toe, heel, linear, and postlinear regions. The tangent modulus (the slope of the stress-strain curve  $\Delta\sigma/\Delta\epsilon$ ) in the linear deformation region lies between 1 and 2 GPa, in agreement with the values reported in the literature [136, 137]. In the heel region, the measured values (0.5– 1 GPa) also match those obtained by atomistic modeling for single wet micro fibrils [138]. These values are both significantly lower than what estimated for collagen molecules from atomistic models and Brillouin light scattering (between 4 and 9 GPa), suggesting that the deformation of collagen fibers is distributed to the different hierarchical levels, and does result from only the stretching of single collagen molecules. To confirm this hypothesis, we monitored the changes of the vibrational modes of the collagen molecule through the entire tensile experiment.

Raman isotropic spectra registered within toe, heel, and linear region of the stress–strain curve (blue dots in Figure 9b) are shown in Figure 10a.



**Figure 10: a) Isotropic Raman spectra acquired in three characteristic regions of the stress–strain curve of RTT (blue dots in Figure 9b). There was no spectral difference caused by those strains, which indicates no structural change on the molecular level of collagen. b) The table shows the Legendre parameters, which were derived from PRS (as described in chapter 1.4) measurements at different strains of the RTT: 0, 5, 8 and 11%. [2]**

Isotropic spectra were calculated following the procedure reported by Lefèvre et al. [139]. These spectra are characterized by identical peak position as well as peak intensities, suggesting that the molecular vibrational units of the backbone of collagen were not perturbed in the entire range of strains applied. For these strain ranges, significant spectral changes were detected for other macromolecular constituents of natural materials, as for example silk [140] or cellulose in wood [141]. In cellulose, the peak due to the C–O–C bonding is observed to shift when the tissue is strained, indicating that the glycosidic backbone is loaded and strained as well. In silk, several bands associated with the peptide bonds in  $\beta$ -sheets undergo changes when the fiber is stretched. This indicates an alteration in force constants and/or dihedral changes of the bonds in the polypeptide chains. The fact that the Raman peaks from the collagen molecules did not shift during the tensile test may be due to the low stress level attained within the collagen fibers in this case (one order of magnitude lower than in the aforementioned cases). This result also suggests that bonding environment within the triple helix remained unchanged during the tensile test.

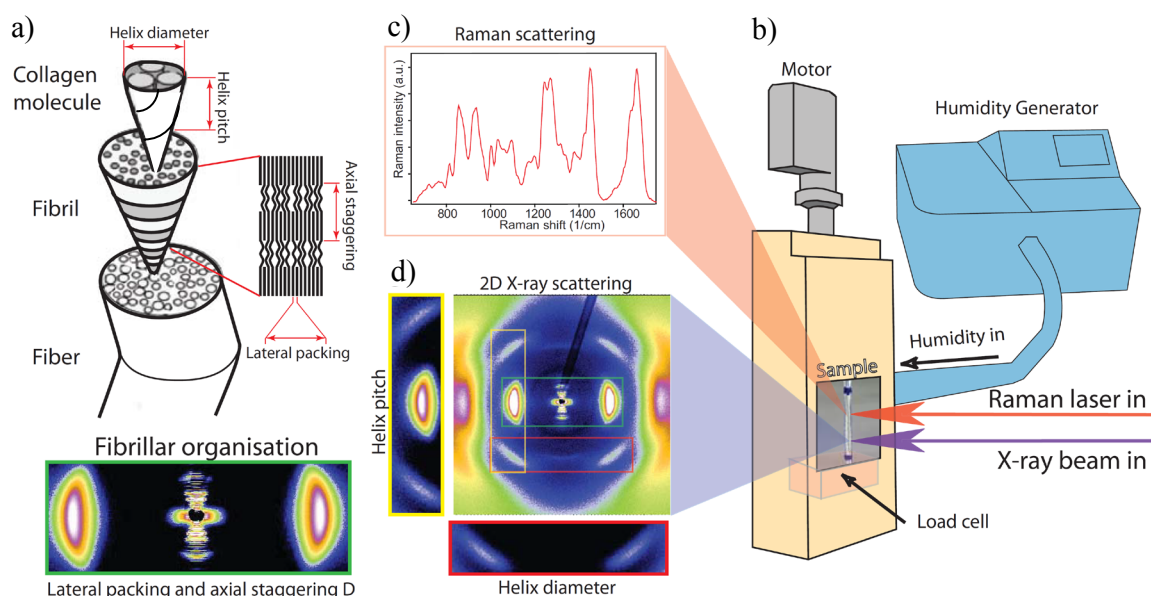
From the same PRS spectra sets used to produce isotropic spectra, we calculated  $P_2$  and  $P_4$  order parameters related to the amide I band for different intermediate steps of strain (Table in Figure 10b). The details of the PRS procedure are reported in Chapter 1.4. Negative values of  $P_2$  indicate the transverse orientation of the amide I vibrational unit (mainly stretching of C=O) with respect to the main axis of the collagen molecule and fiber. Applying the Legendre addition theorem for nested distributions, these values can be used to calculate  $P_2$  and  $P_4$  order parameters of the distribution of collagen molecules with respect to the fiber axis in the analyzed region (Table in Figure 10b).

However, when the applied strain reached the linear region of the curve, a sharpening of the distribution  $f_{mp}$  (eq. (22)) occurred due to the alignment of the collagen molecules compared to the toe and heel regions. The corresponding distribution functions  $f_{mp}$  are plotted in (Figure 20) together with the determined distributions calculated after collagen dehydration. This PR results are in good agreement with X-ray scattering results and atomistic simulations that indicate the collagen molecules are straightened, in the heel strain regime, starting from the gap region and then extending within the entire fibril [135, 138]. At the tissue level, straightening of the crimp can be observed optically when passing from the toe to the heel region. Molecular level reorientation occurs only in the linear part of the curve, indicating further straightening of collagen molecules with respect to the direction of applied stress.

In summary, the results presented here are in agreement with common models of the hierarchical deformation of RTT. Applied strain does not affect the molecular vibrational levels of the collagen structure, but it is rather distributed via higher levels of hierarchy through reorientations and lateral sliding of collagen molecules. However, PRS offers interesting strategy in obtaining both; structural orientation, and changes in chemical interactions in molecular units of collagen.

### 2.2.2 Dehydration of RTT induces high tensile forces and conformational changes on intermolecular levels

After the investigation of the structural changes of strained fibrillar collagen in hydrated conditions, the effects of dehydration on the RTT were explored. The scope of the observations was to monitor changes at several hierarchical levels simultaneously. Therefore, *in-situ* Raman and X-Ray diffraction measurements were taken during mechanical testing on RTT in a fully controlled environmental chamber.



**Figure 11: a) Schematic drawing of different hierarchical levels of collagen, b) experimental setup, c) a typical Raman spectrum and d) an X-Ray diffractogram of RTT collagen are shown. The presented x-ray pattern provides information on the pitch and the diameter of the collagen triple-helix as well as on the axial staggering and lateral spacing.**

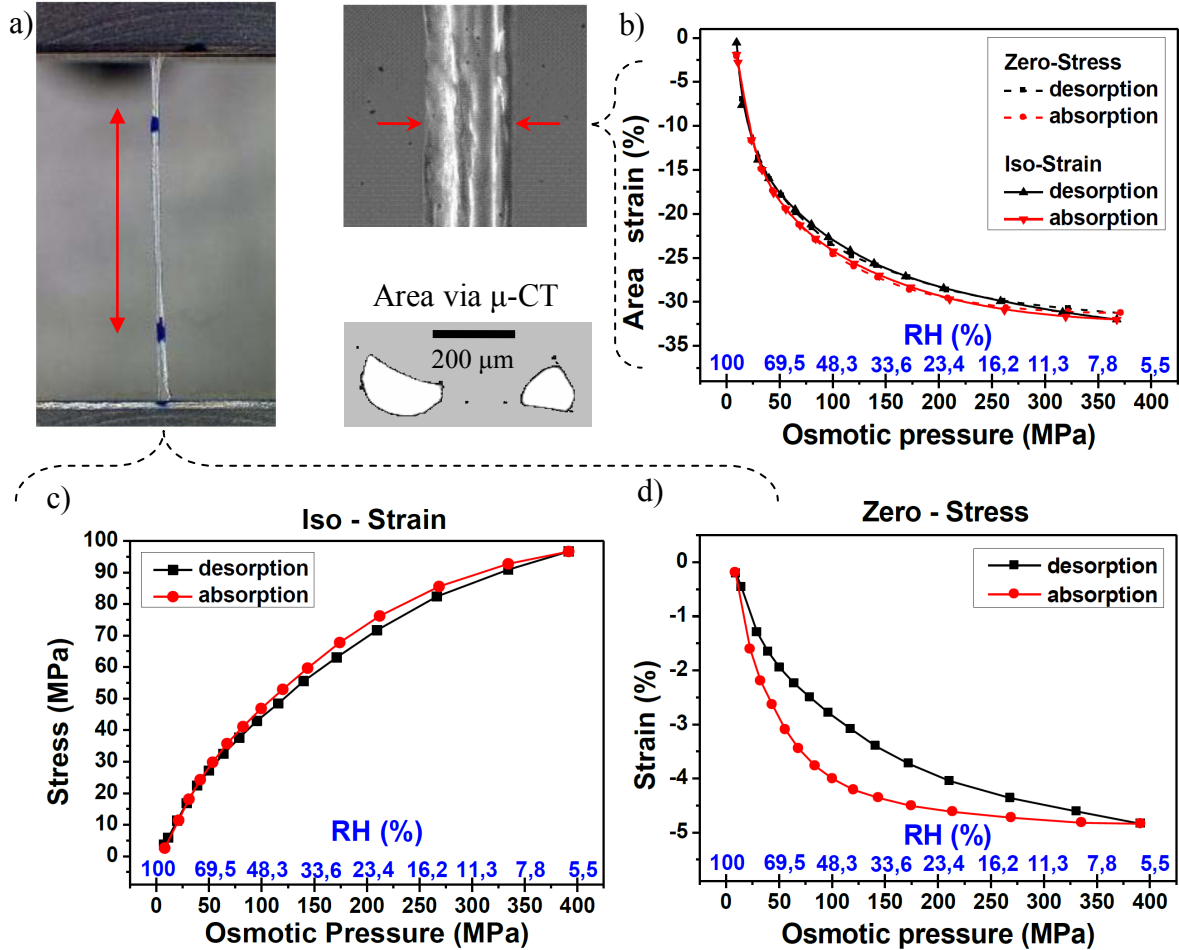
Figure 11 shows a schematic drawing of the different hierarchical levels of collagen (a), the experimental setup (b), the typical Raman spectrum (c) and X-Ray diffractogram (d) of RTT collagen. The schematic drawing includes the important key descriptors with the corresponding X-Ray diffraction patterns of this descriptors: “helix diameter” - diameter of the collagen molecule, “helix pitch” - molecular length section until the triple helix completes its turn and starts to repeat the coil, “lateral packing” - lateral distance between individual molecules, “axial staggering” - D-period, along the collagen fibrils, see chapter 1.1. These keywords are important to the discussion of the results.

Shrinkage is the typical response of collagen to drying, when water is removed from the different hierarchical levels. The conformational changes due to drying on the molecular level induce forces that produce work on the macroscopic level. Quantitative characterization of the arising stresses and the structural changes accompanying the force generation due to drying was the goal of these experiments. Therefore, two complimentary experimental strategies were applied: the iso-strain and zero-stress controlled experiments. In iso-strain, the fascicle was fixed in the wet state at the strain required for the fascicle reach the heel region of the stress-strain curve. The arising forces due to fascicle drying were monitored. In zero-stress mode, the motors were interactively moved by the software to maintain a tensile force at low positive values, and the strains were recorded while the fascicle dried. In both experiments the changes in fascicle thickness were measured with a high resolution camera. The area strain was calculated from the thickness strain of the fascicles using a perfect cylindrical fascicle cross section for calculations. The longitudinal strain was measured by means of the motor distance. Beforehand, in several dehydration experiments the motor displacements under force was compared and has been found in absolute agreement with the videotensometric results when marks on the sample were used (Figure 12a). No slippage of the sample at the clamping site occurred.

The results are shown in Figure 12b. They show that the cross sectional area was reduced by up to approximately 30% in both experimental approaches. This means that the applied stress or strain along the fiber did not affect the lateral macroscopic behavior of collagen fibers during de- and re-hydration. The strain in the longitudinal direction reached -5% Figure 12d.

For the stress calculation (Figure 12c), the absolute fascicle cross-sectional area is required. For this purpose, we measured the cross-sectional area and the force generation of 12 fascicles in iso-strain approach in the very dry state: 3-5 %RH. After the experiment, the

cross-section of the fascicles was measured by means of a  $\mu$ -CT scan at room temperature and humidity, and corrected according to the area strain curves to the final dry condition. The estimation from room condition to the dry state was required because it was not possible to create a very dry ambient inside the  $\mu$ -CT device for the measurement.



**Figure 12: Zero-stress and iso-strain macroscopic video extensometric experiments of RTT in length and width during humidity changes. a)** Optical camera view of the clamped sample during the experiment and a post experimental  $\mu$ CT cross section scan of two different fascicles, demonstrating the irregular shape. **b)** Cross-sectional area of the fibers was measured and plotted as a function of RH for both zero-stress and iso-strain experiments. In both experiments the fascicle area was reduced approximately 30% upon drying. The area strain was calculated from the measured diameter/thickness change. The x-axis is plotted in both relative humidity and osmotic pressure units. **d)** In relation to the longitudinal direction in the case of zero-stress experiment, fiber shrinkage was observed and reached approximately 5% of total strain in length at 5% RH. **c)** In the iso-strain experiment when the fiber is constrained from shrinking, internal stresses were generated.

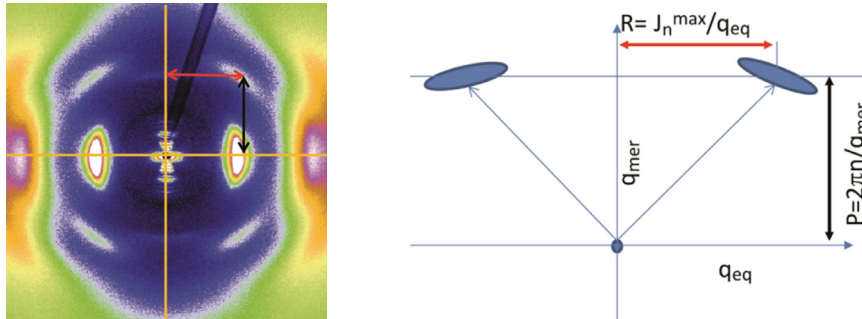
Measured stress at 3-5 %RH: 102 (+/-15) MPa, (mean value and standard deviation)

To calculate the force per molecule of drying tendon, the distance between single molecules in dry tendon collagen of 1.1 nm (1.55 in wet condition) was used [39, 40]. The molecule area of a hexagonal, equidistant arrangement is:

Area (dry) of a molecule =  $a \cdot h = a \cdot \frac{a\sqrt{3}}{2} = 1.0479 \text{ nm}^2$  ( $a$  is the side length (molecular distance) and  $h$  is the height of each triangle inside the hexagon).

Calculated force per molecule: 107 (+/-16) pN (mean value and standard deviation)

To compare the macroscopic strains with the analogous changes on the fibrillar and molecular levels, the data on this scale was obtained by means of 2D X-Ray scattering measurements. To extract the helix parameters (i.e. pitch and radius) from the WAXS measurements, according to Okuyama [142], the 2D diffraction patterns in the  $q$  space can be assigned to the collagen structural parameter space using the 7/2 model for the collagen triple helix structure (see chapter 1.1). For every pixel with coordinates  $(q_{eq}, q_{mer})$ , it holds (Figure 13):



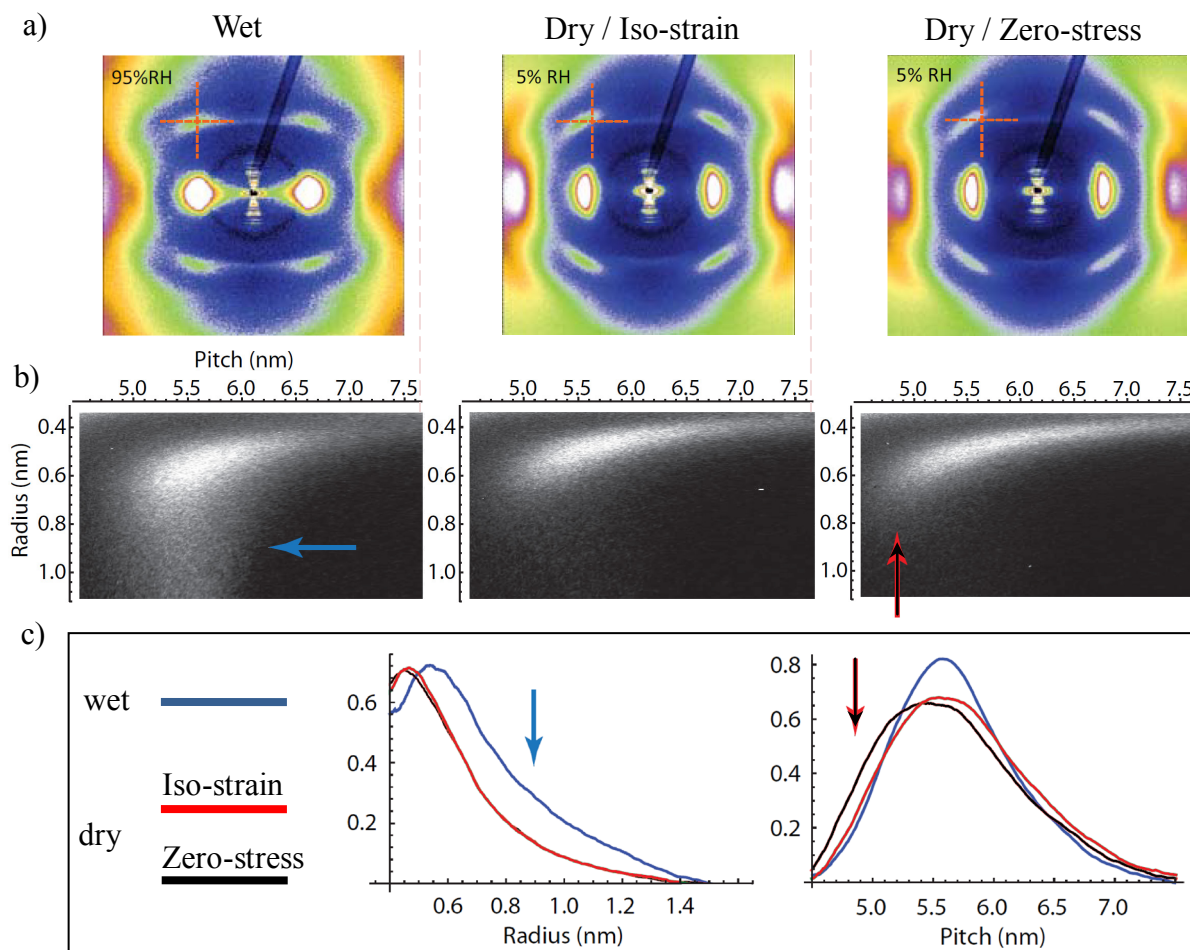
**Figure 13: A typical 2D X-ray diffraction pattern of RTT. The position of helix reflection peaks ( $Q$  space) is converted into the triple helix diameter and pitch (real space) as described in the text.**

$$P = \frac{2\pi n}{q_{mer}} \text{ and } R = \frac{J_n^{\max}}{q_{eq}} \quad (23)$$

where  $P$  is the axial period of the collagen molecule, that corresponds to 1/3 of the pitch length,  $n$  is the order of the layer line and  $J_n^{\max}$  is the position of the first maximum of the  $n^{\text{th}}$ -order Bessel function of the first kind. As we considered the 7/2 model for collagen, the reflection we studied is the one corresponding to the second layer line, so that  $n=2$  and  $J_n^{\max}$  is 3.



In Figure 14 the radius and the pitch of the molecular triple helix are discussed. The red cross in the 2D diffraction patterns in the  $q$  space (Figure 14a) is fixed at the central position of the related peak in the wet state, and visualizes the scattering shift due to drying. Figure 14b shows calculated 2D maps, which depict the relationship between the collagen helix pitch and radii. Figure 14c shows the corresponding 1D distributions of helix pitches and radii, which were obtained by projecting the aforementioned 2D maps on the vertical and horizontal axes, respectively.

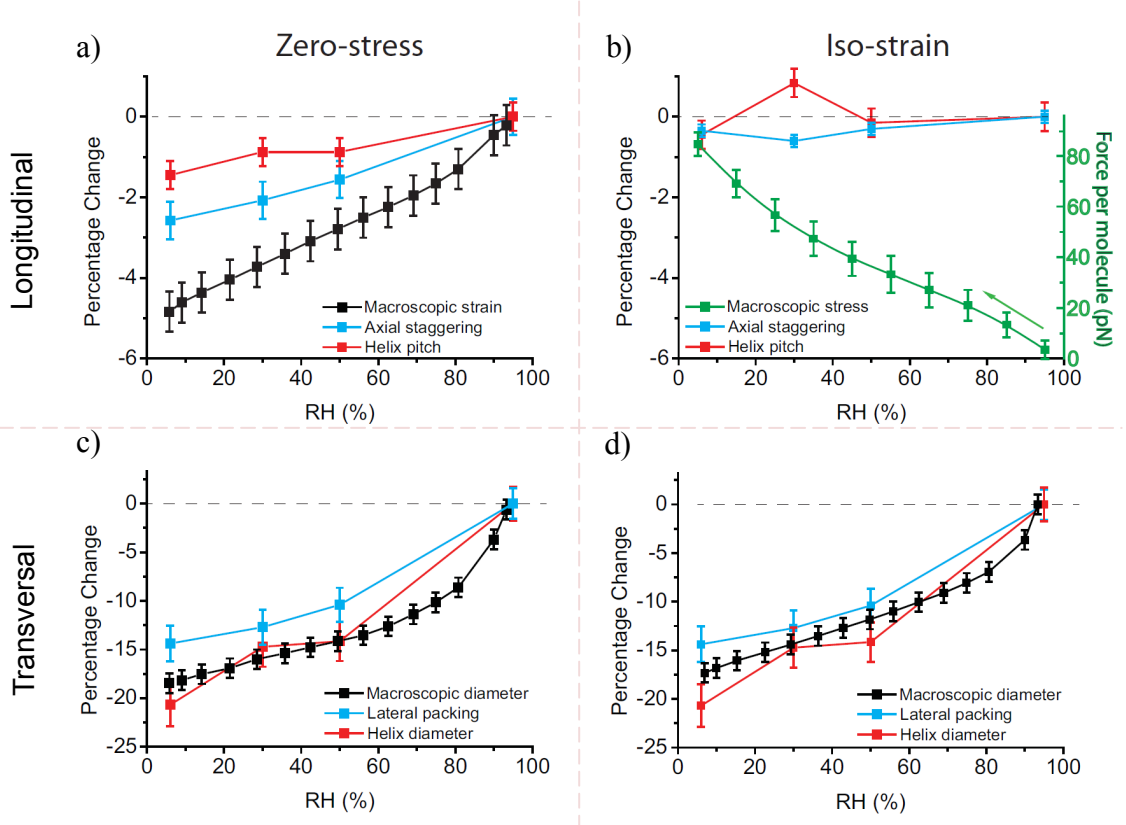


**Figure 14:** a) 2D x-ray scattering in the wet state and after drying at constant length (iso-strain) or without load (zero-stress). The cross indicates the position of the scattering maximum of the collagen triple-helix in the wet state. Note the shift and deformation of the triple helix feature during drying. b) and c) Measured projections of intensities relative to helical radius and pitch from x-ray diffraction of the collagen molecule in the wet (blue curves) and dry states (red and black curves for iso-strain and zero-stress measurements, respectively).

Interestingly, similarly to the macroscopic behavior, the helical radius was reduced similarly for the zero-stress and iso-strain approaches. On the other hand, the helical pitch was unchanged by drying in the iso-strain experiment, but was reduced slightly (1.3%) by the zero-



stress approach. In either case, the scattering distribution in the wet state showed higher variability for the radius of the triple helix, but not for the pitch. (See the tail distributions in Figure 14b, c.) The axial staggering (the D period) and the lateral packing – the distance between the individual molecules – is shown in Figure 15 together with the other X-Ray scattering and macroscopic mechanical results.



**Figure 15: Multi-scale analysis of the mechanical behavior of the RTT collagen during dehydration: mechanical and X-ray scattering results.** The starting point was always the fully hydrated and prestretched state of the fascicle. a, c) represent the dehydration without load (zero-stress) and b, d) at constant length (iso-strain). a, b) show the distance changes in axial direction, the macroscopic length of the fascicle (black), the axial staggering period D of the molecules (blue) and the helix pitch inside the molecule (red). In the case of drying at constant length b) an example curve for the force per unit molecule is also reported (green curve). c,d) show the changes in lateral direction, the macroscopic diameter/thickness (black), the lateral spacing between molecules (blue) and the diameter of the triple-helix (red).

For the evaluation of the first three meridional peaks, the 2D SAXS patterns were integrated in the equatorial direction using the Projection function of Fit2D software [24]. The 1D intensities  $I(q_{mer})$  of meridional peaks were fitted by a Lorentzian curve to find the peak positions  $q_{mer}$  for the modulus of the scattering wave vector and its integrated intensity. The staggering period D under different hydration conditions was calculated, fitting the intensities of the 20<sup>th</sup> reflection. The average values for the triple helical parameters (i.e. pitch and radius)

were obtained by integrating over the distribution function in Figure 14c, after the background was removed. The results in Figure 15 are organized in a 2x2 table manner; the experimental approaches are aligned vertically, and the direction of the strain presented horizontally.

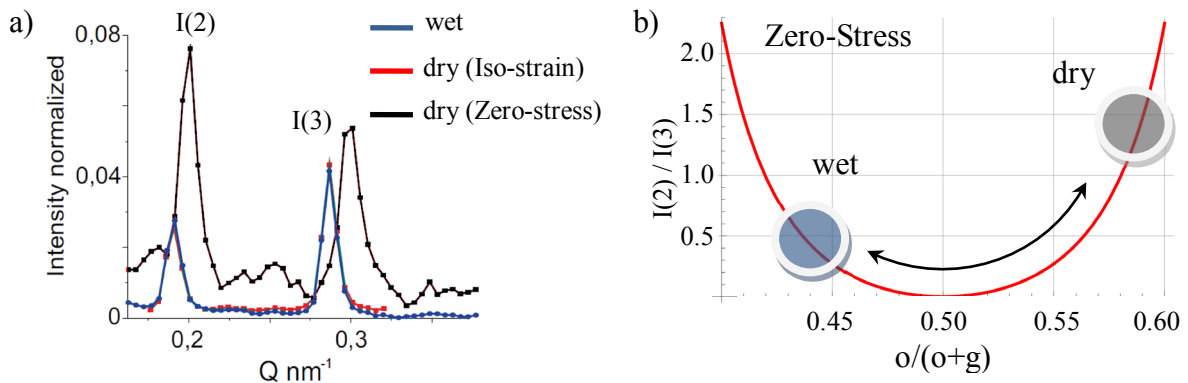
The shrinkage behavior in lateral/ transversal direction is concordant for all the hierarchical levels, from the molecular radius up to the macroscopic fascicle thickness (Figure 15c,d). The relationship between the hierarchical levels is different along the longitudinal direction of the fibrils. There, the axial staggering shrinkage (-2,5%) was two times less than the macroscopic strain (-5%) as the sample was dried in zero-stress experiments (Figure 15a). The measured helical pitch changes (-1,3%) were less than the axial staggering changes. However, both helical pitch and axial staggering did not change in the iso-strain experiment (Figure 15b).

To address the issue of different longitudinal contractions that appear throughout the hierarchical levels, we looked also at the changes in the gap to overlap ratios. According to Sasaki et al [47, 143] the overlap (length O) to staggering period (length D) ratio, that we call  $R_{(O/D)}$ , relates to the intensity of the  $N^{\text{th}}$  reflection  $I(N)$  as follows:

$$I(N) \propto \left( \frac{\sin(\pi \cdot N \cdot R_{(O/D)})}{\pi \cdot N \cdot R_{(O/D)}} \right)^2 \quad (24)$$

From this, the gap to overlap ratio,  $(1 - R_{(O/D)})/R_{(O/D)}$  can be numerically calculated, for example from the intensity of the 2<sup>nd</sup> and 3<sup>rd</sup> reflections  $I(2)$  and  $I(3)$ , and solving numerically:

$$\frac{I(2)}{I(3)} = \frac{9}{4} \cdot \left( \frac{\sin(2\pi \cdot R_{(O/D)})}{\sin(3\pi \cdot R_{(O/D)})} \right)^2 \quad (25)$$



**Figure 16: The changes of the 2<sup>nd</sup> and 3<sup>rd</sup> order intensity ratios correlates with the gap/ overlap ratio changes. a) Second and third order reflections from axial staggering, normalized to the same intensity in the first order. The peaks for the hydrated and the iso-strain dry case overlap (blue and red), while the peak position and intensities are changed after drying with no load (black). b) Correlation curve between the intensities  $I(2)/I(3)$  and the overlap portion over the whole staggering period  $D=O+G$ .**

Figure 16 demonstrates how I(2) and I(3) changed due to dehydration. The gap zone reduced strongly in the zero-stress while it was unchanged from the wet state in the iso-strain measurements.

As it can be read from the Figure 16b; in the hydrated condition, the gap is larger than the overlap (gap>overlap), then: during dehydration I(2) decreases until it disappears (gap=overlap) and then, at a semi-dry state, it starts to rise again to the same amplitude as I(3). In a very dry state, it becomes even larger than I(3) (gap<overlap). Of course, since the curve is a parabola with the vertex located at the point where the gap and overlap are equal, the ratio points of wet and dry conditions can be mirrored on the parabola. Wess et.al. reports for the overlap 0.46 of D in a wet state [7, 144], which is in good agreement with our interpretation of the curve in Figure 16b.

We can now develop a model for the changes in gap and overlap in a drying process without load. In wet conditions, the staggering period (the sum of gap G and overlap O) was  $D = G + O = 66$  nm, as measured by x-rays. The gap to overlap ratio in the wet condition was 0.54:0.46, so the value of G and O can be readily calculated. After dehydration, the D period was decreased by about 2.5% during zero-stress measurements, while the molecular length L decreased only by about 1.3% (Figure 15). If a homogeneous shrinkage over all the collagen molecule is assumed, i.e.  $\varepsilon_g^m = \Delta G/G$  and  $\varepsilon_g^m = \Delta O/O$  are both -1.3%, this would mean that, over 5 periods (330 nm), the collagen molecules should glide side by side to account for the residual 1.2%, i.e. about 4 nm. On the other hand, the same molecular and fibrillar strains can be attained considering that no interfibrillar gliding occurs, but the gap and overlap regions undergo different length changes upon drying. In this case the relationships that have to be satisfied are:

$$O^{dry} + G^{dry} = D^{wet} (1 - 0.025) \quad (26)$$

and

$$5 \cdot O^{dry} + 4 \cdot G^{dry} = L^{wet} (1 - 0.013) \quad (27)$$

Solving this set of equations gives:

$$O^{dry} = L^{wet} (1 - 0.013) \cdot 4 \cdot D^{wet} (1 - 0.025) \quad (28)$$

and

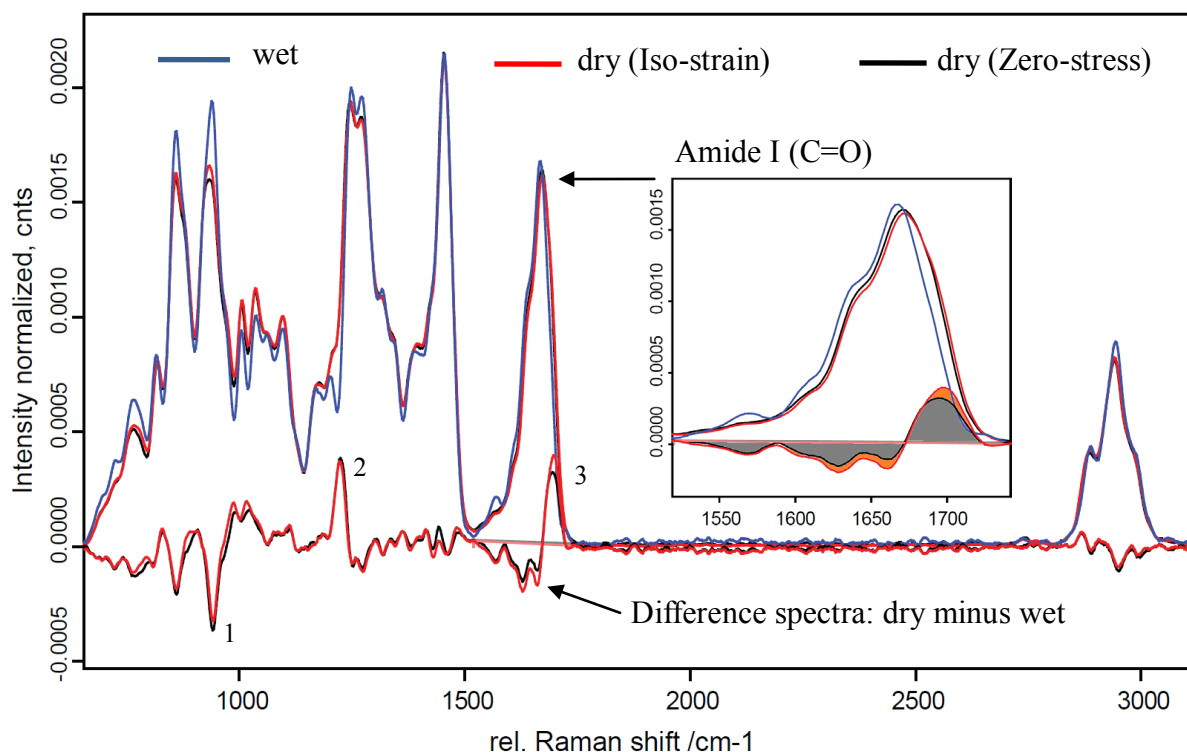
$$G^{dry} = L^{wet} (1 - 0.013) - 5 \cdot D^{wet} (1 - 0.025) \quad (29)$$

The strains for the gap and overlap regions calculated from these equations are -12% ( $\pm 5\%$ ) and +9% ( $\pm 5\%$ ) respectively. In chapter section 2.3 we will bundle the results to a drying model of collagen presented in Figure 21, where we approximate the strain for the gap with -15% and for the overlap with +10%.

In the next step we looked at the spectral changes in Raman, which provide the information about the molecular bonds and molecular conformational changes. During drying, the water molecules are removed, and the RTT contracts axially and laterally in space. The spectral intensities rise after drying due to the higher material density in the probing volume of the confocal Raman laser interacting with the sample surface. This behavior makes a direct comparison between wet and dry Raman spectra difficult, even when the same experimental setups (i.e. laser power and lens) were used; therefore, a normalization approach was required. From literature we know that the  $\delta(\text{CH}_{2,3})$  band at  $1460\text{cm}^{-1}$  shows isotropic distribution [12], which makes it suitable for normalization purposes. However, the conformational properties of this band or the neighboring (shoulder) peaks could change after the dehydration and influence the intensity of the  $\delta(\text{CH}_{2,3})$  peak. When the 532 nm laser is used, the CH bond at about  $2900\text{ cm}^{-1}$  is quite intense, and can be also used for normalization. However, because of the possible fluorescence that is usually characteristic for the collagen based materials (i.e. ancient parchments), we choose to work with the NIR laser line at 785 nm. In the NIR region the intensities at high relative wavenumbers suffer in loss of detection sensitivity. Furthermore, due to absorption, the depth change of the confocal probing volume affects the intensity distribution in the Raman spectrum between lower and higher wavenumbers slightly. This makes the relatively small CH peak in the  $2900\text{ cm}^{-1}$  region, which is quite far from the fingerprint region, problematic for the normalization purpose.

Therefore, for the normalization we used the integral (after baseline correction) of the full range ( $350\text{-}3230\text{cm}^{-1}$ ) of the isotropic spectra using the argument that the full amount of vibrational centers changes linearly with the material density, though they can change their orientation, which do not matter for the isotropic spectrum. However, the influence of the depth change on to the intensity distribution of the whole spectra can then be neglected. Since the collagen spectra are highly anisotropic, each measurement consists of four polarized Raman acquisitions (eq. (14)-(17) in Chapter 1.4), that allows for the calculation the isotropic spectra as described in the literature [145]. Before the normalization, the spectra were cut ( $350\text{ cm}^{-1}$  to

3230  $\text{cm}^{-1}$ ) and baseline corrected (rubber band approach via the 1<sup>st</sup> order in the interactive mode in OPUS7.0).



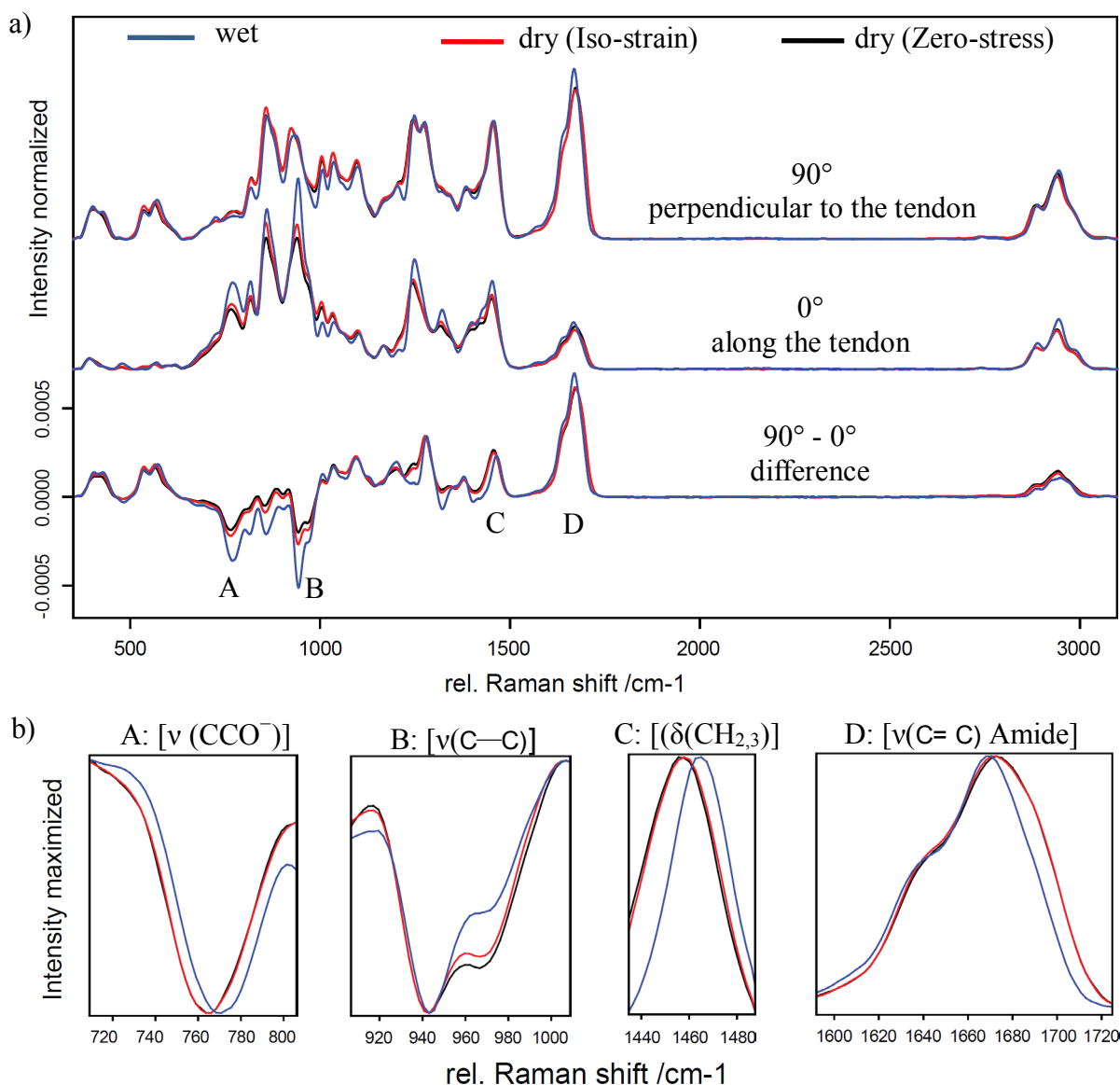
**Figure 17: Raman spectra, 785 nm laser. Calculated isotropic average spectra of RTT in wet (blue), iso-strain dry (5% RH) (red), and zero-stress dry (black) experiments. The lower spectra with positive and negative values around the zero line are the calculated difference between the dry and the wet spectra. The difference spectra shows that both iso-strain and zero-stress do not differ significantly from each other, and are both very different from the wet spectrum. One of the biggest changes (indicated with Arabic numbers) is located in the amide I region (3). The inset of the figure is the enlargement of the amide I region. The negative area of the calculated changes differs to the positive area with less than 10 %, showing that drying causes only a spectral shift.**

The normalized isotropic spectra of both wet and very dry conditions are shown in Figure 17 together with the calculated difference spectra. This normalization approach provided a reasonable result. The presented spectra were averaged from 5 to 7 measurements in different sample areas; in the wet and the iso-strain cases, the spectra were taken from 2-3 different points. The graph shows that the iso-stress and zero-strain spectra differ similarly from the wet spectrum. The strongest differences were assigned with Arabic numbers: 1. is the molecule backbone [ $\nu(\text{C}-\text{C})$ ] stretching, 2. is the amide III [ $\nu(\text{C}-\text{N}) + \nu(\text{C}-\text{C}) + \delta(\text{N}-\text{H})$ ] and 3. identifies the amide I [ $\nu(\text{C}=\text{O})$ ] band [6, 11, 146].

Our main interest was dedicated to the amide I region because we use its strong anisotropic features for the PRS analysis. In the inset, a zoom of the amide I region is presented. Comparison of the wet and dry spectra shows the shift of some subpeaks of the amide I band to higher wavenumbers. The fact that the total area of the integral of the difference spectra is almost zero (only 10% difference between negative and positive) for both experimental approaches indicates the major change was shifts of the peaks, and confirms the accuracy of this normalization approach.

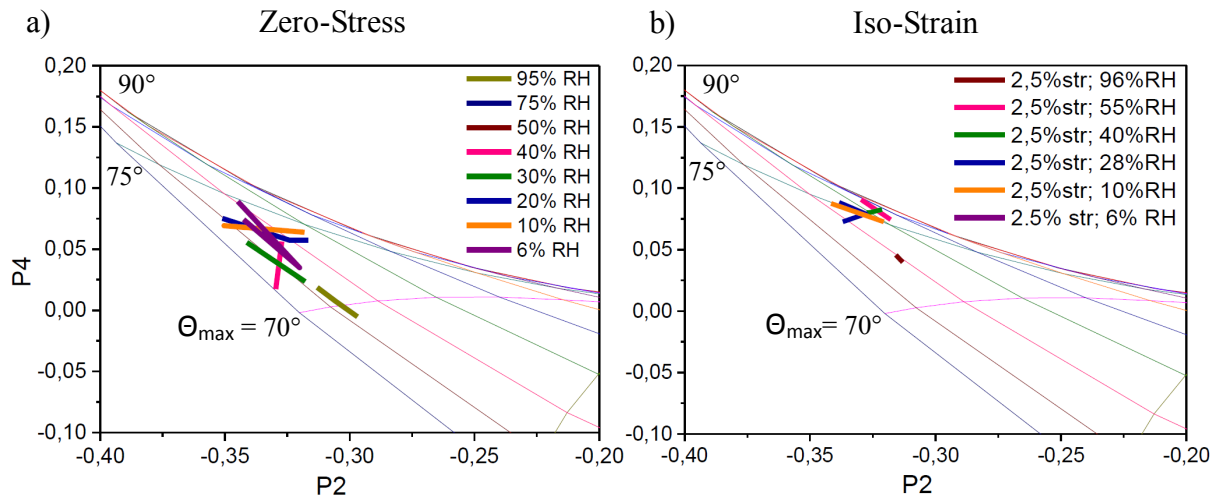
The isotropic spectra in Figure 17 should not reflect the changes that are related to the orientation of the molecular bonds. Therefore Figure 18a presents the polarized dependency of the wet and dry measurements respectively along ( $0^\circ$ ) and perpendicular ( $90^\circ$ ) to the fibril. The calculated difference between  $90^\circ$  and  $0^\circ$  spectra is also shown. The change between wet and dry of the “difference ( $90^\circ - 0^\circ$ )” spectra indicates the change in orientation of the vibrational bonds. In Figure 18b, some of the striking changes are discussed, whereas the intensities are maximized in order to illustrate the spectral shifts. The characteristic spectral changes A, B, C and D that represent different combinations of orientational and spectral changes are discussed in the caption text.

Most of the orientational changes are accompanied with the spectral shift due to the removal of water molecules. The case of B: ( $\nu(\text{C}-\text{C})$  of the backbone) differs from the others. In the  $\nu(\text{C}-\text{C})$  backbone, a strong intensity change, which means changes in orientation was observed, but there was no spectral shift. The removal of water molecules was obviously not directly involved in this vibration, but in any case, the molecule changed its conformation, with no significant difference between iso-strain and zero-stress techniques.



**Figure 18: Raman spectra, 785 nm laser. Orientation change (conformational changes) after dehydration shows;** a) three spectral categories, wet and dry conditions in different colors. The upper spectra were obtained from laser polarization and analyzer orientation at  $90^\circ$  with respect to the fascicle and the molecule. The middle spectra were measured along the molecule. The lower spectra were calculated from the upper spectra, representing the difference between  $90^\circ$  and  $0^\circ$  spectra. Negative values represent the predominant orientation of the vibrational intensities along the molecule, whereas the positive values represent peaks with the perpendicular orientation. Four representative areas around the A, B, C and D peaks are enlarged in b), they show different characteristic behavior of the spectral change due to dehydration. The intensities are maximized in order to point out the shape changes and peak shifts. A ( $\nu(\text{CCO}^-)$  of the backbone) is strongly oriented along the fiber [6] in the wet condition; after drying its intensity gained in the perpendicular direction, and was reduced along the molecule (see in a). This reduced its difference, but also a shift to lower wavenumbers can be observed. The orientation change in B ( $\nu(\text{C}-\text{C})$  of the backbone) was even stronger, there is no spectral shift. Contrary to this observation, C ( $\delta(\text{CH}_2)$ ,  $\delta(\text{CH}_3)$  [11]) intensity does not change dramatically [12], but it showed a clear spectral shift to lower wavenumbers. D ( $\nu(\text{C}=\text{C})$  Amide I) peaks do not change with orientation significantly, but its peak gained a strong shoulder to the higher wavenumbers.

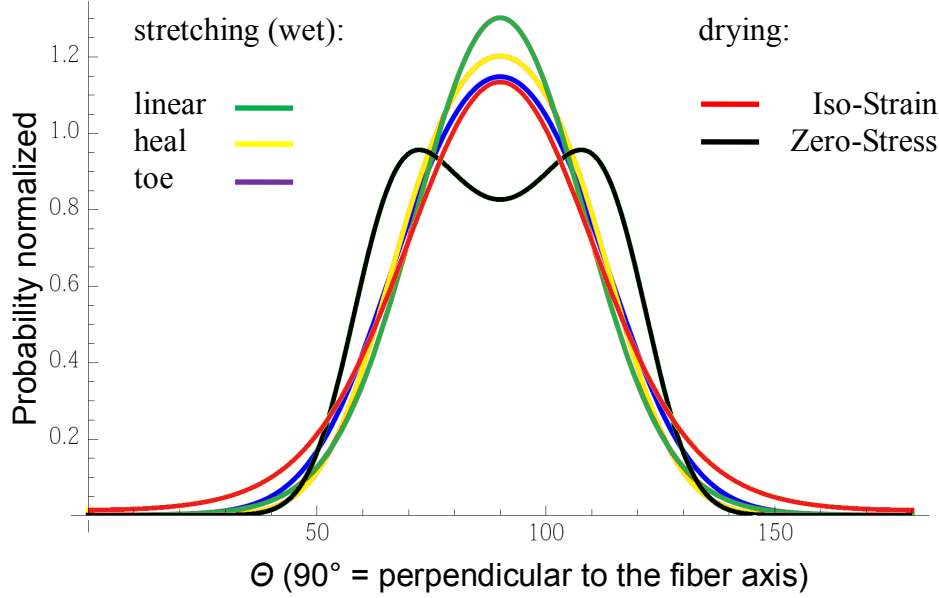
After we have seen that the spectral shift of the amide I band showed very similar isotropic features after dehydration, we now can look at the PRS analysis, which we already applied to study fully hydrated tendon. The results for iso-strain and zero-stress experiments are presented in the P2/P4 space in Figure 19. For the calculations of the Legendre parameters, the integral area of the whole amide I peak was used for the eq. (14)-(17) in Chapter 1.4. At each humidity step, two measurement points were collected, those are connected by a straight colored line for clarity. The grids are the related Gaussian-isotherms as they are defined in Figure 7.



**Figure 19: PRS measurements on collagen fascicle of a RTT during the dehydration are presented in a P2/P4 space. The grid lines in the graph represent the Gaussian parameters  $\theta$  and  $\omega$  as defined in Figure 7. At each hydration level two or more points were measured. For clarity, the measurements of the same state are connected by straight colored lines. a) Zero-stress experiment -the sample was prestretched to remove the crimp before dehydration. b) Iso-strain experiment - the sample was first measured in the wet condition at a strain of 2.5 %. From that point, the length was kept constant, and the sample was measured at different dehydration steps.**

The spread of the PRS measurements in P2/P4 space (Figure 19) shows that the intention of quantitative characterization with the difference between iso-strain and zero-stress approaches has to proceed with caution. No trend was observed inside one dehydration track; all the points of a particular experimental approach, except for the wet, are randomly distributed in a “cloud”. However, a clear difference between the two experimental approaches can be found. In order to highlight the differences, we calculated the corresponding, most probable distributions from P2/P4 values. These estimations are presented with Gaussians in Figure 20 together with the results from the previous chapter section where the RTT was aligned mechanically in the wet condition.





**Figure 20:** Approximation of the probability distribution (eq. (22)) of the amide I band determined by means of PRS approach on RTT collagen fascicles.  $\Theta$  depicts the orientation of the molecule. Amide I band ( $\text{C}=\text{O}$ ) is highly oriented perpendicular to the fascicle. The results show that tensile alignments cause a higher degree of order; on the other hand, drying disordered the distribution of the  $\text{C}=\text{O}$  bonds in the zero-stress approach; a condition when the fascicle was allowed to shrink.

The approximation for the probability distribution of the amide I shift shows a slight trend to higher alignment when the collagen fiber is prestretched and straightened mechanically. Drying induces molecular disorder, which is much higher if the fascicle is not uniaxially loaded while drying. No discrimination could be made with these PRS results about the hierarchical level where the disorder appears; according to this PRS results the disorder could either be at the intermolecular bond (helix) level, or at the fibrillar level where the whole collagen molecules change their orientation.

### 2.3 Structural Model for the interaction of water and collagen

In the first part of the results (1.1.1), the molecular level PR spectroscopic information from tendon collagen in the wet condition was used to study the mechanical behavior of RTT under uniaxial tensile deformation. The results demonstrate the remarkable potential of the PR

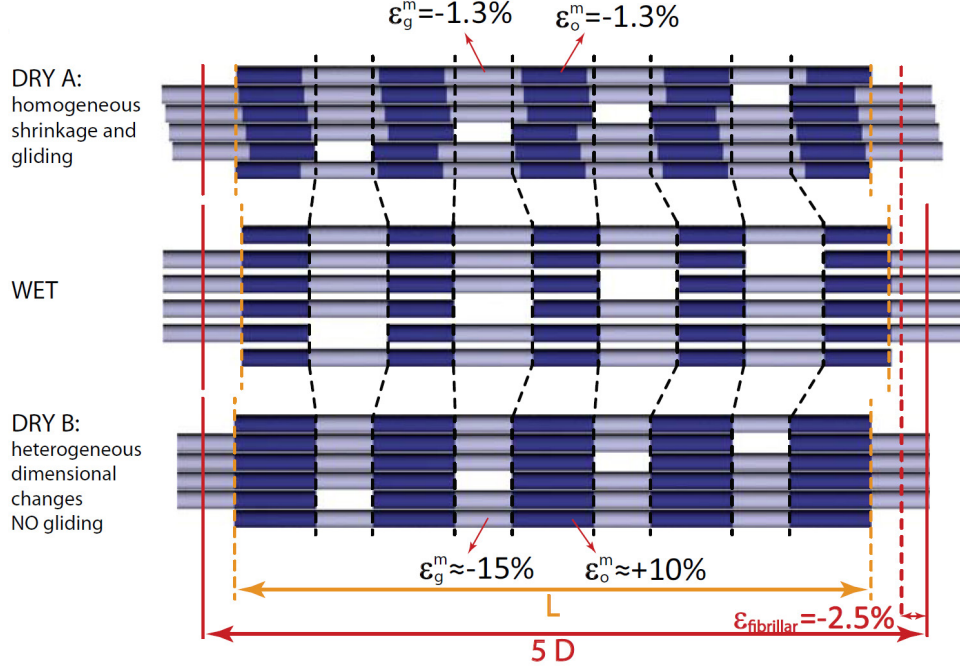
analytical technique to obtain orientational information of collagen molecular assembly. The *in situ* tensile mechanical tests showed that the orientation distribution function of collagen molecules changes its shape throughout the stress-strain curve regions (from the heel to the linear region), indicating an increase in molecular alignment. The externally applied stress, however, resulted only in the reorientation of the collagen molecules, and did not affect any of its vibrational molecular properties (Figure 10 and Figure 20).

Water is an important component of collagen in tendons. In the second part of the results (1.1.1), a multi-scale experimental approach was used to reveal that water is an integral part of the collagen molecule, and removal of water leads to extensive collagen conformational changes. The main consequence of drying is shortening of the collagen molecule that translates into tensile stresses in the range of 100 MPa (Figure 12c), largely surpassing tensile forces of approximately 0.3 MPa generated by contractile muscles [147].

The complete drying of collagen is extremely relevant for technical applications, especially the fabrication of leather or parchment. The knowledge obtained in this chapter will be of fundamental importance in the next chapters, where we will explore the preparation methodologies of the ancient manuscripts. However, stresses observed in dehydration experiments are relatively high at very small osmotic pressures (high RH), indicating that collagen contraction could occur even in biological, hydrated environments. The relationship of collagen stress and strain with the osmotic pressure is shown in Figure 12b-d). It is not excluded, therefore, that water-generated tensile stresses may play a role in living collagen-based materials such as tendon or bone. Based on our results, we developed a possible model that describes changes at molecular and nanoscopic levels related to the dehydration process. From the experiments we conclude that water plays a crucial role in stabilizing the structure of the collagen molecule, and is an essential and active part of the protein unit. The observations by X-ray and Raman scattering are consistent with the full atomistic MD [138] and lead to the following features of the complete drying process:

- (1). the molecule and the fibril shrink by different amounts, 1.3% and 2.5%, respectively. (Figure 15)
- (2). dehydration is accompanied by a reduction of the gap/overlap ratio of the collagen fibrils. (Figure 16)
- (3). shrinkage of the triple-helix is inhomogeneous, as shown by the distribution of helix pitches. (Figure 14)

Moreover, Raman spectroscopy indicates conformational changes of the backbone upon drying (Figure 18, Figure 19). These observations are translated into a simple model as shown in Figure 21. A priori, two possibilities exist that would explain (1) and (2).



**Figure 21: Models reflecting the observations.** The top and the bottom drawings show two deformations of the fibril after drying without applied stress, both compatible with our results. The molecular arrangement in the hydrated fibril is shown in the center. Molecular segments in the overlap region of the fibril are depicted in dark. The length of the triple-helix is  $L$  and the axial staggering period (including gap and overlap) is  $D$ . In both drying models,  $L$  decreases by 1.3%,  $D$  decreases by 2.5% and the gap region decreases relative to the overlap (dashed lines). In the first model (DRY A), we assume that the triple-helix shrinks homogeneously ( $\epsilon_g^m = \epsilon_o^m = -1.3\%$ ) with a side-by-side gliding of neighboring molecules, resulting in a relative shift of the dark segments. In the second model (DRY B), there is no side-by-side gliding but the molecule changes length inhomogeneously with an increase in the overlap ( $\epsilon_o^m = +10\%$ ) and a shortening in the gap ( $\epsilon_g^m = -15\%$ ).

Indeed, a homogeneous shrinkage of the triple helix accompanied by a side-by-side gliding can reproduce all measured length changes, as well as the change in gap/overlap ratio (DRY A, Figure 21). This type of structural change would just be the inverse of the deformation found by uniaxial stretching of fully hydrated collagen fibrils [47, 126, 148, 149]. During passive stretching experiments, side-by-side gliding of neighboring molecules was identified at higher loads after the removal of an initial kinking of the molecules [126]. The analysis of MD modeling results on drying collagen [138] provides the insight that the triple-helix

shrinks substantially in the gap region while it even extends in the overlap region (observation (3)). These results led us to propose a different model (DRY B, Figure 21) for contraction induced by dehydration than the model for extension under an applied force. Instead of a side-by-side gliding of the molecules, the change in gap/overlap ratio is achieved by shrinkage of the triple-helical molecules in the gap region, partially compensated by an expansion in the overlap region. This removes the need for the molecules to glide alongside each other to achieve the observed changes in gap/overlap ratio. In the case of dry tendons, water that may serve as “lubricant” for a side-by-side gliding is removed, so is comforting that a model that does not involve molecular gliding to describe the gap/overlap ratio change has another explanation. Some of the results of MD modeling [150] hint that reality could be a compromise between the two models with (a very small) residual side-by-side gliding accompanying the inhomogeneous shrinkage and a slightly molecular reorientation as it was indicated by PRS, possibly in the gap region as it was suggested in literature [7].

### **Water as an integral part of the collagen molecule**

A better understanding of the changes the collagen molecule undergoes when water is removed from the surrounding can be obtained by redrawing the x-ray scattering patterns to extract the helix parameters at different hydration conditions. In Figure 14 b-c, the distribution of helix pitches and helix radii for the collagen fiber together with the marginal distributions obtained by projecting the 2D distributions on the marginal variable axes are reported. Rigorously, these projections are the convolution of the actual helix parameter distributions with the broadening due to the coherent scattering domain finite size and crystalline imperfection (in the case of the helix pitch) or with the second order Bessel function (for the radius). Since the data do not allow us to deconvolute these effects, we can only give a qualitative interpretation of some of the observations.

The variations of the raise per residue within the collagen molecule was very nicely modeled by Cameron et al. [151], and their results are consistent with our findings, given the limitations of our measurements: the Cameron model predicts a 25% variation in the raise per residue, while the width of the peak corresponds to 40%. The fact that the measured value is larger reflects the additional finite-size broadening. Moreover, water molecules are bound to the triple-helical collagen molecules in the hydrated state and “decorate” it in such a way that water contributes to the helix diffraction spot. Hence the radius of the helix may appear wider, in other words, with a larger radius (blue arrow in Figure 14b).

Furthermore, the distribution of the pitches within the helix widens with dehydration, suggesting that the structure of the collagen triple helix is affected by the presence of water. In particular, water molecules seem to stabilize the collagen triple helix, as the pitch distribution is more homogeneous in the wet state. Although these structural changes are substantial, the average pitch of the helix decreases only by 1.3% from the wet to the dry state, as shown in Figure 15a. When the tendon was not allowed to strain in the axial direction, the average helix pitch remained constant, and the pitch distribution was broadened almost symmetrically.

### Dehydration induces local conformational changes of the collagen backbone

The effects of water on the collagen molecular structure can also be observed with *in-situ* Raman spectroscopy. Significant changes in the shape of the amide and other bands were detected while the sample was dehydrated (Figure 17). These effects, as expected, are very pronounced for the amide bands, as these are very sensitive to the electron density of the collagen backbone induced by the formation/ disruption of H-bonds with water molecules. Spectral shifts were observed for many bonds, such as the stretching  $\nu(\text{CCO}^-)$  of the backbone, the bending deformation  $\delta(\text{CH}_2)$ ,  $\delta(\text{CH}_3)$  (Figure 18) but also the C-H at high wavenumbers ( $2950\text{ cm}^{-1}$ ). Especially the bending of  $\text{CH}_2$  and  $\text{CH}_3$  and the C-H vibrations are almost unaffected by electronic effects, therefore the shifts in the band positions confirm that the drying triple helix backbone underwent extensive local conformational changes. Furthermore, comparison of polarization Raman data in Figure 18 shows a reorientation of some bonds that are accompanied with a peak shift, but also others such as the stretching  $\nu(\text{C}-\text{C})$  of the backbone which spectral position did not change while the orientation was changed.

The distribution analysis of the amide I orientation by means of PRS (Chapter 1.4) generated interesting results. It showed a higher disorder of the bond orientation after drying if the fascicle was allowed to shrink, but no significant changes were observed if the drying fiber was constrained to its initial length (Figure 19, Figure 20). This does not necessarily mean a difference of the conformational change of vibrational bonds on the backbone level of the helix, these observations could also be caused by an alignment of the whole molecules after drying under load. Indeed, the concordance of the isotropic Raman spectra of iso-stress and zero-strain experiments (Figure 17) suggests the latter interpretation to be more plausible.

Even though our PRS results are not sensitive enough to distinguish between the drying procedures on the molecular level of the backbone, they definitely showed a conformational change between wet and dry collagen on that level (Figure 17, Figure 18). Furthermore, Ra-

man analysis suggests that there was an increased disorder of the molecular segments on the higher hierarchical level of molecular packing if the fascicle was allowed to shrink while drying.

The conformational changes of the molecular backbone detected with Raman were also observed by X-Ray scattering measurements. The scattering helical peak related to the collagen helix pitch broadened in the dry state (Figure 14b,c), which indicates more heterogeneity when water was removed from the surrounding of the triple helix, confirming local conformational changes. Furthermore, a shortening of the pitch was also observed in the zero-stress experiment.

### 3 Deterioration Analysis of Collagen Studied by Far In-fra-Red Spectroscopy

In this chapter we explore the use of the Far-IR absorption spectroscopy in the  $500\text{--}50\text{ cm}^{-1}$  ( $\lambda=20\text{--}200\mu\text{m}$ ) spectral region for the deterioration analysis of collagen in parchment. The idea is to provide additional information from the low energy region associated with intermolecular collective vibrations on the triple helical level of the peptide chains, rather than from the separated bonds in the higher energetic spectral region.

In 1974, Gordon et.al [152] measured collagen and gelatin absorbance in the Far-IR region, which is relevant for our study. They showed the temperature dependence of the common peak of collagen and gelatin, which, therefore, can be related to the higher level of the intermolecular assembling of the peptide sequences. Far-IR spectroscopy has been applied in several fields for material characterization; astronomy, medical applications or crystal characterization. In the late 80<sup>th</sup> – beginning of the 90<sup>th</sup> C. Thomsen et al.[153, 154] characterized high temperature superconductors using Far-IR reflectivity. However, only little can be found in the literature about Far-IR application in the biological field, such as collagen or other proteins, mineralized proteins or gelatin.

Recently, the technical developments of both the source and the detection side, revived the investigations in that spectral region, allowing its application in the field of biomolecular systems, analysis of water binding and its dynamics, pharmaceutical applications, trace gases, security monitoring applications etc. However, it is rarely called the Far-IR spectroscopy anymore. The new name, that sounds innovative and more advanced and that almost everybody tries to use for that very same spectral region is the Terahertz (THz) or the Terahertz Time Domain (THz-TD) spectroscopy. Although most of the people restrict the THz-TD to 0.3–3 THz (that corresponds to  $10\text{--}100\text{cm}^{-1}$  and requires a different technology) others prefer to assign it to a wider range between 0.1 and 15THz, which covers also the region of our investigation. Mantsch H. and Naumann D describe this development nicely in their short article “*Terahertz spectroscopy: The renaissance of far infrared spectroscopy*” [155] with the felicitous words: Today, however, the majority of spectroscopists have adopted the increasingly fashionable term of “terahertz spectroscopy”.

THz spectroscopy can widely be found in application of biosystems [156]. Among them it has been applied to study bone in various spectral ranges. Also, the range of  $600\text{--}70\text{cm}^{-1}$  was explored for monitoring of senile osteoporosis development [157]. However, this study does not show a distinct absorption peak of bone in that spectral range. Most of the other THz studies on bone have been done within the spectral window below  $100\text{cm}^{-1}$ .

Wide range of carbonate minerals have been characterized by means of Far-IR studies [158, 159], which showed that remarkable spectral differences occur for different carbonates in the  $650\text{--}70\text{cm}^{-1}$  range. The authors concluded that this Far-IR range may serve as fingerprints for mineral identification and are more useful identifiers of carbonate species than those in any other IR range. Sulfates have been analyzed with this technique as well [160]. These studies showed the identification of cinnabar in a high-quartz ore, cuprite and tenorite in a mixture, calcite and dolomite in a coal refuse sample, dawsonite and dolomite in an oil shale, thenardite in a boiler deposit, and ferrous sulfate in the surface film on pyrite.

Far-IR analysis of inorganic pigments showed the potential of this technique also for the cultural heritage domain [161, 162]. Fukunaga et.al. showed its application as a non-invasive analysis technique [163]. In this context the technique has been explored for art conservation to reveal the history of the work to determine the proper materials for its restoration [164], it has been used for character recognition in medieval manuscripts [165] and for imaging analysis of historic paintings and manuscripts [166].

Oriented films of dry and hydrated DNA have been measured in the range between  $450\text{--}3\text{cm}^{-1}$  in 1986. Recent studies showed the capability of Far-IR ( $600\text{--}70\text{cm}^{-1}$ ) technique to detect lattice vibrations in the field of polymer crystallisation [167] as well. They used the absorptions in the Far-IR region, which is supposed to be more informative than those in the MIR region, because the bands associated with bending and torsion modes appear in the Far-IR region [168–170]. Marker bands as specific spectral signature of different phospholipids and sphingolipids in the Far-IR ( $600\text{--}50\text{cm}^{-1}$ ) could be distinguished [171].

The influence of the state of degradation, the three-dimensional fibrous structure and the presence of calcium compounds on terahertz absorption properties of historic parchment have been studied with terahertz time-domain spectroscopy in transmission mode in the interval  $45\text{--}85\text{cm}^{-1}$ . The state of degradation, i.e. the shrinkage temperature, does not seem to contribute to the absorption properties of parchment in this spectral window. However, this spectral window does not show an outstanding absorption peak of collagen [172]. Nevertheless, also other studies explored the window below 3THz ( $100\text{cm}^{-1}$ ) for skin decease analysis [173–



175]. In this studies water has been identified qualitatively as a major absorber of THz-radiation in skin.

Therefore dehydration of collagen has been monitored explicitly in this spectral range below  $100\text{cm}^{-1}$  [175]. Recent THz studies of collagen have confirmed the earlier identification [152] of an outstanding absorption peak in the Far-IR spectral range of  $600\text{-}100\text{cm}^{-1}$  [176], where they aimed to observe whether change in absorbance spectra of the collagen depends on the collagen morphology comparing Tilapia skin, bovine skin and rat tail by adding NaCl. The conclusion of the authors were restricted to the assumption that spectra change caused by interaction between NaCl and collagen can be observed, which later has been verified by the same authors [177]. We, however, are very much interested in the effect of moisture and degradation on collagen in this particular spectral range between  $500$  and  $100\text{cm}^{-1}$ .

Although the strong synchrotron source was used, the Far-IR experiments need to be conducted in vacuum, which is not the most appropriate condition for biological material, especially when it comes to the influence of humidity. We, therefore, designed and built a sample chamber to keep the sample in a controlled environment. The chamber encases the analyzed sample between two narrow standing windows with transparent features for the Far-IR region to keep the path of the light through the atmosphere as short as possible. The atmosphere parameters such as humidity inside the chamber were monitored and controlled interactively from outside the experimental chamber.

In the PRS approach as presented in the previous chapter 1.1.1 we used fresh RTT as reference material for intact collagen, which unfortunately could not be also used for the Far-IR approach because of its improper thickness ( $150\text{-}300\mu\text{m}$  in diameter). Due to the strong absorption in collagen and the relatively big spot size of the beam, the collagen based reference sample on one hand needs to be very thin (around  $40\mu\text{m}$  in thickness), but on the other hand has to have an area of not less than  $4\text{x}4\text{mm}^2$ . Bone is a nano-composite material consisting of an organic collagen matrix and inorganic mineral particles of carbonated hydroxyapatite [93, 178]. *In vitro* demineralization experiments of bone typically employ Ethylenediaminetetraacetic acid (EDTA) to dissolve the mineral phase, while leaving the structure of the organic phase relatively unaltered [179, 180]. Therefore, collagen obtained from thin demineralized fibrolamellar bone samples fulfils the requirements of our experimental approach, because, before demineralization, stiff bone slides can be polished to the desired thickness.

In our Far-IR studies, we used bovine fibrolamellar bone as model system, since this bone has a well known structure with a preferred orientation of both the collagen matrix and the mineral particles along the axis of the bone [181]. In order to characterize the influence of the structural anisotropy on to the spectral features, we performed linear dichroism experiments with a polarized incident beam. It turned out, that mineral is a strong absorber of Far-IR light and requires very thin sample compared to the pure collagen. We, therefore, performed a stepwise demineralization process exposing the bone sample to the EDTA solution for a short time period and studied the mineral intensity profiles after each demineralization step.

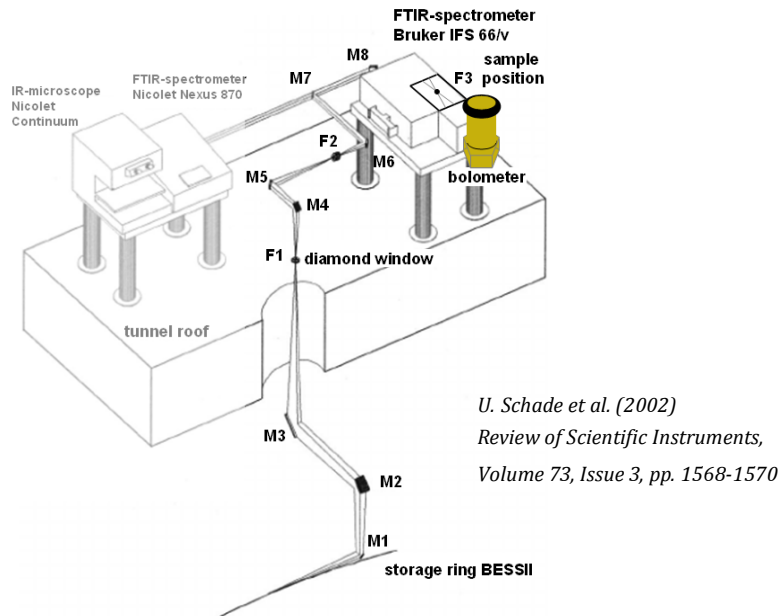
After we have characterized the spectral intensity and orientation-dependent features of the mineral and collagen, we studied the influence of external stress and humidity on the remaining collagen matrix. The latter characterization is of particular importance for the parchment deterioration analysis, since the parchment production process involves intensive water treatment and drying under tension. In the previous chapter we already learned that stress aligns the molecules inside the collagen fiber, however it does not cause any spectral shift in the fingerprint region of PRS, whereas moisture content changes significantly the spectral peak positions. This raises the question of whether this finding is also true for the collective vibrations in the Far-IR region.

After we characterized demineralized bone collagen (intact reference) and the fully gelatinized material (deteriorated reference), we compared these results with various parchment specimens that were cut in thin sections to fit the experimental requirements in transmission approach. Using specific spectral features, we developed a methodology that can be used for parchment deterioration evaluation. However, the technique has limits and drawbacks, which require further development, in particular to enable the backscattered approach for nondestructive analysis of precious ancient specimens.

In this work multi composite materials like fully mineralized or partly demineralized bone or parchment were measured. In our bone samples collagen type I, hydroxyapatite plates and water are the main composites, whose variety in density, distribution and proportion can influence the properties of reflectivity and absorption. In principal, these effects can be addressed by means of “Effective medium approximations” [182, 183], but this would go beyond the scope of this work. Therefore, for this investigation a simplified linear compound model for spectral absorption analysis was used.

### 3.1 Experimental set up and materials measured

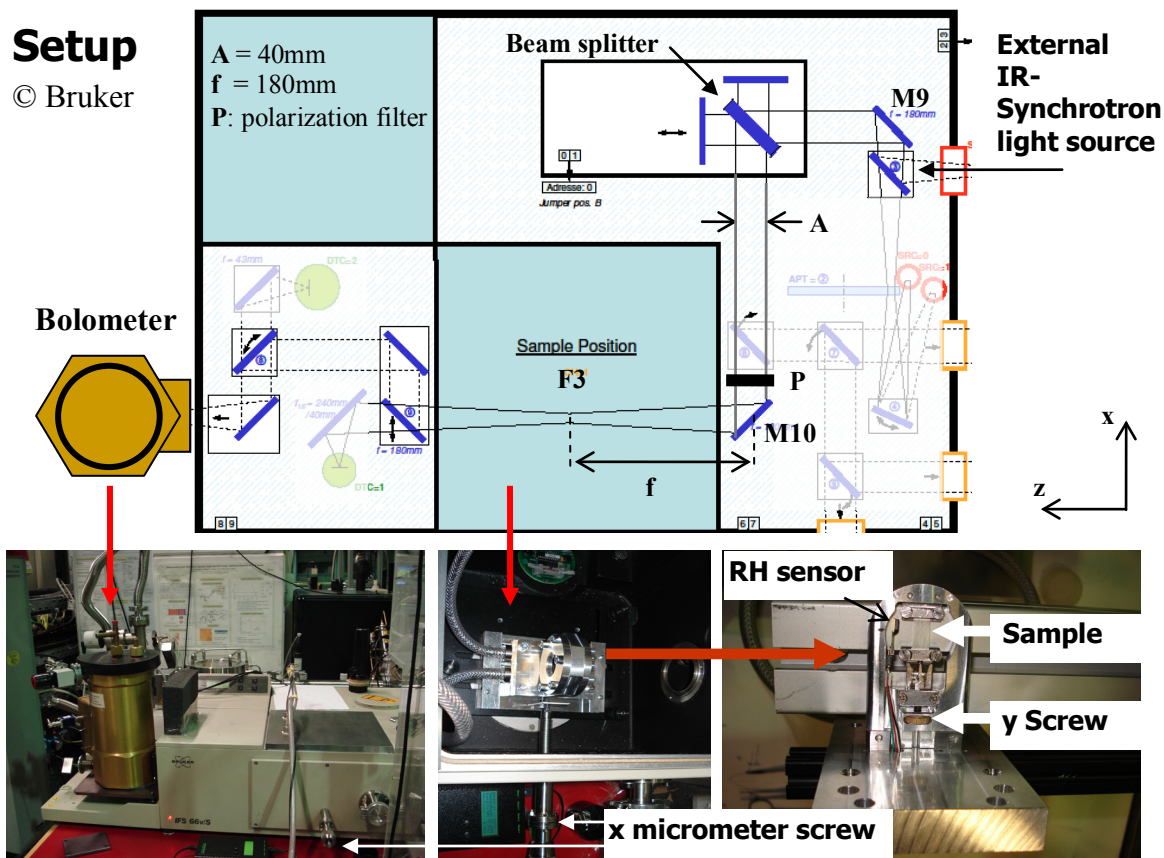
The experiments were conducted at the IRIS beamline of Berlins Synchrotron Radiation Facility (BESSYII) at Helmholtz-Zentrum Berlin (HZB) [8]. Strong and brilliant IR-Synchrotron Edge Radiation (ED) was used as a source for the measurements [184]. Edge radiation appears when a charged relativistic particle passes through the entrance and exit of a bending magnet. The radiation is generated from both edges of the dipole magnet and is emitted interfering to a narrow cone along the straight path through the magnets with an asymmetric extension in the plane direction of the horizontal particle trajectory. The flux distribution inside the emitted cone is very much wavelength dependent. Moreover, the total opening angle of the emitted cone is narrower for higher energies [184-186].



**Figure 22: Drawing of the beam path to the FTIR spectrometer (Bruker IFS 66/v) at the IRIS beamline at BESSYII – HZB. Adopted from [4].**

In Figure 22, the pathway of the beam at the IRIS beam line is presented schematically. The first planer mirror M1, which deflects the light from the edge radiation beam, is placed in a distance of nine meter from the generating dipole magnet [4]. This mirror is split into two halves with a 6mm gap. The high energy portion of the beam is passing this gap and hits a water-cooled absorber. In order to bring the beam out of the storage ring the following two cylindrical mirrors M2 and M3 focus the beam on the focal plane F1 in vertical and horizontal direction, respectively. In the F1 plane a narrow wedge PCV diamond window is placed sepa-

rating the ultra-high vacuum space of the storage ring. However, at the focal point F1 the beam has an asymmetrically elongated spot shape. In the next sealed section of a pre-vacuum it passes through further cylindrical mirrors M4 and M5, which arrangement allow correction of the focus at F2 for more symmetrical shape before the beam is collimated by a toroidal mirror M6. On its path to the spectrometer and the experimental chamber the beam passes further mirrors and a KBr window.



**Figure 23:** Schematic arrangement and pictures of the FT-IR IFS 66v Bruker Spectrometer equipped with bolometer and an atmospheric sample chamber moveable in the x-direction by a micrometer screw from outside the evacuated experimental space. Before the evacuation the sample fixed inside the environmental chamber is adjusted at the write high in the F3 plane. The beam is focused by M10 mirror from a 40mm diameter over 180mm focal distance on to the sample. The polarization filter was placer right before the M10 mirror for the linear dichroizm experiments.

For the experiments in the Far-IR range of ( $30 - 600 \text{ cm}^{-1}$ ) FT-IR IFS 66v Bruker Spectrometer was used with 50 and 125  $\mu\text{m}$  Mylar beam splitter. On the detection side the spectrometer was equipped with liquid He cooled Si-Bolometer 4.2K (spectral range ( $\text{cm}^{-1}$ ) 10-600, max. BW 1kHz, NEP (w/ Hz)  $1\text{e-13}$ ) (Figure 23). The sample chamber with controlled environment contains the sample in the F3 plane facing the incident beam in the Z-direction.

During the experiment the chamber is enclosed in the evacuated experimental space, but it can be moved along the x-axis (horizontal) manually via a micrometer screw that is placed outside the spectrometer.

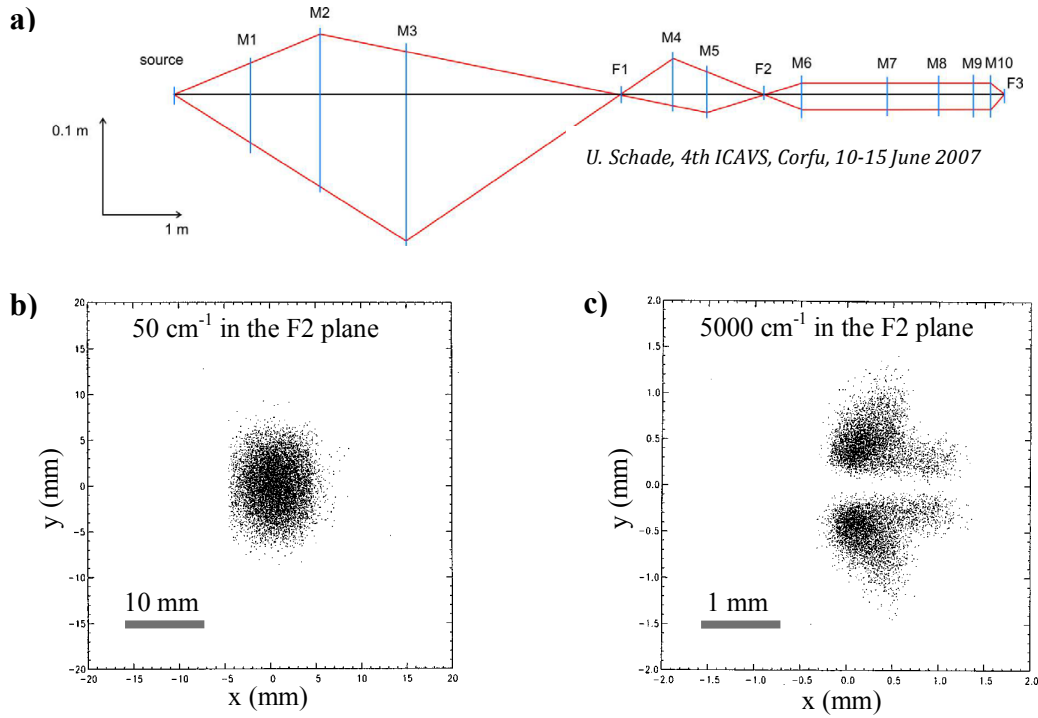
#### 3.1.1 Focal spot

The focal distance  $f$  and the focal spot shape in the F3 plane differ slightly for different wavelengths. Since the ED source has an asymmetric distribution, the focal spot is supposed to have a slightly different shape in horizontal and vertical directions, though it has been corrected via the arrangement of cylindrical mirrors M4 and M5. Moreover, as it was already mentioned, the total opening angle of the emitted edge radiation cone is narrower for higher energies [184-186]. The different opening angles for different wavelengths play a significant role for the shifts of the focal point because the beam is very much divergent, when it passes the high reflective index PCV diamond wedge window in the F1 plane ( $n = 2.38$ : reflective index of a diamond for 30 to 100  $\mu\text{m}$  wavelength [187]), hence different wavelengths are bent differently. The following cylindrical mirrors M4 and M5 are used to compensate the shift and to shape the beam to a single narrow spot in the F2 plane, which subsequently is further optimized and projected to the F3 plane (sample position) by the mirror system of M6-10. However, the position and the focal point remain wavelength dependent as it has been characterized for the F2 plane by Schade et.al. [8] and shown in Figure 24.

In its focal plane F2 the shape for 50  $\text{cm}^{-1}$  depicts the source of the edge radiation, whereas the shape for 5000  $\text{cm}^{-1}$  clearly shows the image of the beam on the first plane mirror M1 with the split between the two halves. The latter is not in its perfect focal plane; however, the total spot size is still much less than for 50  $\text{cm}^{-1}$ . Consequently the beam has similar focal characteristics in F3 plane, where we put the sample for the measurements. For our measurements we adjusted the instrument for the Far-IR region of 500 – 80  $\text{cm}^{-1}$ , the region where bone shows several absorption bands.

In order to characterize the beam profile in the focal area F3 and subsequently to place the sample in the optimal  $z$  position we performed a series of knife edge scans [188, 189] along the optical axis  $z$ . For each knife edge scan a 50  $\mu\text{m}$  thin aluminum foil edge was moved along the  $x$  direction, while the reduction of the transmitted beam was monitored. The optimum was defined at the narrowest beam position (10-90% of the full transmitted intensity), where the width was comparable for all wavelengths at about 1-1,5 mm. Although, for higher wave-

numbers of the spectral region the beam size was not in its narrowest position and it showed similar profile of two separated maxima as presented in Figure 24c for the F2 plane, it was in any case, important to place the sample in the defined optimum because then we made sure that the information we measure originates approximately from the same material area.



**Figure 24: a) Schematic of the optical beam path for horizontal and vertical directions at IRIS Beamline. b) and c) show the intensity profile in the F2 plane for 50 cm<sup>-1</sup>, which is in its optimal focal point, and for 5000 cm<sup>-1</sup> in the same plane, respectively. b) & c) adopted from [8]**

Nonetheless, this approach made the measurements of small specimens challenging, because whenever the coherent synchrotron beam came close to an edge or a crack it has caused interference scattering, where some light gets lost from the detection area. Since the flux profile of the beam is wavelength specific, the presence of an edge or a crack in the beam path causes a spectral modulation making the measurements inaccurate. In case of wide samples of a double the size of the focal spot the measurement could be performed successfully. However, we solved the problem also for smaller specimens by positioning a pinhole behind the sample. The pinhole on one hand narrows and sharpens the beam profile significantly, but on the other hand it causes additional spectral modulation. In any case, this additional modulation could be subtracted from the final spectra after the absorption of pinholes have been characterized without the sample (eq. (30)).

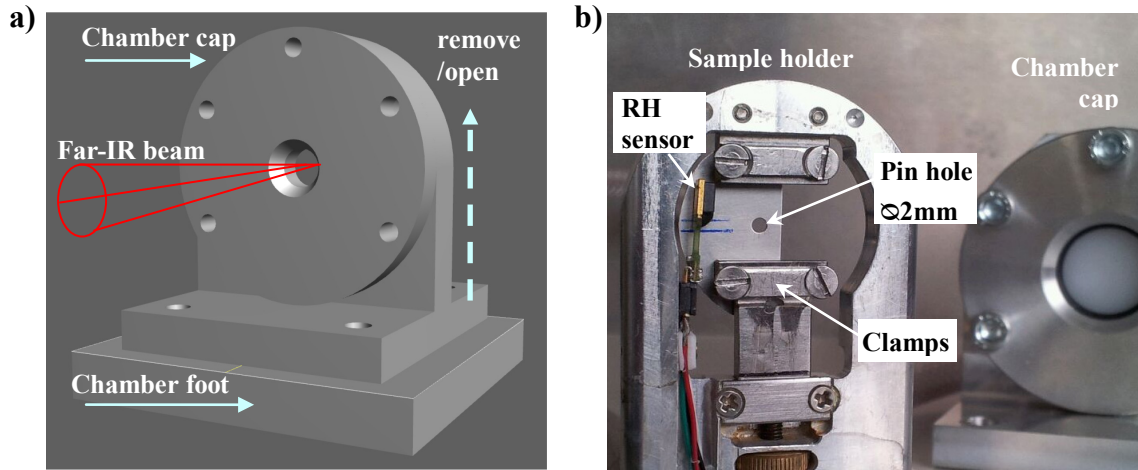
$$I_{\text{measurement}} = I_{\text{background}} \cdot \exp(-\text{Absorbance}_{\text{sample}}) \cdot \exp(-\text{Absorbance}_{\text{pinhole}})$$

$$\Rightarrow \text{Absorbance}_{\text{sample}} = \ln\left(\frac{I_{\text{background}}}{I_{\text{measurement}}}\right) - \text{Absorbance}_{\text{pinhole}} \quad (30)$$

The samples were measured in a controlled environment chamber. Therefore, the background absorbance was determined in a common way next to the sample at the empty side of the pinhole plate, when the beam is passing through both windows and the atmosphere of the sample chamber.

### 3.1.2 Controlled environment sample chamber

A sample chamber (Figure 25) was built with the features to keep the biological sample in a humidity controlled environment, while the measurement takes place in vacuum. The principle idea was to suit the sample between two windows having very small distance between them in order to minimize the absorbance of the Far-IR beam through the atmosphere.



**Figure 25:** a) Schematic drawing of the controlled environment sample chamber. The chamber cap pulled over the sample holder is fixed on the chamber foot. The air from the narrow interior space can be floated from outside through drilled pipes in the chamber foot. The Far-IR beam passes through the window flanges on both sides and hits the sample in between. Two different windows were produced; one with diamond windows and the other with bigger hard polyethylene windows, both materials are transparent for the Far-IR region. b) The sample holder on the left and the removed chamber cap in the back right side. The sample can be fixed with the clamps, which can stretch the sample by the screw weal on the bottom. In the back of the sample position a pin hole is adjusted, which narrows the beam spot and allows improvement of the spectral quality significantly. Digital SENSiRION SHT75 digital humidity and temperature sensor is suited close to the sample.

The main requirements for the windows were: (1) to be transparent to a large spectral range and, in particular, as much as possible to Far-IR range of 50-500  $\text{cm}^{-1}$ . (2) to be big enough so that there would be enough space for the beam to hit the sample and to measure the empty beam near the sample. The light cone of the beam should be able to pass the windows and the sample in a distance of 2 mm from the edges (sample or window edge).

The sample chamber has been built in a way that the narrow 6 mm thick sample holder frame was fixed on the chamber-foot. The chamber-cap, which contains the windows on both sides at a distance of 8 mm, could be pulled over the holder frame and screwed on the chamber-foot, so that the space in the cup slot is sealed from the environment. In this way, the chamber-cup covers the sample holder so that the sample is suited exactly between the two windows. The atmosphere inside the chamber can be controlled from outside by conducting the gas medium via two tubes connected to the holes drilled in to the chamber-foot.

Two different chamber-caps have been built equipped with different materials used as windows:

(1) First chamber-cup windows: CVD Diamond with a good transparency of a wide spectral range of 25,000 – 33  $1/\text{cm}$ , but with a relatively small diameter. (CVD Diamond Window, Diafilm OP; Dimensions:  $\text{Ø}15.0 \pm 0.1\text{mm}$ ; Thickness: 0.5 to mm  $\pm 0.05\text{mm}$ ; Flatness:  $< 5$  fringes @ 632.8nm in reflection; Roughness:  $< 15$  nm Ra Measured on 1mm<sup>2</sup>; wedge:  $1^\circ$ ).

(2) The second cup was equipped with big windows of 24mm in diameter made out of high density Polyethylene, which has a good transparency in the Far-IR region of 600-30  $1/\text{cm}$ .

In this work we present only the measurements that were conducted with the big high density Polyethylene windows. The big windows make the experimental handling easier; the beam could pass through the sample and the empty space on its side without touching any edges. Furthermore, the humidity controlled chamber was equipped with a small SENSORION SHT75 digital humidity and temperature sensor fixed on the inner frame edge of the sample holder only a few mm away from the sample, Figure 25b. The sensor values were readout by evaluation kit EK-H4 (fa. Sensorion).

First measurements often showed a strong spectral modulation pattern (as discussed in the previous chapter section) disrupting the measured spectrum. It was caused when thin samples had small holes or the sample size was so small that it caused the beam to hit a crack or an edge of the sample. To avoid this it was necessary to cut down the spot size of the beam.

Therefore, measurements were conducted with an additional pinhole of 2mm in diameter on a



metal plate which was fixed behind the sample on the upper clamp. The lower clamp was still moveable by the screw weal at the bottom of the sample holder (Figure 23, Figure 25). Eq. (30) describes the correction of the measurements from the pinhole induces additional modulated absorbance spectrum.

#### 3.1.1 Materials

**Bone collagen:** Thin (20 to 100 $\mu$ m) fibrolamellar bone samples were extracted from the mid-diaphysis of a 12 month old calf, which was provided by a local butcher. The bone was cut in the radially longitudinal sections perpendicular to the long axis with an inner-hole saw (Leica SP1600, Leica Mikrosystem Vertrieb GmbH, Bensheim, Germany). The slides were then polished by means of an automatic polisher (Logitech PM5, Logitech Ltd., Glasglow, UK) with 3 $\mu$ m and 1 $\mu$ m grit-sized diamond particles (DP-Spray P, Struers A/S, Ballerup, Denmark) until the sheets achieved the right thickness. Before the measurements the sheets were cut in 6mm wide and 5-10mm long stripes along the fibrolamellar orientation. For storage the samples were kept at -20°C wrapped by 1% sodium azide in phosphate buffered saline (PBS) solution soaked gauze.

Bone samples, thicker than 20 $\mu$ m, required demineralization in order to give an unsaturated Far-IR spectrum because of the strong absorption by mineral particles. The demineralization was done by means of Ethylenediaminetetraacetic acid – EDTA (0.5M and 8Ph) solution. Two edges of the thin slides were first glued on a plastic frame before immersing them into the EDTA solution. The subsequent fixing in the environmental chamber or optionally further demineralization was done with the plastic frame as well in order not to harm the thin and weak demineralized samples.

**Gelatine:** For the fully gelatinized reference commercial gelatin Type A (fa. ROTH; acidic treatment/ Hydrochloric acid HCl, Sulfuric acid H<sub>2</sub>SO<sub>4</sub> (<48h)) was used. The measurements were conducted on the clamped and stretched to 20-70 $\mu$ m thin gel films.

**Parchment:** Specimens that were analyzed in this study origin from a modern limed parchment that was dried under tension. 40-50 $\mu$ m thin sections were cut in wet and frozen state by means of a Cryo-Microtom.

## **3.2 Results**

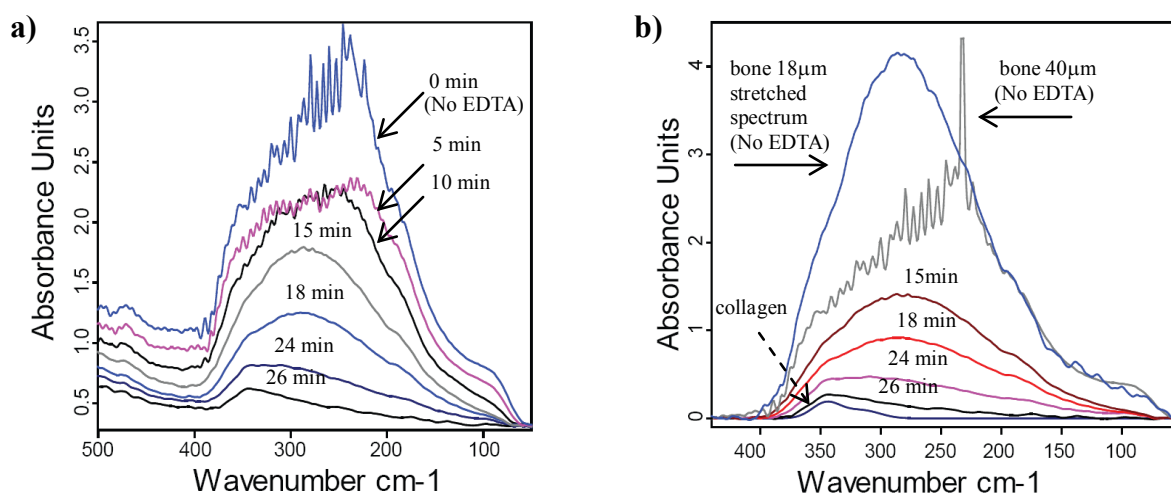
The results section is sub-structured in paragraphs that first characterize spectral properties of bone collagen and gelatin comparing them with the modern parchment spectra in order to characterize the degree of gelatinization of parchment. Parchment is a collagen based product made of skin. Depending on the place on the skin the collagen fiber network can be isotropic, but in some regions also shows a predominant orientation. Furthermore, during the production parchment undergoes several steps of drying and immersion in water until it is finally dried under tension. These effects in the Far-IR region need to be understood. The important spectral properties in this context are influences of the molecular orientation, external stresses and moisture.

Since bone collagen was used as a reference material, we also characterized the spectral contribution of the mineral related to its magnitude and orientation. The orientation analysis has been done by means of linear dichroism.

### **3.2.1 Mineral and collagen contribution in the bone spectrum**

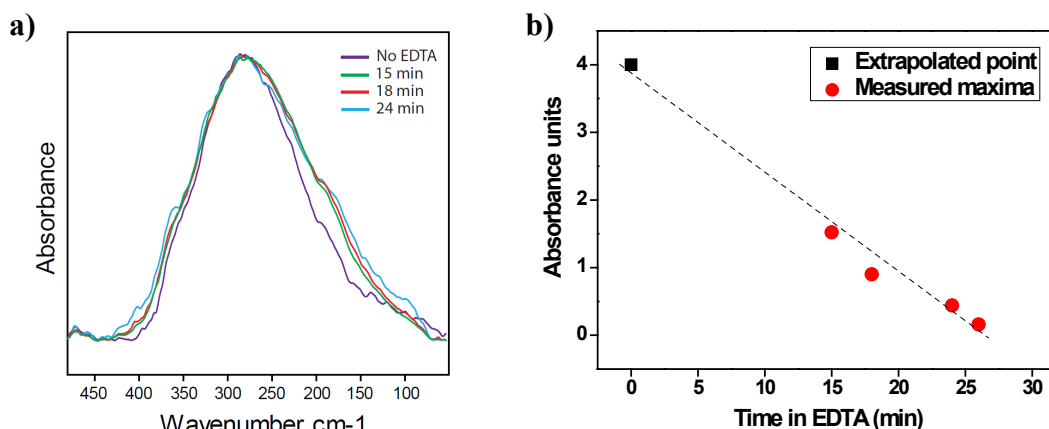
Bone shows a strong absorption band in the  $200 - 400 \text{ cm}^{-1}$  region. For sample thicknesses of more than  $20\mu\text{m}$ , the absorbance spectra go into saturation. As it will be shown in this section, the bone absorbance band contains collagen and mineral components whereas the contribution of the mineral peak area exceeds that of the collagen by an approximate factor of up to 70. In order to get a pure collagen spectrum, the bone slides were demineralized. Due to the fragility of a  $20\mu\text{m}$  demineralized collagen matrix we could not succeed in obtaining spectra from the same fully mineralized and fully demineralized bone sample. Exposed to the air such a thin demineralized bone slide gets very easily cracks, which affect the measurement with spectral modulation as it has been described above (paragraph 3.1.0).

In order to approximate the magnitude mineral contribution versus collagen in the bone absorbance spectrum we compared the intact mineral peak of the thin ( $18\mu\text{m}$ ) sample with the stepwise demineralization series of a thicker ( $40\mu\text{m}$ ) sample, where we could obtain also a good collagen spectrum after full demineralization (Figure 26).



**Figure 26: Far-IR spectroscopy on bone collagen.** a) Demineralization series of bone section (40µm thick, measurement performed at 20%RH). The time (min) stand for the total time the sample spent being immersed into the EDTA solution. The sample was removed from EDTA and washed in distilled water before each of the measurement. b) Same spectral series as in (a) are shown together with thin bone (18(  $\pm$ 3)µm at 20%RH) spectrum, which could be obtained without the demineralization. In the graph the 18µm-bone spectrum is stretched (scaled up) so the peak profile in the 50-200cm<sup>-1</sup> region overlaps with the not treated (No ADTA) thick sample at the undemineralized step. All spectra are baseline corrected by a straight line. The graph shows the proportion of the spectral contribution of mineral and collagen in the bone absorbance.

Figure 26a shows a stepwise demineralization series of a 40µm thick sample. The sample was immersed into EDTA solution for 3-5 minutes before measurement. After the measurement, the sample was immersed again and subsequently washed in distilled water before further measurements. The first not saturated spectrum appears after the 3<sup>rd</sup> demineralization step, which is 15 minutes of total demineralization time in EDTA solution. After 30 minutes the sample was completely demineralized, where only collagen remained. The flanks in the 50-200cm<sup>-1</sup> region of the mineralized spectra before the demineralization are not saturated and can be used for the approximation of the peak size (Figure 26b). The intact mineral peak of the unsaturated spectra of 18µm thin sample was stretched to overlap the flanks of the 40µm sample. Doing so, one has to be aware of possible differences between these two samples, which give different spectral response to the polarized BESSY light. Therefore, this approach is not precise, but gives a good estimation to the spectral magnitudes of mineral and collagen in the bone absorbance spectrum. Additionally, we compared the shape of the mineral peaks of different demineralization steps without the collagen contribution. For this purpose, the collagen contribution was subtracted from the measured spectra shown in Figure 26b. The calculated curves are presented in Figure 27a. When the intensity is maximized, the shape of the mineral peaks of all demineralization steps shows high congruence.



**Figure 27: a) Mineral spectra calculated from different steps of demineralization (after 0, 15, 18 and 24 minutes, Figure 26) reduced by collagen and normalized to its maximum. b) Maxima of the same mineral peaks and of the extrapolated 18 $\mu$ m sample.**

In Figure 27b the maxima of the mineral peaks are plotted. The extrapolated maximum of the intact bone spectrum in Figure 26b hits a linear fit of the other maxima from demineralized steps. This behavior and the conclusion from Figure 27a confirm the peak extrapolation done in Figure 26b and the approximation for the mineral contribution area to be some 60–70 times higher compared to the collagen.

### 3.2.2 Linear dichroism on mineral and collagen in bone

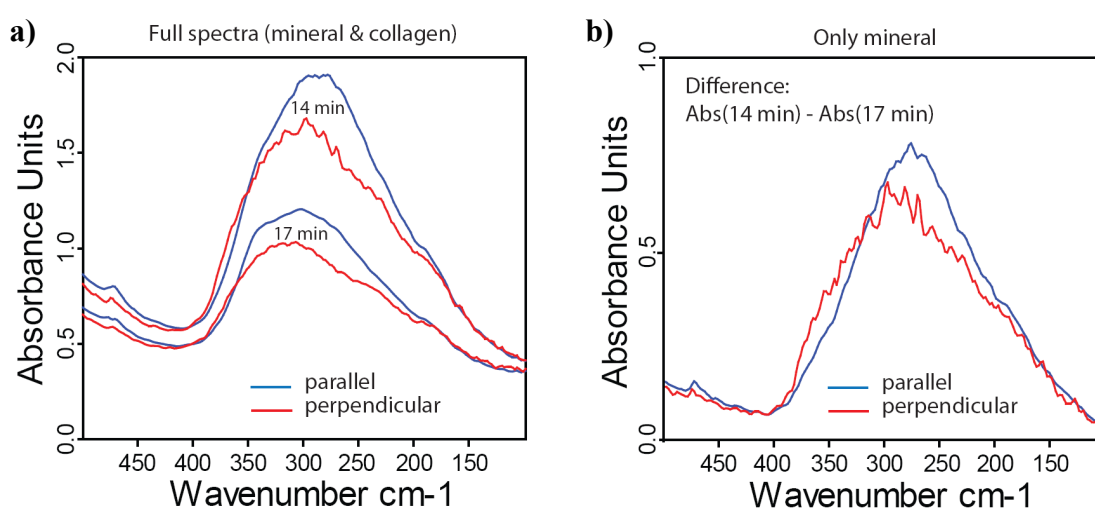
Bone spectrum is a superposition of mineral and collagen contribution, both of which are expected to show anisotropic behavior. Collagen can be analyzed separately from mineral after full demineralization. However, the orientation analysis of mineral component is not straight forward. Using the advantage of the stepwise demineralization we found a way to extract also the pure mineral spectrum without the collagen contribution.

Peak shape comparison discussed in Figure 27a have shown that the shape of the remaining mineral peaks is congruent between different demineralization steps, which means a homogeneous mineral loss for the thin bone samples. This shape congruency can be in particular expected for two successively following demineralization steps. Consequentially, the mineral that has been removed during a demineralization step, that we call “mineral loss”, has the same peak shape and also the same properties of anisotropy.

Therefore, the mineral loss can be obtained by subtracting the spectra of two successively following demineralization steps. The mineral loss represents the pure mineral spectrum

without the collagen because collagen's contribution is approximately the same in both measurements and thus eliminated by the subtraction. This approach was used for orientation analysis of the mineral in the bone spectrum (Figure 28).

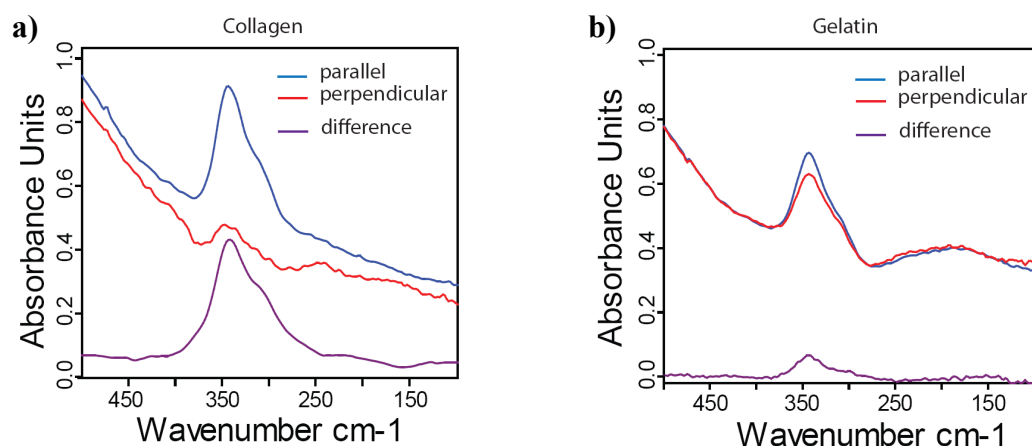
The sample was fixed in the chamber in vertical orientation with respect to the fibrolamellar axis. The synchrotron light is mostly polarized in the same vertical direction along the fibrolamellar axis, only a small portion of horizontal orientation is contained. For dichroism analysis a polarization filter was adjusted into the beam path before the M10 mirror (see Figure 23). We used two polarization directions: the vertical along the lamella and the horizontal perpendicular to the lamella orientation.



**Figure 28: Far-IR dichroism measurements on mineral from partly demineralized lamellar bone are presented after two steps of demineralization: a) after 14 and 17 minutes (total time in EDTA), in parallel (blue) and in perpendicular (red) orientation. b) The calculated spectra of the mineral loss (difference between Abs(14) and Abs(17)) are shown. The mineral loss spectra do not contain any contribution of collagen. The analysis shows the anisotropic features of the pure mineral peak.**

Figure 28a shows the parallel measurements of two successively following demineralization steps (after 14 and 17 minutes total time in EDTA) in blue color and the perpendicular in red. As expected, the spectral quality in perpendicular polarization is noisy due to low intensity of the beam polarization in this direction and the limit of the presaturation state after only 14 minutes of demineralization. In Figure 28b the collagen contribution is removed by subtraction and the pure mineral peak is presented by the calculated mineral loss. It shows the anisotropic behavior of the mineral in the Far-IR region.

In the next step the dichroism analysis were performed on collagen and gelatin. The results are presented in Figure 29.



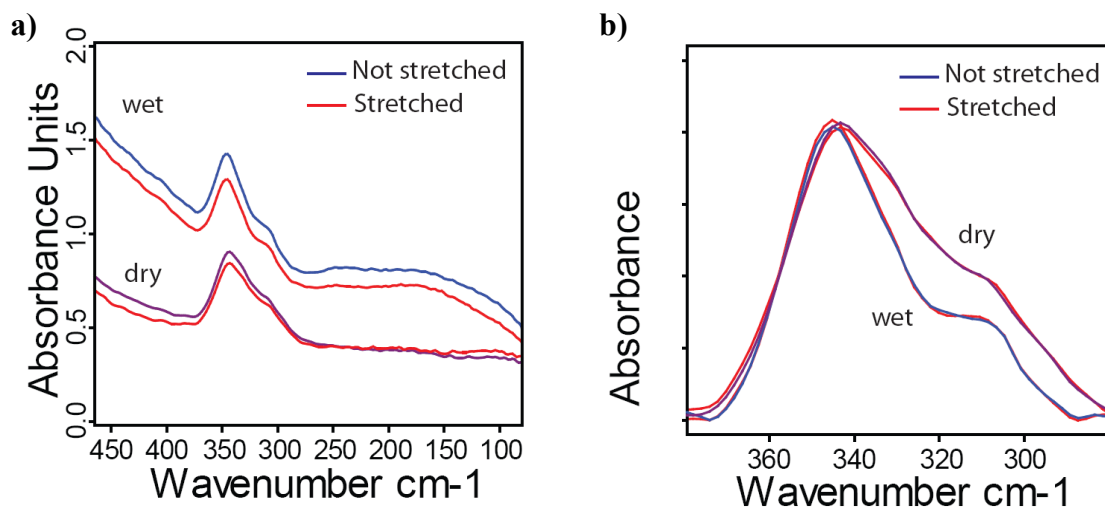
**Figure 29: Far-IR dichroism measurements; the violet spectrum represents the difference between the parallel - vertical (blue) and the perpendicular - horizontal (red) spectra. a) Collagen from demineralized lamellar bone is aligned in vertical orientation. b) The same on gelatin. The sample shows a little anisotropy; this is possibly due to the stretching of gelatin by clamps in vertical direction.**

Figure 29a shows for the complete collagen peak a high anisotropy along the lamellar orientation. For gelatin, a complete isotropy is expected, never the less the calculated difference between the vertical (called parallel) and the horizontal (called perpendicular) polarization measurements (Figure 29b) shows a little anisotropic behavior. The reason for the difference could be the way how the viscous gelatin film was fixed on the sample holder. It was clamped and flattened by stretching along the vertical direction until the sample got the right thickness. This approach could have caused a realignment of gelatin peptides or helical residues along the stretching axis. The spectral difference, however, is very small and the flanks at higher and lower wavenumbers (including the water peak) show the same absorbance and confirm the reliability of the technique is reliable, so that the conclusion about the highly anisotropy of both collagen peaks along the lamellar orientation can be confirmed.

### 3.2.3 Moisture and stress influence on spectral characteristics of collagen

The objective of this section is to understand whether stresses or presence of water would induce changes in the Far-IR spectrum of collagen. A fully demineralized fibrolamellar bone slide was fixed between clamps and put under tension using a micrometer screw on the sample holder (see description of the controlled environment chamber in Figure 23 and Figure 25). The lamellae were oriented along the stretching axis (vertical). The same sample was first

measured under wet and then in dry conditions. After humidifying the sample it was stretched for 8-10% of the initial length and measured again in wet and afterwards in dry condition. All four spectra are shown in Figure 30.

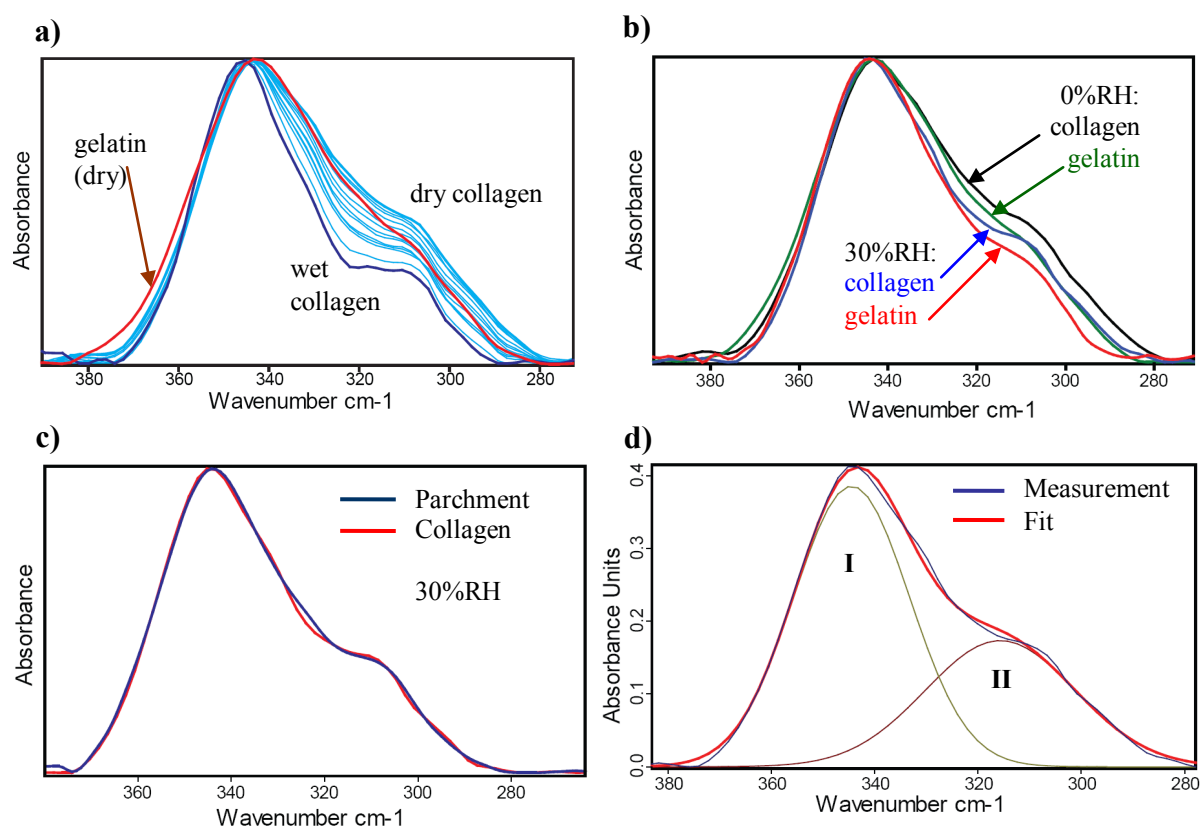


**Figure 30: Far-IR of collagen from fully demineralized bone. a) Comparison of 8-10% stretched to unstretched in wet and dry state. b) Same spectra but baseline corrected and zoomed in. Peaks are normalized to maximum. No difference can be observed related to the externally applied stresses. The dry state increases the intensity of the second/ the smaller peak.**

We do not observe a significant collagen peak shifts caused by the applied stresses. However the moisture content affects the intensity ratio of the two collagen peaks. The smaller peak increases with respect to the bigger peak. In the next paragraph (3.2.3) of the results section this issue will be discussed more in detail by fitting the peaks and comparing with those from gelatin and parchment.

### 3.2.4 Spectral comparison between demineralized bone collagen, gelatin and modern parchment

The results from previous paragraph have shown that moisture influences significantly the spectral features of the collagen double-peak. Therefore, we extensively analyzed collagen in the full range of RH from very dry (<5%RH) to very wet (>90%RH) state. Due to the limited beam time at BESSY and the challenges in handling very thin and fragile samples we could not succeed to measure gelatin and parchment in the full range of RH. However, gelatin spectra could have been measured at very dry and the normal room condition (ca. 30%RH). Parchments were measured mostly at room RH, which is close to its normal storage condition.



**Figure 31: Far-IR spectra of gelatin versus collagen and parchment samples. After baseline correction the absorbance of each curve was normalized to the same intensity. a)** Gelatin (dry) is shown together with a collagen curve series of different RH. Gelatin peak shape shows a difference with respect to collagen. **b)** Gelatin versus collagen curves at 0% and 30% RH are also presented. Both, collagen and gelatin show the same behavior regarding the RH; the smaller peak rises relatively to the big peak in dry condition. In any case, the same principal difference between collagen and gelatin can be observed for both humidity conditions. **c)** Collagen versus parchment at 30%RH. Selected spectrum of modern parchment, contrary to gelatin, shoes high congruence with collagen (demineralized bone). **d)** The collagen peak can be fitted by two Gaussians: the bigger peak  $\nu(I)$  at  $345\text{cm}^{-1}$  and the smaller peak  $\nu(II)$  at  $315\text{cm}^{-1}$ .

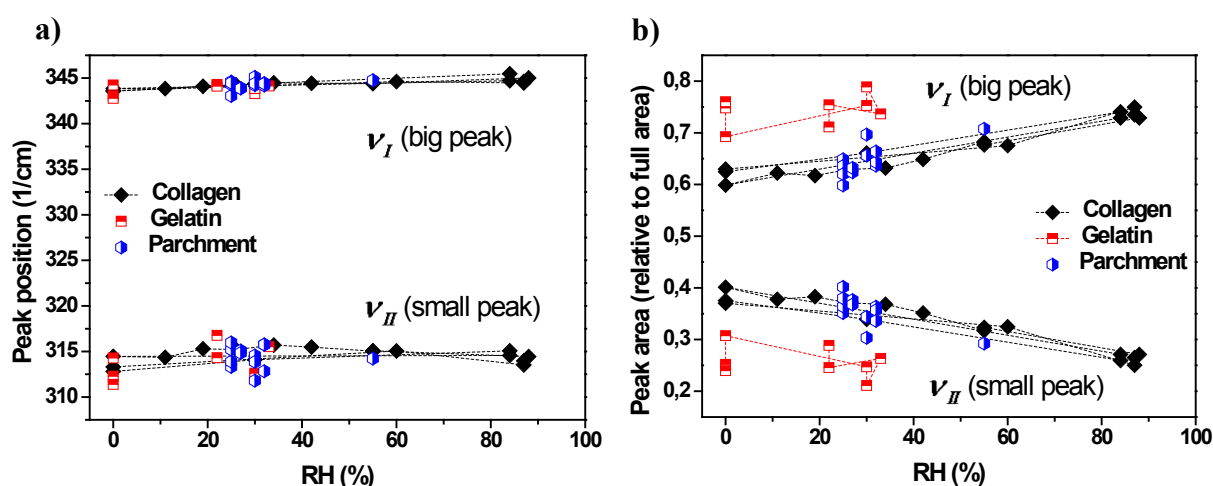
In Figure 31a, normalized spectra of collagen in the full range of RH are presented with blue colors. The trend in spectral features fits with the results from Figure 30b. A dry gelatin spectrum in red is presented in the same graph to highlight the principal difference. The most striking difference is related to the reduction of the smaller peak with respect to the bigger peak for gelatin. For clarity, in Figure 31b we show, separately, the same peak shape difference between collagen and gelatin at two RH conditions: 0%RH and 30%RH.

Based on the dichroism analysis we can conclude that this difference is not due to the orientation features, because both collagen peaks show high anisotropy with the same orientation. Since these peaks have the same orientation, the reorientation of the entire collagen molecules would cause a proportional absorption reduction of both collagen peaks, rather than a



change of the absorption peak shape similar to that found for gelatin. This means that a randomly distributed intact collagen in a sample would lose the anisotropic spectral features, but its peak shape would remain the same and hence always differ to that of gelatin independent on the molecular orientation. Therefore, we can link the shape difference of the double peak to the gelatinization features only. This is also confirmed by the randomly distributed collagen fiber network in parchment, which shows a strong spectroscopic congruence with the highly oriented collagen sample of demineralized bone, as presented in Figure 31c.

For quantitative analysis of this spectral feature we used the Levenberg Maquardt method in OPUS6 to fit the double-peak with two Gaussians, whereas all parameters were kept free to change. The results for the spectral peak position and the normalized peak areas are presented in Figure 32.



**Figure 32: Comparison of the fitting results of collagen based materials with two Gaussians.** The fitting procedure has been performed with the Levenberg Maquardt method in OPUS6, where all fitting parameters (i.e.  $\nu$ ,  $\omega$  and Intensity) were left free. a) The spectral positions of the Gaussians do not shift with humidity change and are the same for collagen, gelatin and parchment. b) Peak area normalized by the full area of the fit is presented. The area, however, of the big (at 345cm<sup>-1</sup>) and small (at 315cm<sup>-1</sup>) peaks definitely show a moisture related behavior for collagen. Moreover, the results also show a difference between intact collagen from demineralized bone and gelatin, whereas parchment have similar characteristics to intact collagen.

The fitting procedure revealed no significant spectral peak shift. The intensity and the width on the other hand are strongly influenced by moisture and gelatinization as well. Both parameters are included in the peak area and presented in Figure 32b. The results show a trend related to the moisture content for collagen and indicates a similar behavior for gelatin. The normalized area of the big and the small peaks can be used for the quantitative characteriza-

tion of degree of the gelatinization. This will be further elaborated in more details in the following discussion chapter section 3.3.

### **3.3 Discussion**

In this chapter we have explored the use of Far-IR spectroscopy for gelatinization analysis of collagen to be applied on parchment. For this purpose we first characterized the spectral properties of intact and fully gelatinized reference materials i.e. collagen matrix from a demineralized fibrolamellar bone and commercial gelatin, respectively. Alongside this study the spectral properties of bone mineral has been analyzed as well. Mineral and collagen peaks overlap to form one absorption peak. Using stepwise demineralization it was found that mineral contributes to the whole bone absorption peak area approximately up to 60-70 time compared to the collagen peak area (Figure 26). Thin bone sections allowed a linear and homogeneous demineralization process in EDTA (Figure 27), a fact that helped to extract the collagen contribution from the mineral peak and analyze its spectral features independently of collagen (Figure 28a).

Linear dichroism analysis revealed spectral polarization features of both the mineral and the collagen peaks. The wide mineral peak is an assembly of multiple speaks that partly show anisotropic properties (Figure 28b). Collagen absorption is characterized by two peaks, one at  $345\text{cm}^{-1}$  and a small one at  $315\text{cm}^{-1}$  forming a shoulder. Both peaks show a parallel linear dichroism anisotropy (Figure 29a). The parallelism of these two peaks is very important for further development of this methodology especially when it comes to evaluation of gelatinization in parchment. In gelatin unfolded and fractured collagen molecules are randomly distributed (Figure 29b), whereas in parchment the intact collagen molecules can either be randomly distributed or they can show a predominant orientation depending on the place of the skin origin on the animal body. However, for this analysis it is crucial to be able to distinguish between isotropic gelatin and randomly distributed intact collagen fibers.

The parallel behavior of both collagen peaks in linear dichroism experiments is a very convenient result, because the misalignment of the collagen fiber does not change the peak shape; it would just cause a proportional reduction of their absorption. This means that the absorption peak shape is expected to be very much the same for both cases; a highly oriented or a randomly distributed intact collagen fiber matrix. Our methodology for gelatinization quantification in parchment is therefore independent from the origin on the body.

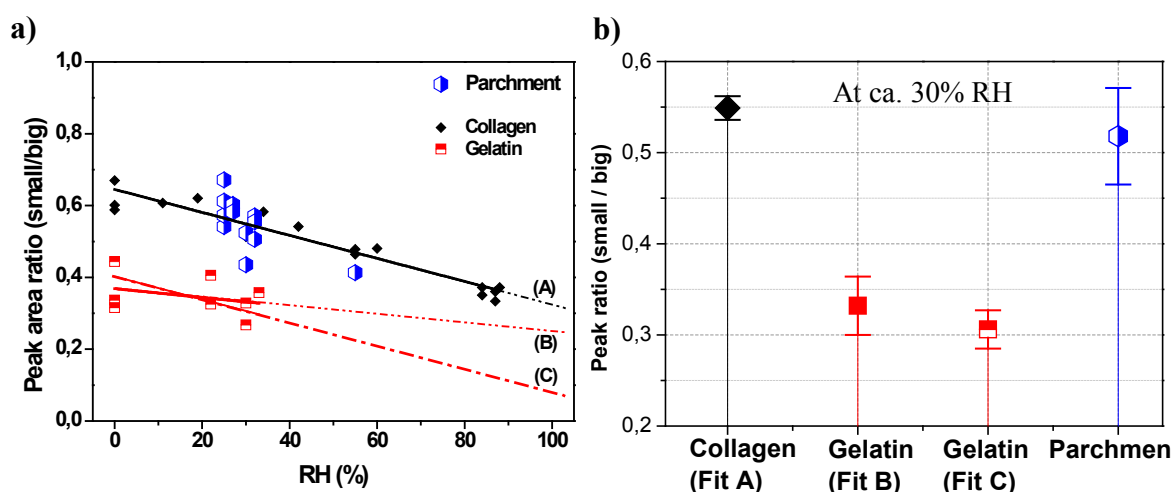
Production of parchment involves circles of drying and hydration with a final step of drying under tension. Therefore, collagen has been measured under tension in wet and dry conditions (Figure 30). It came out that the externally induced stress (caused by up to 10% strain on demineralized lamella bone sample) in wet condition does not influence the spectral properties. Moisture content, however, influences the spectral properties of collagen significantly and needs to be considered when it comes to the deterioration analysis.

In paragraph 1.1.1, we finally gathered all our findings and compared the spectral properties of all three materials: demineralized bone collagen (called just collagen), gelatin and modern made parchment. We have found a clear difference between intact collagen and gelatin (Figure 31a,b). The spectral congruence of a randomly distributed fiber network in parchment and the oriented collagen matrix in demineralized fibrolamellar bone sample (Figure 31c) confirms the linear dichroism results of parallel anisotropy of the two peaks and proves the capability of the approach. The variable collagen orientation in parchment does not need to be considered for deterioration analysis.

However, the gelatin peak was found surprisingly very similar to the double peak shape of collagen, which is related to the triple helical structure of collagen [152]. Gelatin contains fractures of triple helical structures as well, whose amount depends on specific conditions such as pH-value, solvent or temperature [190, 191]. However, Gordon et.al.1974 did similar measurements in the Far-IR region showing a greater difference between denatured collagen (gelatin) and intact collagen. The measurements revealed that increase of temperature (much higher than the normal room condition 23°) causes the disappearance absorption peaks [152]. This was related to the higher degree of the disorder decreasing the amount of triple helical formation in the gelatin gel at high temperatures. For our experiments we were using either gelatin Type A, or denaturized bone collagen prepared by humidified heat treatment for longer time period. Our experiments, however, were conducted at normal room temperature where reformation of the collagen-like peptide structure is possible, as it has been shown by measuring the optical rotation changes, the viscosity and density product value of the gelatin gel system during radiation treatment [73].

For the final quantitative characterization a two Gaussian peak fitting analysis was applied (Figure 31d), where all the freedom parameters (i.e. spectral position, width and intensity) were free. The fitting analysis revealed the normalized peak area to be a useful tool for the gelatinization characterization (Figure 32b). The ratio of the two peak areas i.e. small/big are plotted in Figure 33a. Since collagen was analyzed for the full range of RH, the area ratios

could be fitted with a linear fit (A). Gelatin measurements in hydrated state are missing, therefore, two scenarios (B) and (C) for the linear fits are proposed. The slope of Fit (B) was calculated by mean square and it differs from the collagen slope. It is also reasonable to assume that the slope of gelatin would actually be the same as for collagen (Fit (C)). In any case, both fits (B) and (C) do not differ much for the room condition RH (about 30%RH), where we have some statistics for gelatin on one hand and almost all measurements done on parchment on the other hand.



**Figure 33: Peak area ratios (small / big) comparison between demineralized bone collagen, gelatin and parchment. Areas were obtained by fitting presented in Figure 32. a) Collagen has enough points in the full RH range for a precise linear fit. Gelatin peak ratios on the contrary are presented with two possible fit scenarios that differ in the wet condition because of the measurement lack in that state. The linear Fit(B) was calculated by the fitting software, whereas Fit(C) is just a parallel shift of the collagen Fit(A). However, both possible gelatin fits intersect approximately at room condition (in BESSY) where some measurements statistics are available for gelatin and parchment as well. b) RH room condition (ca. 30% RH) is used for quantitative comparison of all three materials; demineralized bone collagen:  $0.55(\pm 0.01)$ , gelatin:  $0.32(\pm 0.03)$  and parchment:  $0.52(\pm 0.05)$ . The error bars are the standard deviation calculated in Origin7. Further gelatinization of parchment is expected to shift the peak area ratios to lower numbers between 5 and 3 and therefore can be quantitatively characterized.**

Room condition (RH) is the natural environment of parchment. We therefore can set our quantitative characterization for the room condition as follows: demineralized bone collagen:  $0.55(\pm 0.01)$ , gelatin:  $0.32(\pm 0.03)$  and parchment:  $0.52(\pm 0.05)$ . The state of the analyzed parchment samples is close to that of collagen, whereas its high error is caused by the low spectral quality of the most parchments measurements. However, further deterioration would shift the peak area ratio (small/big) towards gelatin value of 0.3.

We explored a new tool for quantitative deterioration analysis of parchment samples on macroscopic area. In any case, the transmission approach is not applicable for the parchment analysis in particular when it comes to ancient material from cultural heritage because of the destructive way of the sample preparation. This technique needs to be developed further to be applied in backscattered geometry where no destructive sample preparation is required. With this investigation we proved the potential of this methodology for deterioration analysis.

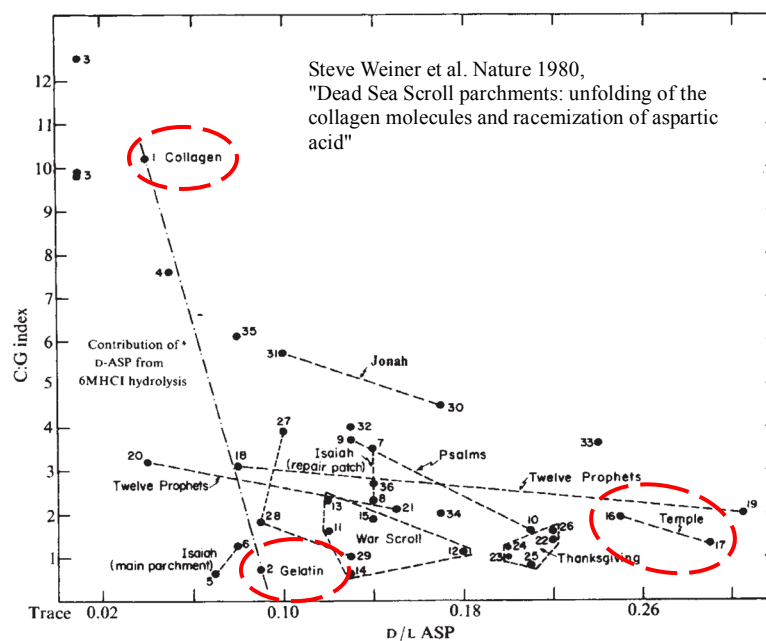
# The Temple Scroll



R. Schütz, L. Bertinetti, I. Rabin, P. Fratzl and A. Masic  
Quantifying degradation of collagen in ancient manuscripts:  
the case of the Dead Sea Temple Scroll

#### **4 *In-situ* damage assessment of collagen within the Temple Scroll on microscopic scale**

Ours is not the first material study of the TS. Already in 1980, an X-ray diffraction study of the DSS collection done by Steve Weiner indicated that the high degree of degradation of the TS contrasted strongly with the appearance of a good state of preservation [192] (Figure 34). Later, scientists from the Getty Institute who analyzed the parchment of the scrolls within the framework of a preservation project arrived at the same conclusion [193]. Therefore, quantitative damage assessment of this scroll seems to be crucial for monitoring its state and for its further preservation.



**Figure 34: Deterioration analysis of the DSS including TS by means of X-Ray scattering [192]. The low C:G index stands for strong gelatinization and the higher D/L value (racemization of aspartic acid) is correlated to a progressed aging process of a biological material. The graph shows that among the DSS the Temple Scroll is most badly affected in its degradation.**

Parchment is a final product of the processing of animal skin and consists mainly of type I collagen, the most abundant constituent of the dermal matrix. Only in the remains of the thin outer epidermis layer on the parchments hair side and its appendages the major structural proteins are not collagenous but keratinous, constituting up to 85% of fully differentiated

keratinocytes [194]. Deterioration of parchment is caused by chemical changes due to gelatinization, oxidation and hydrolysis mainly of the collagen chains [7]. Historically, the state of degradation of collagen within parchments has been studied using several physical and chemical methods. Methods such as shrinkage temperature [195], X-ray scattering [68, 117], thermal analysis [196], AFM [197], and solid state NMR [198] provide qualitative information on the physical and chemical integrity of collagen at various levels of the hierarchical structure. However, they are usually invasive, i.e. require small samples of the original material. This fact, together with the intrinsic heterogeneity of the skin material, explains why none of these methods can be used to monitor the state of preservation of the ancient parchment. Therefore, an efficient and non-invasive technique for quantitative damage assessment has great potential for early warning and monitoring systems [199]. Recent attempts to describe the evolution of parchment deterioration use NIR [200], and multispectral imaging techniques [201]. It seems, however, that low spatial resolution and sensitivity result in inaccuracy that outweighs the advantage of the ease of application. Recently, unilateral and solid state NMR techniques showed potential for determining the state of conservation of collagen indirectly, through the relaxation behavior of water molecules involved in the stabilization of the collagen triple helix [198, 202, 203].

Raman spectroscopy has long been explored as a method for assessing damage to parchments [204-207]. Its non-invasive and nondestructive nature made it an attractive candidate for both damage assessment and monitoring. However, small changes in spectral features and the low sensitivity of the method itself prevented the acquisition of sufficiently accurate information to be routinely applied for damage assessment. Recent technical developments in polarized Raman spectroscopy (PRS) showed huge potential in structural studies of collagen-based materials [208, 209]. The possibility of obtaining both chemical (molecular interactions) and structural (orientation) information [2, 12, 115, 210] in a single experiment opens the way to the use of PRS for studies on orientation changes induced by deterioration. The methodology is based on the sensitivity of Raman scattering bands (associated with distinct molecular vibrations) to the polarization direction of the incident laser light. The method can be applied in order to map fibrous materials within other heterogeneous tissues and, in principle, it is possible to concurrently map the distribution of other chemical components associated with it [104, 112].



## 4.1 Materials and Methods

### Materials

Collagen fibers from two regions of interest on several analogue fragments of ca. 5x5mm<sup>2</sup> of the TS were analyzed (TS3 and TS4 from Table 2 in chapter 5). Furthermore, collagen fibers of specifically prepared reference samples have been investigated. As a reference for a sample with high orientation anisotropy, a rattail tendon (RTT) was stretched by 10% of its length and analyzed in the dry state. In addition, fibers of recently manufactured new parchment (NP) were studied. As a reference for the isotropic collagen network, gelatin was prepared from RTT and NP by a thermal treatment (80°C) in water for more than 4 hours.

### Theoretical background of Polarized Raman Analysis

The PRS approach is a consolidated methodology and has been frequently applied on systems with uniaxial symmetry in the last decade. A compact guide to the basic concepts that have been applied in the study of TS is presented in chapter 1.4. The PRS equipment used in this study is specified in chapter 1.1. The measurements were performed with 785 nm laser excitation, and a 100x lens (Olympus MPlan IR, NA = 0.95) with  $\approx 1 \mu\text{m}$  lateral and  $\approx 2 \mu\text{m}$  depth resolution.

### Polarized Raman Data acquisition and processing

In the TS fragments, the collagen fibers are characterized by a diameter in the range of 5 to 10  $\mu\text{m}$ . The size of the focal spot of the used 100x (Olympus MPlan IR, NA = 0.95) lens lies in the range of  $1 \mu\text{m}^2$  laterally and around  $2 \mu\text{m}$  along the optical axis. The confocal setup ensures that the measured spectra are representative of a single collagen fiber and not of several overlapping collagen fibers.

To determine the intensity ratios  $R1 = I_{0-90}/I_{0-0}$  and  $R2 = I_{90-0}/I_{90-90}$ , the analyzer for polarization has been placed in the path of the backscattered light. The analyzer orientation is indicated by the second indices of the intensity ( $I_{0-90}$ ; 0°- polarizer and 90°-analyzer regarding the fiber orientation (z-axis)). Four experiments are needed to calculate the orientation parameters and one additional control measurement at the 0–0° position is performed on the same spot. The control measurement is used to check the stability of the spot position on the selected fiber during the 4 minutes needed for complete measurement. Forty to sixty accumulations

with an integration time of 1 s were used for each of the four polarization adjustments of a single spot analysis.

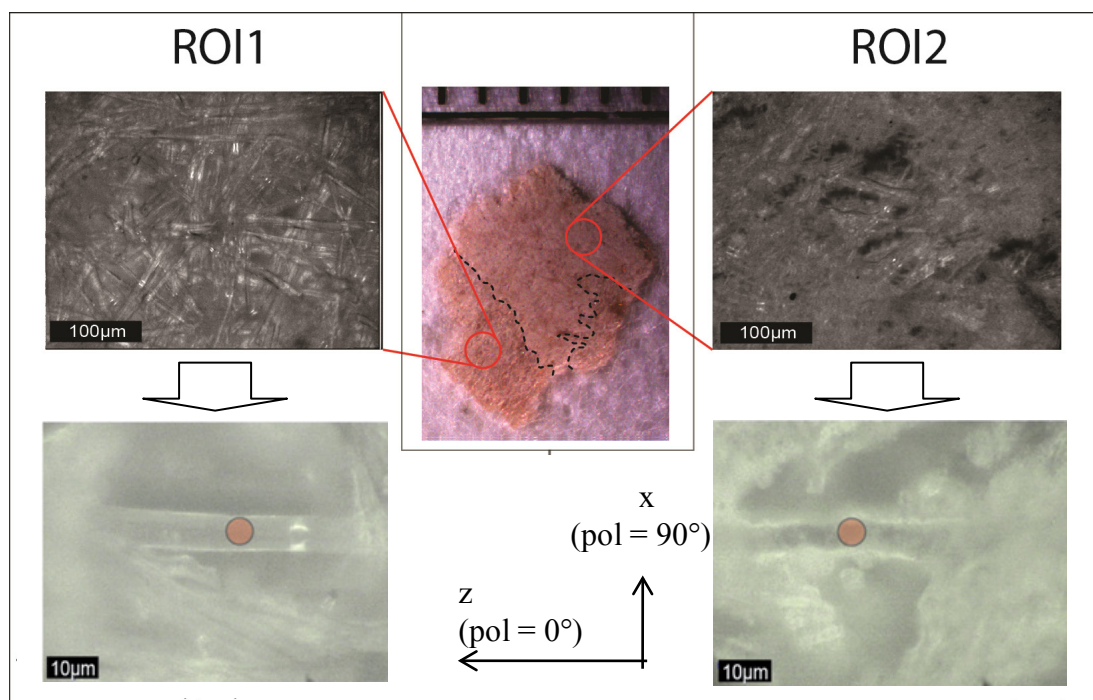
The spectra were acquired with the WITec Program 1.94® and then processed in three steps with OPUS 6.0®:

1. Cut the region around the amide I band ( $1517\text{--}2000\text{ cm}^{-1}$ ).
2. Baseline correction (straight line).
3. Integration over the spectral range between  $1600$  and  $1720\text{ cm}^{-1}$ .

The laser power at the sample is kept low (less than 4 mW). This is of particular importance when measuring the precious TS fragment, which has to be investigated non-destructively. The signal-to-noise ratio of the spectra under these conditions is not optimal, especially for the cross-polarized configuration (0–90 and 90–0), where the intensities are very close to the spectral noise level. For such spectra, neither accurate peak fitting nor intensity maxima can be obtained and therefore an integral over the whole Amide I region was used. For the calculation of Legendre polynomials  $P_2$  and  $P_4$  (for details see chapter 1.4) the ratio  $R_{\text{iso}} = 0.20 \pm 0.015$  (gelatin) of an isotropic reference material and a refractive index of  $n = 1.5 \pm 0.02$  (for 40%RH) [211] were used.

## **4.2 Results**

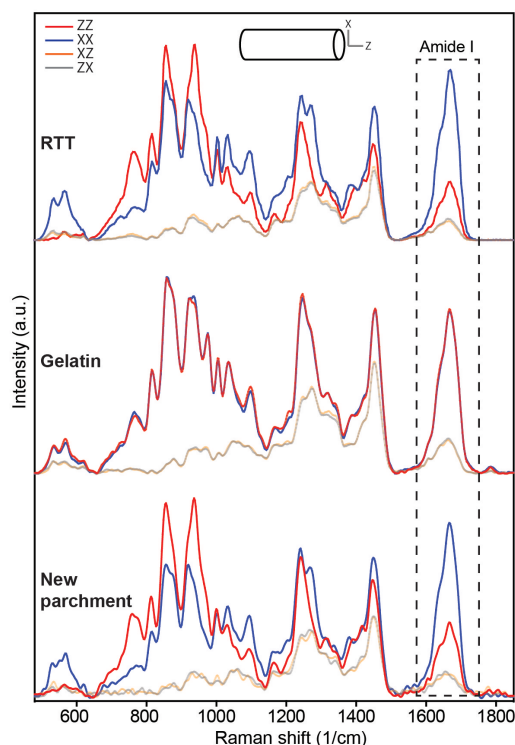
Good knowledge of the Temple Scroll's state of deterioration is of great importance for the preservation methodology and other related studies. The main organic constituent of parchment is a network of collagen type I fibers. Thus, a quantitative analysis of deterioration based on the unfolding degree of molecules in the fibers has been done by means of polarized Raman Spectroscopy (PRS principles in Chapter 1.4). The concept of the methodology and the quantitative results are presented in this chapter. The methodology is based on the fact that the orientation of a molecular unit within a biomolecule can be quantified from Raman band anisotropy measurements, if the Raman band tensor of the relevant molecular unit is known [108, 110]. In the case of the amide I band, the tensor properties are well documented in the literature and can be used for this purpose. From parameters provided by the PRS, it is possible to determine the arrangement or orientation of the C=O vibrational units with respect to the fibrous system [111, 112, 114, 212].



**Figure 35: Stereo- and optical microscopy images (top) of two ROIs of the TS3 fragment. Collagen fibers can be found in both ROIs. The bottom part shows single collagen fibers in both ROIs.**

For this study the TS3 fragment was chosen, because a part of the inorganic layer is detached and the collagen fibers from beneath were exposed (Table 2 in chapter 5.0). Additionally, other TS4 fragments have been measured where exposed fibers could be found in cracks or at the edges. From the macroscopic morphological observation of the surface of the analyzed TS fragments, it was possible to distinguish between two regions. The first region of interest (ROI1), with a clearly visible intact collagen fiber network, was originally covered by another foreign inorganic layer. The second region (ROI2) is on top of the inorganic layer where some fibers can be identified on the surface (Figure 35). The Analysis of the inorganic layer is presented in the results section 1.1 of the previous chapter. The layer is mainly composed by Sodium and Calcium Sulfate particles accompanied by Silicon. The collagen fibers on the surface layer appear to be more damaged; contrary to the fibers of ROI1, these fibers have continuously been exposed to the environment since the date of its production.

For damage quantification, we first considered two borderline cases, namely (i) fresh collagen fibers from rat-tail tendon (RTT) and new parchment, and (ii) completely gelatinized collagen.



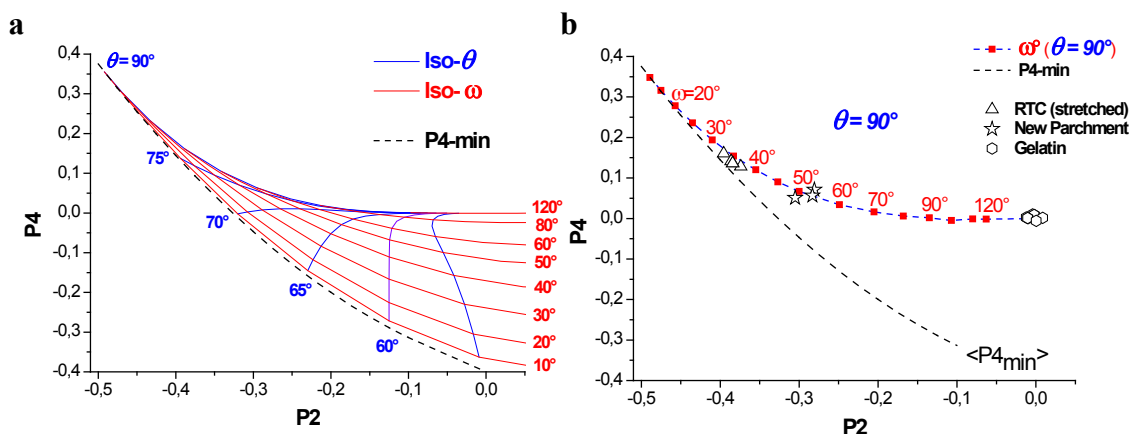
**Figure 36: Polarized Raman spectra @785nm of rat tail tendon (RTT) fiber (top), gelatin (middle) and newly prepared parchment fiber (bottom). The dashed box highlights the amide I region used for evaluating orientation parameters. Amide I anisotropy is evident (comparing XX (blue) and ZZ (red) configurations) for RTT and new parchment fibers, but completely vanishes in the gelatin sample.**

In Figure 36 the polarized Raman spectra of RTT, gelatin and new parchment (NP) fiber samples are presented. Red spectra are acquired by placing the polarizer and the analyzer parallel to the fiber axis (ZZ), whereas blue spectra are acquired with the polarizer and the analyzer perpendicular (XX) to the fiber axis. Grey and orange spectra are cross-polarized configurations (XZ and ZX) useful for calculating orientation parameters. Longitudinally stretched RTT was used to obtain perfectly aligned collagen fibers as a calibration standard (Figure 36, top).

In our PRS analyses we focus on the collagen backbone vibrational modes, and in this context, an intense band centered at  $1665\text{ cm}^{-1}$  is observed, corresponding to the amide I vibration, which is mainly due to C=O stretching vibration. Further intense bands can be seen at  $\sim 1450$  and  $\sim 1250\text{ cm}^{-1}$ , which are assignable to C–H bending and amide III vibrations, respectively. It is a clearly visible band anisotropy (differences in scattered intensities that are related only to the orientation of the laser polarization), particularly in the amide I region (highlighted with the dashed box in the figure). Because collagen carbonyl groups are oriented mainly perpendicularly, the amide I band is more intense in the direction that is perpendicular

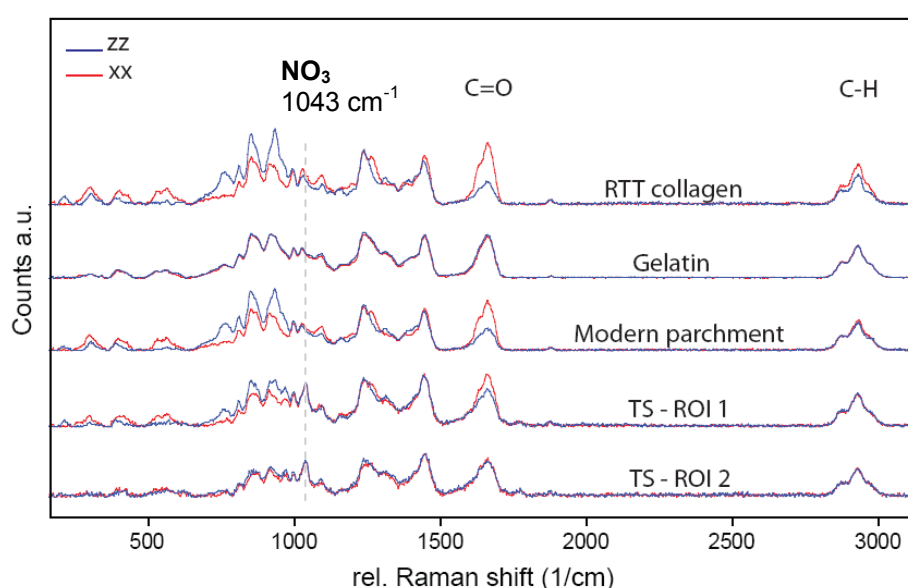
to the collagen molecular axis (blue spectra in Figure 36) [2]. Very similar anisotropic behavior is found for collagen fibers within the NP sample, whereas the anisotropy of all bands completely vanishes in the case of gelatin. The latter result of gelatin is to be expected, considering the complete loss of the supramolecular organization of collagen molecules.

Here we propose an efficient way of quantifying disorder in collagen fibers. It is possible to calculate the associated P2 and P4 values for any distribution, by approximating molecular distribution of vibrational units around the fiber axis by a Gaussian curve. In this way, for any P2 and P4 there will be a corresponding distribution characterized by a given angular maximum ( $\theta_{\max}$ ) and ( $\omega$ ) - a full width at half maximum (FWHM). The angular maximum corresponds to the most likely orientation of collagen units, whereas FWHM is linked to the variability of the orientation. Plotting the iso-  $\theta_{\max}$  and iso- $\omega$  lines in the P2–P4 space (Figure 7 and Figure 37a) enables a simple correlation between the order parameters and the distribution of the vibrational units and therefore allows the quantification of the order–disorder in a fiber. In the case of collagen based materials, the C=O distribution is always centered at  $90^\circ$  but can vary in  $\omega$  (FWHM). These results can be depicted in the P2–P4 space spread along the  $\theta_{\max} = 90^\circ$  line. Figure 37b shows such a plot, where P2 and P4 values were obtained for all three reference samples: Stretched tendon fibers from rat tail with a relatively narrow  $\omega$  compared to the fibers from a new parchment, whereas gelatin shows the widest  $\omega$ . The characterization of the distribution function of the Amide I bond in collagen and hence of its degree of deterioration can be reduced to one parameter:  $\omega$  : FWHM the width of the Gaussian.



**Figure 37: Distribution function parameters in P2-P4 space. a) Any Gaussian distribution parameters  $\theta$  : position and  $\omega$  : FWHM can be expressed by means of Legendre parameters P2-P4. The corresponding Iso-curves are presented. b) Measured C=O distribution parameters of stretched RTC, New Parchment and Gelatin in P2-P4 space show the main orientation following the  $\theta_{\max} = 90^\circ$ . They differ in only one parameter:  $\omega$  : FWHM.**

Now this methodology can be implemented to collagen fibers in the Temple Scroll. Figure 38 compares the PR spectra from two characteristic fibers selected from the different areas of a single TS fragment together with the previous reference spectra; RTC, NP and gelatin. The PRS approach was applied to suitable fibers that were optically located in both of the aforementioned ROI1 and ROI2. From a simple comparison of the anisotropic responses of the amide I band, it can clearly be concluded that the fiber from the ROI1 shows a very similar anisotropic pattern to that found in the new parchment, whereas the fiber from the ROI2 matches better with the gelatin spectral features (Figure 38).

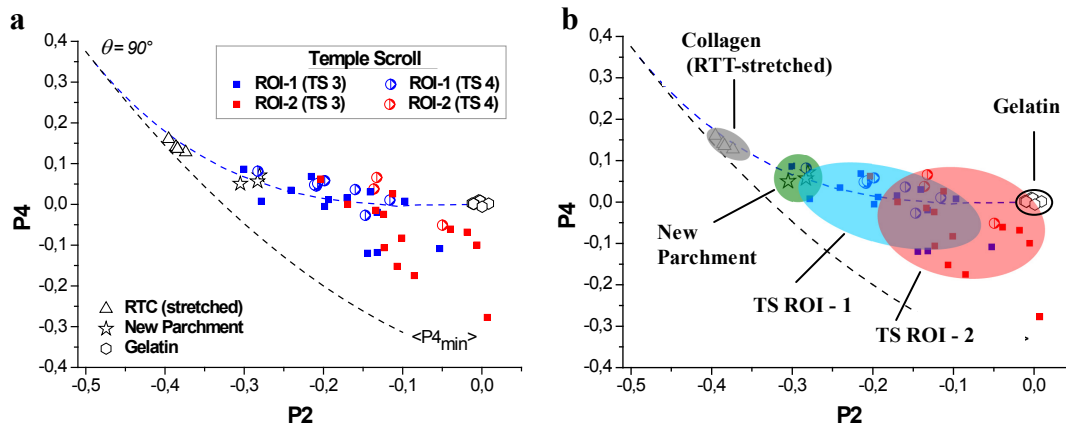


**Figure 38: Polarized Raman spectra @785nm of reference materials (RTT collagen, gelatin and new parchment) together with two typical TS fibers. One is from ROI-1 with a relatively high anisotropy and the other from ROI-2, the latter shows very similar properties to gelatin. The TS spectra contain an additional peak at  $1043\text{ cm}^{-1}$ , which is not related to the PR response but to a  $\text{NO}_3$  molecule that could be found in all analyzed fragments.**

The TS spectra show an additional specific peak at  $1043\text{ cm}^{-1}$ , it is the  $\text{NO}_3$  peak that could be measured on collagen of our TS fragments (see Figure 48 in the result section 1.1 of the previous chapter). The TS material is very fragile and hence requires a sensitive approach. Although its Raman spectrum shows much less fluorescence compared to most other scrolls found in Qumran or archaeological material in general, the laser intensity has to be kept as low as possible. So in our case, we used a 100x magnification lens with ca.  $2\mu\text{m}^3$  probing volume where on one hand the laser energy density in focus is high but on the other hand the fluorescence from surrounding material could be reduced. The laser power was increased slowly until a reasonable spectral intensity could be achieved. Never the less, especially in the

cross polarization geometry ( $0^\circ$ - $90^\circ$  or  $90^\circ$ - $0^\circ$ ) the spectral noise was very high and lead to a significant error for the individual measurements.

The P2 and P4 parameters of the TS are shown in Figure 39. The majority of the points are following the  $90^\circ$  line, which is the expected case since the C=O bond is mainly oriented perpendicular to the collagen backbone axis.



**Figure 39: a) P2–P4 plot of orientation parameters relative to all samples analyzed in this study. b) Characteristic regions found for different samples indicative of different states of the preservation of collagen.**

In some cases, though, points drift down to higher negative P4 values; this is mostly the case in ROI2, where due to lower intensity the signal to noise ratio is much lower than in ROI1 cases. The other reason for this drift could be the internal out of plane reorientation of the molecule bunch inside the strongly deteriorated fiber, which is not recognizable by the outer fiber shape. Although these drifted points most probably do not reflect the real distribution function inside the fiber, they still are part of the overall measurement and hence they have to be included in the final result. However, even with the increased error the overall trend can be determined;

Sample	P2	P4
RTT	-0.38 $\pm$ 0.01	0.14 $\pm$ 0.02
New parchment	-0.29 $\pm$ 0.01	0.06 $\pm$ 0.01
TS (S1 and S2) ROI1	-0.2 $\pm$ 0.07	-0.08 $\pm$ 0.09
TS (S1 and S2) ROI2	-0.09 $\pm$ 0.06	-0.01 $\pm$ 0.07
Gelatin	-0.00 $\pm$ 0.01	0.00 $\pm$ 0.01

**Table 1: Average Legendre coefficients P2 and P4 for all samples.**

Table 1 shows the calculated averaged values of two main orientation parameters (Legendre polynomials P2 and P4) relative to the amide I band for RTT, NP, gelatin and several fibers within TS samples. The average values of the order parameters vary significantly among different samples. As expected, values obtained for the RTT and new parchment are in the range of highly ordered molecular units, whereas the P2 and P4 (close to zero) found for gelatin indicate complete disorder. In the case of the TS, the parameter values lie between the two just discussed limits, with ROI1 apparently more organized than ROI2.

### **4.3 Discussion**

Though a simple visual inspection of the Temple Scroll demonstrates the heterogeneity of the collagen degradation, its degree cannot be established in a simple way. Furthermore, the heterogeneous state of degradation leads to a different response of the various parts of the scroll to conservation treatments and environmental storage conditions (such as humidity and temperature) and therefore a quantitative estimation of the fibers' integrity is crucial. We found a suitable sample for this purpose; TS3 (studied TS fragments from different locations within the scroll are presented in Table 2 chapter 5.0). In the TS3 a part of the inorganic layer is detached and the collagenous network beneath is directly accessible. These collagen fibers defined as ROI-1, were protected from the environment over the centuries. On the other hand, collagen fibers can be recognized being embedded and exposed on the surface of the inorganic layer as well: ROI-2 (Figure 35). The fiber diameter size in both regions is usually about 5 $\mu$ m, which is larger than the lasers beam probing volume. So, we can address the fibers individually by means of Polarized Raman Spectroscopy. In this study a quantitative damage assessment methodology has been established based on the specific polarization response. The Amide I band corresponds to the C=O vibration, which is strongly polarization dependent as it is presented in Figure 36 for three reference materials: stretched rat tail tendons (RTT), modern made parchment (NP) and gelatin (Figure 36). From four polarization measurements (excitation vs. scattering pol. direction adjustments) the first Legendre parameters P2 and P4 can be calculated for the distribution function regarding the molecular axis (chapter 1.4). In the case of a Gaussian – the distribution function can be characterized also by means of the angle regarding the molecular axis and the width of the Gaussian peak. Hence, any Gaussian distribution function can be expressed by P2 und P4 parameters and depicted in the P2-P4 space (Figure 7).



It appears that the main difference between various collagen samples (RTT, new parchment and gelatin) lies in the width of the Gaussian distribution function at  $\theta_{\max} = 90^\circ$  (Figure 37). Thus, a well-preserved collagen fiber will have a width of  $30\text{--}40^\circ$ , while a strongly gelatinized one will have a width larger than  $120^\circ$ . The highly organized collagen of the stretched RTT was found to have a FWHM of  $40^\circ$ . The Gaussian distribution function of the results of the NP has a FWHM of  $60^\circ$ . This is supposed to correspond to the best state of preservation of collagen in a parchment treated with lime, particularly in historical parchments. The broadening of the distribution function with respect to that of the RTT, indicates a slight disorganization of collagen in freshly prepared parchments, probably induced by treatments necessary for depilating and finishing.

The collagen spectra of the ancient TS show the same polarized characteristics as the modern collagen materials (Figure 38). The results of the P2 and P4 coefficients for both areas of the TS fragments display a wider scattering around the  $\theta_{\max} = 90^\circ$  line than in the case of NP or RTT (Figure 39). The reason for the stronger variations from the  $\theta_{\max} = 90^\circ$  line is likely to be found in the weak and noisy signal intensity in the spectra of the 2000-year old collagen fibers. Nevertheless a tendency can be recognized along the  $\theta_{\max} = 90^\circ$  distribution curve in the P2–P4 space. The collagen fibers of the formerly covered ROI1 show P2 values that are significantly different from those of the ROI2. Spread over a large range from  $60^\circ$ , the FWHM values found for ROI-1 are equivalent to a well-preserved modern parchment, with some points going up to  $120^\circ$ , which is very close to strongly disorganized collagen in gelatin. The FWHM values related to the ROI-2 lie in the range between  $80^\circ$  and  $120^\circ$  of width, indicating a greater degradation of the collagen in this area than in the ROI-1. It is worth repeating that previous studies on the TS fragments show very high level of gelatinization (Figure 34, [192]). In contrast, we find that several fibers in the ROI1 are relatively well-preserved. The mentioned previous studies were done by means of XRay diffraction whereby the information was gathered from all layers indistinguishably. In the paragraph “Preparation of the inorganic layer” of the discussion section of the previous chapter 5 arguments and evidences are discussed for a high probability of a significant presence of gelatin inside the inorganic layer. It is likely that gelatin made from the TS skin’s dermis was used as a binder. This presence of gelatin in the inorganic layer would surely shift the X-Ray diffraction measurements into the spectroscopic features of deteriorated collagen.

This simple experimental evidence is extremely important because it shows that the TS, commonly considered heavily gelatinized, locally contains collagen fibers that are in a relatively good state of preservation. Furthermore, it shows that some fibers, although lacking any

order at the molecular level of the structure, can preserve its macroscopic fibrous morphology. Starting from this spectroscopic evidence, and assuming that deterioration of collagen material will naturally lead to a general disorder of collagen structural units, we can now design a new approach for the damage assessment of the collagen fibers.

The methodology described here is based on a single parameter, i.e. FWHM of the distribution function, and results in a reliable and simple way to quantify the amount of degradation that leads to the disorder of molecular units of collagen in ancient parchments. The disorder, however, can be induced by several factors, such as gelatinization, hydrolysis, oxidation, etc. Orientation parameters defined in this work reflect global structural changes induced by all of these degradation processes and do not carry any information about the cause of the disorder. However, through an analysis of the spectral features of the Raman bands, it would be possible to address these points. We believe that the combination of this latter approach with the methodology presented here could provide further insights into deterioration pathways.

## **5 The Temple Scroll analysis**

The Temple Scroll passes different types of historical processing information to us: social/communal interactions, and also technical knowledge. The knowledge can be stored in the written content of the Temple Scroll, but it also contained in its physical material. Our goal and responsibility is to understand as much as can be learned from the Temple Scroll as possible, and to preserve it for the generations to come, which should create more advanced technologies to continue the work of Temple Scroll analysis. Today's question is; what information can be revealed from the physical material of the Temple Scroll, and how can it be useful to answer archaeological questions? Reconstruction of the production technique through analysis of chemical and physical compositions can indicate which materials and which technologies were used to produce the Temple Scroll. This knowledge can then support the discussions as to where it could have been produced, and possibly also by whom.


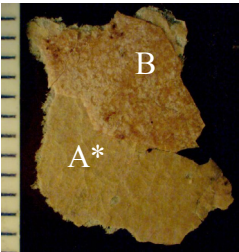
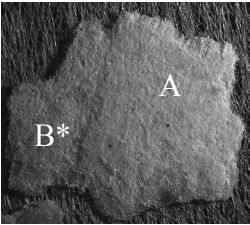
### **5.1 Materials and Methods**

#### **Samples Studied**

TS fragments from different locations within the scroll that were studied and described in chapters 1 and 5 are presented in Table 2.

We analyzed samples that were known to be from the inner (enveloped) part (TS1) of the scroll, as well as samples that were broken from the edges of the scroll (TS2-TS4). The exact locations from which these edge pieces came remain unknown. To identify the constituents found in the TS, diverse salts such as sulfates and nitrates (and mixtures of these salts), sediments and other materials that could be related to the scroll, the Dead Sea or the Qumran environment were also analyzed. These reference materials are not listed explicitly in "Materials and Methods" section, but in the case of positive results, they will be specified and presented in the results section together with the analysis of the TS material.

**Table 2: The Temple Scroll samples that were analyzed are listed.**

Sample Name	Description	Applied Methods
TS1 	This fragment originates from the inner part of the scroll, near the column LII. Its back side is fixed on a cellulose support, therefore only the written side of the fragment is available for analysis. It has an approximate size of 1cm <sup>2</sup> . The fragment belongs to the Shrine of the Book of the Israel Museum.	SEM-EDX, $\mu$ -XRF, PIXE, confocal Raman
TS2 	The exact origin of this fragment on the TS is not known, it may originate from a scroll edge. This fragment can be analyzed from both sides. The picture of the fragment's back side shows how a part of the back side layer (B) is missing. Therefore the rear (A*) of the front text layer is exposed, and can also be analyzed.	$\mu$ -XRF mapping, XRD, SEM-EDX mapping, confocal Raman
TS3 	Similar to TS2, the exact location of this fragment from the TS is not known. This fragment is also missing one part of one layer, but contrary to TS2, this fragment is missing a part of the front text-layer (A). The inner side (B*) of the back side layer consists mostly of distinct collagen fibers. This makes the sample very useful for the collagen deterioration analysis by means of polarized Raman (PRS).	PRS
TS4	TS4 comprises three similar samples with no special features. The exact locations of these samples within the scroll are not known.	$\mu$ -XRF, XRD, SEM-EDX, FT-Raman, PRS
TS5	Collagen powder that was scratched from the text side surface on an inner sheet of the TS.	Confocal PRS

### Particle Induced X-Ray Emission - PIXE

PIXE measurements were performed at the INFN (Italy's National Institute for Nuclear Physics) tandem particle accelerator facility in Catania. The 2 MeV proton beam energy was reduced to 1.3 MeV by a 75  $\mu$ m Kapton foil. The samples were irradiated by a 0.6 - 1.2 nA beam, with a spot size 1-1.5 mm in diameter. The spectra were measured with a Si-drift detector (160 eV) through a 80  $\mu$ m<sup>2</sup> window (beryllium, 25  $\mu$ m) at a distance of 20-30 cm from the sample.

### **X-Ray diffraction - XRD**

XRD measurements were performed in two setups. Salt samples from the Dead Sea “DS Salt White” and “DS Salts Yellow” were measured at the INFN in Catania with 6.4 keV, 40 kV and 250  $\mu$ A. All other XRD patterns that are presented in this study were collected at the Max Planck Institute of Colloids and Interfaces (MPIKG) in Potsdam using a Bruker D8 diffractometer with Cu-K $\alpha$  radiation ( $\lambda_1 = 1.54053$  Å) and Kevex (Sol-X) Detector. Data were measured over the range of  $2\Theta = 5^\circ$  to  $60^\circ$ , at a step size of  $0.05^\circ$  and an integration time of 2 sec per step.

### **Micro X-Ray Fluorescence Spectroscopy - $\mu$ XRF (Tornado)**

A tabletop Bruker 2D  $\mu$ -XRF spectrometer (Tornado M4) was used to obtain detailed, spatially resolved elemental maps from large sample surface areas. The probe contained an air-cooled, low-power Rh ( $K\alpha_1 = 20.2$  keV) X-ray tube, operated at 50 kV and 600  $\mu$ A, with polycapillary X-ray optics and an electro-thermally cooled Xflash detector. The spectrometer was evacuated to enhance detection of the light elements. Major improvements in data collection included the use of a small measurement spot of 25  $\mu$ m, and a high-speed x-y sample stage. The fluorescence signal was measured continuously while the stage moved with predefined step sizes.

### **Scanning Electron Microscopy with Energy Dispersive X-Ray Detector - SEM-EDX**

Near-surface analyses of the scroll fragments were performed with a Tescan Vega Environmental Scanning Electron Microscope (ESEM) equipped with a Bruker XFlash 5030 Energy Dispersive Spectrometer (EDS), which is located in the Wyss Institute for Biologically Inspired Engineering at Harvard University in Cambridge, Massachusetts. Elemental mapping and compositional analysis for each sample were performed under identical conditions:  $E_{\text{kin}} = 20$  keV and 12 Pa.

### **Fourier Transformed Raman Spectroscopy – FT-Raman**

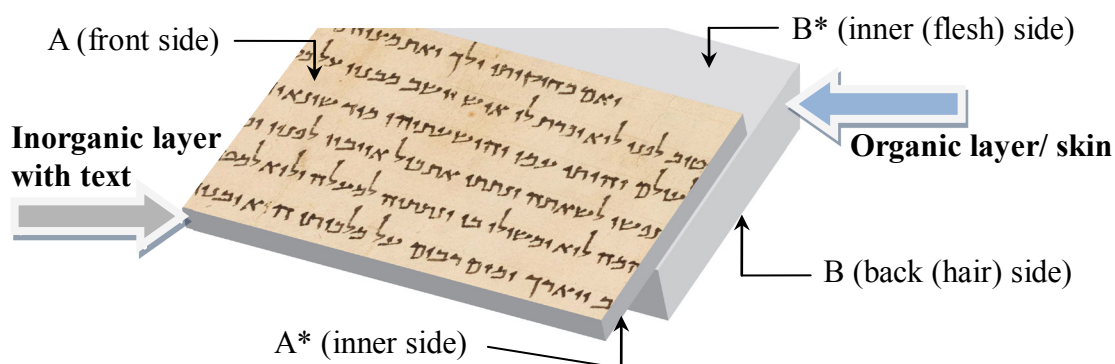
In order to obtain Raman measurements with higher spatial average for samples with strong fluorescence, a Bruker FT Raman spectrophotometer (RFS 100/S) was used. The instrument was equipped with Ge-diode detector cooled with liquid nitrogen (77 K), and a near infrared [YAG:Nd] laser operating at 1064 nm. Measurements were carried out with the laser output power of 50-100 mW, and spectra collected in the spectral range 100-3600  $\text{cm}^{-1}$  with a spectral resolution of 4  $\text{cm}^{-1}$ . 4000 scans were co-added per spectrum. The spot size of the beam on the sample was approximately 400  $\mu$ m in diameter.

## Confocal Polarized Raman Spectroscopy – PRS

The PRS equipment used in this study is specified in chapter 1.1. The measurements were performed with 785 nm laser excitation, and a 100x lens (Olympus MPlan IR, NA = 0.95) with  $\approx 1 \mu\text{m}$  lateral and  $\approx 2 \mu\text{m}$  depth resolution.

## 5.2 Results

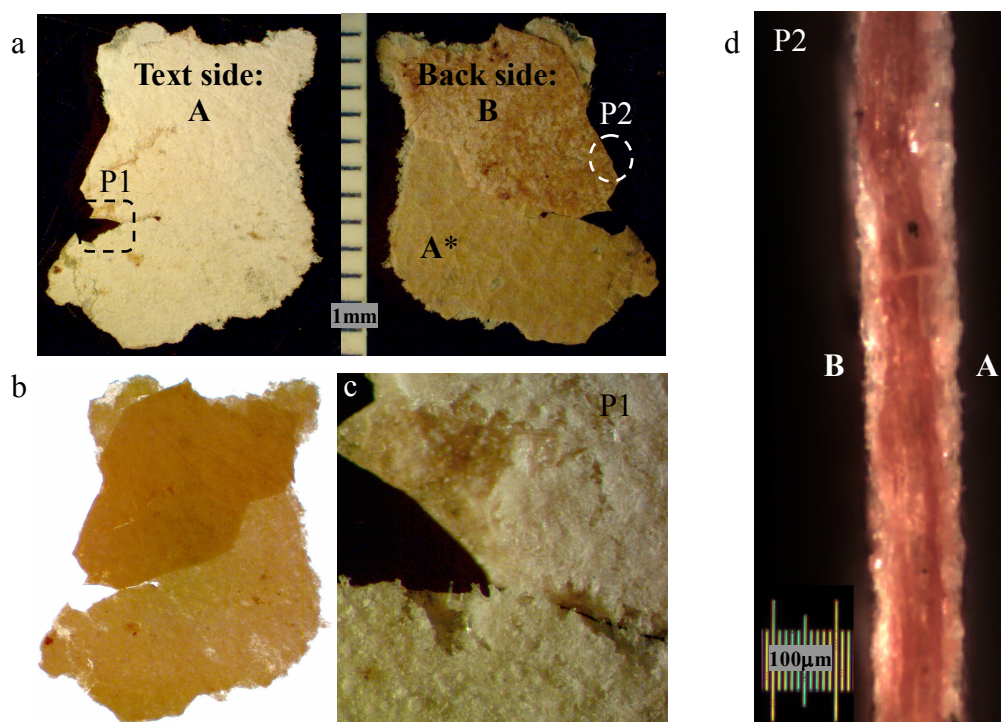
The flesh side of the parchment is covered by a thin layer that is enriched with inorganic materials, henceforth it will be termed the “inorganic layer” (Figure 2). Therefore, the complex material of the TS can roughly be grouped into two layers: an inorganic layer that was applied on the organic support, which is the skin. Further classification defines two sides of the scroll; front side (A) and back side (B). By side A we define the surface of the inorganic layer on which the text is written. The B side of the scroll is composed of skin; the outer surface is the hair-side of the skin. The inner sides of the inorganic and skin layers, which face each other between the layers, are termed (A\*) and (B\*), respectively. In summary, we define two layers and four sides (Figure 40);



**Figure 40: Nomenclature assignment of the layered TS material.**

In Figure 41 the optical micrographs of the TS2 fragment are presented. It shows a sandwich-like layered system, where on the back side (B) of the fragment, a part of the organic layer (skin) is missing. This gives us the opportunity to approach the inner side of the inorganic layer (side A\*) directly. The sample can be roughly characterized with two colors; the

slightly yellowish sides B and A\*, and a very bright ivory-colored layer on the text side A. The inorganic layer contains some cracks, which also expose the yellowish organic layer (Figure 41c). The B-surface, however, also shows some whitish colored regions, but they are not very intense nor consistent.



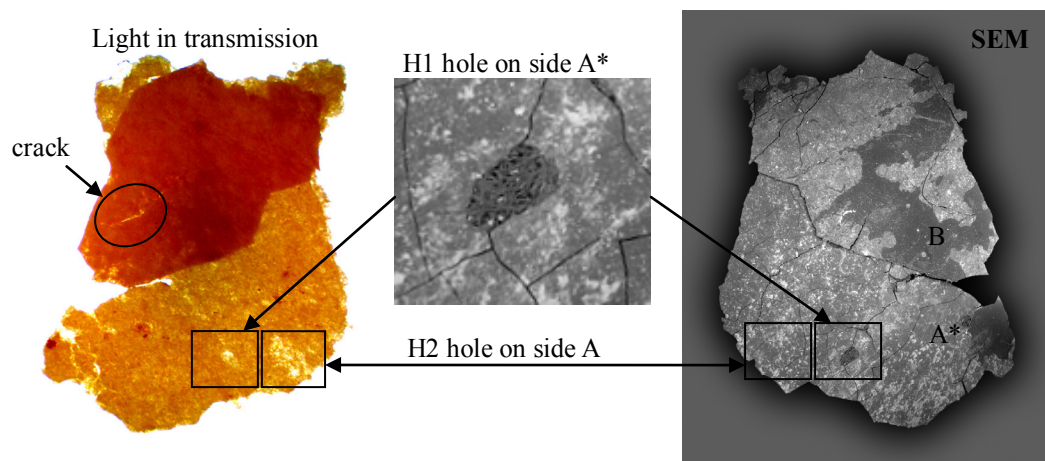
**Figure 41:** TS2 fragment; a) both, front text side (inorganic layer) and back sides (organic layer). The lower part of the organic backside layer is missing, the side A\*(inner side of the inorganic layer) appears instead. The areas P1 and P2 are presented in c) and d), respectively, whereas P2 is the cross section. b) The same fragment, but in transmittance. The thicker section with two intact layers appears darker.

The cross-sectional image at the edge in Figure 41-d shows the layered system of the fragment. The full thickness is about 100 μm, and this thickness is consistent throughout the whole length. The darker organic layer, which makes up 60% to 80 % of the full thickness, is less straight; it winds between the inorganic coatings. On side A, the inorganic layer is continuous, whereas on the back side B the inorganic material is used intermittently to fill topographic irregularities, creating a final product of uniform thickness from a thin parchment of uneven thickness.

Before reporting the XRF elemental maps, attention should be directed to three defect locations on the fragment: two holes (H1 and H2) and a crack in the inorganic layer that expose different layers that make possible the reconstruction of the elemental depth distribution inside the layered system. Figure 42 presents the defect locations on the fragment from both: A



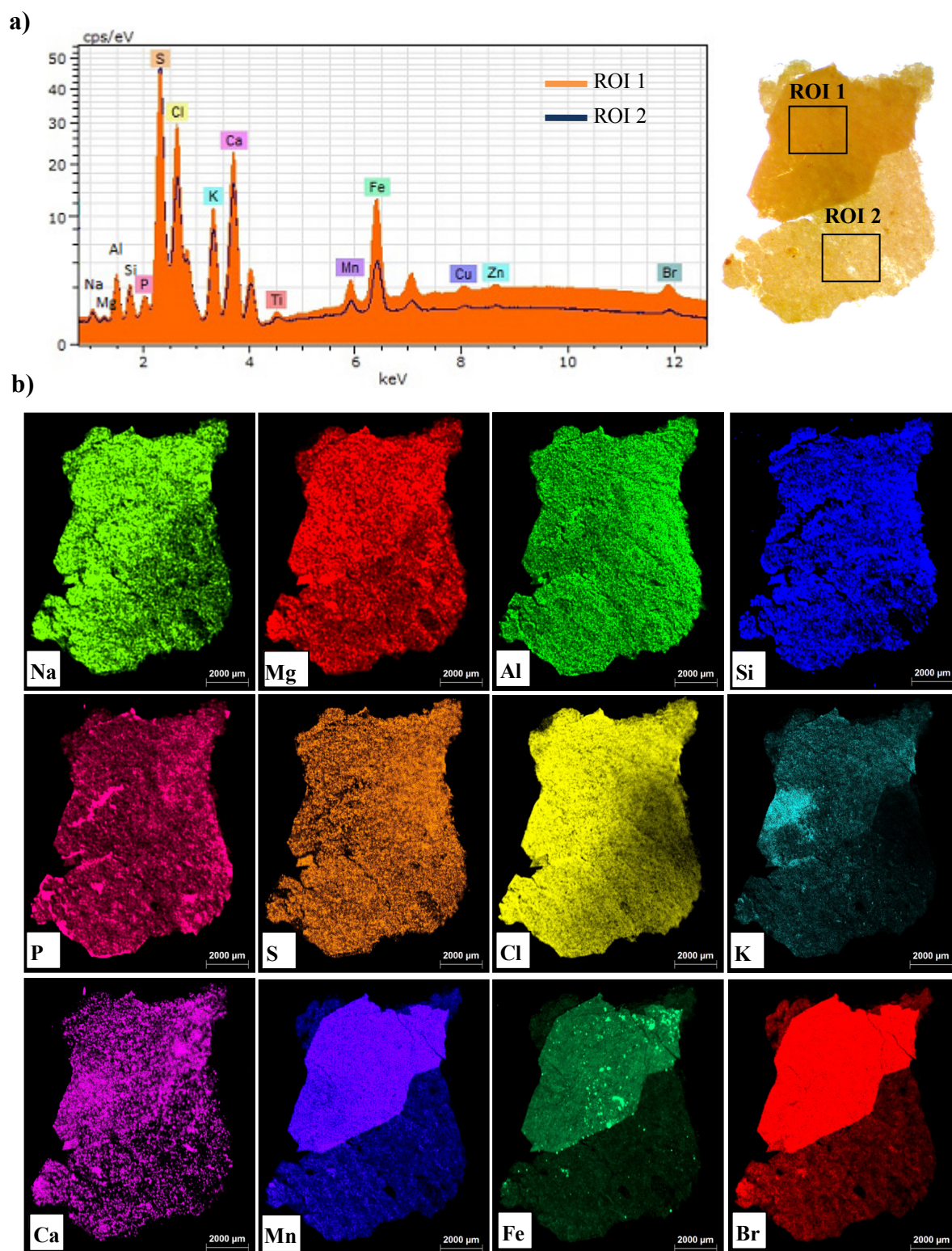
(transmission light microscopy) and B (scanning electron microscopy (SEM) sides. In the transmission light microscopy image of the front side A both holes H1 and H2 can be identified on the thinner section where a part of the organic layer is missing.



**Figure 42:** The Sample TS2 is presented from the front A-side with transmission light microscopy (left) and from its back B-side with a SEM image. H1 and H2 are two holes in the inorganic layer. H1 is present only on the inner side A\* and H2 can be observed only on the outer side A. These holes were helpful for reconstruction of elemental depth distribution, shown in Figure 43 and Figure 44. The crack is located on the inorganic outer layer, side A.

In the SEM picture in Figure 42 the H2 hole is not visible on the A\* side, indicating that the lacuna is only on the surface of the inorganic layer on side A. The depth from which secondary electrons are emitted for SEM topographic images is approximately 20nm in bone [213], which has a large component of collagen. As this technique is only sensitive to the near surface depth, and it clearly shows the H1 hole on the A\*-side with a typical collagen fiber structure behind it, it can be assumed that the H1 hole is present only on the sample surface on the A\*-side and not on the A-side. Our Raman measurements confirmed that the fibers inside the H1 hole are collagen, and that inorganic material covers the fibers on the front side A. This reveals that the lower part of the fragment is not a pure inorganic layer; some collagen fibers assumed to be from the organic layer remained embedded in the inorganic material after the organic layer was detached. These remaining collagen fibers were exposed to the environment and hence they gelatinized with the time forming a glossy film on side A\* covering the few other embedded collagen fiber. The crack also seen in the light transmission image in Figure 42 is located on the surface of the inorganic layer on side A.



$\mu$ XRF measurement of the front side

**Figure 43:**  $\mu$ XRF mapping of the front side (facing the inorganic layer on which the text is written) of the TS2 fragment. a) The spectra compare the upper, thicker part (ROI 1) with the lower, thinner part (ROI 2) of the fragment; a micrograph from Figure 41b is used for clarity. b) The elemental distribution maps of the 12 most evident elements are presented. For larger images in grey scale see also S 1 in supplementary materials.



### $\mu$ XRF measurement of the back side

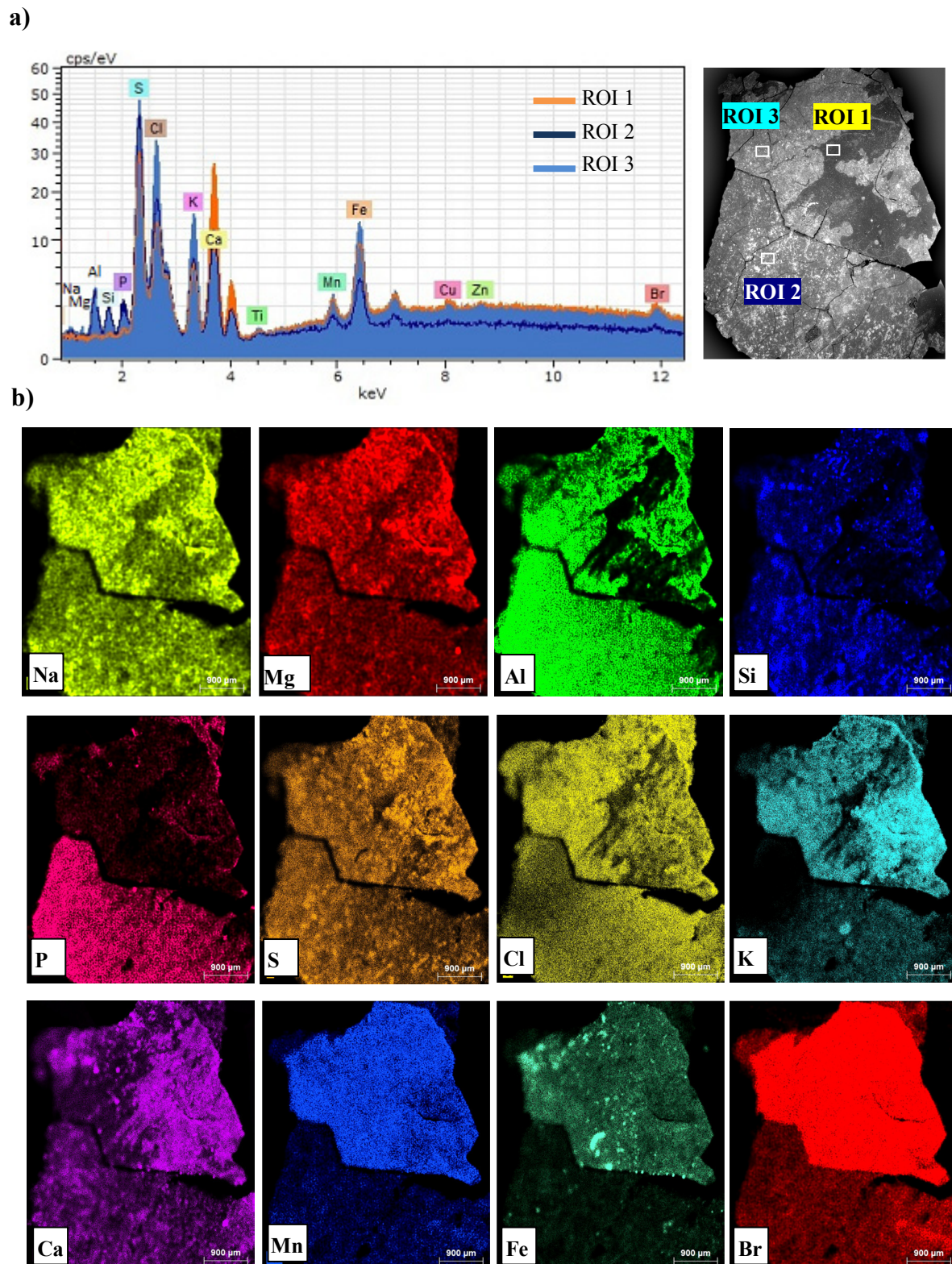


Figure 44:  $\mu$ XRF mapping of the back side of TS2 fragment. a) Spectra of three different ROIs are presented together with b) the elemental distribution maps. The SE micrograph on the right side of a) is used for clarity.



SEM EDX - front side

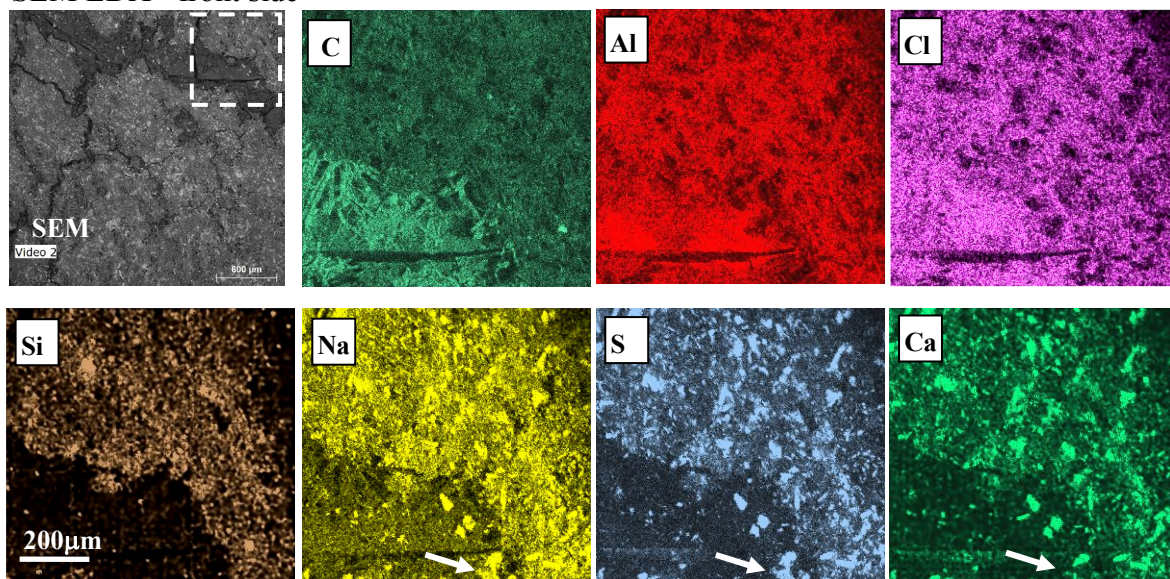


Figure 45: EDX elemental maps of the area with a crack on the front side (inorganic layer) of the TS2 fragment. It shows particles in the inorganic (carbon-poor) region consisting of Na, S and Ca. Si is also present in the inorganic layer, but not in the particles. Al and Cl were found with higher concentration in the organic material, and also between these particles. The arrows show the presence of some elemental clusters where the particles contain only Na and S but only little Ca. Other particles with only Ca without Na and S were also identified.

SEM EDX - back side

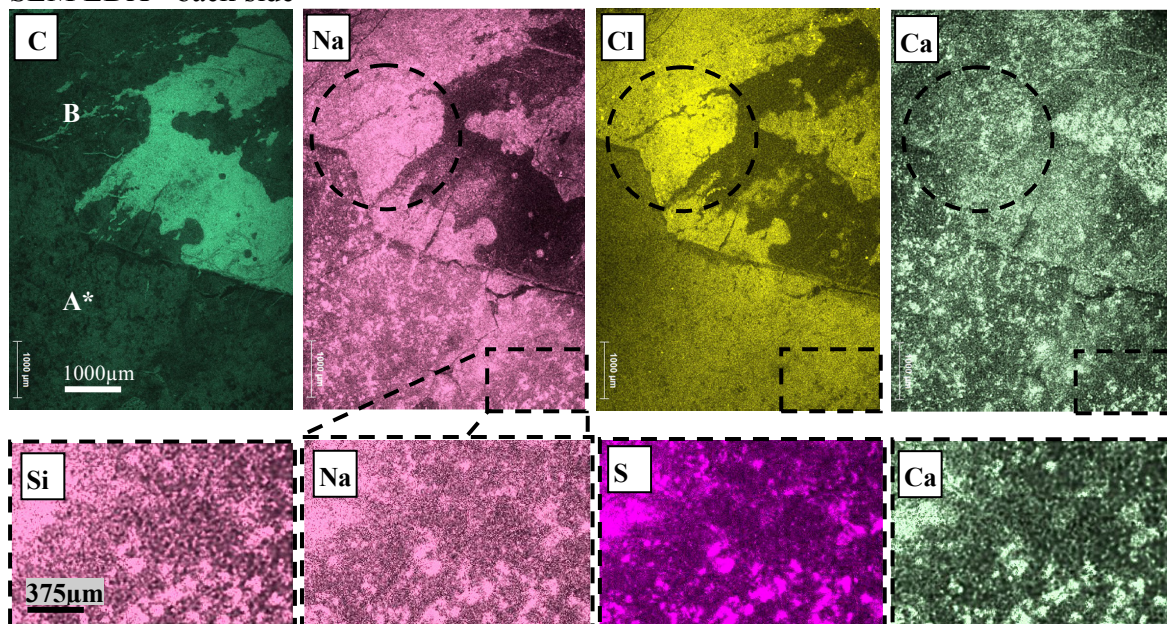


Figure 46: EDX elemental maps of the back side of the TS2 fragment. The maps show that Na origin from two different sources; 1) in the upper part (B-side); Na correlates with Cl but not Ca, probably NaCl (dashed circle). 2) in the lower part (A\*-side); Na can be found in particles containing Na, S, Ca and Si. The presence of Si inside the particles here (A\*-side) differs from the particles found on the front side A. It is also noteworthy to highlight that the area with very high C-concentration on (B) is most probably an adhesive, for example from post discovery treatment, although topographically it could not be confirmed with optical microscopy.

We performed a full area scan by  $\mu$ XRF (Tornado, Bruker instrument) on the front and the back sides of the fragment. The sum spectra of some Regions of Interests (ROI's) are presented together with the elemental (K-lines) distribution maps in Figure 43 and Figure 44. For larger images in grey scale see also S 1 in supplementary materials. Elements were excited through the entire sample thickness. However, elements with lighter atomic masses were detected only from the near surface depth because of the absorption.

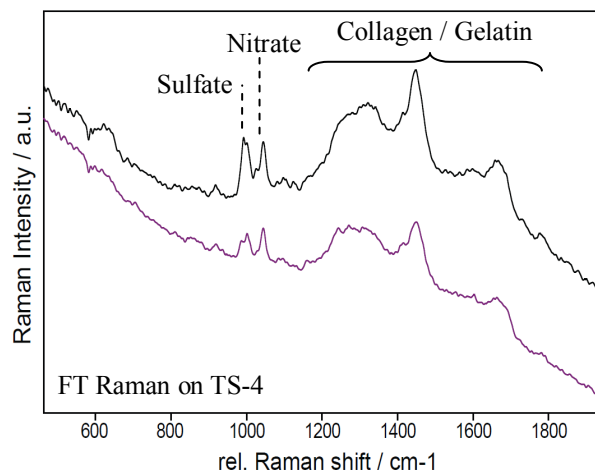
Additionally, the sample was measured by means of SEM-EDX. Due to very high lateral resolution and the relatively short depth penetration of the electrons, this technique allowed for the collection of elemental identification from only the near surface depth, and also identified distinct surface particles. The elemental maps of magnified areas of some ROIs are shown in Figure 45 and Figure 46. Reconstruction of the elemental depth distribution and the assignment to distinct material layers are done in Table 3 in the discussion of this chapter.

The SEM and XRF studies provide a clear picture of the elemental composition, but do not provide information about the molecular nature of the compounds on the TS fragments. To explore the molecular composition of the elements that can be found in the inorganic layer and in the collagen fibers, vibrational spectroscopy such as Raman and IR can be applied. In combination with mapping, vibrational spectroscopy methods provide information on both the molecular composition and distribution on a sample surface. Raman offers the advantage of a backscattered experimental geometry, and a less invasive approach, since no sampling is required. These characteristics make Raman spectroscopy the first choice for rare objects of cultural heritage value.

The drawback with analyzing ancient materials with Raman is the often strong fluorescence that appears if Raman scattering is excited near electronic transition. The fluorescence intensity can be several magnitudes higher than the weak Raman spectrum, making the Raman spectrum impossible to measure. This was the case for almost all materials found in Qumran, including the scrolls. The origin for the strong fluorescence in the scrolls can be associated with impurities and material degradation, but also be attributed to agents such as tannins that could have been used for skin treatment during the manufacture. The TS was a surprisingly exception, as it exhibited less fluorescence in the Raman spectra if a lens with high depth resolution (100x, NA=0.95) was used, thus reducing the spot size of the confocal probing volume in order to separate from the fluorescing spots in the close vicinity.

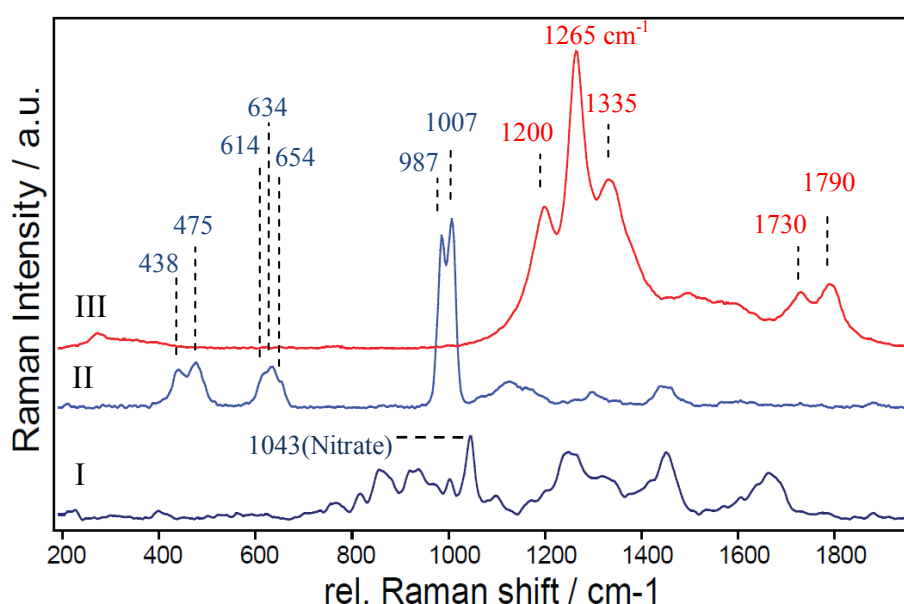
However, before focusing and magnifying particular regions of interest on a  $\mu$ m scale, we needed to know the Raman spectrum of the full sample material averaged over the macro-

scale. Unfortunately, fluorescence became an issue for the TS as well. For that reason we analyzed a TS fragment by means of FT-Raman, using a 1064 nm excitation wavelength, and a spot size of 400  $\mu\text{m}$  in diameter. The use of such a low excitation energy significantly reduced the fluorescence but the measurement lacks in spatial resolution (Figure 47).



**Figure 47: FT-Raman@1064 nm spectra of two regions of a TS4 fragment measured on the front side (text side: A). The spectra are representative of the whole fragment due to the large spot size (400  $\mu\text{m}$  in diameter) of the laser on the sample. It shows three main components: a double peak of sulfate at 987 $\text{cm}^{-1}$  and 1003  $\text{cm}^{-1}$ , a nitrate peak at 1044  $\text{cm}^{-1}$  and the typical proteinoeous contribution of collagen or gelatin.**

The Raman spectrum identifies strong peaks in the sulfate region (at 987  $\text{cm}^{-1}$  and 1003  $\text{cm}^{-1}$ ) and nitrates (at 1044  $\text{cm}^{-1}$ ). The rest of the spectra can be assigned to a proteinoeous tissue, i.e. collagen or gelatin, including the C-H peaks around 3000 $\text{cm}^{-1}$ .



**Figure 48: Confocal Raman@785 nm spectra of TS-2. I: Collagen spectrum; collagen fibers in all TS 2 – 4 fragments always contain a nitrate peak at 1043  $\text{cm}^{-1}$ . II: Sulfate spectrum of particles with Na, S and Ca constituents (Figure 45). III: Unidentified particles spread in the inorganic surface layer (Figure 50c), its Raman signal is very resonant at 785nm laser excitation.**



By means of confocal Raman spectroscopy in the NIR region using a 785 nm laser, we focused on specific non-fluorescent regions of interest of about  $2\text{ }\mu\text{m}^3$  probing volume in the fragment, and localize the findings of FT-Raman measurements. The main results are presented in three spectra in Figure 48.

Below are further detailed descriptions of the confocal Raman spectra I, II and II of Figure 48.

#### **Spectrum I - Collagen Fibers:**

We collected spectra from collagen fibers in the big crack on side A, as well as inside the H1 hole of side A\* and at the edges of the TS2 fragment. All measured collagen spectra contained a nitrate peak at  $1043\text{cm}^{-1}$ , which can be associated with the  $\nu_1$  of  $\text{NH}_4(\text{NO}_3)$  [214, 215]. A representative collagen graph is presented as spectrum I in Figure 48. Exposed organic regions were also observed on the B side, but those regions fluoresced in the confocal Raman spectrum, and hence no spectra could be obtained. However, the nitrate peak was identified in all collagen spectra of TS 2 – 4 fragments. Only the collagen powder TS-5 was not characterized by the nitrate signal. Unfortunately we could not obtain collagen spectra of the TS-1 fragment from the inner part of the scroll. Hence we cannot say whether it contained nitrate or not. In any case, nitrate was not detected in the inorganic layer when collagen was not also present in the Raman spectra.

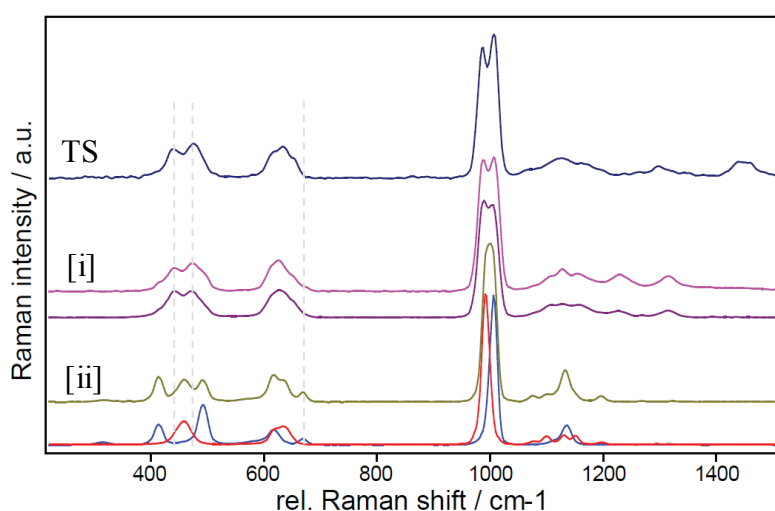
#### **Spectrum II – Na,S,Ca particles:**

Spectrum II is associated to “Na, S, Ca” particles as identified in Figure 45 and Figure 46 of the inorganic layer on sides A and A\*. It shows a sulfate ( $\text{SO}_4^{2-}$ ) spectrum with two main peaks. The intensity ratio of these peaks varied from case to case throughout the TS fragment, as did their spectral position by  $\pm 3\text{ cm}^{-1}$ . Comparison with glauberite ( $\text{Na}_2\text{Ca}(\text{SO}_4)_2$ ) and other related reference spectra from the database of minerals: [www.RRUFE.info](http://www.RRUFE.info), and air dried, self-prepared, aqueous mixtures of  $\text{CaSO}_4$  and  $\text{Na}_2(\text{SO}_4)$ , did not provide satisfactory matches with the TS-“Na, S, Ca” particle spectra. The measured Raman spectra of the pure air dried aqueous mixture of calcium sulfate can be related to gypsum ( $\text{CaSO}_4 \cdot 2\text{H}_2\text{O}$ ) rather than to less hydrated bassanite and anhydrite [216]. Hydrated sodium sulfate found as mirabilite ( $\text{Na}_2\text{SO}_4 \cdot 10\text{H}_2\text{O}$ ) is metastable and turns easily into thenardite ( $\text{Na}_2(\text{SO}_4)$ ) in dry air.

Particularly the Raman peaks of the air-dried, synthetic  $\text{Na}_2(\text{SO}_4)$  and  $\text{CaSO}_4$  aqueous mixture located around  $450\text{ cm}^{-1}$  and  $630\text{ cm}^{-1}$  differ from the TS spectrum II. However, drying

this synthetic mixture by fast evaporation on a heating plate set to 250°C resulted in different material formations showing higher variety among the measured Raman spectra (measured at ambient conditions), some of these Raman spectra were very similar to the TS Raman spectrum.

Representative spectra of both dried synthetic samples are presented in Figure 49: [i] Raman spectra from the mixture, which was fast dried by heating and [ii] slow air dried at room conditions. The Raman and the XRD results, which will be presented next, refer to measurements performed at ambient room conditions ( $\sim 25^{\circ}\text{C}$ ,  $\sim 45\%$  RH).



**Figure 49: Confocal Raman@ 785 nm. Comparison between TS and a mixture of synthetic  $\text{Na}_2(\text{SO}_4)$  and  $\text{CaSO}_4$ .** [i]: the two spectra are from the synthetic mixture after fast drying by evaporation on a heating plate set to 250°C. They are in agreement with the TS “Na,S,Ca”-particles. [ii]: three representative spectra are shown from the same synthetic mixture dried slowly at room temperature. The upper measured spectrum (green) is a superposition of pure  $\text{Na}_2(\text{SO}_4)$ -(red) and  $\text{CaSO}_4 \cdot 2\text{H}_2\text{O}$ -(blue) measured in the same air-dried mixture.

The spectra presented in Figure 48 (I and II) are statistically the most common and representative because they are in agreement with the average shown by FT-Raman measurements in Figure 47. In some rare cases, other spectra were identified on the micron scale. For instance, some Ca particles without Na and S constituents that were identified in SEM-EDX elemental maps, generated a calcite Raman spectrum. In one other case, a Ca-poor (low Ca concentration) particle was found between the collagen fibers (marked by an arrow in Figure 45), that produced a Raman spectrum with a high concentration of nitrate with  $\nu_1$  at  $1047\text{ cm}^{-1}$  and  $\nu_2$  at  $720\text{ cm}^{-1}$ . It is possible that the nitrate was in the vicinity of the Ca-poor particle with S and Na, and was not part of the particle structure. In the discussion of the TS material

composition and the possible reconstruction of its manufacturing technology, only the characteristic average spectra will be considered because they represent the most reliable data.

Additionally, various other synthetic mixtures of sulfates and nitrates were prepared and compared to the TS spectrum by Raman and XRD. These results did not lead to a fully satisfying agreement with the Temple Scroll inorganic layer data. To completely identify all the original compounds present in the TS inorganic layer, we plan further systematic studies of natural and synthetic materials prepared in the lab. Our preliminary comparison with some reference and synthetic materials provides a baseline for future investigation with the aim to precisely reconstruct the manufacturing procedure of the TS.

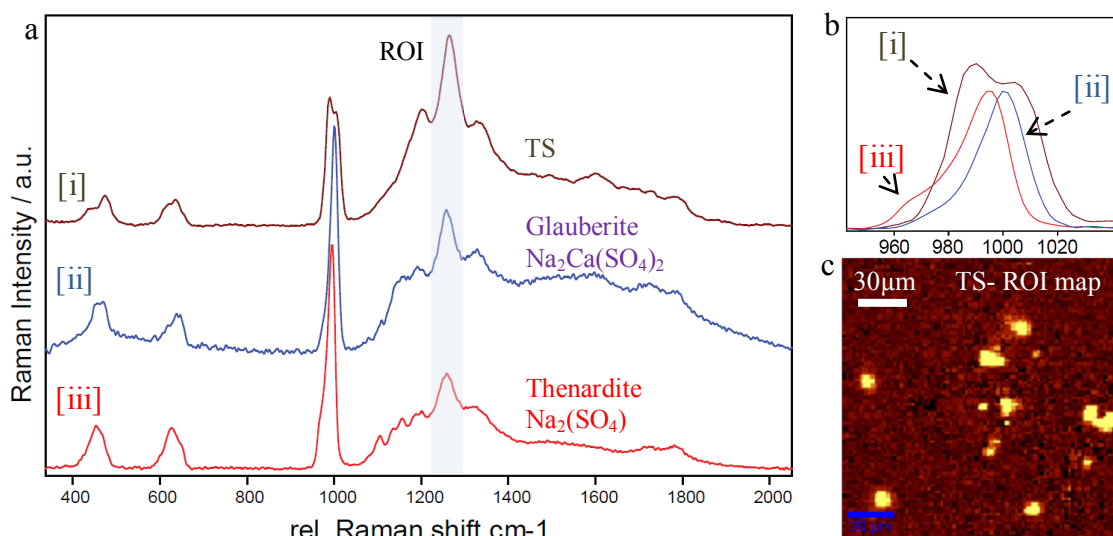
### **Spectrum III – Unidentified particles:**

Spectrum III (Figure 48) belongs to small particles or clusters of about 5 to 15  $\mu\text{m}$  in diameter that have been found spread over the inorganic layer (accessible from side A or A\*). These particles generated a very resonant Raman behavior to the 785 nm laser, which made it possible to perform a Raman imaging with a very low laser intensity that would not harm the TS fragment (Figure 50c).

These particles could not be assigned by a precise elemental composition so far. They are referred to as “Na<sub>2</sub>-X” particles because after studying all relevant mineral spectra from the database [www.RRUFF.info](http://www.RRUFF.info), only two spectral examples of sulfates that contained Na (thenardite and glauberite) showed the same spectral peaks as presented in Figure 50a. Furthermore, it was identified in one “Na,S” particle (without Ca) on the TS, which is marked by arrows in Figure 45. This confirms that Na and not Ca is the predominant element that is involved in this Raman vibration.

The „Na<sub>2</sub>-X“ spectrum could be found in one example of glauberite (Na<sub>2</sub>Ca(SO<sub>4</sub>)<sub>2</sub>) and in other example of the thenardite (Na<sub>2</sub>(SO<sub>4</sub>)) reference spectra in the RRUFF database. Other examples for glauberite and thenardite from the RRUFF database do not have the same “Na<sub>2</sub>(SO<sub>4</sub>)-X” spectral components. This may be due to differences in particular geological formation processes, which either forms under specific circumstances and hence can be found only in particular regions, or may be due to specific impurity in the database samples and the TS inorganic material.





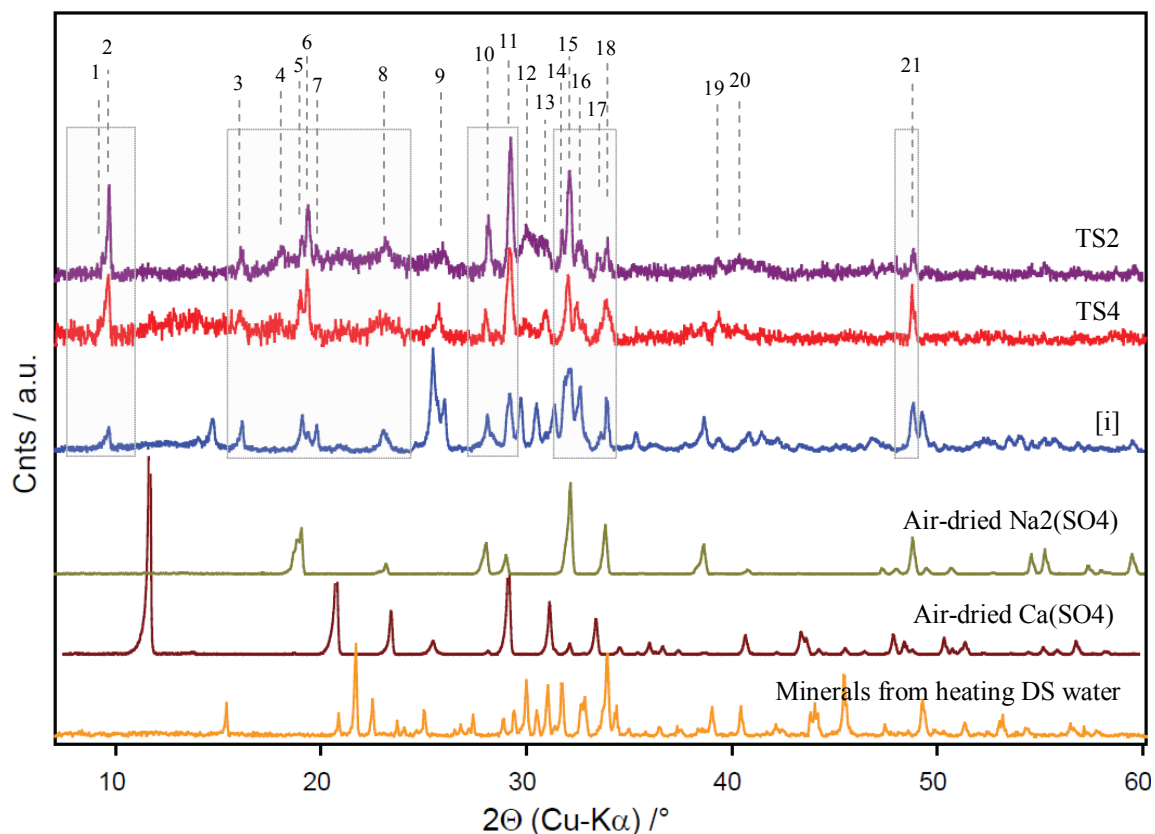
**Figure 50:** a) Raman @ 785 nm, the resonant spectrum of “Na<sub>2</sub>-X” particles measured in the TS [i] (compare with spectrum III in Figure 48) could be found in two examples of a sulfate spectra from the Raman database “RRUFF”; glauberite [ii] and thenardite [iii], with common components 2 Na<sup>+</sup> and (SO<sub>4</sub>)<sup>2-</sup>. The “Na<sub>2</sub>-X” spectra could not be matched with any other sulfate spectra in the database or in the synthetic mixtures including other glauberite and thenardite spectra from the “RRUFF” database. b) Zoom of the main sulfate peak. The TS sulfate material differs from the two reference spectra (thenardite and glauberite). c) Confocal Raman map shows the distribution of the ROI around the 1365 cm<sup>-1</sup> peak of the “Na<sub>2</sub>-X” particle in the inorganic layer.

Figure 50b shows that the  $\nu_1$  sulfate peaks of glauberite and thenardite from the database do not coincide exactly with the sulfate peaks of the TS. Although “Na<sub>2</sub>-X” was not observed in the average spectra of the FT-Raman measurement (Figure 47), we still can say it is very much representative and characteristic of all the fragments from the main body of the scroll (TS1-5) that we measured. Its typical distribution is presented in the measured Raman map in Figure 50c. The reason why it was not present in the average spectra of FT-Raman but observed clearly with confocal Raman @ 785 nm is that this material is resonant at the 785 nm excitation, and hence shows a high enhancement in this measurement condition.

It should be noted again that the spectrum [i] in Figure 50a is a mixture of two different materials that were found also separately in the TS (see also in Figure 48). One material contains sulfate, and the other belongs to the “Na<sub>2</sub>-X” material. Both of them also appeared independently in the sample.

In the next step of the investigation, XRD patterns of TS fragments with similar inorganic materials and synthetic mixtures as discussed previously (Figure 51) were compared. The

aqueous mixture of  $\text{Na}_2(\text{SO}_4)$  and  $\text{Ca}(\text{SO}_4)$  that was dried by heating (boiling) [i], offers the best match with the TS XRD pattern. The air-dried, pure  $\text{Na}_2(\text{SO}_4)$  was also identified in the TS diffraction pattern.

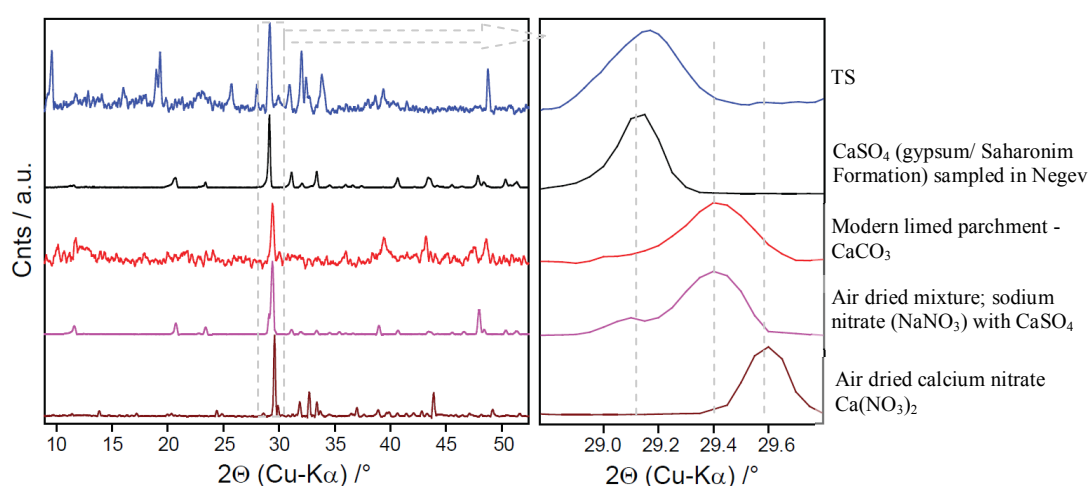


**Figure 51:** XRD measurements of two different TS samples (TS 2-4) show that they have the same material composition. Pattern [i] is an aqueous mixture of  $\text{Na}_2(\text{SO}_4)$  and  $\text{Ca}(\text{SO}_4)$  that was fast dried by heating (boiling). Its diffraction pattern is in agreement with many peaks from the TS. It is the same material described in Figure 49[i]. Pure, air-dried  $\text{Na}_2(\text{SO}_4)$  and  $\text{Ca}(\text{SO}_4)$  are also presented. The spectrum obtained from the minerals resulting from drying by boiling Dead Sea water (lowest/orange spectrum). TS peak assignment: (1):9.3°, (2):9.6°, (3):16.1°, (4):18.1°, (5):19°, (6):19.3°, (7):19.8°, (8):23.1°, (9):25.9°, (10):28.1°, (11):29.2°, (12):30°, (13):30.9°, (14):31.8°, (15): 32.1°, (16):32.6°, (17):33.5°, (18):33.9°, (19):39.3°, (20):40.4°, (21):48.8°.

Furthermore, minerals produced by evaporation of the water from the Dead Sea (DSS) by heating (boiling) were analyzed by XRD. The diffraction pattern of DSS shown in Figure 51 does not match well with the TS diffraction pattern. Although some components of the polycrystalline minerals formed by evaporated Dead Sea water may coincide with some TS peaks, the coincidence is not substantial enough to make the argument that they match the TS pattern.

Peak matching using the highest intensity powder XRD peak is useful for samples composed of many minerals, as the smaller peaks may not be detected with high background

noise, and are difficult to distinguish between different minerals. Peak number 11 at  $29.2^\circ$  ( $2\theta$ ) is the strongest in the TS diffraction pattern, but it is not the strongest peak in the most similar, synthetic reference spectrum [i] in Figure 51. While, peak intensity can also be a function of sample preparation (preferred orientation) and crystal shape (a long crystal along a particular axis), the strongest peak of the TS pattern could also represent another material addition. We addressed this question by comparison with other relevant reference spectra that showed a strong scattering peak in the region of peak number 11 in, Figure 52. A list of the minerals whose spectra could be relevant (Figure 52):



**Figure 52:** The strongest XRD diffraction peak of the TS at  $2\theta = 29.2^\circ$  (No. [11] in Figure 51) is compared with other relevant reference spectra that showed a primary (higher intensity compared to the rest of the spectrum) scattering peak in the region of No. (11): 1)  $\text{CaSO}_4 \cdot 2\text{H}_2\text{O}$ : gypsum from the natural Saharonim formation that was sampled in the Negev (Israel). 2)  $\text{CaCO}_3$ : calcite in modern limed parchment. 3) Air dried mixture of mainly sodium nitrate  $\text{NaNO}_3$  with  $\text{CaSO}_4$  addition. 4) Air dried calcium nitrate  $\text{Ca}(\text{NO}_3)_2$ . The right graph (zoom) shows that TS peak No. (11) can be assigned to this naturally formed gypsum ( $\text{CaSO}_4 \cdot 2\text{H}_2\text{O}$ ).

- 1)  $\text{CaSO}_4 \cdot 2\text{H}_2\text{O}$  gypsum from the natural Saharonim formation that was sampled in the Negev.
- 2)  $\text{CaCO}_3$  calcite in modern parchment that was treated with lime.
- 3) Air dried mixture of mainly sodium nitrate -  $\text{NaNO}_3$  with  $\text{CaSO}_4 \cdot n\text{H}_2\text{O}$  addition.
- 4) Air dried calcium nitrate  $\text{Ca}(\text{NO}_3)_2$ .

Given the detection of nitrate from Raman measurements, its presence in the diffraction pattern of the TS would be expected. However, the primary TS No. (11) peak matches with naturally formed gypsum (Figure 52 -right graph). In conclusion, in the XRD results as presented in Figure 51 and Figure 52 sodium and calcium sulfates can be identified individually as well as in a specific form of a conjoined formation.

### **5.3 Discussion**

2000 years is a significant age, especially for an organic, biological material such as ancient parchment. In such a time period, several molecular changes can take place such as: deterioration of polymer network, other chemical transformations, and/or uptake of foreign elements from the environment. The remaining traces of the production process evident in the Scroll, the influences from the Scroll usage, and the storage time in the caves are all very important aspects to be distinguished from the post discovery treatment and all of these aspects need to be considered in the analysis. The post discovery treatments are not always well-documented, but can sometimes be confounded with the historical information available within the material or even destroy it. When we study these ancient materials, we need to be aware of all the variety of possible influences when the results are interpreted. Moreover, another important aspect to consider is how much a point measurement represents the whole sample/fragment of the scroll, how many fragments are required to represent the whole scroll? Only a combination of results from several experimental methodologies allows for a proper interpretation of the analytical results. During our investigations, we were frequently forced to review our previous conclusions according to newer results. In other cases, some of our material evidence did not confirm previous findings by archaeologists or scholars, which are not less important than analytical, measured values. The reconstruction of historical processes has to consider aspects from all scientific fields. This research is comparable to detective work, requiring sophisticated judgment of all evidences.

It therefore was essential for the investigation to apply several complementary noninvasive techniques, which could reveal the information of elemental distribution and its molecular arrangement on a pointwise microscopic but also on a higher average macroscopic scale. We started with important fragments from the inner part of the Scroll, which have written letters

on its surface; TS1 (Table 2, Figure 2). The first observation of the TS parchment by means of light microscopy, SEM and XRF measurements revealed a layered system of at least two layers; one is organic and the other consists mostly of foreign inorganic components, the most prominent of them being S and Ca (Figure 2). In those few single spot measurements we identified Al and K as well. Hence our first assumption was that the inorganic layer could consist of gypsum and K-alum. It is known that K-alum has been used in parchment treatment since the Middle Ages. The Raman measurements revealed the presence of sulfates with two  $\nu_1$  peaks that nearly coincide with those of gypsum and K-alum.

This Raman result confirmed our first assumptions, which were presented at the ICOM-CC (Roma) in 2010 [217]. However, these conclusions, which were based on a few single spot measurements, needed to be tested on other parts of the scroll. For example, further analyses that provide information of higher material average and distribution, such as elemental mappings, were required. These further analyses are presented in the results section, and will be discussed further down. In summary, these results disproved the first assumptions about the presence of K-alum in the inorganic layer.

The identification of nitrates that were identified on TS fragments from the outer part/edge of the scroll (TS 2-4) but not on those of inner part (TS-1 and TS-5) also needed verification with further analysis. Because we found it only on fragments from the outer parts our first assumption was that the origin of the nitrates could be the environment where the TS was stored: the cave No11, which is inhabited by bats. The new results expanded the possibilities of possible nitrate signal interpretations and sources, and will also be discussed in a proceeding section.

A further important observation was that the text was written on the inorganic layer of the scroll, which covers the collagen fibers of the flesh side of the skin. The normal thickness of parchments found at the Dead Sea measure 200 to 300  $\mu\text{m}$ , but the TS is abnormally thin; only 100  $\mu\text{m}$  including both layers (Figure 41d). This TS thickness is an indication of a split parchment. With the current results, we will address with more detail the question arising from the uncommon observation of writing on the flesh side of the scroll, and the question of a split parchment.

The strategy of comparing results from different methods is required in order to reconstruct the material composition of the layered parchment. In another technique, we applied PIXE in an atmospheric environment. This technique provides simultaneous information of heavy and light elements. The applied beam spot was up to 1.5 mm in diameter, and hence a good spatial

average could be achieved. PIXE measurements that were obtained from the TS1 fragments (spectra are not presented here), confirmed the presence of S and Ca as it was evident from XRF measurements. However, this technique also identified the presence of the lighter elements Na, Mg, Al, Si, and P. Furthermore, Cl, Fe and Br were also identified in the PIXE spectra.

Recently the Cl/Br concentration ratio inside ancient parchments was used in order to address the question of provenance of the parchment used for the DSS [218]. The production of parchment involves intense treatment with water at different steps. The high concentration of Br in the DS water leads to an approximately 7 times lower Cl/Br ratio compared to normal seawater [219, 220]. These elemental traces remain in parchment and reveal information of its potential processing origins. The PIXE analysis, however, was not quantitative, and not appropriate for determination of the Cl/Br ratio. Moreover, the Cl and Br were differently presented within the complex, layered TS, and hence they could have different sources of origin within the scroll.

For further analyses, we used the less “precious” fragment TS2 (Figure 41) from the edge without letters in order to address the question of elemental distribution (including light elements) by means of SEM-EDX and XRF mapping in a low pressure environment (Figure 43 – Figure 46). For larger images in grey scale see also S 1 in supplementary materials. A low pressure environment allowed for the study the lighter elements, but could also induce high stress on the collagen through dehydration as shown in Chapter 2.

For the reconstruction of the elemental depth distribution, some marks (holes and cracks) were identified on the layers (Figure 42). The detailed discussion of all the individual elemental distributions is presented in Table 3. In the conclusion we will consider some of the elemental distributions that assisted us with building a reconstruction model of the TS manufacturing procedure. The elemental maps revealed that the main source of Cl appears to be accompanied by an even Na distribution (Figure 43 and Figure 46-circle), which most probably originates from a treatment involving a NaCl (halite) solution. However, the Na distribution also appeared independently from Cl in distinct particles in the inorganic layer. The inorganic layer contains mainly “Na-S-Ca” particles (Figure 45) on the outer side A, and “Na-Si-S-Ca” particles (Figure 46) on the inner side A\* that is in direct contact with the organic parchment (skin) layer.

**Table 3: Notes about the elemental distribution in the TS2 fragment as revealed by means of  $\mu$ XRF - and EDX mapping in Figure 43 - Figure 46 and S 1 in supplementary materials.**

<p><b>Na:</b> Sodium was identified on all the sides of the layers that are accessible on this fragment; A, A* and B. It appears in two forms; both strongly pronounced and distinct particles found in the inorganic front layer accessible from sides A and A*. On side A these particles contain S and Ca (Figure 45) but on A* they contain Si as well (Figure 46). Beside the distinct particles, Na shows also a smooth distribution that correlates to the Cl distribution, especially on B (Figure 46, dashed circle). The latter is an indication for NaCl salt solution that was used for a treatment independent from the inorganic material.</p>
<p><b>Mg:</b> Magnesium cannot be assigned to a distinct layer. On one hand its XRF elemental map in Figure 43 (S 1 in supplementary materials) clearly shows much less magnesium in the H2 hole on side A, which means it is present in the front inorganic layer. On the other hand, the map does not depict the crack in the inorganic layer on the upper part of the fragment.</p>
<p><b>Al:</b> Aluminum can hardly be assigned to one specific layer as well. It was more present among the gelatinized collagen on side A* than inside the inorganic materials on side A, because the intensity inside the crack is definitely stronger, and the H2 hole is not recognizable in the XRF elemental map (Figure 43 or S 1 in supplementary materials). The only region where aluminum is not detected is the ROI 1 in Figure 44, which is a carbon-rich region on the back side B. The high C-concentration in this region is shown by means of SEM-EDX in Figure 46. Aluminum is a light element, and hence it can be observed only from near surface layer. It is possible that in this region, a foreign adhesion (additional layer) that covers the surface of the original fragment (post discovery?) is present, although topographically it could not be confirmed via optical microscope. Furthermore, with low statistics, the aluminum K-line cannot be easily distinguished from the L-line of bromine. Therefore a mixture of both Al and Br could be presented in the Al map.</p>
<p><b>Si:</b> Silicon provided a strong signal from the inorganic layer on side A. The crack and the H2 hole clearly lacked Si-emissions in the Si-elemental map in Figure 43 (S 1 in supplementary materials). The SEM-EDX elemental distribution of side A shows that Si never coincided with the distinct Na-S-Ca particles (Figure 45). However, contrary to side A, Si was definitely also a component of the Na-S-Ca particles on the A* side, as can be seen in Figure 46. This was confirmed by the appearance of the hole H1 on the back side in Figure 44, which means that the source of the Na-Si-S-Ca particles signal lies mostly inside or very close to the gelatinized collagen on side A*, whereas Na-S-Ca particles can be found on side A distinct from the Si particles surrounding them.</p>
<p><b>P:</b> Phosphorus was measured most on the organic inner sides A* and B*, as it was clearly detected through holes and cracks on side A in Figure 43 (S 1 in supplementary mat.). Figure 44 confirms this from the back side, where P is present on side A*, and not on side B. Interestingly, H2 exhibited no P-signal, although A* should be exposed there. A possible explanation is that organic surfaces that were not directly exposed to the environment for a long time contain more phosphorus than the surfaces exposed to the environment (outer sides A and B). Somehow, environmental exposure could have reduced the P-content. This would suggest that the material in the H2 hole was exposed to the environment a very long time ago.</p>
<p><b>S:</b> Sulfur was co-located with the same layers as silicon, especially in the inorganic layer on side A but also on side B. On side A it was present in the Na-S-Ca particles, and on A* it was present in Na-Si-S-Ca particles. On side B, sulfur does not show a consistent association with Ca in all regions, but it is sometimes associated with it.</p>

**Cl:** Chlorine was co-located with the gelatinized collagen on side A\*, it results from the pronounced H1 hole that appears on the front side. Cl transmits through the inorganic layer (Figure 43 or S 1 in supplementary materials) without depicting the structure of the inorganic mixture. It is generally accompanied by the even distribution of Na as indicated by the dashed circle in Figure 46 (see discussion for Na). The even distribution indicates a treatment of the skin in a NaCl salt solution, which penetrates into the collagen on both sides of the skin. No NaCl was identified in the inorganic mixture.

**K:** The presence of potassium is inhomogeneous; it appears also in clusters of high concentration (Figure 43 or S 1 in supplementary materials). However, on the back side B (Figure 44), one could find it in all regions. The exception is again the area with the assumed foreign adhesion. Since the H1 hole was also evident from both sides, but not the H2 hole, K was associated with the organic material.

**Ca:** Calcium was present in all layers. On sides A and A\*, it appeared mostly within particles consisting of Na-S-Ca and Na-Si-S-Ca, respectively (Figure 45, Figure 46). Some regions that showed calcium separately from Na, S or Si could be identified mostly on side B. In any case, side B did not reveal a consistent and homogeneous inorganic material distribution. The inorganic material on side B did not show common origin with the inorganic front layer.

**Mn:** Manganese distribution can hardly be assigned to a particular layer or depth; It's XRF distribution map depicted both wholes, which means that Mn is present in both layers. The intensity in the thicker upper part that consists of all layers was higher than in the thin lower part (Figure 43 or S 1 in supplementary materials and Figure 44), which consists mostly of the inorganic layer and some residual of collagen. The contrast in the map between the two parts, however, seems to be disproportionately high compared to the thickness difference. This suggests a higher Mn-concentration in the organic part rather than in the inorganic. However, it is not possible to estimate the material density and the exact thickness of these two regions that would be needed for quantitative conclusion. The other indication for its presence in the organic part rather than in the inorganic was the missing structural border between ROI-1 and ROI-3 on surface B (Figure 44). Since the inorganic material on the B surface was very inconsistent and inhomogeneous regarding its elemental composition (see Figure 44 and Figure 46), the border line should be clearly pronounced. The Mn- distribution is however, very even and homogeneous. Furthermore, the only pronounced structural intensity contrasts are caused by the cracks in the organic (skin) layer. (Figure 43, Figure 44). In any case, the intensity contrast pattern coincides very much with those of Fe and Br.

**Fe:** The presence of iron has two sources; one is regularly distributed and corresponds with Mn and Br throughout the entire fragment, with higher concentration in the organic parts. The other source are the distinct Fe-particles, mostly located on side B.

**Br:** Bromine distribution follows the same pattern as Mn and the even distribution of Fe that were mostly present in the organic skin layer as described above (see: Mn). These elements are present in higher concentrations in Dead Sea water compared to normal sea or ground waters [221-225]. The smooth NaCl distribution was also co-located with the organic skin. This could suggest a skin treatment with the Dead Sea water before the inorganic layer on the front side (text side) was applied.



FT-Raman measurements deliver the information of molecular composition on a macroscopic scale, which provides a representative average (Figure 47) of the fragments. Beside collagen, the spectra also showed the presence of two sulfate peaks and a nitrate peak. Using the confocal Raman with a 785 nm laser with a probing volume of only few microns, the sulfate and nitrate were localized inside the material, as shown in Figure 48 – II and I, respectively. The spectral position of the nitrate peak in collagen fibers corresponds to the  $\nu_1$  of ammonia nitrate  $/\text{NH}_4(\text{NO}_3)$  [214, 215]. Nitrate was never detected in the inorganic layer without collagen, and collagen was never measured without the nitrate peak in the fragments TS2-4. We did not measure either nitrate or collagen by means of Raman on the TS-1 fragment, and hence we cannot comment on the presence of a nitrate peak with collagen in that sample. TS-1 is the fragment from the inner part of the scroll. Raman spectra of collagen powder that was scraped from some of the inner TS sheets (TS-5, see Table 2) exhibited no nitrate peak.

Both Raman sulfate peaks belong to the spectra of the “Na-S-Ca”-particles on the inorganic layer. In the inorganic layer, additional unidentified yet small (ca. 3-5  $\mu\text{m}$  in diameter) material clusters or particles were localized. These particles showed a resonant behavior for Raman shifts generated with a 785 nm laser (Figure 48-III), leading to very strong visible signal which was not present in spectra of the FT-Raman generated with a 1064 nm laser. These are called the “Na<sub>2</sub>-X” particles, because their spectrum could also be found in some of the Na<sub>2</sub>(SO<sub>4</sub>) and Na<sub>2</sub>Ca(SO<sub>4</sub>)<sub>2</sub> measurements from the RRUFF (online minerals Raman database), where the common components between both materials are  $2\text{Na}^+$  and  $(\text{SO}_4)^{2-}$  (Figure 50). Nevertheless the “Na<sub>2</sub>-X” spectrum appeared independently and without the sulfate component in the TS. It might arise from an impurity related to this minerals, or play a role as an analytical characteristic that future investigations could use to identify the material, its origin or its possible treatment.

In order to identify the materials in the inorganic layer, some laboratory self-made aqueous mixtures of reasonable components were tested in different proportions, and with different drying methods. A mixture of sodium sulfate and calcium sulfate (gypsum) in water could partially match the TS sulfate Raman spectra only if the aqueous mixture was fast dried using a heating plate at 250°C while stirring the mixture, but not by slow evaporation at ambient room conditions (Figure 49). In a fast drying process such as heating, different polycrystalline forms can appear together. Each of these phases would probably require different conditions and circumstances for the individual formation if dried slowly in an ambient environment. The self-made reference mixtures and evaporates from the DS water were compared with the

TS by means of XRD. The XRD pattern comparison shows the best match with the sodium sulfate and calcium sulfate mixture after fast drying by heating while stirring (Figure 51). Pure sodium sulfate was also identified in the XRD pattern of the TS. Therefore, one could expect to find pure calcium sulfate such as gypsum in the TS XRD pattern as well, at least some little indication in the noise.

The strongest diffraction peak (No.11) in the XRD pattern of the TS shows an outstanding behavior (Figure 51). Due to the fact that the compared reference materials do not show the same spectral features of an strong peak at that position (including pure calcium sulfate that was prepared in the lab), can indicate the presence of an additional component. We addressed this issue by comparison with additional related materials that showed similar spectral features of an outstanding diffraction peak at this position (Figure 52). We looked for materials, where all other peaks are small enough that they could possibly vanish in the spectral noise if this material is represented in the TS XRD pattern in small amounts.

The TS peak No.11 matches the gypsum XRD pattern ( $\text{Ca}[\text{SO}_4] \cdot x\text{H}_2\text{O}$ ) of the Saharonim formation that was sampled in the Negev (Israel). The XRD pattern of this gypsum sample showed a characteristic of an outstanding peak at the same position as peak No.11 of the TS. It can be concluded that most of the TS XRD pattern can be assigned to the presence of sodium- and calcium sulfates as thenardite and gypsum, but also in a combined molecular formation. A combined molecular formation could be glauberite, however, its XRD pattern (from <http://rruff.info/glauberite/R070322>) could not be identified in the TS. More samples of natural formed glauberite, thenardite and gypsum from different places in Israel and the surrounding regions are needed for further comparison, including the effect of different temperature treatment on the crystal structures.

The identification of the source and possible treatment processes of the inorganic material, which we have characterized here, is an ongoing project. Hence, in order to reconstruct a manufacturing model of the TS, the presented results should be considered as a guideline for further investigations. In the discussion further down we will develop a preliminary model based on our findings at this stage of the investigation progress.

One important remark needs to be said about the TS2 fragment, the sample that we used the most for elemental and molecular analysis (Figure 41). This sample was suitable for our measurements because of the missing part of the layer on the back side of the fragment which is mostly organic. The back surface side of this partly detached organic layer also contains inorganic regions. This could not be confirmed for all the fragments. However, this inorganic

material is not homogeneous and not consistent with regard to thickness and elemental distribution. It shows regions of high homogeneous Na and Cl correlation indicating halite and surprisingly only little presence of Ca (circle in Figure 46). It differs very much from the consistent inorganic material from the front layer of the scroll that we have characterized and discussed above. Therefore, one cannot conclude that parts of the front side inorganic layer of the opposite sheets, have become detached and transferred to the back side of this fragment. Moreover, the consistent thickness of the whole fragment indicates that this possible assumption of the detachment is less likely (cross section in Figure 41-d). The side view clearly shows that sometimes the organic skin layer is curved between the inorganic layers, which form straight surface lines. These observations lead to the conclusion that the back side inorganics on the fragment TS2 originate from the manufacturing procedure rather than being transferred from the opposite surface layer. The inorganic material on the back side could possibly represent residues from an intermediate step involving salts treatment during the parchment manufacturing process. Regarding the presence of the inorganics on the back side, no further conclusions for the entire scroll can be made at this stage of the investigation.

These are the main findings as presented in the results chapter section 1.1. Further discussion on these findings will be structured according to topics that are relevant to the creation a possible model of an antique manufacturing technique for parchment, which could have been applied to the TS. These are the topics that will be discussed in the next chapter (chapter 6):

“Split and unstretched parchment”,

“Treatment with DS water”,

“Presence of nitrates”,

“Text written on the inorganic layer on the skin’s flesh side” and finally

“Preparation of the inorganic layer”.

# Parchment preparation



**Figure 53: Proposed splitting procedure: A wet skin is soaked in a very high saturated salty bath for a short time. The salt induces high osmotic pressure and causes a high humidity gradient throughout the skin's cross section whereby the skin's outer layers become dry and stiff. The skin is then susceptible to rupture exactly along the wet core between the outer layers.**

**Picture © Rimma Schuetz.**

## **6 Reconstruction of an Unknown Ancient Manufacture Practice**

### **Split and unstretched parchment in the Temple Scroll**

The main observation that indicates a split parchment in the TS is the abnormally thin thickness (100  $\mu\text{m}$ ) of the scroll, whereby approximately 70 to 90  $\mu\text{m}$  of the TS is composed of the actual organic material, the skin (Figure 41d).

Skin splitting needs to be undertaken when the skin is wet. As we have shown in Chapter 2, collagen develops very high forces in dry conditions, and its Young's modulus rises significantly [138]. In a dry state, collagen is very resistant. The optimum frame condition for skin splitting would be when the skin is dry on both of the outer surfaces, but still wet inside the skin. In this case, splitting would favour a rupture along the inner wet collagen, leaving the less ductile outer layers intact. To achieve the state of dry outer surfaces with a hydrated core, fast drying that induces a high humidity gradient is required. Drying in the air is a slow process, whereby the humidity gradient throughout the depth of the skin is not very large. Therefore another drying process is suggested, where the skin is soaked in a strongly saturated salty solution (Figure 53, page 128).

Due to the high osmotic pressure induced by the salt, both of the outer layers of the skin will dehydrate in a relatively short time, becoming stiff and dense (see Chapter 2). During this process, the core of the skin tissue remains humid and ductile, therefore amenable to tearing. In collagen-based materials of higher density, the humidity gradient caused by soaking in a saline bath would be even larger, because the shrinking induced by the drying in the outer layers will render them less permeable. There would be a larger resistance for the moisture in the core of the skin to migrate to the surface, and therefore remain trapped within the skin for a longer time.

This leads us to the question of whether or not the TS parchment was stretched while drying before finishing. For clarity reason it should be pointed out that this drying step while the treated skin is stretched is one of the finalizing steps of parchment manufacturing process and it is to distinguish from the splitting procedure by pulling the two dehydrated outer layers as proposed above. When the parchment is not stretched it becomes transparent after drying. The

dense packed collagen fibers form a single gel-like layer. While after stretching, due to the strong decrease in its material density, the parchment becomes whitish and not transparent after drying. Stretching separates the fibers in the collagen network; when light passes through the stretched network, it refracts several times on individual fibers. This refraction causes photon diffusion, which makes the material opaque.

However, the usual procedure of parchment preparation involves the drying when the skin is under tension fixed on a frame but the hypothesis that the TS was possibly split leads to some interesting questions. If the TS parchment was stretched, was it done before or after the splitting? As the wet stretching reduces the material density in disrupting the collagen network, it would be better to avoid stretching the skin before splitting it, in order to maintain a large humidity gradient to favour splitting, as discussed above. On the other hand, stretching the skin after it is split and therefore became very thin and fragile poses a larger risk for damaging the large sheets. Furthermore, thin stretched skin would be less resistant for usage due to the reduced material density. It therefore may be most favorable not to stretch the split parchment at all, even though it would then remain transparent. In such a case a very thin and transparent scroll would be undesirable for writing purposes. In further sections we will discuss how this processing dilemma could nonetheless fit with the manufacturing concept of the Temple Scroll.

## **Treatment with DS water**

Since the Temple Scroll was found near the Dead Sea, the potential usage of DS water in its production process receives particular attention. When considering the use of saline solutions for the splitting procedure as discussed in the previous paragraph, DS water shows suitable criteria. A quantitative Cl/Br ratio could possibly give an indication if DS water was infused in the skin, but we could not succeed in measuring this ratio in this work. Nevertheless, our measurements reveal the higher concentrations of Br in the organic part of the TS material. Its even elemental distribution in the organic material corresponds with the even distributions of Fe and Mn (Table 3 in chapter 1.1); all of them are present in the DS water with relatively high concentration [221-225]. Na, S and Ca are also present in DS water in high concentrations, but these elements are not helpful for elucidating the use of DS water in parchment processing because these elements are also components of the distinct particles from the inorganic layer of the TS.

The observed homogeneous distribution of Br, Fe and Mn indicates an aqueous treatment that would evenly infiltrate the skin. In contrast, the K distribution and additional Fe particles (see discussion in Table 3 in chapter 1.1) were identified within distinct solids in the parchment. Furthermore, the fact that Br, Fe and Mn were found mostly in the organic layer, and not in the inorganic layer, testifies to the possibility of two different water sources that could have been used to produce these two layers.

The XRD and Raman measurements of the material in the inorganic layer show nothing in common with the mineral salts from DS water. The DS salts were examined in three different states: 1) salt formations gathered at the shore, which consists mostly of NaCl (halite), 2) residues from evaporated DS water through heating, and 3) solids precipitated through slow evaporation of DS water at room conditions. The precipitates produced by the two latter processes were notably hygroscopic. Hence even the precipitates from the boiling process returned to a moist and viscous state after exposure to ambient environmental conditions (Chapter 5).

Following these arguments, it is possible that DS water was involved in the treatment of the skin, particularly in the splitting procedure. However, its mineral salts are not part of the inorganic layer. To explore the possibility of a salt immersion process being used to split skins, a few preliminary tests on a modern parchment on a small scale of 10 x 30 mm<sup>2</sup> using DS water were undertaken. In one case, the two layers of an unstretched parchment could be separated easily after being immersed for 15 min in DS water. Another fragment was kept in DS water overnight; this process completely changed its physical properties. The soaked skin became fragile and rotten, and took a very long time to dry. The potential use of DS water to partially dehydrate and aid in the skin splitting procedure requires further systematic investigation that was not undertaken for this thesis.

However, in order to split the skin by means of the soaking procedure described above, any other salty saturated solutions could probably achieve the same result; however, this also needs to be proved. If this is the case, there is no need to use exclusively DS water to split skins. Indeed, there are substantial arguments that speak against its use. In the introduction chapter 1.1 “Content of TS”, a passage of the TS is presented where it speaks about the purification regulations for skins that are allowed to be used inside the city of the Temple (Jerusalem?).

“... No skin of a clean animal that has been slaughtered <sup>8</sup>in other cities is to enter My city. Certain in other cities they may use <sup>9</sup>them for their work, whatever the need may be, but such skins are not to be brought into My city. <sup>10</sup>The reason: their degree of purity corresponds with that of the animals flesh. ...” TS-11Q19, Col.47:4-18 [13]

According to the material analysis; the Temple Scroll reveals a very unique and elaborate procedure of manufacture among all the scrolls found in Qumran, whereas, its content is 50 % dedicated to the construction of the Temple. If the same scroll, which demands such a high degree of purification for any skins that are allowed to be used in the city of the Temple (“The city <sup>4</sup>that I shall sanctify by establishing My name and temp[le] there must be holy and <sup>5</sup>pure from anything that is in any way unclean, by which one might be defiled.” Col.47:4-5), certainly this scroll itself would be produced with the highest possible effort of purification.

Since this scroll, which might be a copy, is dated to the Second Temple period, it is possible that not only the animals of this skins but also the ingredients including water used to process it could have a relation to the city of the Temple (Jerusalem) or at least fulfill the purity requirements. Water plays an especially important role in the religious purification rituals. Surely, it was not possible that a tannery would be inside the city of the Temple, but it could be located in close proximity. Ezekiel of all prophets, the one who describes the architecture of the Temple of God in the Hebrew Bible (Old Testament) speaks about pure and living water coming out of the Temple Mount and bringing life to everything it touches, including Dead Sea water that then becomes “healed” or “fresh”. This might speak against the use of DS water for the TS treatment.

“... <sup>8</sup>Then he said to me, These waters issue forth toward the eastern region, and shall go down into the Arabah (the Jordan Valley); and they shall go toward the sea (Dead Sea); into the sea [shall the waters go] which were made to issue forth; and the waters shall be healed. ...” World English Bible, Ezekiel 47:1-12.

There is another archaeological argument that questions the relationship of the TS to the DS area where it has been found. As currently understood, the TS was not a regular scroll, it is likely that for the makers it supposed to be like a “Scroll of the Scrolls”; very precious and very unique amongst all other scrolls found in Qumran. The largest collection of DS scrolls has been found directly in the vicinity of the Qumran’s ruins, deposited in caves, which were



sometimes difficult to approach. The TS was deposited in Cave 11, about 1.5 km north of the ruins. Cave 11 is an exposed cave, which at least in the last centuries, has been protected only by the presence of foul smelling inhabitants, namely bats. Such an unceremonious deposition of the scroll, some distance away from the Qumran center, does not correspond to the honored attention which it received during its manufacture. It gives rise to the possibility that the TS did not belong to the Qumran collection, but it was hastily deposited in Cave 11 due to a great distress or emergency. As bats usually inhabit caves for very long time periods (several thousands of years and even more), it is possible that the people who placed the TS in Cave 11 were unfamiliar with Qumran area, which means that the scroll could have been used and manufactured elsewhere.

In summary, we identified material evidence for the TS discovered at the DS that suggests the use of DS water in the skin treatment. On the other hand, we also present here strong arguments suggesting another geographical origin of the TS, and against the use of DS water in the manufacturing process. A possible solution for the contradicting arguments that brings the puzzle pieces together at this stage of our understanding involves a hasty deposition of the Temple Scroll in the DS area, but its production and use was elsewhere; possibly close to Jerusalem, a 1-2 days walk. The DS water was not directly involved in the treatment of the skin, but appears on the TS as crystallized salts from the DS shore, a region that was the main salt source in the region that could have been transported elsewhere for use. The DS salt contains elemental traces of DS water. DS water could have been used for the skin splitting procedure as explained in ((Figure 53), or for temporary conservation after the flying. However, there is no further evidence for the DS salt or the DS water being involved in the production of the TS inorganic layer.

## **Presence of nitrates**

The  $\nu_1$  nitrate peak ( $1043 - 1045 \text{ cm}^{-1}$  Raman and FT-Raman measurements at room condition) can be assigned to the ammonia nitrate (phase IV)  $\text{NH}_4(\text{NO}_3)$ . In our measurements of the TS, the  $\nu_1$  nitrate peak always appeared with collagen spectra, except for one measurement with  $\nu_1: 1048 \text{ cm}^{-1}$  (one of about 50 or more measurements). In that particular case, nitrate was found in high concentration as a particle or a cluster among collagen fibers within the inorganic layer.

The reasons for the predominant location of nitrate being only in the organic component of the parchment are either a result of the parchment production, or introduction into the scroll post-production, for example, during the sojourn in the cave. The latter could have happened through a direct contact with soil, where we have also detected nitrate with FT-Raman. Parchment nitrates could also be produced by the uptake of  $\text{NO}_2$  from the atmosphere, followed by the formation of  $\text{NO}_3$  within the collagen molecule [226, 227]. As was already mentioned earlier, bats also inhabited Cave 11, where TS was deposited for two millennia. Whether their excrements (urea / dung) could have been the source of ammonium nitrate located inside the parchment is not yet confirmed, however it is a possible nitrate source. This nitrate source would more likely contaminate the parchment at the scrolls edges than the parchment within the rolled scroll, which was more protected over the centuries.

We addressed the question of the effect of parchment protection within the rolled scroll by comparing some deteriorated samples from the outer sheets with the TS-1 fragments with samples from the inner part of the scroll. The surface of the outer fragments was free from the inorganic layer and the collagen was gelatinized because they were exposed to the environment and therefore strongly damaged. These exterior samples as well as the TS 2-4 fragments demonstrated clear nitrate peaks in the Raman spectra, whereas the surface of the TS-1 fragment did not generate a nitrate Raman shift. Based on these results, we attributed the nitrate to the cave sojourn, and proposed the activity of bats as the source of the nitrate contamination [217]. Unfortunately at the time this conclusion was made, we did not identify the correlation of the nitrate peak appearing only with the collagen Raman spectrum.

The surface of the measured TS-1 fragment is composed predominantly of inorganic layer; therefore we do not have any collagen Raman spectra from the inner part of the scroll at this moment that could confirm our first conclusion concerning the nitrate source. However, there are other interesting findings that could support the hypothesis of bats as the source of the nitrate Raman peak. By means of FT-Raman we also identified the nitrate peak in the textile in which the scroll was wrapped. Furthermore, the Raman measurements of the TS-5 sample show mainly pure collagen with some of the characteristic inorganic material, but no indication of the nitrate peak. TS-5 sample is a yellowish powder that was scraped from the surface in the inner part of the scroll by the conservators. However, extended investigations on more samples from the inner part of the scroll are needed in order to clarify the question of the origin of the nitrate Raman shift. If other inner scroll samples demonstrated same nitrate peak, and the nitrate peak identification was independent of the location of the sample inside the

scrolls, then the nitrate peak may have originated from the chemistry of the skin processing process, before the inorganic layer was added.

### **Text written on the inorganic layer on the skin's flesh side**

In Jewish law scriptures, the text is usually written on the hair side of the skin. The flesh side is less smooth and hence less suitable for writing purposes. This also includes those scrolls found in Qumran, including another copy of the Temple scroll, which curiously enough, was also found in Cave 11. No other distinct copies of the TS scroll were found in Qumran. However, as it is often the case in Jewish tradition, details pertaining to rituals and their objects are stipulated by intricate regulations and such is the case for the making of law scriptures.

As an example, the Talmud, which was written about 400-500 years after the TS, discusses the exact procedures for parchment manufacture for the writing of texts used for different ritual purposes. It deals with the question of the side on which to write if the skin is split or if it is not split. Apparently this subject is a matter of disagreement in rabbinic literature due to contradicting definition of the hair side and flesh side if the skin is split; the two terms used are qlaf and dukhsustos. Furthermore, the Talmudic regulation also requires treatment of the parchment surface with tannin (oak gall) before writing on it. Tannin treatment gives the scroll a brownish color, and also causes a very strong fluorescence signal in the Raman spectrum, even in the NIR region at 785 nm excitation.

The TS scroll, however, is different. It has a whitish color, and in most cases a Raman spectrum without fluorescence is generated if a high magnification lens (100x) is used. Therefore it is hypothesized that this scroll was most probably not treated with tannins. Moreover, as was seen in the archive photographs made by Zuckerman (unfortunately a direct access to the backside of the scroll was not available at the time of our investigation), hair follicles can be recognized on the back of the scroll in all of its sheets. In Figure 1d, hair follicles are very pronounced, and this confirms identification of the hair side of the sheet. This observation indicates that the TS text is written on the flesh side of the skin.

The elemental distribution generated by  $\mu$ XRF maps and presented in Figure 43 (S 1 in supplementary materials) and Figure 44 shows the presence of phosphorus in much higher concentration on the inner flesh side of the scroll's skin. This observation was made with the help of the cracks in the inorganic layer, on the text side of the scroll. In literature it is report-

ed that the P concentration is up to 20 times higher in the inner layer of the epidermis (stratum germinativum) compared to the outer hair layer of skin (stratum corneum) [228]. The main proteinous component of stratum corneum is keratin (80-90%) and not collagen [229], which results in different physical properties of the different skin layers. The phosphorus distribution can be partly attributed to the epidermal phospholipids [230, 231]. Depending on the original parchment treatment processing, phosphorus concentration could be a distinguishing marker between the hair and flesh side of small fragments. Both features of the two layers of the epidermis, the keratin-rich layer of the stratum corneum and the increased concentration of phospholipids in the stratum germinativum, could play a role in the skin splitting process by means of the dehydration effect as discussed previously ((Figure 53).

Skin splitting generates a rough surface on the flesh side of the skin. Before writing was applied to the TS, this rough surface was first covered by an inorganic white layer. This inorganic layer was embedded within the collagen fiber matrix, and made the surface of the thin skin smooth and hard for writing purposes. The question for the possible reason for such a preparation technique is addressed in the next section “Preparation of the inorganic layer”.

### **Preparation of the inorganic layer**

Before we reconstruct how the inorganic layer could have been prepared, the possible purposes of the inorganic layer should be discussed. What reasons could explain the preparation of the scroll with text written on the flesh side of the skin covered with an inorganic layer, and not on the hair side, which is the more practical and common way to do? A simplified skin treatment procedure for ancient scrolls involves rubbing the skin with salt after flying to arrest rotting while storage or transportation. Before the further treatment, the hide was washed and cleaned again. After this process the flesh and the hairs were removed typically by an enzymatic bath, and by subsequent physical rubbing with special tools. The processed skin was stretched in all directions with the use of a frame, and then dried in air. After drying, the relatively thick and stable skin remained expanded and opaque. The stretched and dried skin could then be further processed with some finishing agents such as tannins. One would then write on the relatively smooth surface of the hair side of the skin.

The Temple Scroll underwent a different and more complicated treatment. Here we summarize our understanding as described in previous subsections of the discussion. After salting and depilation, the thickness of the skin was reduced to the minimum size of the epidermis

layer. This very thin hair side layer was very transparent at this processing step. It is possible that the size reduction was performed with the splitting procedure, by means of dehydration of the outer skin layers. After drying without stretching the remaining thin and transparent hair split was stabilized and smoothened by the application of a layer of opaque inorganic material. The text was then written on the inorganic layer on the skins flesh side.

The extra effort and complicated process for producing the TS parchment could indicate its unique value for the people who used it. They saw in the TS a very unique and sacred scripture, where God himself (in the first person singular) describes the architecture of the Temple – the place of his presence. This Temple Scroll, which was surely prepared with a very purified and honorific process, should present a unique and most beautiful appearance. After two millennia, its organic part has experienced deterioration in terms of material- and appearance changes, yet TS remains one of the most beautiful scrolls. Given its age, it can be imagined in that the appearance of the TS during its time of use would have been amazingly beautiful. We can only imagine the impression of text written on a very white smooth surface, where the bright whiteness is transmitted on to the back side of the scroll through the transparent thin parchment.

The aesthetic beauty that results from the special TS production effort may also have a practical motivation. As we have learned from the content about the purity regulations for skins allowed to be used in the city of the temple, this scroll had probably to be prepared only from highly purified animals, which may have been raised and slaughtered in in a special place like Jerusalem. As a very precious material, its use would not be wasteful. As the TS is more than 8 m length, it is the longest scroll that has been found in Qumran. For economical purposes, it would make sense to split the purified skin, and create two writing surfaces from one skin. However, but splitting the skin, the flesh side of the split skin would have two rough surfaces, both of which are not as suitable for writing as the hair side.

To allow for writing, at least one of the rough surfaces of the flesh side split layer should be stabilized and smoothened with the application of an inorganic gel layer. For reasons of consistency, the split sheet with the hair side should also be written on a similar inorganic layer. This inorganic layer could have been applied to the rough inner surface, opposite to the hair-side surface, where there would be improved adhesion provided by the residues of the collagenous fiber network. This processing would result in the hair follicles being located on the back side of the scroll on some of the sheets and some without. This processing option

would results in the back sides of some TS sheets being the skin hair side, and others the skin flesh side.

The question of inorganic material adhesion to skin is a key question for understanding the possible preparation method of the inorganic layer. This will be addressed further in the discussion. However, the photographs of the back side of the intact larger part of the scroll revealed the skins hair side throughout the whole scroll by appearance of the hair follicle pattern as it can be seen in Figure 1b. The hair follicles were also observed on the back side of the scroll fragments from the damaged outer sheets. The presence of hair follicles on the back of the TS throughout the entire scroll, with no evidence of flesh side on the back side of the TS does not support the hypothesis that economical use of prepared skins was a motivation for splitting the skins before writing on them. Unfortunately, today the scroll is fixed on a paper support, and closed in an exhibition frame, so the hypothesis cannot be tested further. For conservation reasons, at the time of our investigation, access was not granted to the back side of the TS.

A third perspective on the purpose of the inorganic layer approaches our understanding of a “scroll” as a general term from an unconventional direction.

“Once on the mountain of Sinai, God wrote the law and the commandments on two plates of stone with His finger and gave the two tables of the Testimony to Moses”  
(Rephrased and composed from Exodus 24:12 and 31:18, Bible).

When God wrote the law, He did this on stone. As it is described in the introduction (chapter 1.1), the text of the Temple Scroll addresses Moses directly from the first person singular. God himself is supposed to be the author of this conceptualized text. Consequently, the material on which his words can be written cannot be less “everlasting” than stone. Considering this perspective, the inorganic layer of the TS could have been produced to mimic a white stone plate that was produced in the useful form of a flexible, 8 m long, beautiful scroll. The organic skin layer of the TS would act as the flexible supporting material for the primary ‘building block’ of the **Temple** – **“Stone”** – **Scroll**.

The proposed perspective is just a speculation and it is based on considerations done by Dr. Ira Rabin, the head of the Qumran research project at the Federal Institute for Materials Research and Testing (Berlin) and by Dr. Adilfo Roitman, the director of the Shrine of the Book (Jerusalem) – “the cave” that is the current dwelling of the TS. They investigated how far the

commandment that “the law has to be written on a white wall” can be related to the white inorganic layer of the Temple Scroll, where the text, which contains some law commandments, is written on.

Whatever the motivation was for the application of the inorganic layer, be it for unique esthetic beauty, or as a “stone” or “white wall” substitute, or maybe both, the inorganic material had to be fixed on the thin skin by means of a suitable binder. This binder adhered what may have originally been powdered inorganic materials on the skin surface, and maintained the integrity of the inorganic layer to modern times. The binder and its preparation procedure would require a consequent continuation in the purification concept.

Materials known to be used as a binder could be resins such as gum arabic, it could also be egg white or gelatin. Resins would change the color to darker brownish and the Raman spectra are usually strongly fluorescent, both are not the cases for the TS. An important difference between egg white and gelatin is the temperature used during the binder application. If egg white was used as a binder, the powdered inorganic material would have been mixed and applied to the scroll at room temperature. Dove eggs could have been used for their egg whites, because doves are the only poultry that were allowed for sacrificial rituals in the Temple, as required by the Torah (Lev 1, 14 and 15). The use of chicken egg white as a binding material is less likely if one considers the TS with the other Qumran literature and the Qumran settlement. There is an ongoing discussion amongst archaeologists and scholars regarding the purity of chickens for use in Jerusalem among priests during the Second Temple period. Although according to the Torah chicken is a kosher animal, priests avoided their use. Furthermore, no evidence of chickens was found at the Qumran excavation site [232], whereas bones of other animals that were used for food have been discovered in a big amount.

We don't want to participate in this debate about the cultural importance of eggs but for our context the use of egg white as a binder versus gelatin includes practical considerations. Egg white would be a new raw material, whereas gelatin can be produced from the same skin material from which the parchment is produced. However, gelatin has to be treated at high temperatures. To produce gelatin, the collagen-rich part of the skin, for example the inner dermis layer of a split skin must be boiled in water until it completely dissolves as gelatinous “bullion”. Upon continued boiling, the water is evaporating, and the gelatin forms a gel that remains viscous for parchment treatment as long as the gelatin paste is still hot. The boiled gelatin becomes hard and glossy at room temperature.

Mixing the inorganic phase with gelatin would be difficult once the gelatin has cooled. It would be advantageous to mix the inorganic powder with the boiling gelatin “bullion” before it is gelatinized, and to keep it on a high fire until the water evaporated by boiling. At a suitable consistency the mixture of gelatin and inorganic material could then be spread on the inner side of the transparent split skin, with the hair side on the back side. This gelatin-inorganic material mix would embed within the exposed collagenous fiber network. This mix could form a smooth and stable surface layer, which is suitable for writing. As it was already discussed, our Raman and XRD results from reference mixtures indicate a possible heat treatment of the inorganic material (Figure 49 and Figure 51). This data supports the hypothesis that gelatin was used as a binding material. However, of course it is also possible that these Raman and XRD spectral features could also be caused by a particular natural formation of the inorganic minerals.

This work elaborates a model for an unknown till our days antique manufacturing technique, as it has been applied for the TS production, by suggesting some motivations for why the skin for the TS was split, why only the thin outer skin side of the skin was used as a supporting parchment, and why and how the inorganic material was applied on the flesh side of this transparent mostly epidermis layer. For the development of this model, deeper understanding of collagen as a biological building stone and other material evidences found inside the TS as well as archaeological and cultural background were considered. With our work we contributed in several scientific subjects. If summarizing them in two major they would be: the one is the basic understanding of the biological material collagen in its physiological functionality, which opens new understanding of collagen in its medical context, and the other is the study of the heartrending DSS in the context of cultural heritage.



## 7 Conclusion

In this work, the molecular structure and mechanical behavior of the collagen-water system was investigated on different length scales. Application of a wide range of characterization techniques showed how dehydration changed the collagen fiber structure throughout most of the hierarchical levels. The drying collagen molecule shrank and developed surprisingly high stresses of up to 100 MPa, which is much larger than the stresses generated by muscles. These stresses were so large that even slight changes of osmotic pressure within totally hydrated collagen produced significant forces. This result suggests a possible role of extracellular matrix collagen in fundamental, biologically relevant processes such as signaling, tissue prestress and tissue biomechanics. It can be concluded that water plays a crucial role in stabilizing the structure of the collagen molecule, and is an essential and active part of the protein unit. The observations by X-ray and Raman scattering are consistent and lead to the following conclusions:

- (i) the drying collagen molecule and the fibril shrink by different amounts, 1.3% and 2.5%, respectively;
- (ii) dehydration is accompanied by a reduction of the collagen fibril gap/overlap ratio;
- (iii) triple-helix shrinkage is inhomogeneous, as shown by the distribution of helical pitches.

These observations were translated into a simple model that is characterized by heterogeneous dimensional changes that involve shrinkage of the triple-helical molecules in the gap region that is partially compensated by an expansion of the overlap region. Moreover, Raman spectroscopy indicated reversible conformational changes of the collagen backbone upon drying, whereas stretching collagen fibers did not induce any peak shifts in the Raman spectra.

Complementary to the Raman and X-rays scattering approaches, conformational and condition-related collagen structural changes were also investigated using far-IR spectroscopy ( $80\text{--}500\text{cm}^{-1}$ ) at the synchrotron radiation facility BESSY. Absorption in this spectral range involves collective skeletal vibration of the triple helical structure of collagen. For the far-IR measurements, a special environmental sample holder was designed with the requirement of controlling the humidity while protecting the collagen sample from the vacuum while the

beam path through the atmosphere was as short as possible. Via stepwise demineralization of thin fibrolamellar bone samples, the overlapping peaks bundles of collagen (around  $345\text{ cm}^{-1}$ ) and mineral ( $100\text{-}400\text{ cm}^{-1}$ ) were distinguished. The fully demineralized collagen samples were used for further analysis. In agreement with the Raman results, far-IR analysis showed no significant spectral changes due to collagen stretching, but the influence of dehydration was very clear in the spectra. Based on this effect, far-IR spectral parameters were developed for collagen damage assessment, and the study of the gelatinization process in parchments. In the framework of these investigations, the spectral properties of mineral and collagen orientation inside a longitudinal fibrolamellar bone were also studied.

In this doctoral work, a special effort was directed towards the development of the confocal PRS approach to assessing damage of individual collagen fibrils. Useful parameters were defined through the analysis of highly ordered fresh collagen from rat tail tendon and fully degraded gelatin. Considering its non-invasive and non-destructive nature, we showed the potential of PRS for application in cultural heritage studies. In particular we used the technique to study conservation of ancient manuscripts, and developed a methodology for quantitative assessment of collagen damage within the Dead Sea Scrolls.

In the last part of the work we focused on the characterization of materials associated with the Temple Scroll with two main goals: (i) to assess the collagen damage and (ii) to explore an unknown ancient parchment production technology. PRS analysis allowed non-invasive collagen damage assessment and showed the presence of collagen fibers in a relatively good state of preservation, mainly due to the fact that they were protected by an inorganic surface layer. Fibers on the outer inorganic layer were more exposed to the environment, and as a consequence, showed extensive levels of damage/gelatinization.

To further investigate the material properties of the TS, a set of complementary and non-invasive techniques that includes confocal  $\mu$ -Raman, FT-Raman, PIXE,  $\mu$ XRF, ESEM and XRD were applied. Samples from the outer parts of the TS and their collagen fibers were accompanied by traces of ammonium nitrate. This contamination could originate from the environmental, as the cave where the TS dwelt for 2000 years was inhabited by bats. It could also be a result of the treatment associated with the parchment production procedure. More investigations are needed in order to exclude some of the above-mentioned hypothesis. The surface inorganic layer contained sodium and calcium sulfate particles that could be reproduced in the lab. Additionally,  $\mu$ -particles with a high resonance in Raman at  $785\text{ nm}$  excitation wavelength were found dispersed within the inorganic layer. These Raman-resonant

particles have been associated with some naturally-occurring minerals that were also found in TS surface layer.

With this interdisciplinary analysis approach that considered physical material characteristics, textual notes, and also reflections over the functionalities or possible purposes of the identified scroll components, a model for the unknown parchment manufacturing technique was proposed and discussed in the last chapter of this thesis. The proposed model suggests that the skin was split in order to produce gelatin from the inner (flesh) side of the skin, and was used as a binding material for the inorganic layer. The splitting procedure is discussed in the last chapter, and suggests the possible use of sodium chloride as a dehydrating agent, as it was identified with a smooth distribution inside the organic parchment layer. However, the presence of sodium chloride in the skin is not surprising, since it was commonly used for skin conservation after flaying. The hot, viscous gel-like mixture composed of whitish minerals and gelatin was distributed on the surfaces of the velvet-like flesh side of the thin and transparent skin surface. After cooling, the whitish inorganic layer was shone through the skin, and the text was written on the glossy, hard surface of the inorganic layer. The beautiful appearance of the Temple Scroll must have been breathtaking to the people who produced and used it in antiquity.

The findings of this work open new questions related to archeological aspects of the TS, and about the functionalities of collagen in physiological conditions, especially with respect to the effect of osmotic pressure. This research provides useful tools for assessment of collagen fiber conformational changes in collagen fibers, which can be related to the deterioration progress in parchments.

## List of Abbreviations

TS	Temple Scroll
DSS	Dead Sea Scrolls
PRS	Polarized Raman Spectroscopy
Far-IR, IR	Far Infrared, Infrared Spectroscopy
ED	Edge Radiation
FT-Raman	Fourier Transformed Raman Spectroscopy
THz-TD	Terahertz Time Domain Spectroscopy
PIXE	Particle Induced X-Ray Emission
XRD	X-Ray Diffraction
PGs	Proteoglycans
AGAGs	Anionic glycosaminoglycans

## References

1. Yadin, Y., *The Temple Scroll: The Hidden Law of the Dead Sea Sect*. WEIDENFELD & NICOLSON, 1985: p. 264.
2. Masic, A., et al., *Observations of Multiscale, Stress-Induced Changes of Collagen Orientation in Tendon by Polarized Raman Spectroscopy*. *Biomacromolecules*, 2011. 12(11): p. 3989-3996.
3. Broshi, M., *The Gigantic Dimensions of the Visionary Temple in the Temple Scroll*. *Biblical Archaeology Review*, 1987. Temple Scroll Revisited.
4. Schade, U., et al., *New infrared spectroscopic beamline at BESSY II*. *Review of Scientific Instruments*, 2002. 73(3): p. 1568-1570.
5. Zeugolis, D.I., J.C.Y. Chan, and A. Pandit, *Tendons: Engineering of Functional Tissues*, in *Tissue Engineering*, N. Pallua and C.V. Suscheck, Editors. 2011, Springer Berlin Heidelberg. p. 537-572.
6. Edwards, H.G.M., et al., *Fourier-transform Raman spectroscopy of ivory .2. Spectroscopic analysis and assignments*. *Journal of Molecular Structure*, 1997. 435(1): p. 49-58.
7. Kennedy, C.J. and T.J. Wess, *The structure of collagen within parchment - A review*. *Restaurator-International Journal for the Preservation of Library and Archival Material*, 2003. 24(2): p. 61-80.
8. Peatman, W.B. and U. Schade, *A brilliant infrared light source at BESSY*. *Review of Scientific Instruments*, 2001. 72(3): p. 1620-1624.
9. Fratzl, P., I. Burgert, and H.S. Gupta, *On the role of interface polymers for the mechanics of natural polymeric composites*. *Physical Chemistry Chemical Physics*, 2004. 6(24): p. 5575-5579.
10. Wiener, H., *Another Perspective - RECOVERING LOST PROPHETS*. <http://www.tech-news.com/another/ap200802.html>, 2008.
11. Frushour, B.G. and J.L. Koenig, *Raman-Scattering of Collagen, Gelatin, and Elastin*. *Biopolymers*, 1975. 14(2): p. 379-391.
12. Janko, M., et al., *Anisotropic Raman scattering in collagen bundles*. *Optics Letters*, 2010. 35(16): p. 2765-2767.
13. Wise, M.O., M.G. Abegg, and E.M. Cook, eds. *The Dead Sea Scrolls - A New Translation*. 2005, HarperSanFrancisco. 688 pages.
14. Hoffman, H., W.E. Torres, and R.D. Ernst, *Paleoradiology: Advanced CT in the evaluation of nine Egyptian mummies*. *Radiographics*, 2002. 22(2): p. 377-385.
15. Murphy Jr, W.A., et al., *The iceman: Discovery and imaging*. *Radiology*, 2003. 226(3): p. 614-629.
16. O'Brien, J.J., et al., *CT imaging of human mummies: A critical review of the literature (1979-2005)*. *International Journal of Osteoarchaeology*, 2009. 19(1): p. 90-98.
17. Plenderleith, H.J., D. Barthelemy, and J.T. Milik, *Discoveries in the Judean desert I*. Clarendon Press, Oxford, 1955: p. 39-40.
18. Yadin, Y., *The Temple Scroll*. *Biblical Archaeology*, 1967. 30: p. 135-139.

19. Söderhäll, C., et al., *Variants in a Novel Epidermal Collagen Gene <italics>(COL29A1)</italics> Are Associated with Atopic Dermatitis*. PLoS Biol, 2007. 5(9): p. e242.
20. Fratzl, P., *Collagen: Structure and Mechanics, an Introduction*, in *Collagen*, P. Fratzl, Editor. 2008, Springer US. p. 1-13.
21. Fratzl, P., et al., *Structure and mechanical quality of the collagen-mineral nano-composite in bone*. Journal of Materials Chemistry, 2004. 14(14): p. 2115-2123.
22. Benjamin, M. and J.R. Ralphs, *Tendons and ligaments--an overview*. Histol Histopathol, 1997. 12(4): p. 1135-44.
23. Thornton, G.M., N.G. Shrive, and C.B. Frank, *Altering ligament water content affects ligament pre-stress and creep behaviour*. Journal of Orthopaedic Research, 2001. 19(5): p. 845-851.
24. Fullerton, G.D. and M.R. Amurao, *Evidence that collagen and tendon have monolayer water coverage in the native state*. Cell Biology International, 2006. 30(1): p. 56-65.
25. Kannus, P., *Structure of the tendon connective tissue*. Scandinavian Journal of Medicine & Science in Sports, 2000. 10(6): p. 312-320.
26. Kjaer, M., *Role of extracellular matrix in adaptation of tendon and skeletal muscle to mechanical loading*. Physiological Reviews, 2004. 84(2): p. 649-698.
27. Wang, J.H.C., *Mechanobiology of tendon*. Journal of Biomechanics, 2006. 39(9): p. 1563-1582.
28. Kastelic, J., A. Galeski, and E. Baer, *The Multicomposite Structure of Tendon*. Connective Tissue Research, 1978. 6(1): p. 11-23.
29. Fraser, R.D.B. and B.L. Trus, *Molecular Mobility in the Gap Regions of Type-I Collagen Fibrils*. Bioscience Reports, 1986. 6(2): p. 221-226.
30. Wess, T.J., *Collagen Fibrillar Structure and Hierarchies*, in *Collagen: Structure and Mechanics*, P. Fratzl, Editor. 2008, Springer Science+Business Media, LLC: New York. p. 49-80.
31. Hay, E.D., *Cell Biology of Extracellular Matrix*. 1991.
32. Lodish, H., et al., *Mol. Cell. Biol.* 2004.
33. Hulmes, D.J.S., et al., *Analysis of the primary structure of collagen for the origins of molecular packing*. Journal of Molecular Biology, 1973. 79(1): p. 137-148.
34. Itoh, T., M. Kobayashi, and M. Hashimoto, *The role of intermolecular electrostatic interaction on appearance of the periodic band structure in type I collagen fibril*. Japanese Journal of Applied Physics Part 2-Letters, 1998. 37(2A): p. L190-L192.
35. Orgel, J.P.R.O., et al., *The in situ supermolecular structure of type I collagen*. Structure, 2001. 9(11): p. 1061-1069.
36. Ottani, V., M. Raspanti, and A. Ruggeri, *Collagen structure and functional implications*. Micron, 2001. 32: p. 251-260.
37. Venturoni, M., et al., *Investigations into the polymorphism of rat tail tendon fibrils using atomic force microscopy*. Biochemical and Biophysical Research Communications, 2003. 303(2): p. 508-513.
38. Minary-Jolandan, M. and M.-F. Yu, *Nanomechanical Heterogeneity in the Gap and Overlap Regions of Type I Collagen Fibrils with Implications for Bone Heterogeneity*. Biomacromolecules, 2009. 10(9): p. 2565-2570.
39. Price, R.I., S. Lees, and D.A. Kirschner, *X-ray diffraction analysis of tendon collagen at ambient and cryogenic temperatures: Role of hydration*. International Journal of Biological Macromolecules, 1997. 20(1): p. 23-33.

40. Fratzl, P. and R. Weinkamer, *Nature's hierarchical materials*. Progress in Materials Science, 2007. 52(8): p. 1263-1334.
41. Scott, J.E., *Collagen-Proteoglycan Interactions - Localization of Proteoglycans in Tendon by Electron-Microscopy*. Biochemical Journal, 1980. 187(3): p. 887-&.
42. Rees, S.G., et al., *Catabolism of aggrecan, decorin and biglycan in tendon*. Biochem. J., 2000. 350(1): p. 181-188.
43. Scott, J.E., et al., *Peptide sequences in glutaraldehyde-linked proteodermatan sulphate : collagen fragments from rat tail tendon locate the proteoglycan binding sites*. Biochemical Society Transactions, 1997. 25(4): p. S663-S663.
44. Scott, J.E. and A.M. Thomlinson, *The structure of interfibrillar proteoglycan bridges ('shape modules') in extracellular matrix of fibrous connective tissues and their stability in various chemical environments*. Journal of Anatomy, 1998. 192: p. 391-405.
45. Fratzl, P., et al., *Fibrillar structure and mechanical properties of collagen*. Journal of Structural Biology, 1998. 122(1-2): p. 119-122.
46. Folkhard, W., et al., *Quantitative analysis of the molecular sliding mechanisms in native tendon collagen — time-resolved dynamic studies using synchrotron radiation*. International Journal of Biological Macromolecules, 1987. 9(3): p. 169-175.
47. Sasaki, N. and S. Odajima, *Elongation mechanism of collagen fibrils and force-strain relations of tendon at each level of structural hierarchy*. Journal of Biomechanics, 1996. 29(9): p. 1131-1136.
48. Gupta, H.S., et al., *In situ multi-level analysis of viscoelastic deformation mechanisms in tendon collagen*. Journal of Structural Biology, 2010. 169(2): p. 183-191.
49. Engel, J. and H. Bächinger, *Structure, Stability and Folding of the Collagen Triple Helix*, in *Collagen*, J. Brinckmann, H. Notbohm, and P.K. Müller, Editors. 2005, Springer Berlin Heidelberg. p. 7-33.
50. Vitagliano, L., et al., *Stabilization of the Triple-Helical Structure of Natural Collagen by Side-Chain Interactions*. Biochemistry, 1993. 32(29): p. 7354-7359.
51. Brodsky, B., et al., *Triple-helical peptides: an approach to collagen conformation, stability, and self-association*. Biopolymers, 2008. 89(5): p. 345-53.
52. Okuyama, K., et al., *Helical twists of collagen model peptides*. Biopolymers, 2006. 84(4): p. 421-432.
53. Okuyama, K., et al., *Crystal and Molecular-Structure of a Collagen-Like Polypeptide (Pro-Pro-Gly)<sub>10</sub>*. Journal of Molecular Biology, 1981. 152(2): p. 427-443.
54. Gonzalez, L.G. and T.J. Wess, *The effects of hydration on the collagen and gelatine phases within parchment artefacts*. Heritage Science, 2013. 1(1): p. 14.
55. Ramachandran, G. and R. Chandrasekharan, *Interchain hydrogen bonds via bound water molecules in the collagen triple helix*. Biopolymers, 1968. 6: p. 1649 - 1658.
56. Pineri, M., M. Escoubes, and G. Roche, *Water-collagen interactions: Calorimetric and mechanical experiments*. Biopolymers, 1978. 17: p. 2799 - 2815.
57. Zhang, D., U. Chippada, and K. Jordan, *Effect of the structural water on the mechanical properties of collagen-like microfibrils: a molecular dynamics study*. Ann Biomed Eng, 2007. 35: p. 1216 - 1230.
58. Mrevlishvili, G., et al., *Hydration of native-type collagen fibers*. Dokl Akad Nauk SSSR, 1974. 215: p. 457 - 459.
59. Mrevlishvili, G., *Low-temperature heat capacity of biomacromolecules and the entropic cost of bound water in proteins and nucleic acids*. Thermochim Acta, 1998. 308: p. 49 - 54.

60. Mrevlishvilli, G. and D. Svintradze, *Complex between triple helix of collagen and double helix in DNA in aqueous solution*. Int J Biol Macromol, 2005. 35: p. 243 - 245.
61. Cheng, W., et al., *The content and ratio of type I and III collagen in skin differ with age and injury*. African Journal of Biotechnology, 2011. 10(13): p. 2524-2529.
62. Kielty, C.M. and M.E. Grant, *The Collagen Family: Structure, Assembly, and Organization in the Extracellular Matrix*, in *Connective Tissue and Its Heritable Disorders*. 2003, John Wiley & Sons, Inc. p. 159-221.
63. Scott, J.E., C.R. Orford, and E.W. Hughes, *Proteoglycan-Collagen Arrangements in Developing Rat Tail Tendon - an Electron-Microscopical and Biochemical Investigation*. Biochemical Journal, 1981. 195(3): p. 573-&.
64. Kjellen, L. and U. Lindahl, *Proteoglycans - Structures and Interactions*. Annual Review of Biochemistry, 1991. 60: p. 443-475.
65. Poole, J.B. and R. Reed, *The preparation of leather and parchment by the Dead Sea Scrolls community*. Technology & Culture, 1962. 3: p. 1-36.
66. Sivasubramanian, S., B.M. Manohar, and R. Puvanakrishnan, *Mechanism of enzymatic dehairing of skins using a bacterial alkaline protease*. Chemosphere, 2008. 70(6): p. 1025-1034.
67. Money, C.A., *Procter Memorial Lecture - Unhairing and dewooling - Requirements for quality and the environment*. Journal of the Society of Leather Technologists and Chemists, 1996. 80(6): p. 175-186.
68. Kennedy, C.J., et al., *Microfocus X-ray diffraction of historical parchment reveals variations in structural features through parchment cross sections*. Nano Letters, 2004. 4(8): p. 1373-1380.
69. Gonzalez, L. and T. Wess, *Use of attenuated total reflectance - Fourier transform infrared spectroscopy to measure collagen degradation in historical parchments*. Appl Spectrosc, 2008. 62: p. 1108 - 1114.
70. Sionkowska, A., *Thermal denaturation of UV-irradiated wet rat tail tendon collagen*. Int J Biol Macromol, 2005. 35: p. 145 - 149.
71. Kato, Y., K. Uchida, and S. Kawakishi, *Oxidative-Degradation of Collagen and Its Model Peptide by Ultraviolet-Irradiation*. Journal of Agricultural and Food Chemistry, 1992. 40(3): p. 373-379.
72. Larsen, R., *The Chemical Degradation of Leather*. CHIMIA International Journal for Chemistry, 2008. 62(11): p. 899-902.
73. Galant, S., *Formation of Collagen-Like Structure of Gel after Radiation Modification of Gelatin*. Colloid and Polymer Science, 1983. 261(5): p. 445-451.
74. Budrugaec, P. and L. Miu, *Effect of accelerated thermal ageing on the thermal behaviour of the recently made parchments*. Journal of Thermal Analysis and Calorimetry, 2008. 94(2): p. 335-342.
75. Raman, C.V., *A change of wave-length in light scattering*. Nature, 1928. 121: p. 619-619.
76. Landsberg, G. and L. Mandelstam, *A new occurrence in the light diffusion of crystals*. Naturwissenschaften, 1928. 16: p. 557-558.
77. Lyon, L.A., et al., *Raman spectroscopy*. Analytical Chemistry, 1998. 70(12): p. 341r-361r.
78. *Introduction to Vibrational Spectroscopy*, in *Handbook of Vibrational Spectroscopy*, P.R.G. John M. Chalmers, Editor. 2006, John Wiley & Sons, Ltd. p. 4000.



79. Bower, D.I., *INVESTIGATION OF MOLECULAR ORIENTATION DISTRIBUTIONS BY POLARIZED RAMAN-SCATTERING AND POLARIZED FLUORESCENCE*. Journal of Polymer Science Part B-Polymer Physics, 1972. 10(11): p. 2135-2153.
80. Bower, D.I., *ORIENTATION DISTRIBUTION-FUNCTIONS FOR UNIAXIALLY ORIENTED POLYMERS*. Journal of Polymer Science Part B-Polymer Physics, 1981. 19(1): p. 93-107.
81. Turrell, G., *Analysis of Polarization Measurements in Raman Microspectroscopy*. . Journal of Raman Spectroscopy, 1984. 15(2): p. 103-108.
82. Bremard, C., et al., *The Effect of High-Numerical-Aperture Objectives on Polarization Measurements in Micro-Raman Spectrometry*. Applied Spectroscopy, 1985. 39(6): p. 1036-1039.
83. Bremard, C., J. Laureyns, and G. Turrell, *Polarization Measurements in Raman Microspectroscopy .3. Optical-Properties and Sample Orientation*. Journal De Chimie Physique Et De Physico-Chimie Biologique, 1989. 86(6): p. 1245-1251.
84. Bremard, C., et al., *Polarization Measurements in Raman Microspectroscopy .1. Isotropic Samples*. Journal of Raman Spectroscopy, 1987. 18(5): p. 305-313.
85. Bremard, C., et al., *Polarization Measurements in Micro-Raman and Microfluorescence Spectrometries*. Journal of Molecular Structure, 1986. 142: p. 13-16.
86. Ikeda, R., B. Chase, and N. Everall, *Basics of Orientation Measurements in Infrared and Raman Spectroscopy*, in *Handbook of Vibrational Spectroscopy*. 2006, John Wiley & Sons, Ltd.
87. Rousseau, M.E., et al., *Study of protein conformation and orientation in silkworm and spider silk fibers using Raman microspectroscopy*. Biomacromolecules, 2004. 5(6): p. 2247-2257.
88. Buffeteau, T., et al., *Biaxial orientation induced in a photoaddressable azopolymer thin film as evidenced by polarized UV-visible, infrared, and Raman spectra*. Macromolecules, 2004. 37(8): p. 2880-2889.
89. Labarthe, F., T. Buffeteau, and C. Sourisseau, *Orientation distribution functions in uniaxial systems centered perpendicularly to a constraint direction*. . Appl Spectrosc, 2000. 54(699-705).
90. Sourisseau, C., *Polarization measurements in macro- and micro-Raman spectroscopies: Molecular orientations in thin films and azo-dye containing polymer systems*. Chemical Review, 2004. 104(3851-3891).
91. Bremard, C., et al., *The Effect of High-Numerical-Aperture Objectives on Polarization Measurements in Micro-Raman Spectrometry*. Applied Spectroscopy, 1985. 39(6): p. 1036-1039.
92. Pottel, H., et al., *On the Significance of the 4th-Rank Orientational Order Parameter of Fluorophores in Membranes*. Chemical Physics, 1986. 102(1-2): p. 37-44.
93. Weiner, S. and H.D. Wagner, *The material bone: Structure mechanical function relations*. Ann Rev Mater Sci 1998. 28: p. 271-298.
94. Seto, J., et al., *Tough lessons from bone: Extreme mechanical anisotropy at the mesoscale*. Advanced Functional Materials, 2008. 18(13): p. 1905-1911.
95. Diepgen, T.L. and V. Mahler, *The epidemiology of skin cancer*. RBr J Dermatol, 2002. 146(Suppl 61): p. 1-6.
96. Daxer, A. and P. Fratzl, *Collagen fibril orientation in the human corneal stroma and its implicaton to the pathology of keratoconus*. Invest. Ophth. Vis. Sci., 1997. 38: p. 121-129.

97. Makareeva, E., et al., *Structural heterogeneity of type I collagen triple helix and its role in osteogenesis imperfecta*. Journal of Biological Chemistry, 2008. 283(8): p. 4787-4798.
98. Avery, N.C. and A.J. Bailey, *Restraining Cross-Links Responsible for Mechanical Properties of Collagen Fibers: Natural and Artificial*, in *Collagen: Structure and Mechanics*, P. Fratzl, Editor. 2008, Springer Science+Business Media, LLC: New York. p. 81-110.
99. Silver, F.H. and W.J. Landis, *Viscoelasticity, Energy Storage and Transmission and Dissipation by Extracellular Matrices in Vertebrates*, in *Collagen: Structure and Mechanics*, P. Fratzl, Editor. 2008, Springer Science+Business Media, LLC: New York. p. 133-154.
100. Gupta, H.S., et al., *In situ multi-level analysis of viscoelastic deformation mechanisms in tendon collagen*. Journal of Structural Biology, 2009. 169(2): p. 183-191.
101. Boyde, A., et al., *Collagen orientation in compact bone: I. A new method for the determination of the proportion of collagen parallel to the plane of compact bone sections*. Metabolic Bone Disease and Related Research, 1984. 5(6): p. 299-307.
102. Freund, I. and M. Deutsch, *Second-harmonic microscopy of biological tissue*. Opt. Lett., 1986. 11(2): p. 94-96.
103. Williams, R.M., W.R. Zipfel, and W.W. Webb, *Interpreting second-harmonic generation images of collagen I fibrils*. Biophysical Journal, 2005. 88(2): p. 1377-1386.
104. Raghavan, M., et al., *Quantitative polarized Raman spectroscopy in highly turbid bone tissue*. Journal of Biomedical Optics, 2010. 15(3).
105. Falgayrac, G., et al., *New Method for Raman Investigation of the Orientation of Collagen Fibrils and Crystallites in the Haversian System of Bone*. Applied Spectroscopy, 2010. 64(7): p. 775-780.
106. Bonifacio, A. and V. Sergo, *Effects of sample orientation in Raman microspectroscopy of collagen fibers and their impact on the interpretation of the amide III band*. Vibrational Spectroscopy, 2010. 53(2): p. 314-317.
107. Hulmes, D.J.S., *Collagen Diversity, Synthesis and Assembly*, in *Collagen: Structure and Mechanics*, P. Fratzl, Editor. 2008, Springer: New York. p. 15-48.
108. Tsuboi, M., et al., *Raman tensor of the carboxylate anion: A basis for determining aspartate and glutamate side-chain orientations in proteins by polarized Raman spectroscopy*. Biophysical Journal, 2002. 82(1): p. 457a-458a.
109. Lefevre, T., M.E. Rousseau, and M. Pezolet, *Determination of molecular orientation in protein films and fibres by Raman microspectroscopy*. Canadian Journal of Analytical Sciences and Spectroscopy, 2005. 50(1): p. 41-48.
110. Tsuboi, M., et al., *Determination of the amide I Raman tensor for the antiparallel chain beta-pleated sheet*. Biophysical Journal, 2005. 88(1): p. 559A-559A.
111. Tsuboi, M., et al., *Determination of the amide I Raman tensor for the antiparallel beta-sheet: application to silkworm and spider silks*. Journal of Raman Spectroscopy, 2006. 37(1-3): p. 240-247.
112. Tsuboi, M., *Raman scattering anisotropy of biological systems*. Journal of Biomedical Optics, 2002. 7(3): p. 435-441.
113. Overman, S.A., M. Tsuboi, and G.J. Thomas, *Orientations of tyrosine residues (Y21 and Y24) in coat protein subunits of the filamentous virus Ff*. Biophysical Journal, 1998. 74(2): p. A73-A73.

114. Rintoul, L., et al., *Keratin orientation in wool and feathers by polarized Raman spectroscopy*. Biopolymers, 2000. 57(1): p. 19-28.
115. Lefevre, T., M.E. Rousseau, and M. Pezolet, *Protein secondary structure and orientation in silk as revealed by Raman spectromicroscopy*. Biophysical Journal, 2007. 92(8): p. 2885-2895.
116. Bi, X., et al., *A novel method for determination of collagen orientation in cartilage by Fourier transform infrared imaging spectroscopy (FT-IRIS)*. Osteoarthritis and Cartilage, 2005. 13(12): p. 1050-1058.
117. Maxwell, C.A., T.J. Wess, and C.J. Kennedy, *X-ray diffraction study into the effects of liming on the structure of collagen*. Biomacromolecules, 2006. 7(8): p. 2321-2326.
118. Heidemann, E., *Fundamentals Leather Manufacturing*. 1993, Darmstadt: Eduard Roether KG Druckerei und Verlag. 211.
119. Bella, J., B. Brodsky, and H. Berman, *Hydration structure of a collagen peptide*. Structure, 1995. 3: p. 893-906.
120. Wess, T.J. and J.P. Orgel, *Changes in collagen structure: drying, dehydrothermal treatment and relation to long term deterioration*. Thermochimica Acta, 2000. 365(1-2): p. 119-128.
121. Buehler, M.J. and Y.C. Yung, *Deformation and failure of protein materials in physiologically extreme conditions and disease*. Nature Materials, 2009. 8(3): p. 175-188.
122. Porter, D. and F. Vollrath, *The role of kinetics of water and amide bonding in protein stability*. Soft Matter, 2008. 4(2): p. 328-336.
123. Petruska, J.A. and A.J. Hodge, *Subunit model for tropocollagen macromolecule*. Proceedings of the National Academy of Sciences of the United States of America, 1964. 51(5): p. 871-&.
124. Fraser, R.D.B., T.P. MacRae, and E. Suzuki, *Chain conformation in the collagen molecule*. Journal of Molecular Biology, 1979. 129(3): p. 463-481.
125. Bozec, L., G. Van Der Heijden, and M. Horton, *Collagen fibrils: Nanoscale ropes*. Biophysical Journal, 2007. 92(1): p. 70-75.
126. Puxkandl, R., et al., *Viscoelastic properties of collagen: synchrotron radiation investigations and structural model*. Philosophical Transactions of the Royal Society of London Series B-Biological Sciences, 2002. 357(1418): p. 191-197.
127. Misof, K., G. Rapp, and P. Fratzl, *A new molecular model for collagen elasticity based on synchrotron x-ray scattering evidence*. Biophysical Journal, 1997. 72(3): p. 1376-1381.
128. Buehler, M.J., *Nature designs tough collagen: Explaining the nanostructure of collagen fibrils*. Proceedings of the National Academy of Sciences of the United States of America, 2006. 103(33): p. 12285-12290.
129. Morgan, M., et al., *In situ monitoring of tendon structural changes by elastic scattering spectroscopy: Correlation with changes in collagen fibril diameter and crimp*. Tissue Engineering, 2006. 12(7): p. 1821-1831.
130. Cribb, A.M. and J.E. Scott, *Tendon Response to Tensile-stress - an Ultrastructural Investigation of Collagen - Proteoglycan Interaction in Stressed Tendon*. Journal of Anatomy, 1995. 187: p. 423-428.
131. Orgel, J., et al., *Microfibrillar structure of type I collagen in situ*. Proceedings of the National Academy of Sciences of the United States of America, 2006. 103(24): p. 9001-9005.

132. Diamant, J., et al., *Collagen: Ultrastructure and its relation to mechanical properties as a function of aging*. Proc. R. Soc. London, B, 1972. 180: p. 293.
133. Hulmes, D.J.S., et al., *Radial packing, order and disorder in collagen fibrils*. Biophysical Journal, 1995. 68: p. 1661-1670.
134. Fratzl, P., et al., *Fibrillar structure and mechanical properties of collagen*. J. Struct. Biol., 1997. 122: p. 119-122.
135. Fratzl, P., et al., *Fibrillar structure and mechanical properties of collagen*. J Struct Biol, 1998. 122(1-2): p. 119-22.
136. Rigby, B.J., et al., J. Gen. Physiol., 1959. 43: p. 265.
137. Gentleman, E., et al., *Mechanical characterization of collagen fibers and scaffolds for tissue engineering*. Biomaterials, 2003. 24(21): p. 3805-13.
138. Gautieri, A., et al., *Hierarchical Structure and Nanomechanics of Collagen Microfibrils from the Atomistic Scale Up*. Nano Letters, 2011. 11(2): p. 757-766.
139. Lefèvre, T., M.-E. Rousseau, and M. Pézolet, *Orientation-Insensitive Spectra for Raman Microspectroscopy*. Applied Spectroscopy, 2006. 60(8): p. 841-846.
140. Lefèvre, T., et al., *Study by Raman spectromicroscopy of the effect of tensile deformation on the molecular structure of Bombyx mori silk*. Vibrational Spectroscopy, 2009. 51(1): p. 136-141.
141. Gierlinger, N., et al., *Molecular changes during tensile deformation of single wood fibers followed by Raman microscopy*. Biomacromolecules, 2006. 7(7): p. 2077-2081.
142. Okuyama, K., *Revisiting the Molecular Structure of Collagen*. Connective Tissue Research, 2008. 49(5): p. 299-310.
143. Sasaki, N., et al., *Time-resolved X-ray diffraction from tendon collagen during creep using synchrotron radiation*. Journal of Biomechanics, 1999. 32(3): p. 285-292.
144. Orgel, J.P., T.J. Wess, and A. Miller, *The in situ conformation and axial location of the intermolecular cross-linked non-helical telopeptides of type I collagen*. Structure, 2000. 8(2): p. 137-142.
145. Lefevre, T., M.E. Rousseau, and M. Pezolet, *Orientation-insensitive spectra for Raman microspectroscopy*. Applied Spectroscopy, 2006. 60(8): p. 841-846.
146. Gniadecka, M., et al., *Structure of water, proteins, and lipids in intact human skin, hair, and nail*. Journal of Investigative Dermatology, 1998. 110(4): p. 393-398.
147. Gordon, A.M., A.F. Huxley, and F.J. Julian, *Variation in Isometric Tension with Sarcomere Length in Vertebrate Muscle Fibres*. Journal of Physiology-London, 1966. 184(1): p. 170-+.
148. Henninger, H.B., et al., *Effect of sulfated glycosaminoglycan digestion on the transverse permeability of medial collateral ligament*. Journal of Biomechanics, 2010. 43(13): p. 2567-2573.
149. Reese, S.P., S.A. Maas, and J.A. Weiss, *Micromechanical models of helical superstructures in ligament and tendon fibers predict large Poisson's ratios*. Journal of Biomechanics, 2010. 43(7): p. 1394-1400.
150. Admir Masic, L.B., Luca Bertinetti, Roman Schuetz, Shu Wei Chang, Hartmut Metzger, Markus J. Buehler, Peter Fratzl, *Osmotic pressure induced tensile forces in tendon collagen*. Nature Communications, 2014.
151. Cameron, G.J., D.E. Cairns, and T.J. Wess, *The variability in type I collagen helical pitch is reflected in the D periodic fibrillar structure*. Journal of Molecular Biology, 2007. 372(4): p. 1097-1107.

152. Gordon, P.L., et al., *The Far-Infrared Spectrum of Collagen*. Macromolecules, 1974. 7(6): p. 954-956.
153. Thomsen, C. and R. Stephanie, *Raman Scattering in Carbon Nanotubes*. 2007.
154. Litvinchuk, A.P., et al., *Far-Infrared Spectroscopy of the Superconductor Yba2cu4o8*. Zeitschrift Fur Physik B-Condensed Matter, 1992. 86(3): p. 329-335.
155. Mantsch, H.H. and D. Naumann, *Terahertz spectroscopy: The renaissance of far infrared spectroscopy*. Journal of Molecular Structure, 2010. 964(1-3): p. 1-4.
156. Plusquellic, D.F., et al., *Applications of terahertz spectroscopy in biosystems*. Chemphyschem, 2007. 8(17): p. 2412-2431.
157. Knyazev, B.A., et al., *Using of terahertz radiation for monitoring of senile osteoporosis development*. 2007 Joint 32nd International Conference on Infrared and Millimeter Waves and 15th International Conference on Terahertz Electronics, Vols 1 and 2, 2007: p. 555-556.
158. Brusentsova, T.N., et al., *Far infrared spectroscopy of carbonate minerals*. American Mineralogist, 2010. 95(10): p. 1515-1522.
159. Angino, E.E., *Far Infrared (500-30 Cm-1) Spectra of Some Carbonate Minerals*. American Mineralogist, 1967. 52(1-2): p. 137-&.
160. Karr, C. and J.J. Kovach, *Far-Infrared Spectroscopy of Minerals and Inorganics*. Applied Spectroscopy, 1969. 23(3): p. 219-&.
161. Kendix, E., et al., *Far infrared and Raman spectroscopy analysis of inorganic pigments*. Journal of Raman Spectroscopy, 2008. 39(8): p. 1104-1112.
162. Jackson, J.B., et al., *A Survey of Terahertz Applications in Cultural Heritage Conservation Science*. Ieee Transactions on Terahertz Science and Technology, 2011. 1(1): p. 220-231.
163. Fukunaga, K. and I. Hosako, *Innovative non-invasive analysis techniques for cultural heritage using terahertz technology*. Comptes Rendus Physique, 2010. 11(7-8): p. 519-526.
164. Fukunaga, K., et al., *Terahertz spectroscopy for art conservation*. Ieice Electronics Express, 2007. 4(8): p. 258-263.
165. Fukunaga, K., et al., *Application of terahertz spectroscopy for character recognition in a medieval manuscript*. Ieice Electronics Express, 2008. 5(7): p. 223-228.
166. Fukunaga, K., et al., *Terahertz imaging for analysis of historic paintings and manuscripts*. 2008 33rd International Conference on Infrared, Millimeter and Terahertz Waves, Vols 1 and 2, 2008: p. 13-15.
167. Vasanthan, N. and M. Yaman, *Crystallization studies of poly(trimethylene terephthalate) using thermal analysis and far-infrared spectroscopy*. Journal of Polymer Science Part B: Polymer Physics, 2007. 45(13): p. 1675-1682.
168. Damman, P., et al., *Crystallinity of Poly(Aryl Ether Ether Ketone) by Vibrational Spectroscopy*. Macromolecules, 1994. 27(6): p. 1582-1587.
169. Garton, A., et al., *Far-infrared spectroscopy of polyamide fibers and fabrics*. Journal of Polymer Science: Polymer Letters Edition, 1980. 18(2): p. 85-88.
170. Dacosta, V.M., T.G. Fiske, and L.B. Coleman, *Far-Infrared Reflection-Absorption Spectroscopy of Thin Polyethylene Oxide-Films*. Journal of Chemical Physics, 1994. 101(4): p. 2746-2751.
171. Hielscher, R. and P. Hellwig, *Specific Far Infrared Spectroscopic Properties of Phospholipids*. Spectroscopy-an International Journal, 2012. 27(5-6): p. 525-532.

172. Bardon, T., et al. *Material characterization of historical parchment using terahertz time-domain spectroscopy*. in *Infrared, Millimeter, and Terahertz waves (IRMMW-THz)*, 2014 39th International Conference on. 2014.
173. Corridon, P.M., et al., *Time-domain terahertz spectroscopy of artificial skin - art. no. 608007*. Advanced Biomedical and Clinical Diagnostic Systems IV, 2006. 6080: p. 8007-8007.
174. Woodward, R.M., et al., *Terahertz pulse imaging of ex vivo basal cell carcinoma*. Journal of Investigative Dermatology, 2003. 120(1): p. 72-78.
175. Woodward, R.M., et al., *Terahertz pulsed imaging of skin cancer in the time and frequency domain*. Journal of Biological Physics, 2003. 29(2-3): p. 257-261.
176. Mizuno, M., et al., *Absorption Properties of Oriented Collagen in Terahertz Band*. 2011 36th International Conference on Infrared, Millimeter, and Terahertz Waves (IRMMW-Thz), 2011.
177. Mizuno, M., et al. *Terahertz observation of salt penetration in collagen fibers*. in *Infrared, Millimeter, and Terahertz waves (IRMMW-THz)*, 2014 39th International Conference on. 2014.
178. Fratzl, P. and R. Weinkamer, *Nature's hierarchical materials*. Progress in Materials Science, 2007. 52(8): p. 1263-1334.
179. Kanawka, K., *Ultrastructural Deformation in the Fibrillar Matrix of Demineralised Bone*. Diploma Thesis, 2006-2007.
180. Reznikov, N., et al., *Three-dimensional imaging of collagen fibril organization in rat circumferential lamellar bone using a dual beam electron microscope reveals ordered and disordered sub-lamellar structures*. Bone, 2013. 52(2): p. 676-683.
181. Currey, J.D., *Bones: structure and mechanics*. Princeton University Press, New Jersey., 2002.
182. Bruggeman, D.A.G., *Calculation of different physical constants of heterogen substances I Dielectric constants and conductivity of mixtures from isotrop substances*. Annalen Der Physik, 1935. 24(8): p. 665-679.
183. Weiglhofer, W.S., A. Lakhtakia, and B. Michel, *Maxwell Garnett and Bruggeman formalisms for a particulate composite with bianisotropic host medium (vol 15, pg 263, 1997)*. Microwave and Optical Technology Letters, 1999. 22(3): p. 221-221.
184. Schade, U., et al., *Measured characteristics of infrared edge radiation from BESSY II*. Nuclear Instruments & Methods in Physics Research Section a-Accelerators Spectrometers Detectors and Associated Equipment, 2000. 455(2): p. 476-486.
185. Smolyakov, N., H. Yoshida, and A. Hiraya, *Edge radiation and its potential to electron beam diagnostics at HiSOR*. Nuclear Instruments & Methods in Physics Research Section a-Accelerators Spectrometers Detectors and Associated Equipment, 2000. 448(1-2): p. 73-75.
186. Bosch, R.A., *Edge radiation in an electron storage ring*. Nuovo Cimento Della Societa Italiana Di Fisica D-Condensed Matter Atomic Molecular and Chemical Physics Fluids Plasmas Biophysics, 1998. 20(4): p. 483-493.
187. Zaitsev, A., *Optical Properties of Diamond: A Data Handbook*. Springer, 2001.
188. Suzaki, Y. and A. Tachibana, *Measurement of Mu-M Sized Radius of Gaussian Laser-Beam Using Scanning Knife-Edge*. Applied Optics, 1975. 14(12): p. 2809-2810.
189. Skinner, D.R. and R.E. Whitcher, *Measurement of Radius of a High-Power Laser-Beam near Focus of a Lens*. Journal of Physics E-Scientific Instruments, 1972. 5(3): p. 237-&.

190. Wustneck, R., et al., *The Modification of the Triple Helical Structure of Gelatin in Aqueous-Solution .1. The Influence of Anionic Surfactants, Ph-Value, and Temperature*. Colloid and Polymer Science, 1988. 266(11): p. 1061-1067.
191. Kozlov, P.V. and G.I. Burdygina, *The Structure and Properties of Solid Gelatin and the Principles of Their Modification*. Polymer, 1983. 24(6): p. 651-666.
192. Weiner, S., et al., *Dead-Sea Scroll Parchments - Unfolding of the Collagen Molecules and Racemization of Aspartic-Acid*. Nature, 1980. 287(5785): p. 820-823.
193. Ginell, W.S., unpublished work.
194. Fuchs, E., *Keratins and the skin*. Annual Review of Cell and Developmental Biology, 1995. 11: p. 123-153.
195. Cohen, N.S., M. Odlyha, and G.M. Foster, *Measurement of shrinkage behaviour in leather and parchment by dynamic mechanical thermal analysis*. Thermochimica Acta, 2000. 365(1-2): p. 111-117.
196. Badea, E., G. Della Gatta, and P. Budrugaec, *Characterisation and evaluation of the environmental impact on historical parchments by differential scanning calorimetry*. Journal of Thermal Analysis and Calorimetry, 2011. 104(2): p. 495-506.
197. Bozec, L. and M. Odlyha, *Thermal Denaturation Studies of Collagen by Microthermal Analysis and Atomic Force Microscopy*. Biophysical Journal, 2011. 101(1): p. 228-236.
198. Aliev, A.E., *Solid-state NMR studies of collagen-based parchments and gelatin*. Biopolymers, 2005. 77(4): p. 230-245.
199. Rabin, I. and O. Hahn, *Dead Sea Scrolls Exhibitions around the World: Reasons for Concern*. Restaurator-International Journal for the Preservation of Library and Archival Material, 2012. 33(2): p. 101-121.
200. Mozir, A., et al., *On oxidative degradation of parchment and its non-destructive characterisation and dating*. Applied Physics a-Materials Science & Processing, 2011. 104(1): p. 211-217.
201. Marengo, E., et al., *Development of a technique based on multi-spectral imaging for monitoring the conservation of cultural heritage objects*. Analytica Chimica Acta, 2011. 706(2): p. 229-237.
202. Badea, E., et al., *Study of deterioration of historical parchments by various thermal analysis techniques complemented by SEM, FTIR, UV-Vis-NIR and unilateral NMR investigations*. Journal of Thermal Analysis and Calorimetry, 2008. 91(1): p. 17-27.
203. Masic, A., et al., *Solid-state and unilateral NMR study of deterioration of a Dead Sea Scroll fragment*. Analytical and Bioanalytical Chemistry, 2012. 402(4): p. 1551-1557.
204. Facchini, A., et al., *Ancient parchment examination by surface investigation methods*. Journal of Colloid and Interface Science, 2000. 231(2): p. 213-220.
205. Bicchieri, M., et al., *Non-destructive spectroscopic characterization of parchment documents*. Vibrational Spectroscopy, 2011. 55(2): p. 267-272.
206. Mannucci, E., et al., *Recovery of ancient parchment: characterization by vibrational spectroscopy*. Journal of Raman Spectroscopy, 2000. 31(12): p. 1089-1097.
207. Edwards, H.G.M. and F.R. Perez, *Application of Fourier transform Raman spectroscopy to the characterization of parchment and vellum. II - Effect of biodeterioration and chemical deterioration on spectral interpretation*. Journal of Raman Spectroscopy, 2004. 35(8-9): p. 754-760.
208. Kazanci, M., et al., *Raman imaging of two orthogonal planes within cortical bone*. Bone, 2007. 41(3): p. 456-461.

209. Kazanci, M., et al., *Bone osteonal tissues by Raman spectral mapping: Orientation-composition*. Journal of Structural Biology, 2006. 156(3): p. 489-496.
210. Gierlinger, N., et al., *Cellulose microfibril orientation of Picea abies and its variability at the micron-level determined by Raman imaging*. Journal of Experimental Botany, 2010. 61(2): p. 587-595.
211. Wang, X.J., et al., *Group refractive index measurement of dry and hydrated type I collagen films using optical low-coherence reflectometry*. Journal of Biomedical Optics, 1996. 1(2): p. 212-216.
212. Overman, S.A., M. Tsuboi, and G.J. Thomas, *Orientations of tyrosine residues (Y21 and Y24) in coat protein subunits of the filamentous virus Ff*. Biophysical Journal, 1998. 74(2): p. A73-A73.
213. Donnelly, E., *Methods for Assessing Bone Quality: A Review*. Clinical Orthopaedics and Related Research, 2011. 469(8): p. 2128-2138.
214. Chalmers, J.M. and P.R. Griffiths, *Handbook of Vibrational Spectroscopy*. 1999-2013: Wiley.
215. Richard A. Nyquist, et al., *Handbook of Infrared and Raman Spectra of Inorganic Compounds and Organic Salts*. 1996: ACADEMIC PressINC.
216. Prasad, P.S.R., A. Pradhan, and T.N. Gowd, *In situ micro-Raman investigation of dehydration mechanism in natural gypsum*.
217. Rabin, I., et al., *Analysis of an antique alum tawed parchment*, in *A Holistic View for Historic Interiors*. 2010: Roma.
218. Mantouvalou, I., et al., *3D Micro-XRF for Cultural Heritage Objects: New Analysis Strategies for the Investigation of the Dead Sea Scrolls*. Analytical Chemistry, 2011. 83(16): p. 6308-6315.
219. Bendor, Y.K., *Some Geochemical Aspects of the Dead Sea and the Question of Its Age*. Geochimica Et Cosmochimica Acta, 1961. 25(4): p. 239-&.
220. Nissenbaum, A., *The Microbiology and Biogeochemistry of the Dead Sea*. Microbial Ecology, 1975. 2(2): p. 139-161.
221. Nissenbaum, A., *Minor and Trace-Elements in Dead Sea-Water*. Chemical Geology, 1977. 19(2): p. 99-111.
222. Nishri, A., *The Geochemistry of Manganese in the Dead-Sea*. Earth and Planetary Science Letters, 1984. 71(2): p. 415-426.
223. Epstein, J.A., B. Zelviński, and G. Ron, *Manganese in Sodium-Chloride Precipitating from Mixing Dead Sea Brines*. Israel Journal of Earth Sciences, 1975. 24(3-4): p. 112-113.
224. Steinhorn, I. and J.R. Gat, *The Dead-Sea*. Scientific American, 1983. 249(4): p. 102-&.
225. Steinhorn, I., *Insitu Salt Precipitation at the Dead-Sea*. Limnology and Oceanography, 1983. 28(3): p. 580-583.
226. Boghosian, S., *Structural damage of parchment at the molecular level assessed by Raman spectroscopy*. Rene Larsen ed., European Communities, DG for Research, 2007. "Improved damage assessment of parchment: Assessment, data collection and sharing of knowledge", : p. 105-109.
227. Larsen, R., D. V. Poulsen, F. Juchauld, H. Jerosch, M. Odlyha, J. de Groot, T. Wess, J. Hiller, C. Kennedy, G. Della Gatta, E. Badea, A. Masic, S. Boghosian and D. Fessas, *Damage assessment of parchment: complexity and relations at different structural levels. 14th ICOM-CC Meeting, Hague. . 2005*.



- 228. Xu, W., G.M. Roomans, and B. Forslind, *Elemental Distribution in Guinea-Pig Skin as Revealed by X-Ray-Microanalysis in the Scanning-Transmission Microscope*. Journal of Investigative Dermatology, 1982. 79(3): p. 167-169.
- 229. McGrath, J.A., R.A.J. Eady, and F.M. Pope, *Anatomy and Organization of Human Skin*, in *Rook's Textbook of Dermatology*. 2008, Blackwell Publishing, Inc. p. 45-128.
- 230. Yardley, H.J. and R. Summerly, *Lipid-Composition and Metabolism in Normal and Diseased Epidermis*. Pharmacology & Therapeutics, 1981. 13(2): p. 357-383.
- 231. Gray, G.M. and H.J. Yardley, *Mitochondria and Nuclei of Pig and Human Epidermis - Isolation and Lipid-Composition*. Journal of Investigative Dermatology, 1975. 64(6): p. 423-430.
- 232. Cansdale, L., *Qumran and the Essenes: A Re-evaluation of the Evidence*. 1997.



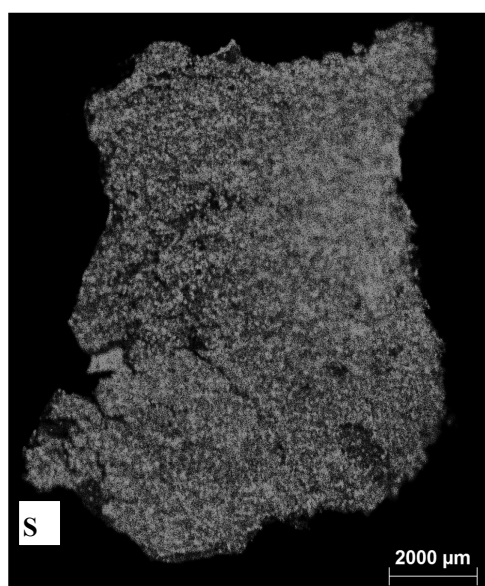
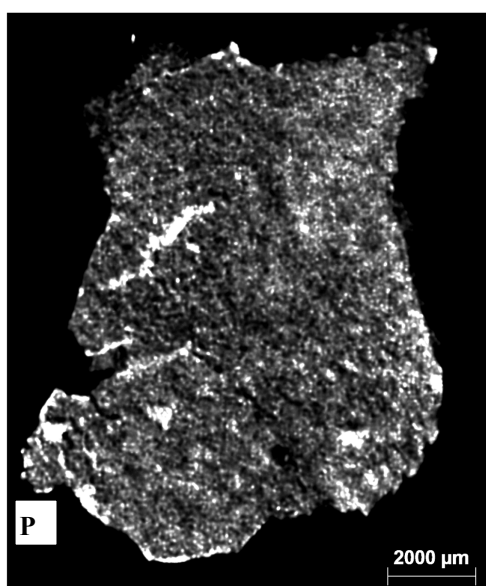
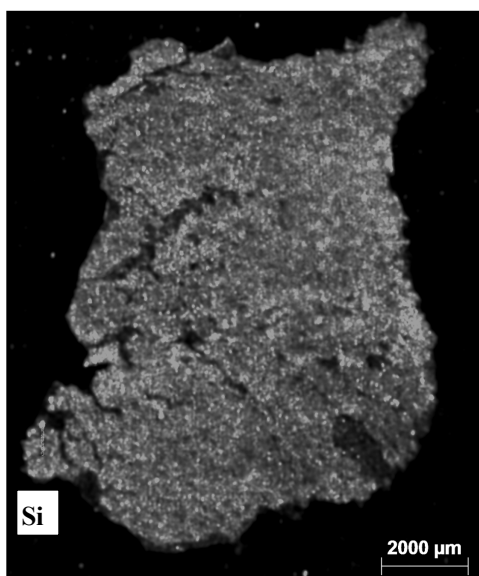
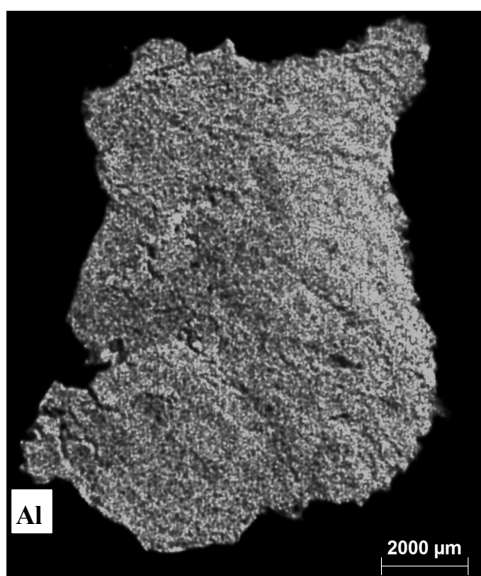
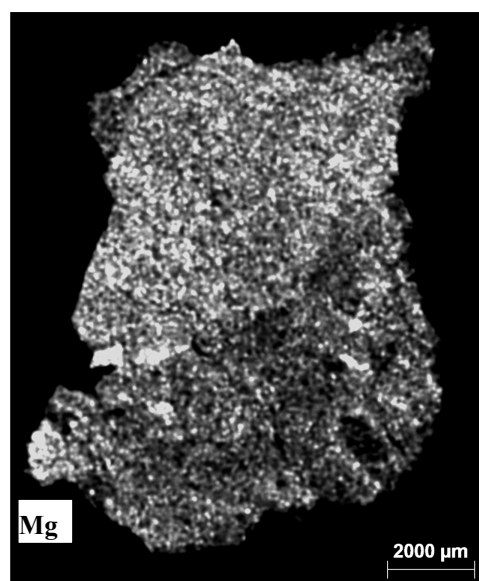
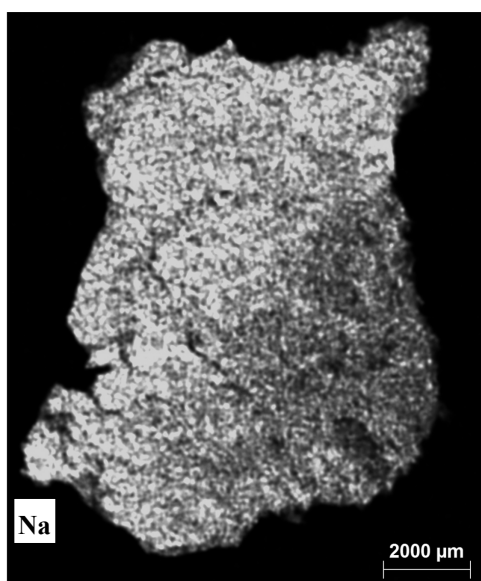
## List of authors' publications related to this work

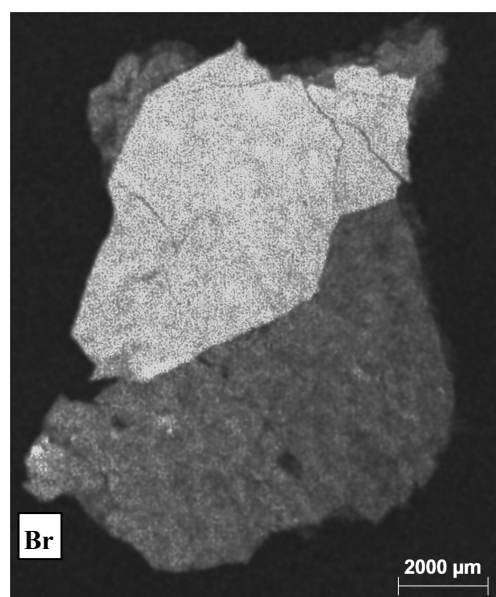
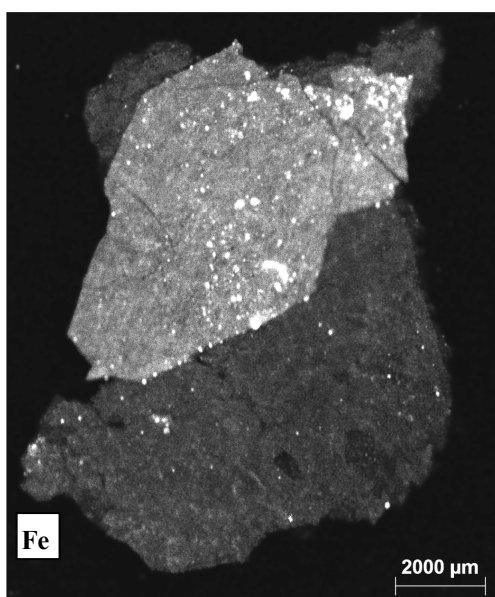
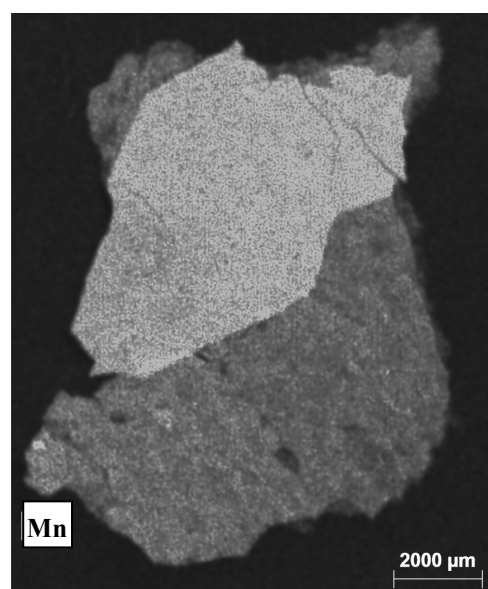
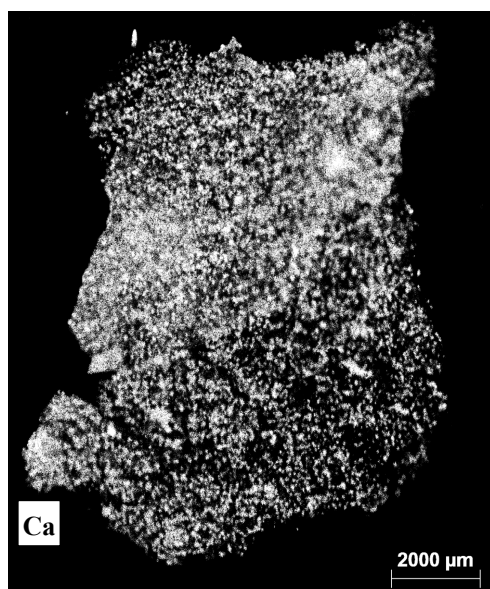
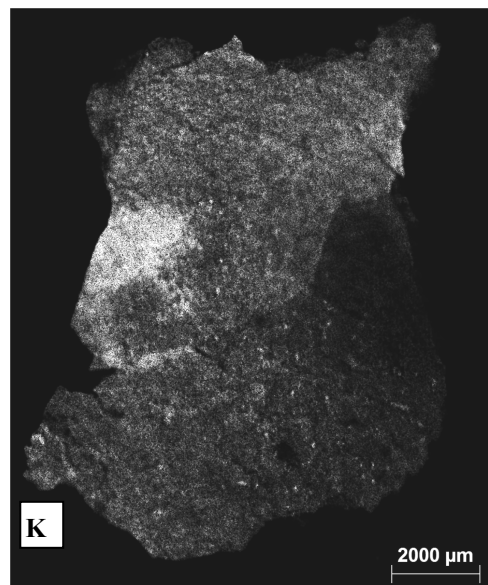
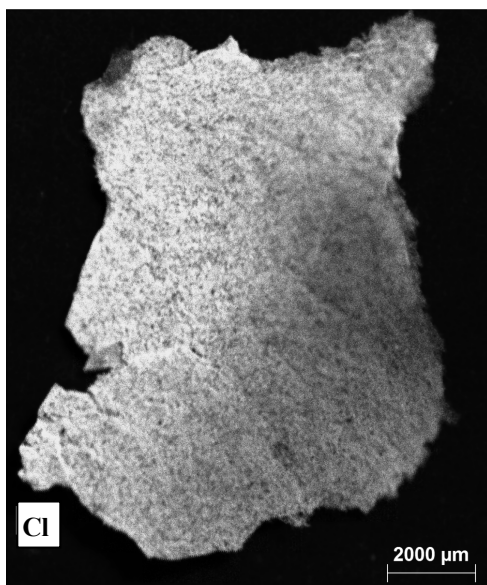
- 2015 Roman Schuetz, D. Fix, U. Schade, E. F. Aziz, N. Timofeeva, R. Weinkamer, and A. Masic, **"Anisotropy in Bone Demineralization Revealed by Polarized Far-IR Spectroscopy"** *Molecules*, vol. 20, no. 4, pp. 5835-5850, **2015**.
- 2014 Admir Masic, Luca Bertinetti, Roman Schuetz, Shu Wei Chang, Hartmut Metzger, Markus J. Buehler, Peter Fratzl, **"Osmotic pressure induced tensile forces in tendon collagen,"** *Nature Communications*, **2014**.
- 2013 Roman Schuetz, L. Bertinetti, I. Rabin, P. Fratzl, and A. Masic, **"Quantifying degradation of collagen in ancient manuscripts: the case of the Dead Sea Temple Scroll,"** *Analyst*, vol. 138, no. 19, pp. 5594-5599, **2013**.
- 2011 A. Masic, L. Bertinetti, R. Schuetz, L. Galvis, N. Timofeeva, J. W. C. Dunlop, J. Seto, M. A. Hartmann, and P. Fratzl, **"Observations of Multiscale, Stress-Induced Changes of Collagen Orientation in Tendon by Polarized Raman Spectroscopy,"** *Biomacromolecules*, vol. 12, no. 11, pp. 3989-3996, **2011**.

## In preparation:

- I. Roman Schuetz, Ira Rabin, Oliver Hahn, Peter Fratzl, Admir Masic, **"Analytical study of the Temple Scroll – Reconstruction of an Unknown Ancient Manufacture Practice"**.
- II. Roman Schuetz, Ira Rabin, Ulrich Schade, Peter Fratzl, Admir Masic, **"Deterioration of Collagen in Parchments Studied by Far-IR Spectroscopy "**.

## Supplemental materials





S 1: Gray scaled  $\mu$ -XRF maps of Figure 43 for clarity reasons.



## **Eidesstattliche Erklärung**

Hiermit versichere ich, dass ich die vorliegende Dissertationsarbeit selbstständig verfasst und keine anderen als die angegebenen Quellen und Hilfsmittel benutzt habe und alle Ausführungen, die anderen Schriften wörtlich oder sinngemäß entnommen wurden, kenntlich gemacht sind. Ein Promotionsverfahren zu einem früheren Zeitpunkt an einer anderen Hochschule oder bei einem anderen Fachbereich wurde nicht beantragt.

Berlin, den 13. Juli 2015

Roman Schütz





## Danksagung

Eine überwältigende Dankbarkeit erfüllt mich, wenn ich mir bewusst mache, was für ein seltener Privileg es ist, an solch einzigartigem und zugleich unendlich interessantem Schatz wie den Schriften vom Toten Meer arbeiten zu dürfen. Als ich bei einer Ausstellung in Köln, damals noch Abiturient, zum ersten Mal von dem faszinierenden Fund erfuhr, habe ich mir bei starrendem Betrachten nicht träumen lassen, dass die außergewöhnlichste von allen dieser Schriftrollen, die Tempelrolle, später so nah an mein Leben heran tritt. Ausgerechnet das Physikstudium, das Fach mit scheinbar geringem Bezug zu den antiken Schriftrollen, ermöglichte es mir die wertvollen Funde nach vielen Jahren unerwartet wieder zu erblicken.

Für diese *Schicksalsfügung* bin ich unendlich dankbar.

Neben vielen anderen interessanten Projekten betreibt Dr. Ira Rabin eine sehr leidenschaftliche und ambitionierte Qumranforschung. Ich bin ihr sehr dankbar dafür, dass sie mich in diese Arbeit und in die Forschungsgruppe von Dr. Oliver Hahn mit einbezogen hat, für dessen Unterstützung und bei der Stiftung Preussischer Kulturbesitz ich mich ebenso bedanke. Dr. Ira Rabin hat sich immer Zeit genommen, sogar an unzähligen Sonntagen, um auf meine Fragen sehr detailliert einzugehen. Sie hat mich in meiner wissenschaftlichen Entwicklung und der gemeinsamen Forschung stets gefördert und inspiriert. Danken möchte ich ihr auch für die Vermittlung an das Forschungsteam von Dr. Admir Mašić am Max Planck Institut unter der Leitung von Herren Professor Dr. Peter Fratzl.

Bei Professor Dr. Peter Fratzl und Dr. Admir Mašić möchte ich mich besonders bedanken für ihre wissenschaftliche Unterstützung, die Bereitstellung von Mitteln und ihre Wohlgesonnenheit gegenüber mir persönlich aber auch dem außergewöhnlichen Projekt, vielen Dank! Die gruppenübergreifend positive, hilfsbereite und freundliche Teamatmosphäre ist Allen voran der Institutsleitung, Herren Professor Dr. Peter Fratzl zu verdanken. Auch dem Dr. Admir Mašić möchte ich für seine dynamische und motivierende Art, mit der er mich stets unterstützt und motiviert hat, besonders danken. Thank you Admir!

Vielen Dank auch an den Promotionsausschuss: Frau Professorin Dr. Birgit Kanngießer, Herr Professor Dr. Christian Thomsen und Herr Professor Dr. Peter Fratzl.

Ebenso möchte ich mich bei Dr. Luca Bertinetti für seine Hilfsbereitschaft aber auch für seine humorvolle und leichte Umgangsart bedanken. Seine Unterstützung hat zum Erfolg der Arbeit entschieden beigetragen.

Auch für das besondere Engagement von Klaus Bienert und Jan von Szada-Borrryszkowski bei der Herstellung experimenteller Mittel bedanke ich mich sehr. Einen besonderen Dank möchte ich auch an Dr. Sidney Omelon und an Dr. Emanuel Schenk aussprechen für die sprachliche Überprüfung des jeweils englischen und deutschen Textes. Diese uneigennützigen Hilfen auch von sehr vielen anderen Kollegen im wissenschaftlichen Alltag am Institut haben mich sehr beeindruckt. Damit möchte ich auch den unzähligen Menschen, Freunden und Kollegen, denen ich während der Promotionszeit begegnet bin für ihre großen wie kleinen Unterstützungen und ihre Wohlgesonnenheit ganz herzlich danken. Einige Kooperationspartner möchte ich namentlich hervorheben, weil ihr Engagement oder die Bereitstellung von Experimentieranlagen sehr wichtig für die Ergebnisse der Forschung dieser Arbeit gewesen sind. Es sind: Dr. Adolfo Roitman und Ms Hasia Rimon (Shrine of the book, Israel museum), Henk de Groot (Inden witten Hasewint), Dr. James Weaver (Harvard University), Dr. Ulrich Schade (IRIS Beamline, BESSY, HMI), Frau Gisela Weinbeg (Fritz-Haber-Institute der MPG), Professor Giuseppe Pappalardo und Dr. Francesco Paolo Romano (Istituto Nazionale di Fisica Nucleare, Catania), Dr. Peter Lasch (Robert-Koch-Institute), Dr. Roald Tagle (Broker, Berlin), Dr. Richard Weinkamer (MPIKG), Dr. Michaela Eder (MPIKG), Dr. Chenghao Li (MPIKG) und Dr. Stefan Siegel (MPIKG).

Zum Abschluss möchte ich mich vom ganzen Herzen bei meinen fantastischen Freunden bedanken, und insbesondere natürlich auch bei meiner wunderbaren Familie – meiner Super-tante Elsa Spiegel, meinen tollen Schwestern: Lia, Inna, Elina und Rimma samt ihren Familien und bei meinen lieben und fürsorglichen Eltern Herta und Andreas Schuetz. Sie und viele andere, die ich hier nicht explizit namentlich genannt habe, haben mich auf die eine oder andere Weise unterstützt, beeinflusst, ermutigt, inspiriert und die Fertigstellung der Dissertation mit mir mitersehnt.

Dankeschön!